INORGANIC ELECTRON-BEAM RESISTS FOR INTEGRATED CIRCUITS

by

Olasebikan Alade Fakolujo, B.Sc.

A Thesis Submitted for the Degree of
Doctor of Philosophy
of the
University of London

Department of Electrical Engineering
Imperial College of Science and Technology
London SW7 2BT

January 1988

ABSTRACT

Anhydrous cadmium chloride ($CdCl_2$) was used as an electron beam (e-beam) resist for Si/SiO_2 feature fabrication: e-beam decomposition of $CdCl_2$ was followed by dry-etching (reactive ion etching) of SiO_2. $CdCl_2$ was chosen as an e-beam resist material because; (i) its e-beam decomposition products, cadmium and chlorine, are volatile at the irradiation temperature, (ii) it has high chemical resistance to fluorine based plasma, and (iii) areas of $CdCl_2$ not exposed to e-beam irradiation are easily removed. The decomposition efficiency of $CdCl_2$ film (140nm thick) was found to be $5mC/cm^2$ for irradiation carried out with a 2keV beam, and at a temperature of 210^oC. The time, gas flow rate, gas pressure, and r.f. power dependence of etch rates were studied. Selectivity values equal to or possibly much better than 16:1 were achieved in etching SiO_2 compared to $CdCl_2$, and a resolution of 100nm (the order of the film grain size) was obtained.

Lead chloride ($PbCl_2$) and $PbCl_2/CdCl_2$(20%) (Pb:Cd elemental ratio was 4:1) films were e-beam irradiated, in order to study the decomposition kinetics and to write metallic and metallic oxide patterns. The decomposition kinetics were studied as a function of temperature, substrate, and current density, by using a quadrupole mass spectrometer to monitor the reaction products, namely cadmium (when appropriate) and chlorine (in all cases). Two classes of reaction mechanisms were used to interpret the results of the decomposition processes in $PbCl_2$ and $PbCl_2/CdCl_2$(20%) films. Patterns of Pb, Pb-Cd, and oxidised Pb-Cd were written, but it was found that Pb films were not continuous, while films of Pb-Cd and Pb-Cd oxide were continuous. The pattern resolutions were found to decrease with increasing irradiation temperature. The resolution of the Pb-Cd patterns were found to be superior to those of Pb patterns. The resolution of Pb-Cd and Pb patterns, written at 135^oC, were 0.18μm and 0.29μm respectively. Sets of Pb-Cd and Pb-Cd oxide lines, of widths ranging between 0.8-3.0μm were written. Ultimate resolution of ~50nm is possible for oxidised Pb-Cd film.

In the course of the above studies, compositional analyses of the samples were carried out by one or more of the following techniques: electron probe micro-analysis (EPMA), electron spectroscopy for chemical analysis (ESCA), and secondary ion mass spectroscopy (SIMS). Surface morphology studies of the samples were performed by scanning electron microscopy (SEM).

To my mother, Adunola Fakolujo, and
In loving memory of my father
John Olowookere Fakolujo

Acknowledgements

I would like to express my profound gratitude to my supervisor, Professor Mino Green, for his enlightened advice and never failing enthusiasm, and support.

I would like to thank my wife, Sijuwola Omobolaji, for her understanding and encouragement, especially in the latter stages of the project.

The efforts of Drs. C.J. Aidinis and J.P.V. Drazin in writing the computer programs used to carry out the electron-beam studies are greatly appreciated.

The major part of this programme was sponsored by the Federal Government of Nigeria, and I acknowledge the Nigerian tax payers for their contribution towards the postgraduate scholarship fund.

Finally, I would like to thank all my friends, who contributed towards the successful completion of this work, and made my stay at Imperial College very enjoyable.

The power of a Thought to materialise depends upon the intensity with which it is held, and the emotional force with which it is applied.

Contents

		Page
Chapter 1:	INTRODUCTION AND LITERATURE SURVEY	9
1.1	LITHOGRAPHY	9
1.1.1	Introduction	9
1.1.2	Optical Lithography	10
1.1.3	Electron Beam Lithography	11
1.1.4	X-Ray Lithography	14
1.1.5	Other Lithography Techniques	17
1.2	DRY ETCHING PROCESSES	20
1.2.1	Introduction	20
1.2.2	Dry Etching Techniques	21
1.2.3	Chemistry and Physics of Etching Reactions	27
1.2.4	Process Parameters Effects	27
1.2.5	SiO_2 Dry Etching for VLSI Technology	31
1.2.6	End-Point Detection	32
1.3	A WAY FORWARD	35
Chapter 2:	SOME PHYSICAL PROPERTIES OF THIN FILMS OF $CdCl_2$ AND $PbCl_2$	36
2.1	INTRODUCTION	36
2.2	CRYSTAL STRUCTURE	36
2.2.1	$CdCl_2$ Crystal Structure	36
2.2.2	$PbCl_2$ Crystal Structure	39
2.3	$CdCl_2.H_2O$ AND $PbCl_2$ GRAIN STRUCTURE AND MEAN GRAIN SIZE DETERMINATION	39
2.4	X-RAY DIFFRACTION STUDIES	43
2.4.1	X-Ray Powder Diffraction of $CdCl_2.H_2O$	43
2.4.2	X-Ray Diffraction of $CdCl_2.H_2O$ and $PbCl_2$ Films	48
2.5	QUARTZ CRYSTAL MICROBALANCE STUDIES	52
Chapter 3:	EXPERIMENTAL TECHNIQUES	56
3.1	SAMPLE PREPARATION AND STORAGE	56
3.1.1	Substrate Preparation	56
3.1.2	Film Deposition Procedure	57

		Page
3.1.3	Sample Handling and Storage	61
3.2	FILM THICKNESS AND REFRACTIVE INDEX DETERMINATION	61
3.3	EXPERIMENTAL SET-UP FOR ELECTRON BEAM RADIOLYSIS	62
3.3.1	Vacuum Equipment	62
3.3.2	Experimental Rig Used for Electron Beam Decomposition Work	62
3.3.3	Experimental Procedures	62
3.4	PLASMA-ASSISTED ETCHING AND END-POINT DETERMINATION: EXPERIMENTAL SET-UP	69
3.4.1	Equipment	69
3.4.2	Etching and End-Point Detection Procedure	69
3.5	THIN FILM ANALYSIS AND SURFACE MORPHOLOGY STUDIES	70
Chapter 4:	$CdCl_2$ INORGANIC RESIST: RESULTS AND DISCUSSION	74
4.1	$CdCl_2$ ELECTRON BEAM DECOMPOSITION RESULTS	74
4.2	PLASMA-ASSISTED ETCHING OF $CdCl_2$ AND SiO_2	80
4.2.1	Plasma Etching Results	80
4.2.2	Reactive-Ion Etching Results	91
4.3	DISCUSSION	101
4.4	SUMMARY	104
Chapter 5:	MATERIALS FOR THE ABSORBER LAYER OF X-RAY MASK: RESULTS AND DISCUSSIONS	106
5.1	ELECTRON BEAM DECOMPOSITION KINETICS	106
5.1.1	Temperature and Substrate Dependence Results	107
5.1.2	Current Density Dependence Results	117
5.1.3	Discussion	122
5.2	LITHOGRAPHY	132
5.2.1	Results	132
5.2.2	Discussion	150
5.3	SUMMARY	164

Page

APPENDICES

I CALIBRATION OF THE QUADRUPOLE MASS SPECTROMETER 167

II LISTING OF SOME COMPUTER PROGRAMS 169

III ELLIPSOMETRIC AND "TALYSTEP" FILM THICKNESS MEASUREMENTS (DESCRIPTION OF BASIC OPERATING PRINCIPLE) 174

III-1 INTRODUCTION 174

III-2 ELLIPSOMETRY FOR FILM THICKNESS MEASUREMENT 174

(a) Basic Theory 175

(b) Experimental Applications 180

III-3 STYLUS INSTRUMENT ("TALYSTEP") 187

IV PRELIMINARY INVESTIGATION OF ELECTRON BEAM IRRADIATION OF URANIUM TETRA-CHLORIDE (UCl_4) 188

V A BRIEF NOTE ON EPMA MEASUREMENTS 190

VI SOLUTION OF THE ORDINARY DIFFERENTIAL EQUATION OF THE FORM $\partial^2 n/\partial x^2 - Jn + K = 0$ (J and K are constants) 191

REFERENCES 192

References for Chapter 1 192

References for Chapter 2 195

References for Chapter 3 196

References for Chapter 4 196

References for Chapter 5 197

References for Appendix III 199

References for Appendix IV 199

References for Appendix V 199

CHAPTER 1

INTRODUCTION AND LITERATURE SURVEY

In the evolution of semiconductors, two opposite but related trends may be observed, on the one hand, an increase in complexity and density of solid state device structures, and on the other hand, feature sizes which are now in the submicron range. These trends are essential to the fabrication of today's and tomorrow's high density integrated circuits (ICs).

The primary processes used to manufacture today's ICs include, chemical vapour deposition of silicon and dielectric films, semiconductor oxidation, ion-implantation and diffusion, metallisation, lithography, and dry etching.

Lithography and dry etching will be reviewed, with emphasis on work that has been done in the field of inorganic electron beam resists, since this is the concern of the work reported in this thesis.

1.1 LITHOGRAPHY

1.1.1 Introduction

Lithography is a pattern definition process, which can be done by the use of a mask or by direct writing , through the use of appropriate resist(s) on the semiconductor wafer. The defined patterns are for making circuits, involving such features as gate electrodes, contact windows, metal interconnections, and so on.

In the past, most lithographic work has been by light (near UV) exposure of photo-sensitive polymer film (known as resist) through a photomask. The resist is then developed, with either exposed (positive resist) or unexposed (negative resist) areas of film removed. Such resists are known as photoresists.

There are other types of resists, such as electron resists, x-ray resists, and ion resists. Multilayer and inorganic resists can be used in any of the above mentioned resist systems. The type of resist used in very large scale integration (VLSI) lithography depends, largely, on the exposure tool used. Exposure tool performance can be evaluated by three parameters: resolution, registration (tolerance), and throughput. Resolution is a measure of the minimum feature that can be defined in a resist [1]. Registration is how well successive mask levels are registered on the resist, and throughput is the number of processed wafers per hour.

The photolithography scheme is capable of ~1μm resolution, 0.5μm registration, and up to 100 exposures per hour [2]. Electron-beam lithography has been used mainly to produce photomasks, but efforts are being directed towards direct wafer exposure to obtain sub-micron resolution. X-ray lithography achieves ~0.5μm resolution and 0.5μm registration, but the scheme is yet to be fully utilised [2].

1.1.2 Optical Lithography.

There are three primary optical exposure methods, known as contact, proximity, and projection printing.

In contact printing, very high resolution is possible, a feature of 1μm in 0.5μm of positive resist is achievable. The main problem in contact printing is dirt, because any dirt on the wafer can damage the mask, and is printed as a defective pattern on subsequent exposures.

Proximity printing is quite similar to contact printing, except that a gap of about 10 to 25μm is maintained between the mask and wafer during exposure. This minimises the mask damage problem that is highly probable in contact printing. The resolution achievable is proportional to $(\lambda g)^{0.5}$ [3], where λ is the wavelength of the exposure light, and g the gap between mask and wafer. Resolution of 2 to 4μm is possible with proximity printing.

The last of these methods, the projection method, has its mask placed some centimeters away from the wafer, and only a small area of the mask is imaged. The whole wafer is then progressively exposed by a step-and-repeat system. The problem of mask damage is eliminated. A resolution of about 1.0μm is achievable [4]. Projection printing is a diffraction limited system. The resolution is given by $0.5(\lambda/NA)$, where NA is the numerical aperture of the projection optics, and λ the exposure wavelength. The depth of focus over which image is not degraded is approximately $\pm 0.5\lambda/(NA)^2$.

In general, a minimum feature of 1.0 to 1.5μm is possible with optical lithography for VLSI circuit fabrication. The major problem with this scheme is the level-to-level registration, and the throughput. Multi-level resist schemes [2] are being devised in order to obtain a resolution of 0.5μm with optical lithography.

1.1.3 Electron Beam Lithography.

The advantages of electron beam (e-beam) lithography for pattern definition are: submicron features can be generated, wafers can be patterned without a mask, the process can be automated, and electron beam has a better depth of focus than an optical lithography system. The e-beam exposure system is capable of detecting features on a silicon wafer, which can lead to extremely accurate level-to-level registration. The main problem with e-beam lithography is the speed of writing.

Poly-methyl-methacrylate (PMMA) and poly-butene-1 sulfone (PBS) are examples of positive-type electron resists, and poly-glycidyl-methacrylate-co-ethyl acrylate (COP) is a negative-type resist, all are examples of polymer electron resist [2]. Negative-type and positive-type electron resists have resolutions of about 1.0 and 0.1μm respectively [2], the relatively poor resolution of negative-type resist is due to swelling during development. In general, slow resists have higher resolution than fast resists, resulting in sensitivity-resolution trade-off in application [5].

The needs of modern lithography in terms of resist behaviour are defined in terms of sensitivity and contrast. The minimum number of electrons (N_m) required to write a pattern in a given pixel, is given by:

$$N_m = \frac{SL_p^2}{e} \qquad \text{--------(1.1.1)}$$

where L_p is the minimum pixel dimension, and e the electronic charge. The electron resist sensitivity, S, is defined either as the electron dose required to ensure complete positive resist development, or to have 50% negative resist thickness undeveloped [5]. Contrast properties are revealed in the edge resolution or "sharpness" of the structures, resulting from the application of the resist.

The major challenge of e-beam lithography is in adapting the existing submicron capability at an economically justified throughput [2]. Brighter and higher current sources are necessary (and being developed) to overcome this disability.

Electron Beam - Resist Coated Surface Interaction.

Depending on the beam energy, resist thickness, and the atomic number of the underlying substrate, backscattered electrons from the substrate will contribute to the total dose received by the resist film. The backscattered contribution can be as much as 30% of the total dose [6]. As the beam energy increases, electrons statistically penetrate further into the target. A convenient measure of the depth of penetration of the primary electrons is the 'range' of the electrons, which is the depth at which the mean energy falls to approximately zero. The range is given by the expression [7],

$$R_p = 10\, E_o^{1.43} \qquad \text{--------(1.1.2)}$$

where R_p is the practical electron range in $\mu g\ cm^{-2}$, and E_o is the beam energy in keV. Fig. 1.1.1 shows the role that the substrate and resist

thickness play in their contribution of the dose received by the resist film, and also the effect of collisional processes on line definition. As a rule of thumb, the minimum line width obtainable is about four times the beam diameter.

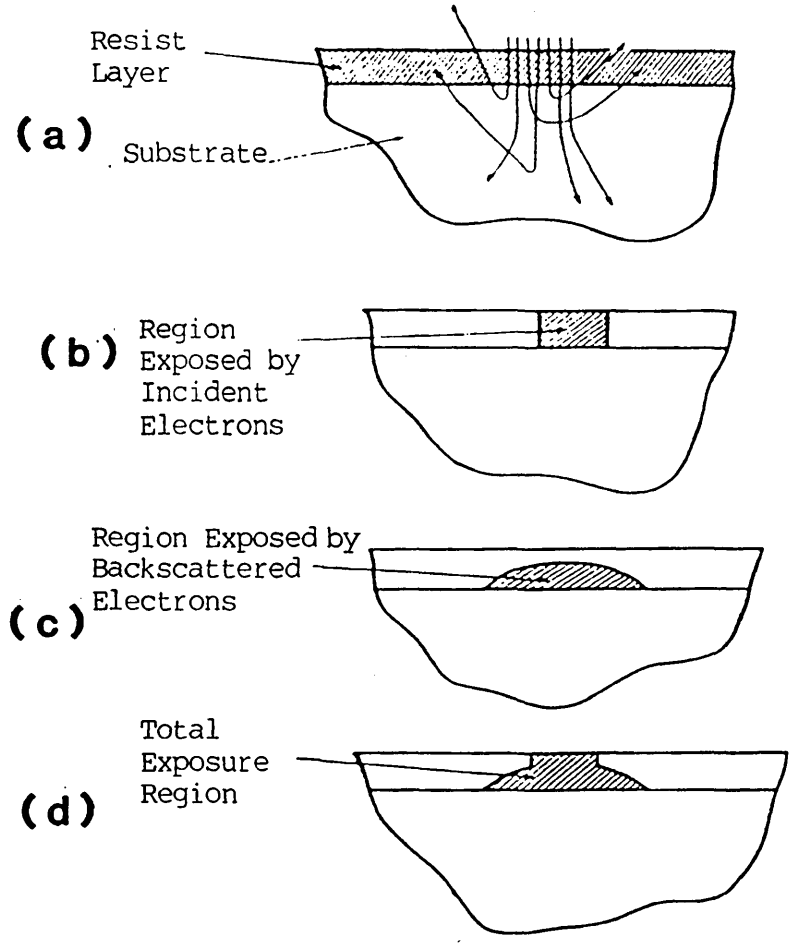


Figure 1.1.1:

(a) An indication of the scattering that occurs in a resist covered substrate.

(b) The lateral extent of the region exposed by incident electrons.

(c) Region exposed by backscattered electrons

(d) Summation of the effects of incident and backscattered electrons.

[After Thornton ref.6]

1.1.4 X-Ray Lithography

This is an extension of optical proximity printing with exposure wavelengths in the range of 1 to 50Å. X-ray lithography is presently limited to shadow printing, due to non-availability of x-ray optical elements. A mask, with x-ray absorbing patterns, and a wafer coated with an x-ray sensitive resist are required for the proximity printing. The attractiveness of x-ray lithography, is due to its capability of high resolution, and high throughput. Secondly, no proximity corrections are needed (because the low energy (10 to 250eV) of soft x-rays reduces scattering effects in both the resist and substrate). Thirdly, any dirt on the mask is not printed as a defective pattern in the resist, since dirt (which generally has low atomic number) does not appreciably absorb x-rays. Finally, due to the low absorption of x-ray resists, a thick resist can be uniformly exposed throughout the entire thickness, resulting in well defined patterns of the mask.

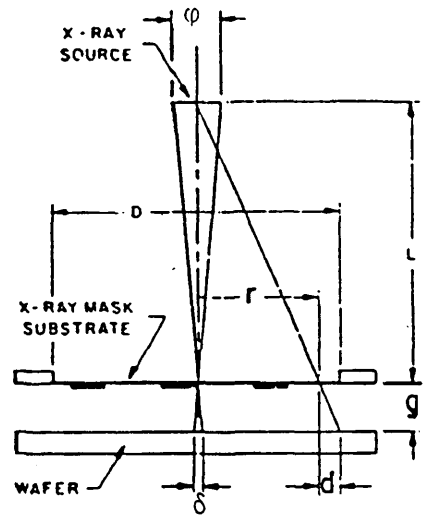


Figure 1.1.2: Geometrical representation of x-ray lithography exposure.[After Fay ref.8]

The resolution of x-ray lithography can be limited by the geometrical effects [8], represented in Fig. 1.1.2, examples of which are:

(i) Penumbral blur, δ introduced on the position of the resist image edge by the extended point source, is given by,

$$\delta = \frac{\varphi g}{L} \qquad \text{-------(1.1.3)}$$

φ is the x-ray source diameter at a distance L from the x-ray mask, and g the mask-wafer separation.

(ii) Lateral magnification error, d, often called run-off, walk-off, or geometrical distortion, is caused by the non-normal incident x-rays at the edge of the wafer. d is given by,

$$d = \frac{r\, g}{L} \qquad \text{--------(1.1.4)}$$

where r is the radial distance measured from the centre of the wafer. Variation in g, either across the wafer or from level-to-level registration, can introduce significant run-off error.

X-ray resist sensitivity can be improved by increasing the x-ray absorption in the resist. The absorption of x-rays in the resist is described by the equation,

$$I_x = I_o \exp(-\rho\alpha\, x) \qquad \text{--------(1.1.5)}$$

where x is the penetration distance of the x-ray into the resist, α is the mass absorption coefficient, and ρ is the density. I_o and I_x, are intensities before and after absorption respectively.

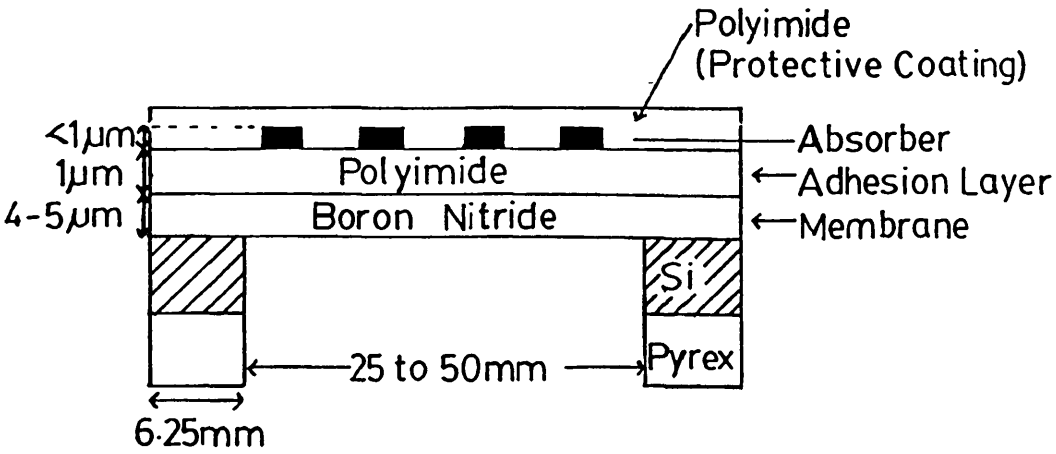


Figure 1.1.3: Schematic diagram of an x-ray mask

A schematic diagram of an x-ray mask is shown in Figure 1.1.3. It consists of a patterned metal absorber, sandwiched between two layers of polyimide. The lower layer of polyimide is used as an adhesion layer and also to improve the mechanical stability and flatness of the mask. The upper layer is used as a protective coating. The boron nitride (BN) is the membrane and it provides mechanical stability for the mask. Usually, gold, and more recently, tungsten, are used as the absorber layer. The polyimide and the BN membrane are "transparent" to x-rays.

The requirements of an x-ray mask are:

(i) Vertical walls on the absorbing metal patterns for high resolution and good feature size control.

(ii) A membrane that forms the mask substrate must be highly transparent to x-rays so that exposure times are minimised. It should be dimensionally stable, rugged in frequent

production use, and transparent to visible light, in case optical alignment techniques are to be used. Many membrane materials [9,10], such as Si, SiC, Si_3N_4, Al_2O_3 and sandwich structures of $Si_3N_4/SiO_2/Si_3N_4$, have been used.

The problems with x-ray mask making are; improving the long-term dimensional stability and eliminating the resolution degrading effects of the mask defect density. These problems are yet to be solved, so that the employment of x-ray masks is not yet a fully developed technology.

1.1.5 Other Lithographic Techniques.

(a) Deep-UV Lithography

This is an optical lithography scheme, with exposure radiation in the wavelength range 2000 - 3000Å, as compared to the normal exposure wavelength range of 3100 - 4500Å, in an attempt to achieve better resolution. B.T. Lin [11] reported a resolution of 0.5μm, by modifying the conventional optical lithographic equipment to operate at shorter wavelengths, and using quartz instead of glass as the mask substrate. For VLSI production in the 1-μm design rule region, Chandross et al [12], have suggested that deep-UV optical lithography may soon become predominant.

(b) Multilevel Resists

The realisation that very thin resist films lead to improved resolution, but thick films are required for IC fabrication, opened the way for multilevel resist systems [13,14]. Multilevel resists are of two categories: those with two or more resist layers for exposure and development, and those in which only the top layer is used as a resist mask for the removal of other layers. In both categories, the bottom layer is usually very thick, about 2 to 4 times the maximum step height on the IC device. The only problem with this resist system is in processing, which is more complex than for a single-layer resist system.

(c) Ion Beam Lithography

Ion beam lithography offers a better resolution than e-beam lithography because ions (due to their mass) scatter much less than electrons, hence the absence of proximity effects [15]. The sensitivity for direct writing is still poor, but the scheme may be useful for making step-and-repeat 1:1 recticles for x-ray lithography [2].

(d) Inorganic Resists (Recent Trends)

O'Keeffe and Handy [16], were the first to use e-beam writing for pattern definition, obtaining a resolution of about 0.6μm. They e-beam exposed selected areas on a silicon oxide sample where windows are to be opened for subsequent diffusion process. It was found that areas exposed to e-beam were more soluble in a solution of 5% by volume hydrofluoric acid, 3% by volume nitric acid, and 92% by volume de-ionised water, (due to some chemical change wraught in the SiO_2) than the unexposed areas, by a factor of three. Since then, direct e-beam writing has been applied to other resist systems, and also for mask making.

Work on silver (Ag) doped GeSe film as an inorganic resist has been carried out by some authors over the past few years: Yoshikawa et al [17] e-beam exposed silver coated GeSe glass film, resulting in silver doped GeSe film, which was insoluble in alkaline solutions (i.e a negative-type electron resist). The sensitivity of the resist was found to be 4×10^{-5} C cm^{-2} when using 5keV electrons, and a contrast of about 8 was obtained. A fine pattern delineation of less than 0.3μm linewidth was achieved. Tai et al [18], were able to print 0.5μm lines with 0.5μm resolution in GeSe film using commercial step-and-repeat optical exposure equipment.

To overcome scattering in the resist and the backscattering effect from the solid substrate, Singh et al [19] used a thin membrane substrate (Si_3N_4) in producing ~40nm linewidth in silver-sensitised Ge-Se film, by electron beam lithography. A contrast better than 5 was obtained, and the sensitivity of the resist was about 10^{-3} C cm^{-2}.

Murray et al [20] employed a completely dry process in writing aluminium patterns, by e-beam exposing AlF_3 film prepared by evaporation. Also patterns of nanometer scale were written into Si_3N_4 by reactive-ion-etching, using AlF_3 as the resist mask. The sensitivity of complete removal of 80nm thick AlF_3 film was found to be 10C cm^{-2} by 100keV electrons. They proposed, through the use of electron energy loss spectroscopy study, that the fluorine ions were first removed, followed by displacement of the metal ions. Similar work had earlier been carried out [21], using NaCl as the resist material, and trenches of less than 2nm wide at an irradiation dose of 100C cm^{-2}, were etched into the resist.

Kolwicz and Chang [22] used a composite film of $AgCl-As_2S_3$ as an inorganic resist, doping the As_2S_3 film with silver through UV light exposure. When used as a photoresist, the sensitivity obtained was about 5 times less sensitive than organic resists in popular use, while as an x-ray resist, it is known to be about twice as sensitive as PMMA. The main advantage is in the nanometer pattern definition.

Kammlott and Sinclair [23], developed Fe_2O_3 films (using glass, oxidised silicon, and silicon as substrates) as a negative type electron resist. Results obtained, were independent of the substrate used. The resist was developed for use as a mask, and a suggestion for use at high temperatures was made, in processes such as ion-implantation, sputtering, and possibly dopant diffusion. A linewidth of 0.8μm was obtained.

CaF_2 was developed as an inorganic resist [24,25,26] for sub-nanometer line definition. Mankiewich et al [25], found that a dose of 10C cm^{-2} was required for writing 30nm lines in CaF_2, which then required a developing step (selective washing in deionised water) to remove the end product (CaO) of radiolysis, done in a vacuum of $5x10^{-7}$torr. Salisbury et al [26], obtained line definition of 3nm in CaF_2, which is an improvement over the work of Mankiewich et al [25], also the wet etching developement stage was not required (as e-beam processing was done in vacuum of about $5x10^{-9}$torr).

1.2 DRY ETCHING PROCESSES

1.2.1 Introduction

Dry etching is a gas/solid chemical process, which essentially occurs in a plasma generating electrode enclosure for the selective etching of materials through the use of a "non-erodable" resist to transfer a defined pattern onto an under-lying substrate.

Etching can be isotropic or anisotropic depending on the etching gas composition and reactor parameters such as gas flow, pressure, power, frequency, temperature and electrode materials.

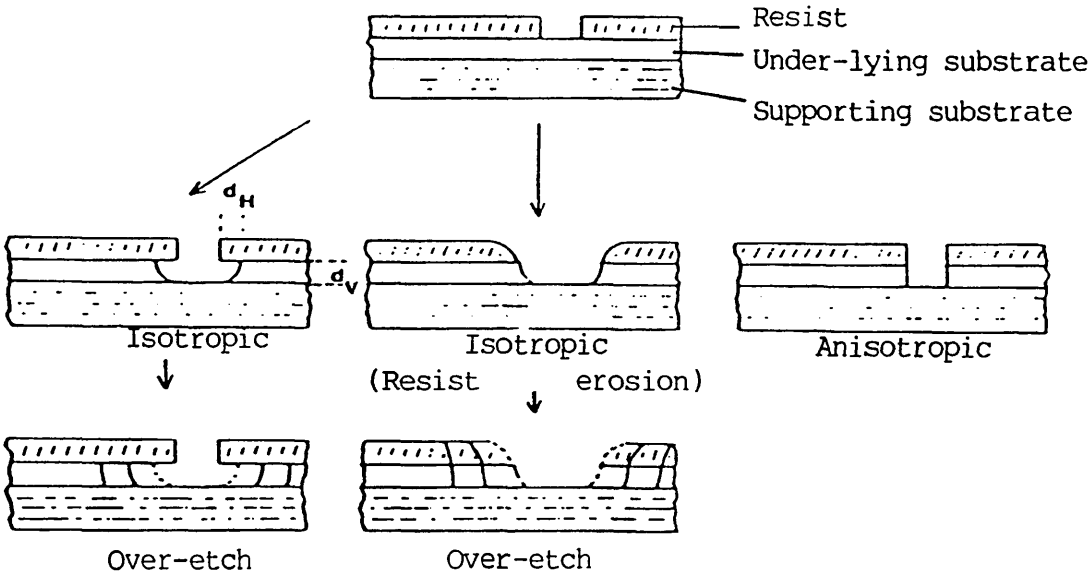


Figure 1.2.1: Isotropic and anisotropic etching profiles [After Flamm et al ref.27]

The degree of isotropic etching (IE), is defined [27] as IE = d_H/d_V, and the degree of anisotropic etching is $1-d_H/d_V$ (Fig. 1.2.1). Isotropic etching is a process whereby etching proceeds at an equal rate in all directions, resulting in $d_H/d_V = 1$. A purely anisotropic etching process is such that there is no lateral etching, in this case the degree of anisotropy is unity. The requirement of transferring patterns accurately, without distortion of critical dimensions, requires etching to be anisotropic and the use of minimum allowable resist thickness. There are instances when isotropic etching is required, such as selective stripping of the photoresist, etching of larger features in silicon, and removal of nitride oxidation masks.

Dry etching has replaced wet etching, owing mainly to the absence of anisotropic wet etches, which are essential for fine line definition. Dry etching also has lower chemical costs, less environmental impact, and ease of production-line automation [28].

1.2.2 Dry Etching Techniques.

Dry etching techniques can be classified into four basic types [28], depending upon the mechanism of etching. Etching mechanisms are functions of the etch gas, pressure range, electrode configurations, and whether the etch sample is in contact with the plasma.

The four etching techniques are physical, chemical, chemical-physical, and photo-chemical etching [28], and the mechanism for each technique is illustrated in Fig. 1.2.2. Photo-chemical etching is generally performed without a plasma, while the other three techniques employ the use of a plasma and can be represented by twelve electrode configurations (Fig. 1.2.3).

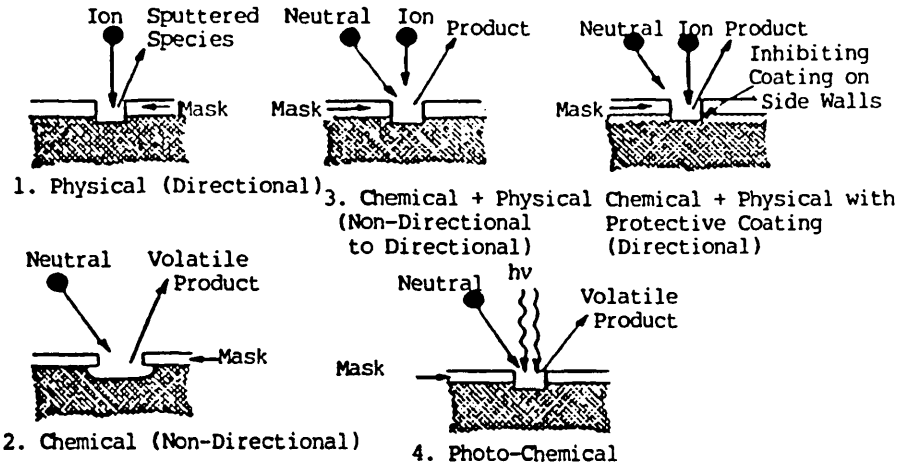


Figure 1.2.2: Dry etching mechanisms [After Fonash ref.28]

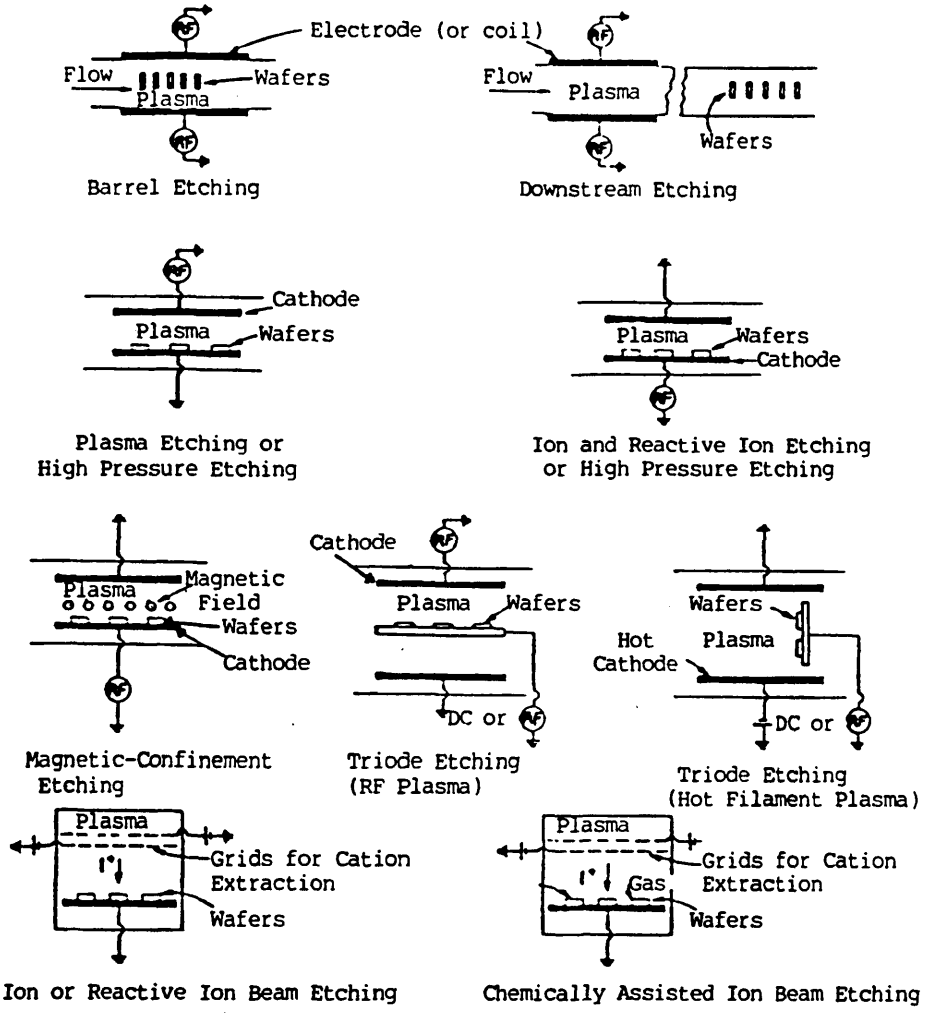


Figure 1.2.3: Electrode configurations used in the twelve dry etching processes involving plasmas [After Fonash ref.28]

(a) Physical Etching

This is essentially ion-milling, which is a process of momentum transfer of impinging ions to the material being etched (similar to sputter etching). This process of etching has the advantages of being a universal etchant (any material can be patterned), has the highest resolution compared with other techniques, and is capable of defining structures below 100Å [29]. It is highly anisotropic, relying on shadow masking for exposure, and does not require superior mask adhesion to prevent undercutting. It is capable of highly directional etching as a result of the flexibility of positioning the substrate at various angles to the impinging beam.

The relatively poor selectivity, of etching one material compared to another which is characteristic of this type of etching, in addition to the radiation damage of the etched sample, limits the use of this technique in silicon technology [30]. Re-deposition of etch materials can occur, since sputter-etch products are generally not volatile.

(b) Chemical Etching

Chemical etching, in this sense, refers to dry etching which occurs purely by chemical reaction of the etch-gas with the surface to be etched, resulting in volatile products, pumped away by the appropriate vacuum pump. Etching is purely isotropic (Fig. 1.2.1). In general, etching is accomplished by the generation of active chemical species from a plasma source. However, Winters and Coburn [31] achieved chemical etching in the absence of a plasma by using XeF_2 gas. Ibbotson et al [32], reported the directional etching of GaAs in a bromine plasma, which could be the result of orientational dependent crystallographic etching [27] of low index planes, a well known phenomenon.

Electrode configurations of etching done chemically are given in Fig. 1.2.3, examples of which are barrel etching, parallel plate etching (in the plasma mode), and downstream etching.

(c) Chemical-Physical Etching

This type of etching combines the mechanism of physical and chemical etching, as explained above. The degree of selectivity and directionality obtainable depends on the process parameters effects in implementing this mechanism. This mechanism is typical of reactive ion etching (RIE) and reactive-ion beam etching (RIBE) processes. Dzioba [33], reported the crystallographic etching of GaAs for this mechanism.

(d) Photo-Chemical Etching

The etching mechanism (Fig. 1.2.2) is the initiation of surface chemical reactions by incoming photons (in the absence of plasma). The degree of anisotropy is good [28] and selective etching is achieved, due to the line-of-sight mechanism. The etching process could be by; excitation of gas phase reactants, excitation of adsorbed species (reactants or products), or excitation of the solid [34].

A summary [28] of the comparison of the various dry etching configurations, and associated problems are presented in Tables 1.2.1 and 1.2.2 respectively.

Table 1.2.1: Comparison of the various type of etching [After Fonash ref.28]

Type of Etching	Selectivity	Profile	Processing Vacuum range (torr)	Wafer Location and Biasing	Electrode Arrangement	Type of Discharge	Ion Energy (eV)	Ultimate Patterning Resolution (Å)	Etch rate* (Å/min)
1. Physical									
(a) Ion-beam milling	Poor	Highly Anisotropic	10^{-4}	On grounded (Cathode) electrode	Planar Triode	DC	200-2000	100	Low (350)
(b) r.f. sputtering	Poor	Anisotropic	0.01-0.1	On cathode	Planar diode or cylindrical (hexagonal) diode	RF	500-5000	1000-5000	Low (<250)
2. Chemical									
(a) Plasma	Very good (If purely chemical) & good (If chemical-physical)	Vary from isotropic to Anisotropic	0.1-10	On grounded (Anode) electrode	Planar diode	RF	5-50	5000-10000	Can be as high as 1000
(b) Downstream or effluent	Excellent	Isotropic	0.1-1	In a rack downstream	Coil or electrodes outside vessel	RF	5-50	5000-10000	<200
(c) Barrel	Excellent	Isotropic	0.1-1	In a tube placed in plasma. Wafers electrically floating	Coil or electrodes outside vessel	RF	5-50	5000-10000	200
3. Physical-Chemical									
(a) Reactive Ion Etching (RIE)	Good	Moderately Anisotropic	0.01-0.1	On cathode	Planar diode or cylindrical (hexagonal) diode	RF	50-500	500-5000	Low (<500)
(b) Reactive Ion Beam Etching (RIBE)	Good	Anisotropic	10^{-4}	On grounded (Cathode) electrode	Planar triode	DC	100-500	500-1000	1000
4. Photo-Chemical	Potentially, may be selective	Potentially, may vary from isotropic to anisotropic	Depends on configuration	Usually not electrically driven	Usually not electrically driven	Usually not electrically driven	Ions may or may not be involved	-	-

*Best etch rate reported for SiO_2

Table 1.2.2: Problems associated with various etching configurations [After Fonash ref.28]

Etching Configuration	Associated Problem	Etching Configuration	Associated Problem
Barrel Etching	1. Isotropic only	Magnetic-Confinement	1. Non-selective
	2. Etch uniformity is flow dependent		2. Redeposition can occur since etch products are not volatile
Downstream (Effluent) Etching	1. Isotropic only	Triode Etching	1. In rf plasma, material from cathode can be re-deposited on the wafer
	2. Etch uniformity is flow dependent		2. In dc plasma, degradation of hot filament occurs
Plasma or High Pressure Etching	1. High pressure results in non-directional etching.	Ion or Ion Beam Etching	1. Non-selective
	2. Damage and impurity effects can be present		2. Low etch rate
			3. Redeposition can occur since etch products are generally not volatile
Reactive Ion Etching	1. Low etch rates	Reactive Ion Beam Etching	1. Etch rates not high enough
	2. Damage and impurity effects can be present		2. Damage and impurity effects can be present
Chemically Assisted Ion Beam Etching	1. More complex system	Photon Assisted Chemical Etching	1. Largely undeveloped
	2. Damage and impurity effects are un-determined		2. Currently involves heating of sample, which could seriously affect device performance.
	3. Etch rates may need to be higher		

1.2.3 Chemistry and Physics of Etching Reactions.

Plasma-assisted etching is done by ionised gases, which consist of ions, electrons, and neutrals (excited and otherwise) produced by low pressure ($\sim 10^{-4}$ to 10torr) electric discharges. The etch gas gains energy by collision with energetic electrons, resulting in ionisation. The ionisation rate must be equal to that of electron and ion losses by plasma-phase and surface recombination, for a plasma to be sustained. Some of the more significant electron-gas and gas-gas reactions are:

Excitation	$A_2 + e^- \longrightarrow A_2^* + e^-$
Dissociation	$A_2 + e^- \longrightarrow 2A + e^-$
Electron Attachment	$A_2 + e^- \longrightarrow A_2^-$
Dissociative Attachment	$A_2 + e^- \longrightarrow A + A^-$
Ionisation	$A_2 + e^- \longrightarrow A_2^+ + 2e^-$
Photoemission	$A_2^* \longrightarrow A_2 + h\nu$
Abstraction	$A + B_2 \longrightarrow AB + B$

Production of atoms and radicals in molecular discharges is essential to etching, as the etch gases themselves in virtually all cases are not reactive. For example, CF_4 is a relatively inert gas when silicon is to be etched, but in a plasma, F atoms, one of the by-products, will react spontaneously with silicon (Si) at room temperature to form SiF_4 [35].

The rate of production of ions, atoms, and radicals depend on discharge parameters such as pressure, power density, frequency and gas flow.

1.2.4 Process Parameters Effects

(a) Gas Flow and Composition

Reactive and inert gases may be used in etching a given material. The choice of gases could be on the basis of producing reactive gas species, and also to yield an anisotropic etch mechanism [36]. As previously described, the dominant etch mechanisms to be adopted in obtaining anisotropic etching should be considered. For instance, if the surface inhibiting coating mechanism is needed, then the percentage of C and H present in the gas is of prime importance [37] (for example CF_4 results in very low polymerisation, while

CHF_3 and CH_3F give progressively higher polymerisation rates). The gas flow rate affects the etch uniformity, through the etch chamber pressure distribution, and the replacement rate of consumed reactive species. Excessive flow rates at constant pressure result in decreased residence time and result in a decrease in the active species generation rate at constant power. Whereas relatively low flow rates leads to depletion of active species and hence a decrease in etch rate [38]. In general, flow rate has little influence on etch rate [35], with more pronounced effect at the extremes. Table 1.2.3 is a list [35] of some gases (mainly halogen containing gases) that have been used for etching in VLSI, except in photoresist stripping and the patterning of organic layers where O_2 plasmas have been used. The choice of halogen-containing gases is made because they are relatively easy to handle and have minimal operating mode hazards. Mixed gases could be used for a desired effect in relation to etch rate, selectivity, uniformity of edge profile [39]. For example, etch rates of Si and SiO_2 in CF_4 plasma are relatively low. Mogab et al [40] achieved better etch rates by using a CF_4/O_2 gas mixture. Addition of H_2 to a CF_4 plasma, resulted in polymerisation induced anisotropy and improved selectivity [41,42].

Table 1.2.3: Some gases used in dry etching for VLSI fabrication. [27,30,35,45]

Material to be etched	Gases used
Si	CF_4, CF_4+O_2, SF_6, $SF_6 + O_2$, $C_2F_2 + O_2$, $C_3F_8 + O_2$, $SiF_4 + O_2$, NF_3, Cl_2, CCl_4, CCl_3F, CCl_2F_2, $CClF_3$.
SiO_2, Si_3N_4	CF_4, $CF_4 + H_2$, C_2F_6, C_3F_8, CHF_3
Al, Al-Si, Al-Cu	CCl_4, $CCl_4 + Cl_2$, $SiCl_4$, BCl_3, $BCl_3 + Cl_2$

(b) Pressure, r.f. Power, and Frequency Effects

Pressure and r.f. power are inter-related, since both affect the generation of free radicals and ions and also the electrode self-bias voltage [36]. High pressure leads to an increase in the etch rate as a result of increased free radical formation, thereby leading to highly isotropic etching. The poor anisotropy (depending on reactor configuration) is the result of decreased cathode voltage, and hence the ion energy. Similarly, increasing the r.f. power also results in generation of more ions and free radicals and hence increased etch rate. The anisotropy which may be lost because of high pressure etching, may be restored by increasing the r.f. power. Lowering the pressure and/or frequency, and increasing power density (r.f. power), increases the mean electron energy and the energy of ions incident on surfaces. The density of radicals and ions in the plasma are also increased. Thus, if etching is ion-assisted, a high degree of anisotropy is achieved. Generally, etch rates increase monotonically with power, at a diminishing rate [35]. The effect of frequency and pressure are interchangeable [27]. At high pressure and high frequency, ion energies are low, surface damage is minimal, and degree of anisotropy achieved is by presence of recombinants. At low pressure, or high pressure and low frequency, ion energies are high and surface-damage-induced anisotropy is observed.

(c) Temperature Effect

In general, the etch rate dependence on temperature follows an Arrhenieus curve (rate $\propto \exp(-Q/(kT))$, where Q is the activation energy, k is Boltzmann's constant, and T, temperature. Interestingly enough, Schwartz and Schaible [43], obtained a decrease in etch rate with increase in temperature, which could be as a result of thermal desorption of etching species from the substrate surface [27]. Since the activation energy is material dependent, variation in temperature can also affect selectivity. For reproducibility in etching and also for uniform etching, the substrate temperature has to be controlled [35].

(d) Loading Effect

Loading effect is such that etch rate decreases with increase in etch surface area and vice-versa, this sometimes occurs in reactive etching. The etch rate, R, dependence on etchable surface area A, in the case of single etchant species is given by [44];

$$R = \frac{B\tau G}{(1 + KB\tau A)} \qquad \text{---------(1.2.1)}$$

where B is a reaction rate constant, τ is the lifetime of active species in the absence of etchable material, G is generation rate of active species, and K is a constant for a given material and reactor geometry. If $KB\tau A << 1$, that is a short lifetime of active species, then the effect of loading is negligible. As material being etched is thinned down to the underlying layer (or substrate), the etch rate increases due to the loading effect. This loading effect can cause lateral etching, leading to undercutting at the end-point. To get around this problem, electrode materials which can act as 'sinks' for reactive species [45] have been used.

(e) Electrode Materials

The choice of electrode materials depends on whether they are chemically or physically inert to the plasma environments. For example, a chemically reactive electrode is needed to control the radial etch rate uniformity and loading effect while etching silicon [45], such as using a silicon-covered electrode [46]. Carbon, "Teflon", or other organic electrode coatings present surfaces that deplete fluorine atoms in the etching of SiO_2, when fluorocarbon gases are used. Chemical or sputtering reactions with stainless steel and other metal electrodes may hinder etch rates, and could result in heavy metal and other contamination of etched surfaces, or produce localised masks that cause roughening of etched surfaces [47].

1.2.5 SiO_2 Dry Etching for VLSI Technology

Dry etching of SiO_2 is used essentially for contact window opening [45] and the degree of anisotropy and selectivity required is high. To achieve high selectivity and anisotropy in etching silicon oxide over silicon and polysilicon in the fabrication of metal-oxide-semiconductor (MOS) devices, combination of gases have been used. For example H_2 gas has been added to fluorocarbon gases (e.g CF_4, C_2F_6) so as to increase the [CF_3 radical] to [F atom] ratio in the etching plasma [35]. This has been done as a result of the suggestion by Heinecke [48] that CF_3 radicals react with SiO_2 in preference to Si.

Ephrath [41] and Heinecke [49], obtained a selectivity of 30:1 in etching SiO_2 compared to Si, by using the etchant CF_4/H_2. Matsuo and Takehara [50,51], obtained a similar result by using CF_4/C_2H_4 gas, while Lehmann and Widmer [52,53] used CHF_3 gas.

Coburn and co-workers [37,54-56], suggested the formation of polymeric films on oxygen free surfaces to explain the high selectivity obtained. On silicon oxide surfaces, the oxygen reacts with the polymeric species to form volatile gases such as CO, CO_2, and COF_2 [37] resulting in the etching of the material. The level of polymerisation increases for etch gases that are more deficient in fluorine (in particular fluorocarbon gases), that is, an increase in C:F ratio. If the C:F ratio is too high (more than 40% H_2 in CF_4/H_2), polymer formation may dominate, resulting in low and unacceptable etch rate of SiO_2 [45].

Other etchants that have been used to obtain good selectivity of SiO_2 over Si are, CHF_3/CO_2 [57], and CHF_3/NH_3 [58]. The CHF_3/CO_2 gas results in an increased C:F ratio in the plasma, as a result, not effective in reducing the polymer formation as O_2. CHF_3/NH_3 on the other hand formed volatile cyanogen derivatives by reaction with deposited fluorocarbon species [45].

Although selectivity over silicon generally improves [35] as operating parameters are optimised to increase the concentration of unsaturates, the tendency to form polymer deposition must be controlled in the attempt to achieve maximum selectivity.

Proper choice of electrode material (see section 1.2.4e) results in selective etching of SiO_2 over Si. Quartz and aluminium are examples of electrode materials that do not substantially deplete the discharge of fluorine [45], which results in increased etch rate of resist and hence reduced selectivity. Increase in SiO_2 etch rate and selectivity over Si is further accomplished by an increase in r.f. power, consistent with an ion-induced reaction. The extent to which the power density could be increased depends on the provision of good heat sinking for the substrates so as to minimise resist degradation.

Sources of contamination on wafer surfaces stem from the level of purity of the cathode cover material. Materials not chemically etched on the cathode, can be physically sputtered, and redeposited on the wafer [59]. Furthermore the possibility of radiation damage and/or surface roughening in silicon exist, especially in ion-assisted etching [45]. A post annealing can be done immediately after contact-hole etching to reduce the damage effect in silicon, introduced as a result of over-etching past the oxide. Alternatively, an effective end-point detection scheme can be employed to avoid over-etching past the oxide [45].

Gorowitz and Richard [45] suggested a dry/wet etch sequence in order to reduce the possibility of contamination and damage effect. This process can only be applied by employing end-point detection scheme (for the dry-etch step) of Egitto et al [57], but there is loss of critical line definition in the whole process.

1.2.6 End-Point Detection

The importance of accurate detection of the end of the oxide etching is emphasised when the etching and oxidation of the under-layer is undesirable, and when undercutting is sensitive to the amount of over etch. Accurate detection of the end-point also increases throughput, by eliminating the tedious procedure of calibrating the etch period: such calibration has the disadvantage of requiring tightly controlled process parameters. There are various

methods for in-situ end-point determination, based on:

(i) measurements on the surface being etched

(ii) measurements of the plasma composition

(iii) measurements of the physical properties of the plasma.

A summary of the different methods is given in Table 1.2.4.

The optical reflectance method monitors what is happening to the wafer surface, without any information about what is going on in the discharge. Emission spectroscopy gives detailed information on the reactive species and etch products that emit light in the discharge. Most of the information is about atomic and diatomic species (electronic transition), and little or no information on poly-atomic species, hence species that may play an important role in the etching process may be undetected. Mass spectroscopy gives information about the stable species in the downstream from the plasma chamber reactor. Hence details of discharge chemistry has to be inferred. For the purpose of end-point monitoring, the information derived from the various techniques is not crucial. However, it is important to understand the etching process, in situations where etching is not properly done, so that the process can be brought to a useful state.

Emission and mass spectroscopic monitoring require approximately 1 cm^2 of wafer area for reasonable end-point determination [60]. The optical reflectance method requires about 0.005 cm^2 of wafer area [61], while impedance and pressure monitoring require relatively large wafer areas.

End-point detection method chosen for application, is based on the following points:

(i) the ease of implementation

(ii) the cost of equipment

(iii) the ease of operation

(iv) and the technical consideration as to which technique is applicable to the monitoring of a particular process.

Table 1.2.4: Summary of End-point detection methods

Method	Equipment	Measurement	Monitoring	End-point
Optical-reflectance	He-Ne Laser source, photo-detector	Interference phenomena or reflectivity differences	Change in film thicknesses	One wafer: in situ etch rate monitor
Thermal wave	Ar^+ laser & He-Ne laser & signal processing	Reflectance change	Change in nature of surface. Also film film thickness	One wafer: in situ etch rate measure-ment
Emission-spectroscopy	Monochromator photodetector	Intensity of light emitted from discharge	Gas composi-tion, gas temperature	Average for all wafers
Mass spectrometer	Quadrupole mass spectrometer	Mass resolved fragmentation spectrum	Gas composi-tion (mainly etch products)	Average for all wafers
Impedance monitoring	Electric bridge	Impedance mismatch	Voltage change	Average for all wafers
Pressure change	Pressure gauge	Total pressure	Change in total pressure	Average for all wafers
Langmuir probe	Probe, voltage source electrometer	Current versus voltage	Electron density, ion density, electron temperature	Average for all wafers

1.3 A WAY FORWARD

Work involving inorganic resists has been done in order to achieve nanometer line definition, which still requires a chemical (wet) development stage, with the exception of the work by Murray et al [20] and Salisbury et al [26]. The need to have a self developing (i.e a completely dry process) inorganic resists may prove highly desirable in precise pattern definition. The processing steps of Figure 4.4.1 are proposed, using $CdCl_2$ as an inorganic electron beam resist, for either mask fabrication or for pattern delineation in oxidised silicon wafer.

Also the need to fill the gap between e-beam and conventional optical lithography, places emphasis on improved mask fabrication for x-ray lithography. An investigation of $PbCl_2$ and $PbCl_2/CdCl_2$(20%), with a view to making the absorbing layer patterns for x-ray masks, was carried out. The lithography steps for fabricating the absorber layer pattern is shown in Figure 5.2.20.

An understanding of electron beam induced decomposition reaction is important. A theory is proposed, to explain the decomposition processes in $PbCl_2$, and $PbCl_2/CdCl_2$(20%) thin films.

CHAPTER 2

SOME PHYSICAL PROPERTIES OF THIN FILMS OF CADMIUM CHLORIDE ($CdCl_2$) AND LEAD CHLORIDE ($PbCl_2$)

2.1 INTRODUCTION

The crystal structures of $CdCl_2$ and $PbCl_2$ are discussed in the following section. The mean grain size of $CdCl_2.H_2O$ and $PbCl_2$ films as a function of film thickness were studied using a scanning electron microscope. Electron probe micro-analysis was carried out to determine the composition of the deposited films.

X-ray diffraction analyses of $CdCl_2.H_2O$ (thin film and powder) and $PbCl_2$ (film) were performed.

Quartz crystal microbalance (QCM) investigations were done to confirm the extent of hydration (observed from the x-ray diffraction results) in $CdCl_2$ film. The QCM studies were extended to investigating the extent of dehydration resulting from placing the samples under vacuum.

2.2 CRYSTAL STRUCTURE

2.2.1 $CdCl_2$ Crystal Structure.

Anhydrous cadmium chloride ($CdCl_2$) has a layer structure [1,2,3,4], apparently characteristic of polar covalent bonds [1]. This substance is termed a "layer structure" because it consists of repeat units (Cl-Cd-Cl)...(Cl-Cd-Cl)...(Cl-Cd-Cl) with contact between adjacent chlorine layers. The cadmium-chlorine bonds are polar covalent while the non-bonded Cl-Cl nearest neighbour interaction is principally of the van der Waals type [4] with the corresponding inter-atomic distances.

Thus the non-bonded Cl-Cl distance is 3.68Å and the collision radius of Cl is estimated to be 1.8Å [5,6] giving 3.6Å for Cl-Cl. On the other hand the covalent radii of Cd and Cl are 1.55Å and 1.00Å respectively, giving 2.55Å for Cd-Cl bond length compared with the 2.74Å found in the solid.

The crystal structure of one layer of cadmium chloride (Fig. 2.2.1a) can then be thought of as the (111) plane of the face centred cubic (fcc) structure. Since the layer stacking sequence of $CdCl_2$ is ABCABC... (cubic closest packing), a second similar layer (Cl-Cd-Cl) is added to the first by placing each sphere in contact with three spheres of the bottom layer. A third layer is added, by placing the spheres in the third layer over the vacancies in the first layer not occupied by the second layer [7]. This is characteristic of the packing in fcc structure.

The symmetry of the structure becomes clearer by the representation of cubic closest packing arrangement of Fig 2.2.1b, where the closest packed layers are stacked parallel to cube diagonal. The primitive unit cell of $CdCl_2$ can also be said to be a rhombohedron containing a single molecule, with atoms at special positions of $R\bar{3}m$:

Cd : 000 Cl : uuu; $\bar{u}\bar{u}\bar{u}$

where u = 0.25Å.

The corresponding cell (Fig 2.2.2) has three molecules with hexagonal pseudo-cell of dimensions:

$a_o' = 3.85Å$ $c_o' = 17.46Å$

The space group notation $R\bar{3}m$ (Hermann-Mauguin system) for $CdCl_2$ could be explained as follows: Symbol R represents the lattice symbol (Trigonal); while the 3 denotes the presence of a 3-fold axis. The bar on 3 indicates an inversion operation (i.e a rotation of π radian followed by reflection in a plane normal to the rotation axis). Letter m represents a mirror plane.

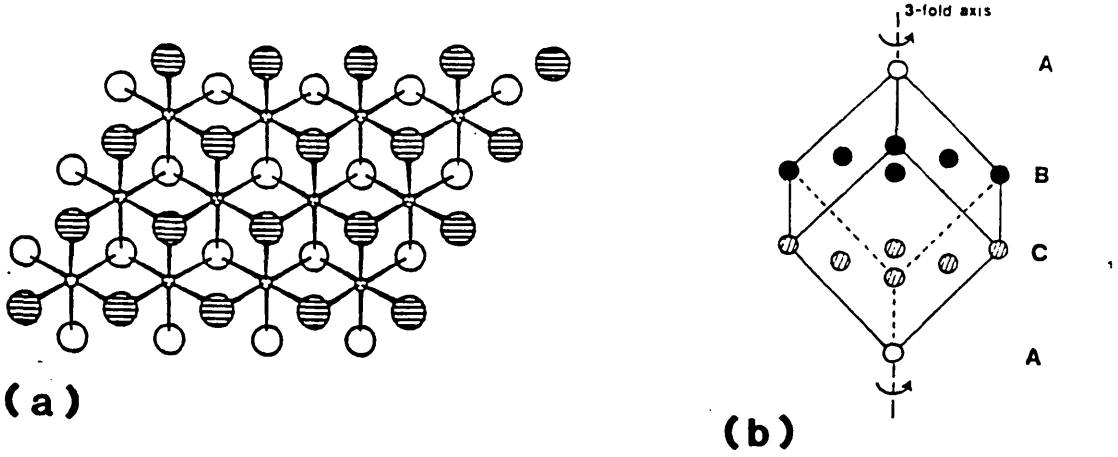


Figure 2.2.1:

(a) Crystal structure of one layer of $CdCl_2$ [After Wells ref.3]

(b) The cubic closest-packing arrangement. Note that the closest-packed layers are stacked normal to the cube diagonal.

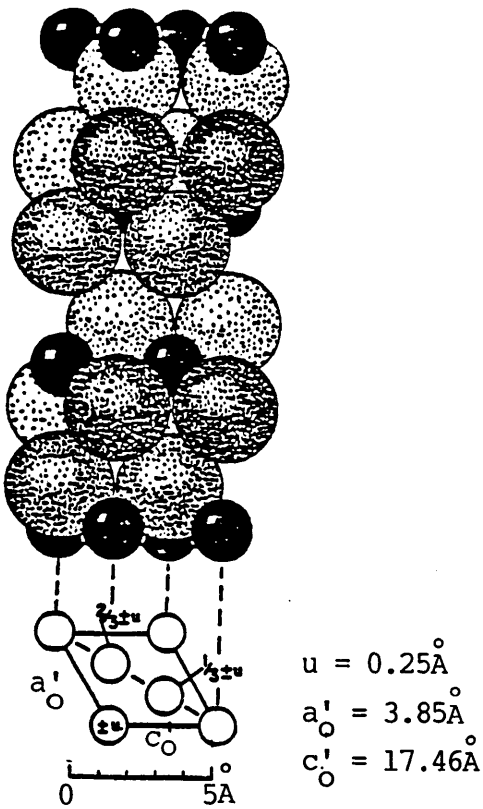


Figure 2.2.2: Two projections of the $CdCl_2$ arrangement in terms of its hexagonal unit. The atoms of the upper projection, looking normal to the $a'_o c'_o$ plane, have been shaded with cadmium atoms black. [After Wyckoff ref.2]

2.2.2 $PbCl_2$ Crystal Structure

$PbCl_2$ structure is complicated with respect to the chlorine atoms [3]. The structure (Fig. 2.2.3) can be thought of as considerable distorted close-packing of Cl atoms, with the Pb atoms accommodated in the same plane with the Cl atoms. There is appreciable spread of the inter-atomic distances (Pb-Cl), but each Pb atom is coordinated by nine Cl atoms [2,3], with two chlorine atoms at 2.67Å, one each at 2.88, 3.05, 3.08Å, two each at 3.13 and 3.29Å. Quite a lot of the Cl-Cl separations vary between about 3.20 and 3.47Å, and are shorter than the sum of the atomic radii [2].

The unit cell of $PbCl_2$ structure is orthorhombic. It consists of three groups of four atoms, all in 4-fold positions [2,3], as shown in Fig. 2.2.3, with tetra-molecular cell dimensions [8];

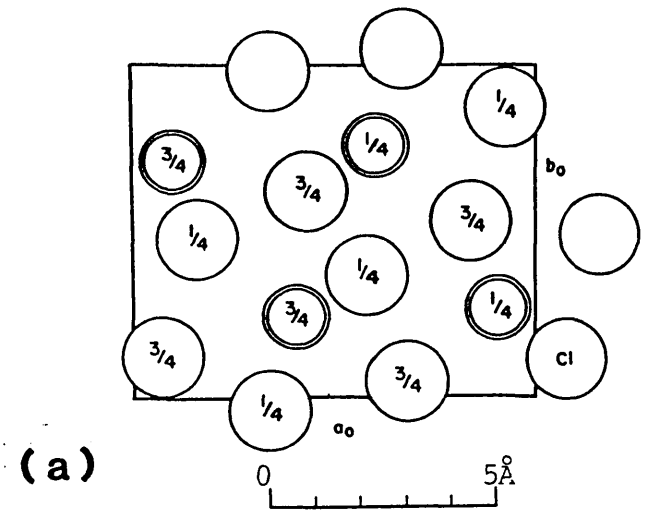
$$a'_o = 7.605\text{Å} \quad b'_o = 9.027\text{Å} \quad c'_o = 4.520\text{Å}$$

The space group notation Pnma for $PbCl_2$ is interpreted as having a lattice symbol P; with n-fold axis ; and m, representing a mirror plane.

2.3 $CdCl_2.H_2O$ and $PbCl_2$ GRAIN STRUCTURE AND MEAN GRAIN SIZE DETERMINATION

The grain structure of films during deposition depend on such experimental parameters as substrate cleanliness, deposition rate and material purity. Thin films are subject to direct contamination effects from the substrate, which may decrease the mobility of the grain boundaries. The proportion of grain boundaries that is mobile has a strong influence on the microstructure of the deposited film. The dependence of grain structure on substrate temperature (T_s) is very similar in both thick and thinner films [9].

It is possible to classify the structure of films into four characteristic zones, depending on the ratio of substrate temperature, T_s, to melting temperature, T_m [9]. The morphologies of the grains found in these four zones [10,11] are shown in Fig. 2.3.1.



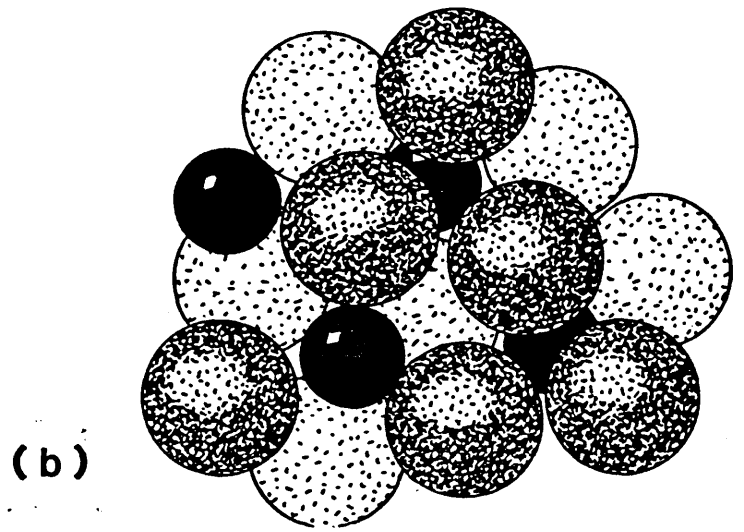


Figure 2.2.3: $PbCl_2$ crystal structure

(a) The orthorhombic structure of $PbCl_2$ projected along its c_o axis. Origin in lower right. Pb atoms are double circle.

(b) A packing drawing of the $PbCl_2$ arrangement viewed along the c_o axis. The lead atoms are black. [After Wyckoff ref.2]

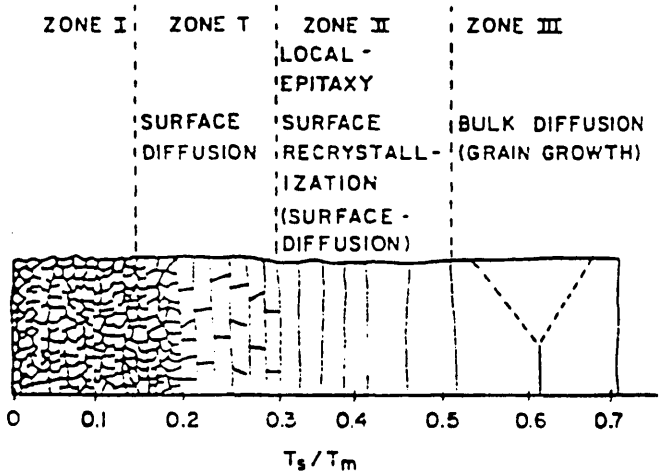


Figure 2.3.1: Zone model for the grain structure of vapour deposited metal films, modified at low temperatures to take into account the fine "equiaxed" grain structure . [10,11]

In the region $0.3 < T_s/T_m < 0.5$ (zone II), all grain boundaries are mobile, as a result of grain boundaries possessing excess energy which is structure, composition, and temperature dependent. In this region, columnar structure is expected, possessing uniform grain diameter, thereby reflecting a nucleation structure [12].

Samples of $CdCl_2$ and $PbCl_2$ films on oxidised silicon substrate were thermally evaporated from a molybdenum electric resistive boat, (detailed description of film preparation is presented in section 3.1). On exposure of deposited films to laboratory air, $CdCl_2$ hydrated to give a film composition of $CdCl_2.H_2O$ (as determined in section 2.5). $CdCl_2.H_2O$ and $PbCl_2$ films examined under the scanning electron microscope (Figs. 2.3.2 a &c), were seen not to be appropriate for the determination of the mean grain size, and a mild "etch" in a solution was found necessary. The etchant used to produce preferential attack of the grain-boundaries was the solution of iso-butyl-methyl-ketone (MIBK) 10% by volume, and 90% by volume n-hexane. Using the etchant, etching was done for about ten seconds, followed by hexane flooding of the etch content to stop the etch process. The resulting structures are shown in Figures 2.3.2b &d .

Figure 2.3.2:

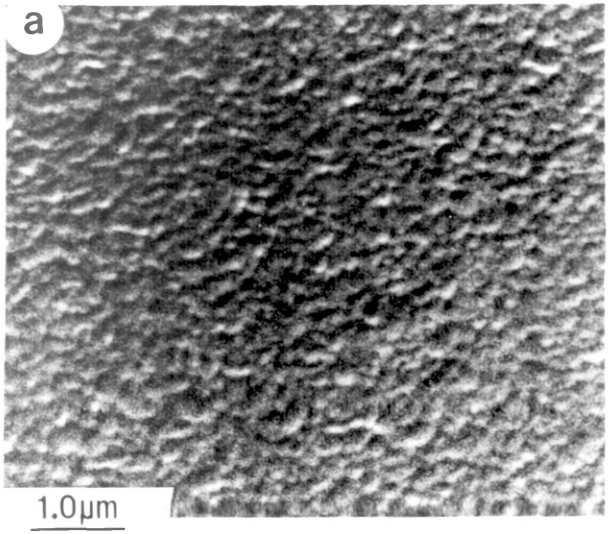
Electron micrographs of deposited and wet-etched films of $CdCl_2.H_2O$ and $PbCl_2$, for mean grain size determination Etching was done using a solution of iso-butyl-methyl-ketone (10%), and n-hexane (90%)

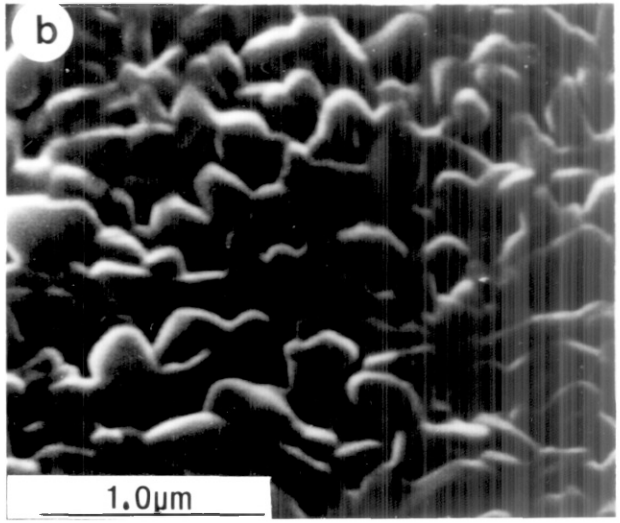
(a) $CdCl_2.H_2O$ surface structure

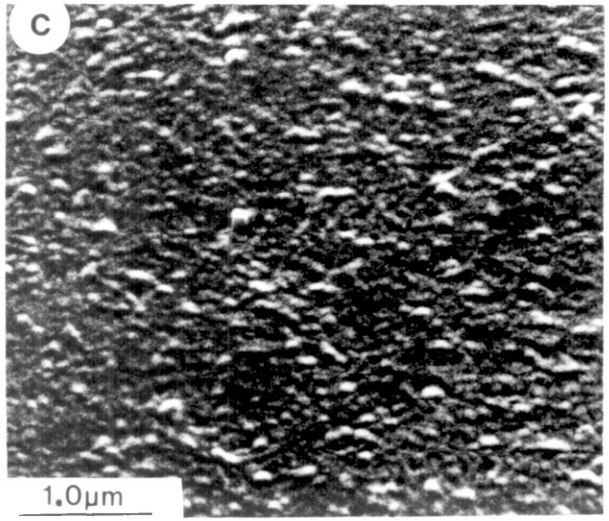
(b) $CdCl_2.H_2O$ grain structure after wet-etching

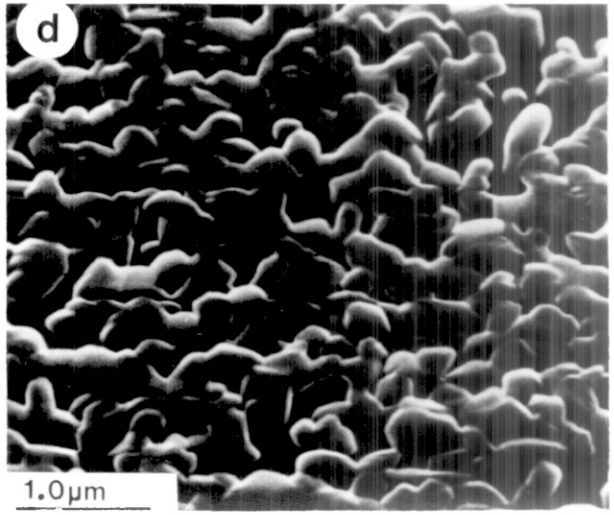
(c) $PbCl_2$ film surface as deposited

(d) $PbCl_2$ surface structure after wet etching.


a
1.0μm


b
1.0μm


c
1.0μm


d
1.0μm

Grain sizes were calculated from the micrographs, by counting the number of grain boundaries, N, within a drawn line of length, L, thereby yielding a grain size of L/N. During each analysis, sufficient grains were counted to result in a minimum deviation of mean grain size. The results of the mean grain size of $CdCl_2.H_2O$ and $PbCl_2$ films, as a function of thickness, are summarised in Fig. 2.3.3. The results show that the grain size increases with thickness. This could be linked with the proposal [9,12] that as film grows, diffusion along the surface (of the film) causes lateral motion of the boundaries, leading to grain coalescence and an increase in the mean grain size.

2.4 X-RAY DIFFRACTION STUDIES

2.4.1 X-Ray Diffraction of $CdCl_2.H_2O$ Powder

When "monochromatic" radiation is used to examine a "powder" specimen on a flat-film camera, there seems to be no general agreement [13] on the name of this method. Klug and Alexander [14], for example, called it the "monochromatic-pinhole technique." It could also be called the "focusing toroid camera technique," employing a transmission or back-reflection camera. Fig. 2.4.1 illustrates the schematic arrangement of the camera in the transmission mode, capable of recording an entire Debye ring on the photographic film, which is a great advantage. On the other hand, the range of Θ values which are recorded is rather limited: either low-angle or high-angle reflections may be obtained (the low-angle Θ was recorded, Fig. 2.4.2a), but not those in the median range of Θ.

The value of Θ (Fig. 2.4.1b) for a particular reflection (in the transmission mode), is calculated from the following equation,

$$\tan 2\Theta = D/(2X) \qquad \text{-------(2.4.1)}$$

where D is the diameter of the Debye ring; and X, the specimen-to-photographic film distance.

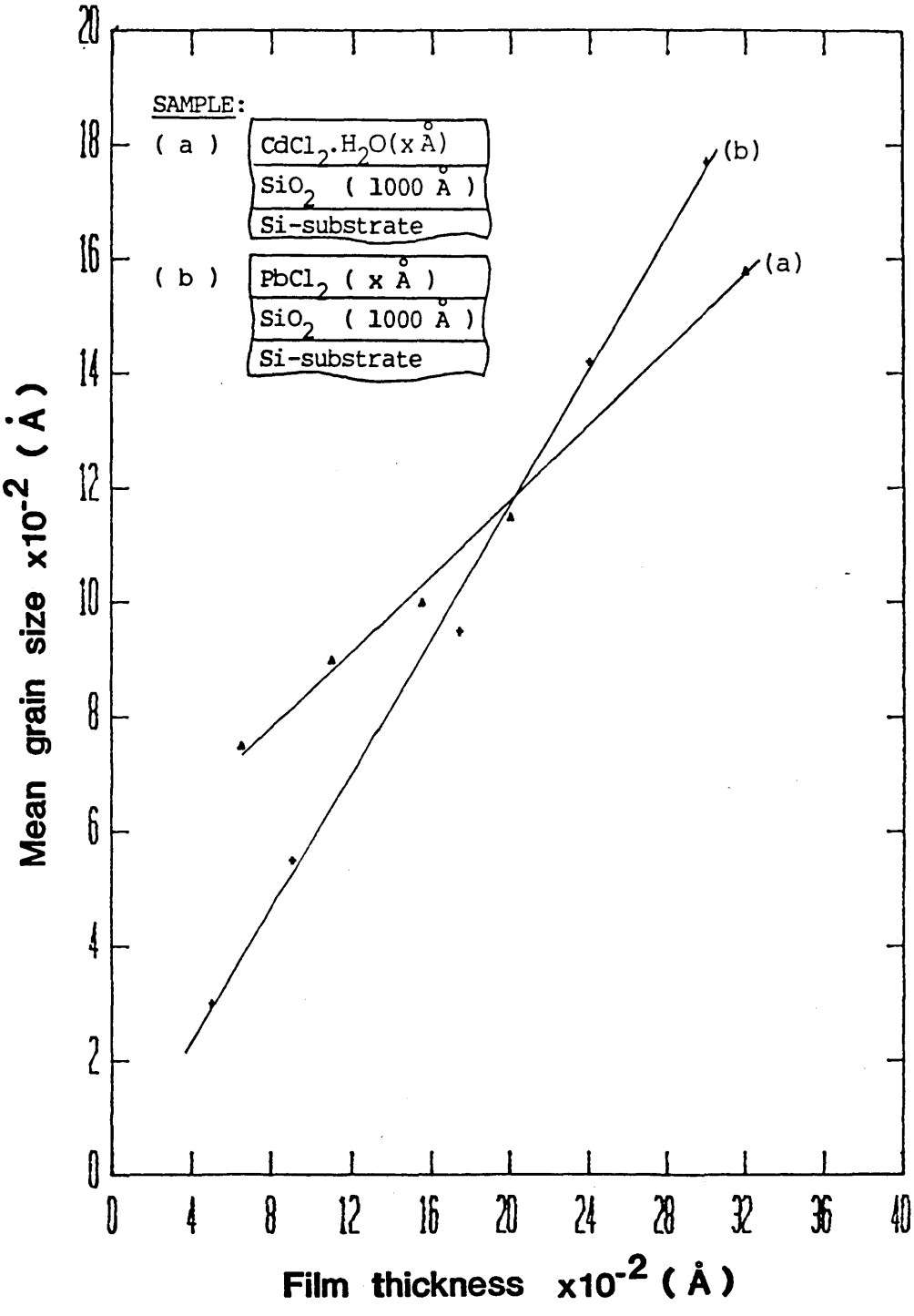


Figure 2.3.3: Mean grain size vs. Film thickness, for $PbCl_2$ and $CdCl_2.H_2O$ samples. Film deposition rate = 40±4Å/s.

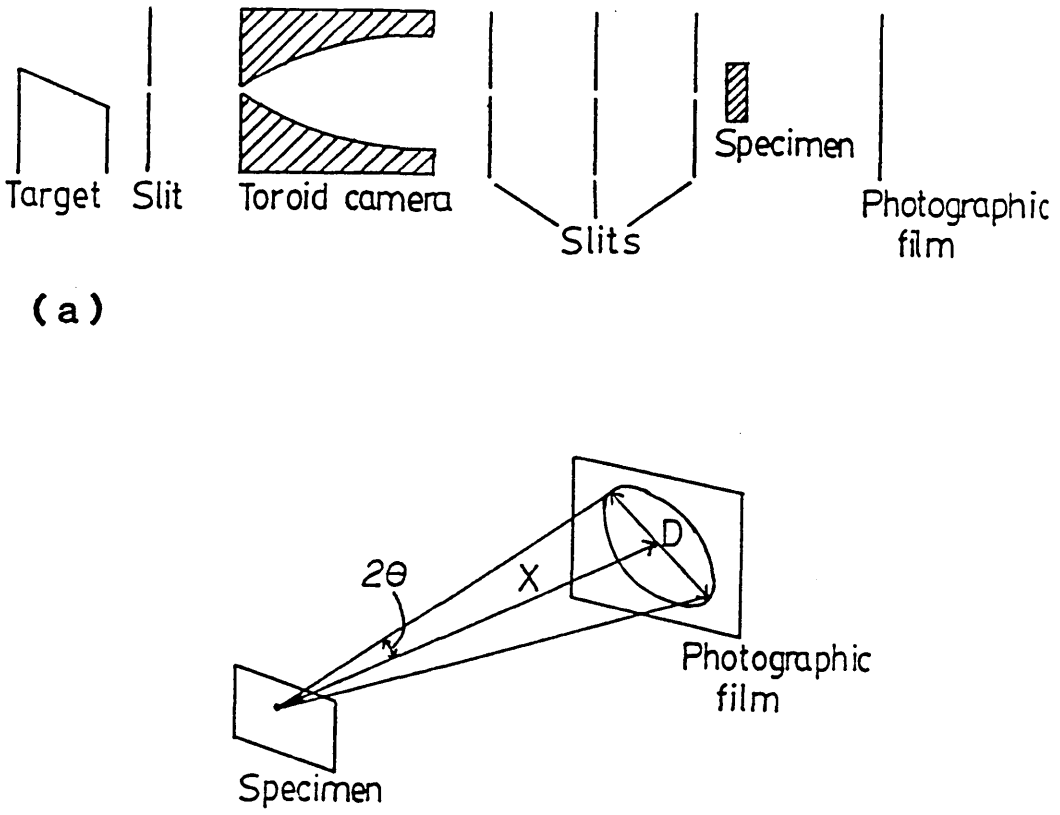


Figure 2.4.1: Basic arrangement of the focusing toroid camera.
(a) Schematic arrangement
(b) Angular relationships.

The photographic film or specimen, or both, is moved during the exposure to produce smooth, and continuous diffraction lines. By rotating or oscillating the photographic film about the axis of the incident beam, the reflections from each reflecting particle or grain are smeared out along the Debye ring. The specimen itself may be rotated about the incident beam axis or about any axis parallel to the incident beam, or translated back and forth in any direction in a plane parallel to the specimen surface. Such movements increase the number of grains in reflection positions, and allow a greater proportion of the total specimen surface to take part in diffraction, thus ensuring that the information recorded is representative of the surface as a whole.

If the specimen is rather too thin (insufficient volume of diffracting material) or too thick (excessive absorption), the diffracted beams will be very weak or entirely absent. So there is an optimum specimen thickness that produces the maximum diffracted intensity, and is given by $1/\mu$, where μ is the linear absorption coefficient of the sample.

The mass absorption coefficient is given by;

$$(\mu/\rho)_{TOTAL} = \sum_i g_i \, (\mu/\rho)_i \qquad \text{------(2.4.2)}$$

where ρ is the density of specimen; g_i,the mass fraction of each element that makes up the specimen. Using equation 2.4.2, the optimum thickness for x-ray diffraction of $CdCl_2.H_2O$, is 13.5μm.

From Bragg's law,

$$n\lambda = 2d\sin\theta \qquad \text{------(2.4.3)}$$

where d is the interplanar spacing, λ is the wavelength of radiation, and θ is the diffraction angle (cf. Fig. 2.4.1b), which then gives,

$$d = 0.77/\sin\theta \qquad \text{-------(2.4.4)}$$

From equation 2.4.1,

$$\theta = 0.5 \arctan (D/(2X)) \qquad \text{-------(2.4.5)}$$

Using equations 2.4.4 and 2.4.5, the d spacings of $CdCl_2.H_2O$ powder is determined from the diffraction pattern of Fig. 2.4.2a, and the results presented in Table 2.4.1

Figure 2.4.2:

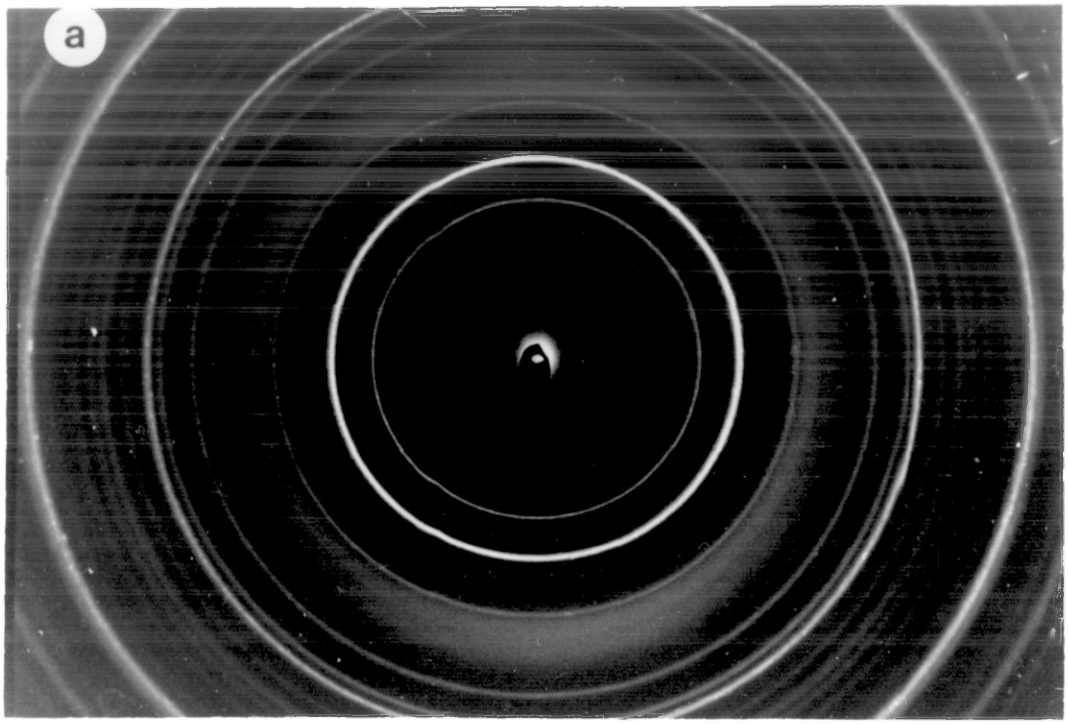
X-ray diffraction pattern of $CdCl_2.H_2O$ (film and powder), and $PbCl_2$ film

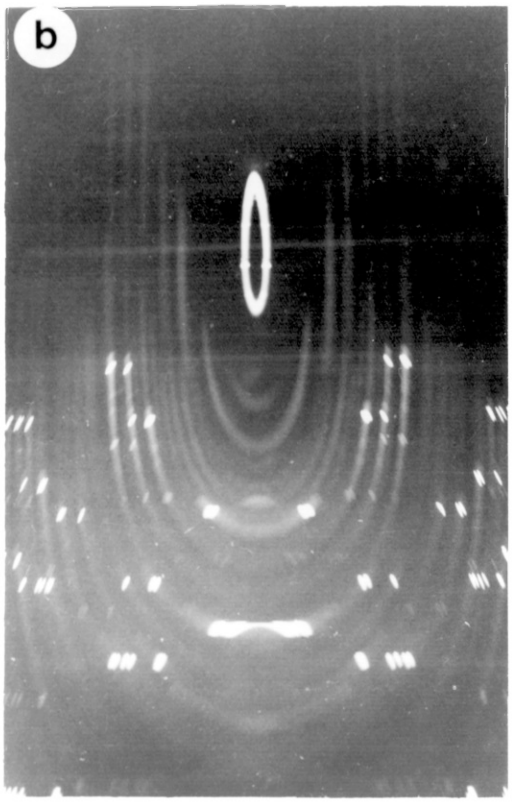
(a) Transmission photograph of $CdCl_2.H_2O$ (powder) Debye ring

(b) Cylindrical texture camera photograph of $CdCl_2.H_2O$ film on Si-substrate. Cu-kα radiation at i=18°

(c) Cylindrical texture camera photograph of $PbCl_2$ thin film on Si-substrate. Cu-kα radiation at i=18°

In (b) and (c), the "spots" is the silicon diffraction pattern, with the horizontal lines the diffraction lines of the films.


a


b

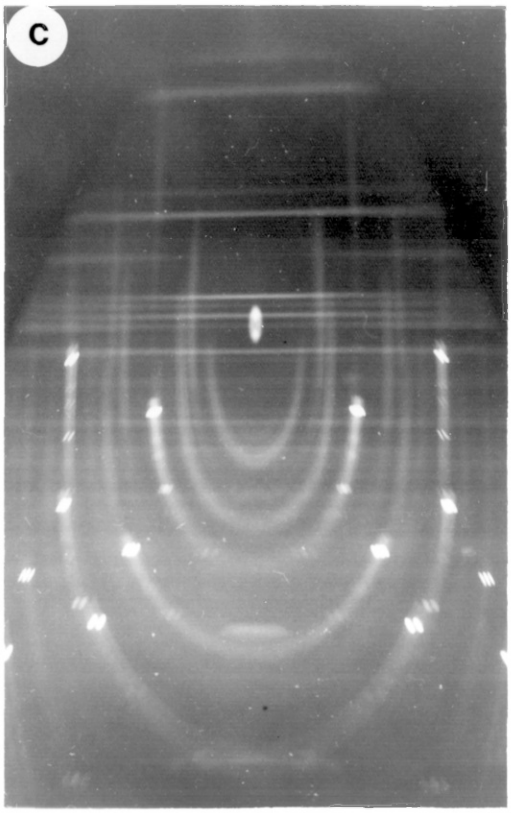

c

Table 2.4.1: d-spacings of $CdCl_2.H_2O$ powder, determined using the focusing toroid camera.
$X = 54 \pm 0.5mm$, $\lambda = 1.5405\text{Å}$

D (mm)	Θ (degrees)	d±0.01 (Å)
22.9	6.0	7.32
28.8	7.5	5.88
36.8	9.5	4.67
48.4	12.2	3.65
52.9	13.2	3.39

Comparing these d values with the standard [15], the specimen was seen to be hydrated cadmium chloride ($CdCl_2.H_2O$). This result confirmed the belief that the $CdCl_2$ powder absorbed water once exposed to the laboratory atmosphere. The shutter-evaporation method, in which degassing was done to remove the water vapour and other impurities in the source material, is of prime importance in depositing films of $CdCl_2$. The focusing toroid camera technique could not be used for thin films, mainly because of the optimum thickness restriction (typical film thickness used for x-ray studies was 0.1μm).

2.4.2 X-Ray Diffraction of $CdCl_2.H_2O$ and $PbCl_2$ Films.

The cylindrical texture camera [16] employs a flat specimen inclined at an angle, i, to the incident x-ray beam, which, is along the cylinder axis. The diffraction cones of constant 2θ intersect the recording film in straight lines (Fig. 2.4.2b & c). The camera uses a cylindrical cassette of 5.73cm (2R) diameter (allowing for the thickness of the photographic film), and 12.5cm length. Collimator and beam-stop tubes, concentric with the camera axis, are mounted at each end of the cassette on discs which act as radiation shields. The experimental arrangement is shown in Fig. 2.4.3. The inclination angle, i, is variable up to 45°, and the position of the specimen along the camera axis is also variable. The inclination angle, i, sets

a lower limit to the range of 2θ values that can be recorded. Also the finite length of the cassette cuts off the diffraction pattern at both ends of the 2θ scale. By altering the position of the specimen, the whole diffraction pattern may be shifted along the axis, so that either the low-2θ (specimen close to collimator), or high-2θ (specimen farther away from collimator) regions may be recorded on the photographic film. The relative positions of the film diffraction lines are unaffected by movement of the specimen along the camera axis, or motor shaft, or variation in i, the only essential alignment is that the incident beam should be accurately coincident with the cylindrical axis.

The specimen, $CdCl_2.H_2O$ or $PbCl_2$ film on a silicon substrate (having a native oxide thickness of about 1nm) was prepared as described in section 3.1. Prepared sample was mounted on a disc perpendicular to the motor shaft, with the specimen surface inclined at 18^o to a beam of nickel-filtered copper radiation, and continuously rotated during exposure. The x-ray tube was operated at 20kV, 20mA, in order to reduce the amount of scattered and fluorescent radiation generated in the substrate, by more penetrating high-energy incident radiation.

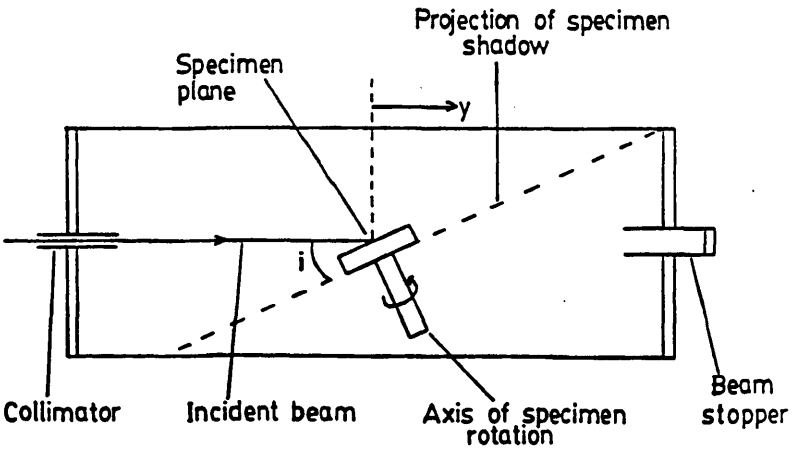


Figure 2.4.3: Schematic diagram of the cylindrical camera. i, the angle of inclination.

The diffraction patterns obtained are shown in Fig. 2.4.2b & c. The d-spacings of silicon substrate [15] were used to obtain corresponding diffraction lines (y-values) by using equations 2.4.3 and 2.4.6, and the results presented in Table 2.4.2. The drawn y-lines were matched with the substrate pattern (dotted features in Fig. 2.4.2b &c), giving the y-origin on the obtained patterns (Fig. 2.4.2b & c). The diffraction lines of the films were then identified by measuring the positions of the diffraction lines, y, along the camera axis. Corresponding values of θ were then derived from the following equation [16],

$$y = R\ \mathrm{Cot}(2\theta) \qquad \text{-----(2.4.6)}$$

The interplanar spacing, d, is then calculated, using the Bragg's relation of equation 2.4.3, and the results presented in Table 2.4.3. The values of the interplanar spacing, d, compare favourably with the $CdCl_2.H_2O$ and $PbCl_2$ of the standard [15].

Table 2.4.2: Silicon-substrate, d-spacings obtained from the "standard" [15], and the corresponding y-values, obtained by using equations 2.4.3 and 2.4.6. R = 2.865 cm, λ = 1.5405 Å.

d (Å)	θ (degrees)	y± 0.10 (cm)
3.13552	14.22	5.29
1.92011	23.65	2.64
1.63747	28.06	1.92
1.35772	34.57	1.09
1.24593	38.19	0.69
1.10857	44.02	0.10
1.04517	47.48	-0.25
0.96005	53.36	-0.86
0.91799	57.05	-1.28
0.85870	63.77	-2.20
0.82820	68.45	-3.06

Table 2.4.3: $CdCl_2.H_2O$ and lead chloride d-spacings.
R = 2.865cm, λ = 1.5405 Å.

Samples	y ± 0.10 (cm)	Θ (degrees)	d ± 0.01(Å)
	6.30	12.2	3.64
	5.80	13.1	3.39
	5.05	14.7	3.02
$CdCl_2.H_2O$	4.23	17.0	2.63
	3.95	18.0	2.50
	3.80	18.5	2.43
	3.68	19.0	2.37
	3.00	21.8	2.07
	2.72	23.2	1.95
	6.60	11.7	3.80
	6.15	12.5	3.56
	4.82	15.4	2.90
Lead	4.52	16.2	2.76
chloride	4.00	17.8	2.51
	3.45	20.0	2.25
	3.20	20.9	2.16
	3.10	21.4	2.11
	2.70	23.4	1.94

The proportion of water in a 80nm thick film of $CdCl_2$ deposited as fully described in section 3.1.2 is negligible. This is because during film deposition, the partial pressure of water was about $5x10^{-8}$torr, resulting in $CdCl_2$:H_2O flux ratio of about 4500:1 at the evaporation conditions. Also a change in colour interference was observed on exposing the $CdCl_2$ film to atmosphere. It can then be concluded that $CdCl_2$ film absorbed water on exposure to atmosphere, and not during deposition.

2.5 HYDRATION-DEHYDRATION OF $CdCl_2$ FILMS USING A QUARTZ CRYSTAL MICROBALANCE (QCM)

The QCM method was used, as it is a very sensitive mass balance [17], and under optimum conditions, could detect a very small change in mass (dm), typically $1x10^{-12}$g [18]. The crystal itself is a plano-convex plate approximately 14mm in diameter and 0.25mm thick, and it is excited into thickness shear vibrations by the external local oscillator unit at a frequency of about 6MHz. Changes in the environment of the vibrating quartz plate causes the resonant frequency to change: such as variations of frequency shift with temperature and pressure. The exact frequency shift is determined by the mass of material which may have been deposited on the crystal surface: the added mass causes a frequency decrease.

Sauerbrey [19], was the first to propose the use of a quartz crystal resonator to monitor the deposition of thin films. He made the assumption that the deposited film would have the same effect as an equivalent distributed mass of crystal represented by;

$$t_m = \frac{N_q \cdot \rho_q}{\rho_m \cdot f^2} \cdot (f_q - f) \qquad \text{-------(2.5.1)}$$

where t_m is the film thickness of material m, ρ_q is the density of quartz crystal, ρ_m is the density of material m, N_q is the frequency constant of the crystal, f is the frequency of loaded crystal, and f_q is the frequency of unloaded crystal. Representing C_q and Δf by the expressions;

$$C_q = \frac{f^2}{N_q \cdot \rho_q}, \quad \text{and} \quad \Delta f = f_q - f$$

where C_q is the mass sensitivity or calibration factor of the quartz crystal, and Δf the frequency shift due to material gained or lost. Equation 2.5.1 can then be represented by,

$$t_m = \frac{1}{C_q} \cdot \frac{\Delta f}{\rho_m} \qquad \text{------- (2.5.2)}$$

Value of C_q can be determined by carrying out the standard calibration procedure of the crystal, using opaque films of aluminium (>500Å). Equation 2.5.2 is then valid for a particular material of known density. The equation predicts that any change in mass of material m,

is viewed as an equivalent increase in the mass (frequency) of the crystal, based on the assumption that C_q is constant. This assumption is usually adequate, provided that very heavy depositions are not made (keeping dm small, within 2 mg cm^{-2}). Deviation from linearity could result if Δf approaches one percent of f.

Anhydrous $CdCl_2$ films were deposited on a quartz crystal, and the frequency shift (Δf) monitored using a film thickness monitor (Intellimetrics (U.K) Ltd). When the crystal was exposed to the laboratory air following the depositions, a time interval was allowed for the frequency shift to stabilise. This was necessary due to the incipient uptake of water to form a hydrated $CdCl_2$ film in the moist atmosphere. The frequency readings as a function of exposure time are presented in Table 2.5.1, for two such experiments.

Table 2.5.1: Extent of hydration in cadmium chloride films, using QCM as the measuring tool.

	Frequency shift on evaporation. (Hz)	Frequency shift on exposure to air time (min)	**f(Hz)	Film thickness (Å) *$CdCl_2.H_2O$	+$CdCl_2$
		t_o^-	1212		
		t_o^+	1300		
run 1	1214	2	1324	920	736
		15	1326		
		30	1335		
		45	1342		
		t_o^-	1716		
		t_o^+	1755		
run 2	1720	4	1872	1230	984
		30	1880		
		45	1884		

t_o^- , is the time just before exposing the film to atmosphere

t_o^+ , is the moment the sample was just exposed to air.

** Boyancy effects (of 36Hz) correction have been made for readings in air.

* Ellipsometric measurements

+ Determined from equation 2.5.3

The final frequency readings (Table 2.5.1) were substantiated by exposing the crystal to the laboratory air for a further twenty four hours. The shift in frequency was within 1% of the reading obtained after 45 minutes of exposure.

In general $CdCl_2$ films of thickness around 1000Å, hydrate to their limit ($CdCl_2.xH_2O$) within a few minutes of exposure (x is the number of moles of water per mole of $CdCl_2$). This was found to be 1.07 and 0.97 for runs 1 and 2 respectively, giving an average of 1.02 [20]. Within experimental error, x could be taken as 1, which is in agreement with the x-ray result on the $CdCl_2.H_2O$ film (section 2.4.2).

Using equation 2.5.2, the density of the $CdCl_2.H_2O$ films was determined to be $3.56 \pm 0.14 g\ cm^{-3}$ [20] (compared with $3.244 g\ cm^{-3}$ given in reference 15). This value was based on a standard crystal calibration procedure using opaque films of aluminium. Using the density determined for $CdCl_2.H_2O$ films, the following relationship for determining the thickness of anhydrous $CdCl_2$ was derived from equation 2.5.2.

$$t_{(CdCl_2)} = 0.8t_{(CdCl_2.H_2O)} \qquad \text{-------(2.5.3)}$$

To conclude, it has been shown that cadmium chloride films has composition of $CdCl_2$ in vacuum, and on exposure to the moist laboratory air absorb water giving $CdCl_2.H_2O$, which is rapidly and reversibly removed in vacuum at ambient temperature (Fig. 2.5.1) [20].

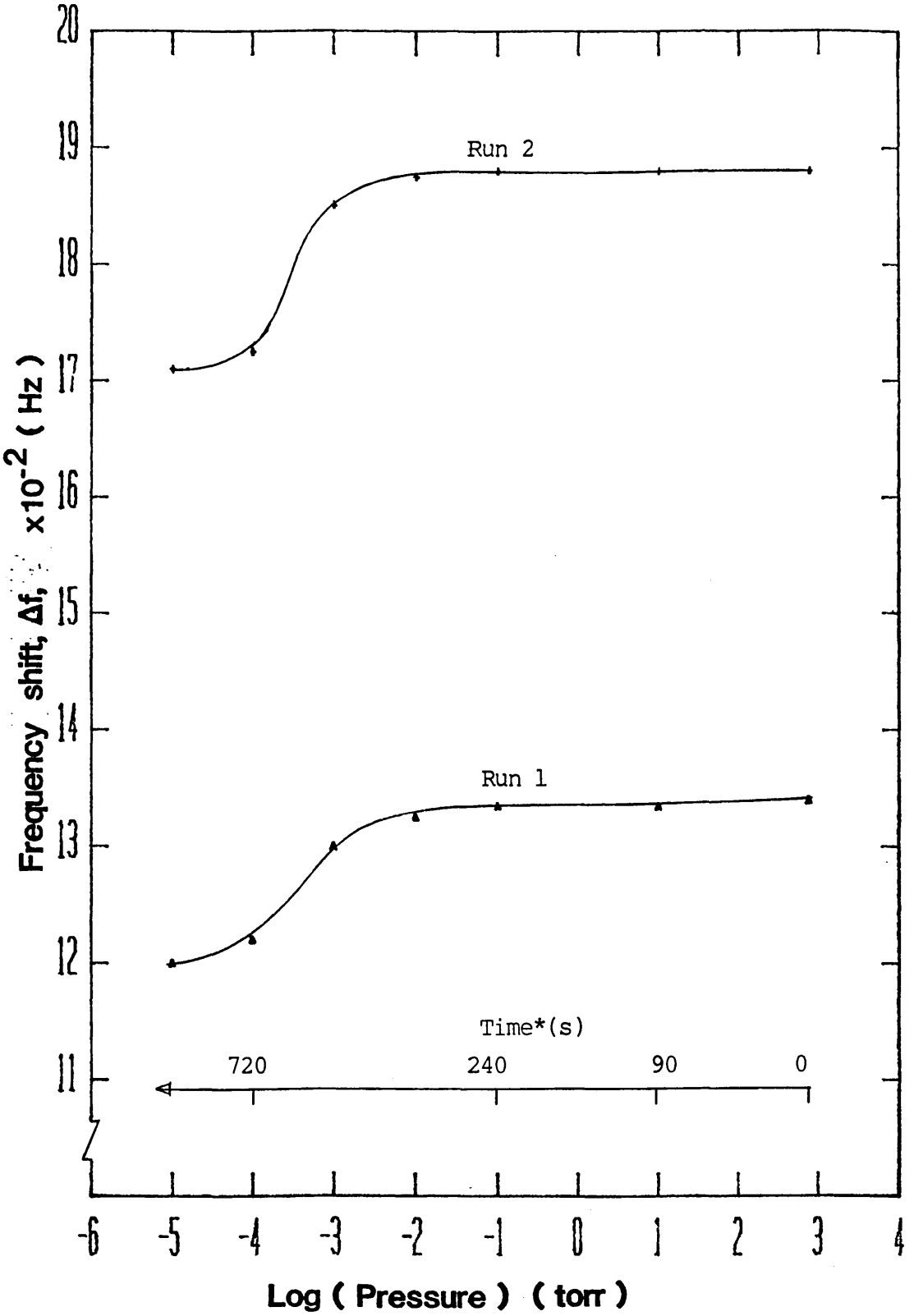


Figure 2.5.1: Weight loss vs. Total chamber pressure, for cadmium chloride (hydrate) films.

*The time origin corresponds to atmospheric pressure, and when pumped-down of the chamber started. The scale is neither a logarithm scale nor a linear scale, but with discrete values at specified pressure points.

CHAPTER 3

EXPERIMENTAL TECHNIQUES.

3.1 SAMPLE PREPARATION AND STORAGE

Samples used in obtaining the results presented in chapters 2, 4 and 5 were essentially individual deposition of lead chloride ($PbCl_2$) and cadmium chloride ($CdCl_2$) films on the following substrates. Aluminium/glass (20nm thick film of aluminium on a glass slide), a silicon wafer having a native oxide thickness of about 1nm, and an oxidised silicon wafer (of oxide thickness of 100nm). A solid solution of $PbCl_2/CdCl_2$(20%) was also deposited and investigated. 95% pure $CdCl_2$ and 99% pure $PbCl_2$ powder obtained from BDH Chemicals (U.K.) Ltd, were used as appropriate, for film deposition.

3.1.1 Substrate Preparation

(a) Oxide Etching of Oxidised Silicon Wafers.

Oxidised silicon wafers were chemically etched in a solution of 20% by volume of concentrated hydrofluoric acid, 14% by volume of concentrated nitric acid, and 66% by volume of distilled water; followed by flooding out of the etch content (with deionised water), to stop the etch process and to have a smooth etched wafer surface. Etching was at 25^{o}C, etch rate of 100nm/min was achieved. The average oxide thickness after appropriate etching time was found to be about 1nm (ellipsometric measurement, see Appendix III). This oxide layer is regarded as a native oxide formed as a result of exposing the etched silicon wafer to laboratory air.

(b) Substrate Cleaning Methods.

Cleaning of the etched and unetched oxidised silicon wafer, and also of the glass slide, were carried out (in a clean room) in order to ensure proper adhesion of deposited films onto the substrate. The cleaning procedures are as follows:

(i) The substrate was washed, wearing disposable polythene gloves, in a 1% solution of "Teepol" in distilled water (that was at ambient temperature).

(ii) Followed by rinsing for about 30 seconds in distilled water.

(iii) An ultrasonic wash for 2 minutes carried out by placing the substrate in a beaker of iso-propyl alcohol (IPA) placed in an ultrasonic bath.

(iv) Step (iii) was repeated using distilled water.

(v) Finally the substrate was re-fluxed in a vapour of IPA for about 1 hour, and allowed to dry in situ.

Clean substrates (which do not allow droplets of deionised water to form at room temperature) were placed inside petri-dishes, and stored in a dry box containing silica-gel. All substrates were used for deposition within a few days of cleaning.

3.1.2 Film Deposition Procedure.

Thin films were thermally deposited in a vacuum coating plant (Speedivac Model 19E6). This has a pumping unit that comprises a Speedivac model F903 oil diffusion pump, and a Speedivac model 1SC450 gas ballast rotary pump. A base pressure, slightly less than 10^{-5}torr could be achieved without a liquid nitrogen trap. By using a liquid nitrogen trap a pressure of $\sim 10^{-6}$ torr was achieved.

A molybdenum electric resistive heating boat was used in the evaporation. The boat was cleaned by washing in a solution of "Teepol", tap water, and IPA in that order. It was then given a slight bake-out in an oven kept at a temperature of 100^{o}C. The evaporation temperature was measured using a chromel-alumel thermocouple stuck very close to the inside of the boat but not actually touching the boat.

Prior to evaporation, a rough estimate of the rate at which materials leave the boat (source) at deposition temperatures of 350°C to 400°C, was determined from the saturation vapour pressure and particle flux curves [1], Figures 3.1.1 and 3.1.2 respectively. The particle flux curves of Figure 3.1.2 were obtained from the following equation [2],

$$\Gamma = \frac{P}{(2\pi mkT)^{\frac{1}{2}}} \qquad \ldots\ldots (3.1.1)$$

where Γ is the particle flux (number of particles per m^2 per second) P is pressure in pascals, m is mass of particle (molecular weight/ Avogadro's number), k is Boltzmann's constant, and T is the absolute temperature. Assuming unity sticking coefficient when materials hit the substrate, the deposition rate R_D, was estimated from the following equation [3],

$$R_D = \frac{\cos\theta}{r^2} \cdot \Gamma \qquad \ldots\ldots (3.1.2)$$

Where r is the substrate-to-source distance, and θ is the angle between the normal to the substrate and the radial vector joining the source to the point on the substrate being considered.The substrate-to-source distance was 20 ± 2cm, so as to have film of fairly uniform thickness (~5% variation over the entire Si-wafer). A shuttered evaporation system was employed so as to eliminate the more volatile impurities, which evaporate first from the source, and be prevented from being deposited on the substrate. This was followed by an intermediate step of achieving steady evaporation rate, and finally the film deposition step (during when the shutter was opened). Evaporation rates and film thicknesses were monitored during deposition by the use of a quartz crystal microbalance (QMC) described in section 2.5. Film deposition rates were in the range of 3nm/s to 5nm/s. Deposited films thicknesses were in the range of 50-200nm. The arrangement inside the chamber allowed the QCM to be exposed to the evaporation source without exposing the substrate during the rate-determining step.

In depositing $PbCl_2/CdCl_2$(20%) films, the amount of $CdCl_2$ and $PbCl_2$ in the source boat was determined by theoretically fixing the source temperature. From the source rates of $PbCl_2$ and $CdCl_2$ (estimated from Fig. 3.1.2), these being equivalent to the deposition rates (equation 3.1.2), the ratio of the particle flux $PbCl_2$:$CdCl_2$ was calculated and the result used to determine the weight ratio of the two compounds inside the source boat. The doping error was found to be ±2%, for all films of $PbCl_2/CdCl_2$(20%) deposited (see section 5.2.1).

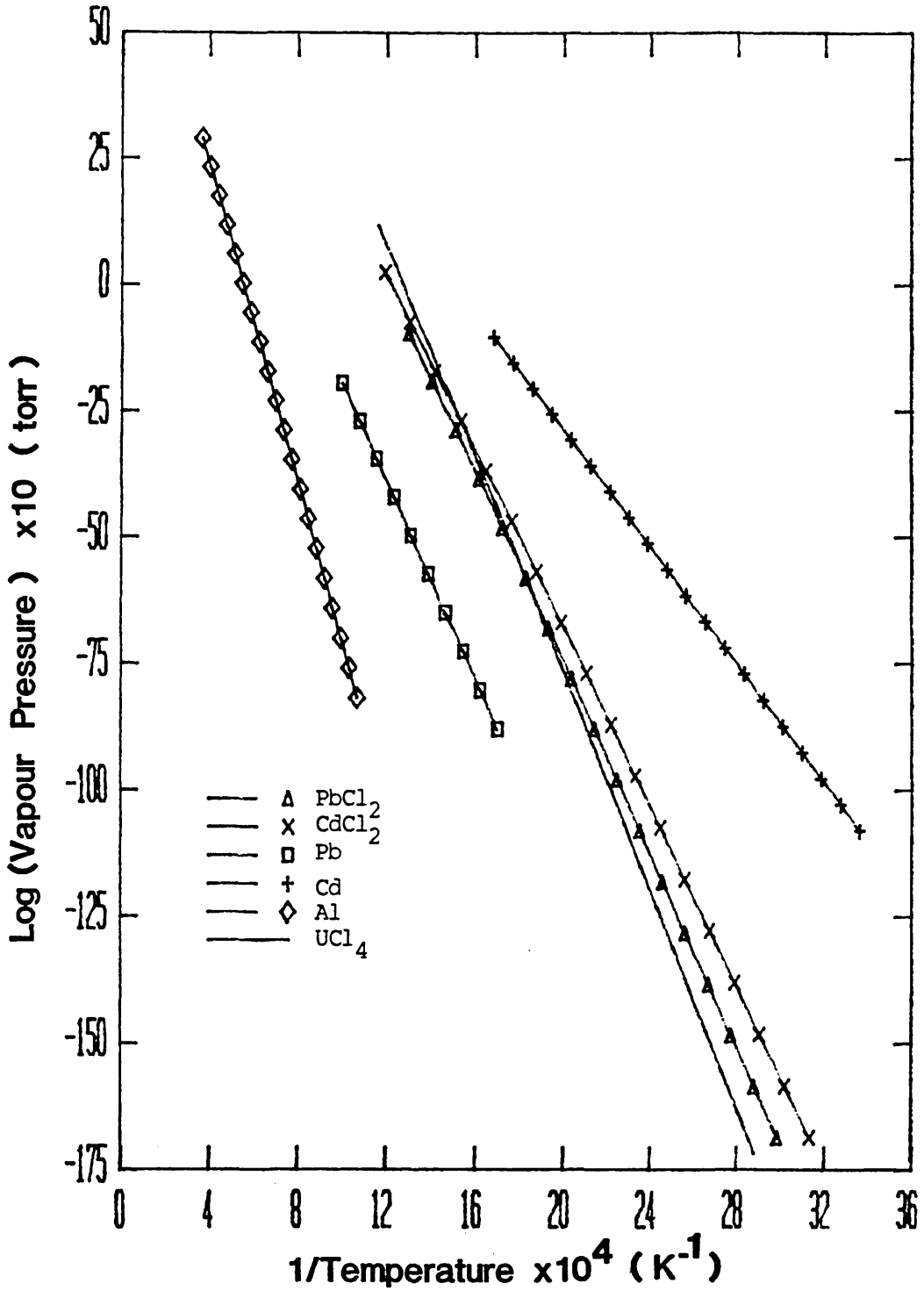


Figure 3.1.1: Vapour pressure curves

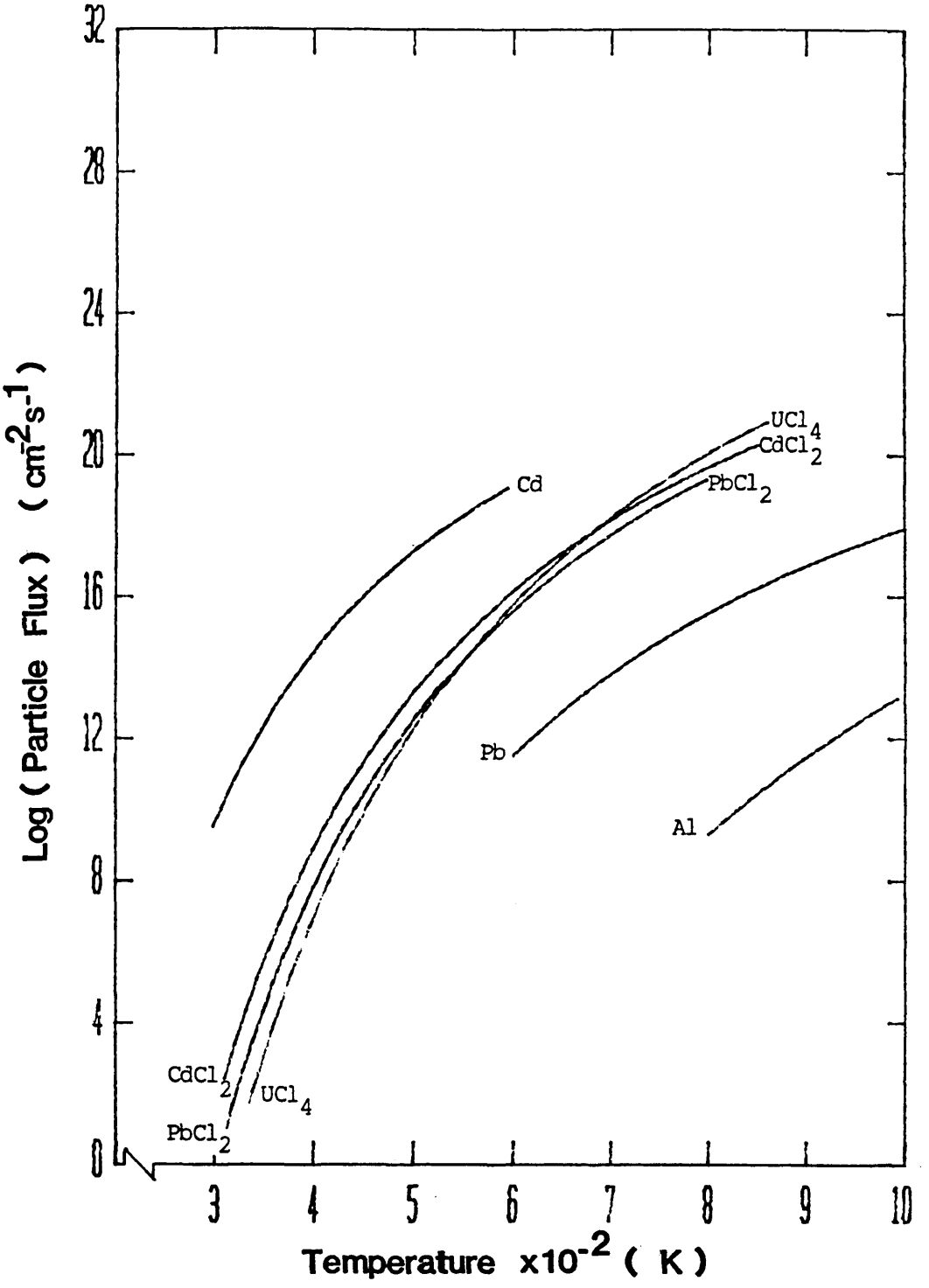


Figure 3.1.2: Particle flux vs. Temperature.

3.1.3 Sample Handling and Storage.

All samples were used within few days of deposition for required experimentation. Prepared samples to be used were stored in a dry box, which contained silica-gel, at ambient temperature. In handling samples, as in cutting for required size, polythene gloves were worn, mouth and nose masks were also worn. Movement of samples were restricted to the bearest minimum to avoid contamination.

3.2 FILM THICKNESS AND REFRACTIVE INDEX DETERMINATION

Evaporated film thicknesses were estimated during deposition, by the method of quartz crystal thickness monitoring (described in section 2.5). Film thickness measurements of deposited films and processed samples, were carried out by ellipsometric method and by using a "Talystep" instrument (described in Appendix III).

Ellipsometric measurements of the refractive index, n, of the films are: $CdCl_2.H_2O$ ($n=1.678 \pm 0.005$), $PbCl_2$ ($n=2.216 \pm 0.005$), and $PbCl_2/CdCl_2.H_2O$ ($n=1.984 \pm 0.005$). The values of $PbCl_2$ refractive indices given in the literature [4] are 2.1999, 2.217, and 2.260. $CdCl_2$ refractive indices [5] are 1.681 and 1.718, ordinary and extra-ordinary values respectively.

3.3 EXPERIMENTAL SET-UP FOR ELECTRON BEAM RADIOLYSIS

3.3.1 Vacuum Equipment.

The vacuum chamber is made of stainless steel with various ports for installation of desired component parts, and windows for viewing, as shown in Fig 3.3.1. This is schematically represented in Fig. 3.3.2. Vacuum was achieved by first using a rotary pump (installed with a foreline trap) to "rough" the system down to about a pressure of 40 mtorr. This was followed by operating a two-inch oil diffusion pump (that has a liquid nitrogen trap) in parallel with a vac-ion pump. After obtaining a pressure in the neighbourhood of 10^{-7} torr, the oil diffusion pump was valved off from the chamber and a titanium sublimation pump (TSP) used in parallel with the vac-ion pump to obtain a vacuum of $\sim 10^{-9}$ torr. Although better vacuum pressures were attainable through baking, this procedure was considered not to be necessary as pressure of $\sim 10^{-8}$ torr was considered satisfactory for all decomposition experiments. To change sample after each set of decomposition experiments, dry oxygen-free-nitrogen gas was admitted into the chamber to attain atmospheric pressure. This is to facilitate quick pump-down of the system for subsequent experimental investigations.

3.3.2 Experimental Rig Used for Electron Beam Decomposition Work.

The decomposition apparatus is shown in Fig. 3.3.1 with all the necessary electronic units used. The arrangement inside the chamber for electron beam radiolysis experiment is shown in Fig. 3.3.3. This shows the electron beam deflection plates, the quadrupole mass spectrometer (QMS), and the sample manipulator (Fig. 3.3.4a) capable of up and down movements, and also with rotation facility.

Complete connections and the attachments of the sample holder is shown in Fig. 3.3.4b, and clearly visible are the decomposed specimen, the phosphor screen, the thermocouple connection, the heater connection, and the Faraday cage for measuring electron beam current.

3.3.3 Experimental Procedures.

The sample holder (Fig 3.3.4) was used to position the specimen for electron beam irradiation, and also had provisions for heating the sample, measuring the sample temperature, as well as measuring the beam current by the use of the Faraday cage arrangement attached.

Easy location of the electron beam for focusing and for decomposition of specific areas of the samples were achieved by the use of a willemite phosphor screen, which was prepared as follows:

(i) A piece of glass slide of required dimension was washed in a solution of "Teepol" and rinsed with isopropyl alcohol and then with distilled water.

(ii) With the clean piece of glass placed inside a beaker, 15ml of 0.002M of barium nitrate solution was added to the beaker.

(iii) 0.8ml of potassium silicate solution, as supplied was added to the content of the beaker.

(iv) 0.8ml of prepared powder suspension solution (20g/litre of phosphor powder in 0.1% by volume of potassium silicate solution) was finally added to the beaker content.

(v) The beaker content was allowed to settle for 30 minutes without disturbance.

(vi) The decanted liquid was removed using a syringe, and the coated glass (which was still inside the beaker) was dried in an oven (kept at $100^{o}C$) for about 5 minutes.

Temperature correlation experiment was done to determine the variations in temperature at various positions on the sample holder. Variations in temperatures were found to be within $5^{o}C$.

Fig 3.3.5 is a schematic representation of the electron beam decomposition set-up. Decomposition products were detected by using the QMS, and the signal analysed was in sychronism with the electron beam which is blanked on a 50:50 duty cycle at a frequency of 128Hz. In this way, line-of-sight of chlorine (Cl^{35}) and cadmium (Cd^{114}) signals were measured using a lock-in amplifier which reduces considerably the effect of background signal. Thus giving the basic data of Cl^{35} and Cd^{114} signals versus time presented in Chapter 5. Experimentation was carried out with electron beam raster scanning (snake-like) a 4mm x 4mm area at 60 lines per frame (beam diameter is 0.3mm) and frequency of 256Hz. The set-up also included a temperature controller and the experiment controlled by a BBC micro-computer.

The electron beam decomposition results presented in section 4.1 was carried out without most of the above e-beam manipulation facilities. The experimentation involved bombarding $CdCl_2$ with a 2keV electron beam at various temperatures: "Talystep" measurements and electron probe micro-analysis of decomposed "spots" were done outside the vacuum chamber.

Figure 3.3.1:

Electron beam decomposition apparatus.

(a) Vacuum chamber (schematically drawn in Figure 3 .3.2)

(b) Electron gun power supply

(c) Scanner and Temperature controller unit

(d) IEEE 488 Inter-Face

(e) Keithley 480 pico-ammeter, for beam current measurement

(f) EG-G 5205 Lock-in amplifier

(g) SX 300 QMS Controller

(h) Ion-pump power supply

(i) Titanium sublimation pump power supply

(j) Pirani/Ion gauge control unit

(k) Bake-out heater control.

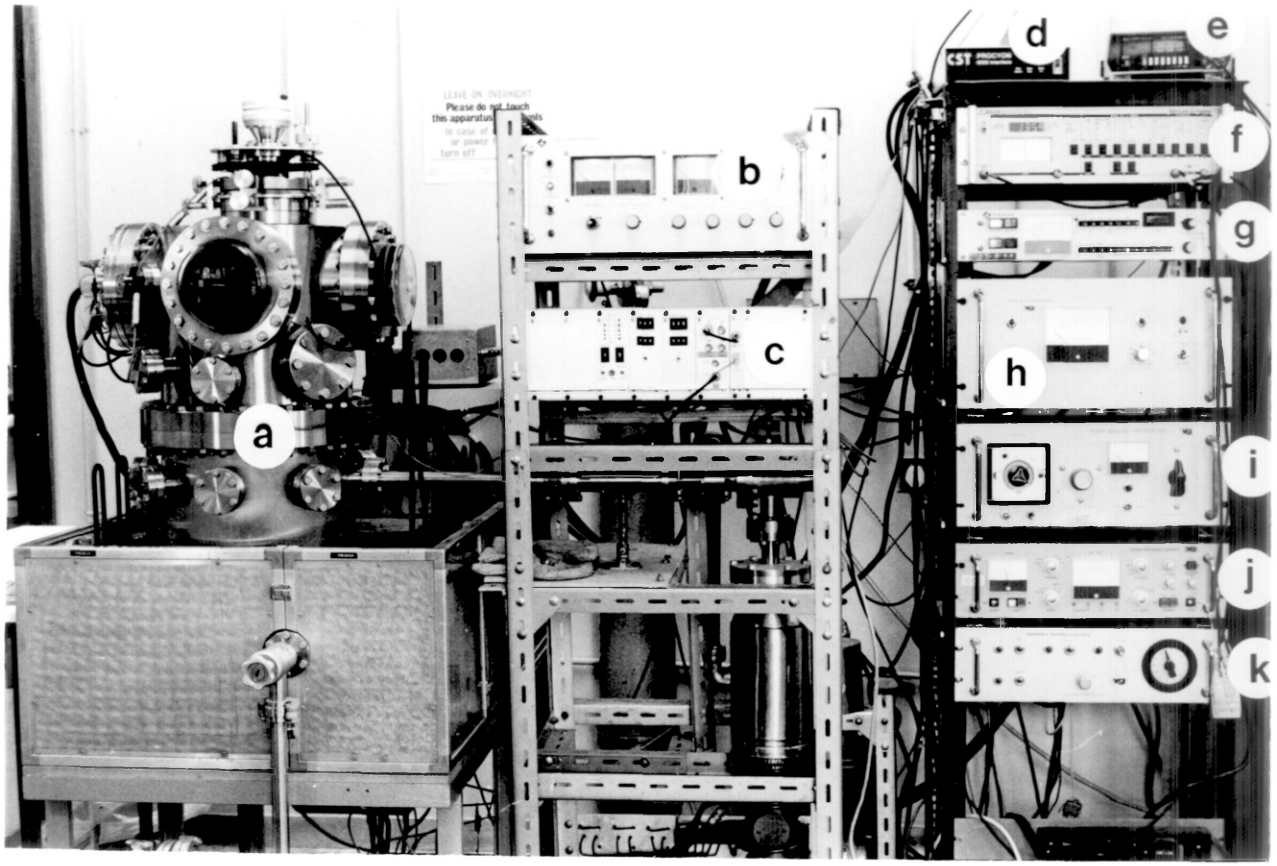

a
b
c
d
e
f
g
h
i
j
k

Figure 3.3.2:

Schematic diagram of the vacuum equipment used for e-beam decomposition studies.

(1) The target manipulator.

(2) Electron gun assembly flange.

(3) Quadrupole mass spectrometer port

(4 & 5) Viewing windows

(6) Ionization gauge

(7) Titanium sublimation pump port

(8) Ion pump port

(9) Liquid nitrogen trap with gold wire gasket at the top flange

(10) Diffusion pump with "Santovac 5" oil

(11) Fore-line trap

(12) Rotary pump

(13) Pirani gauge

(14 - 16) UHV all-metal (stainless steel) valves

(17) UHV micro-leak valve

(18 & 19) Speedivac valves with viton O-ring

(20) To oxygen free nitrogen gas cylinder

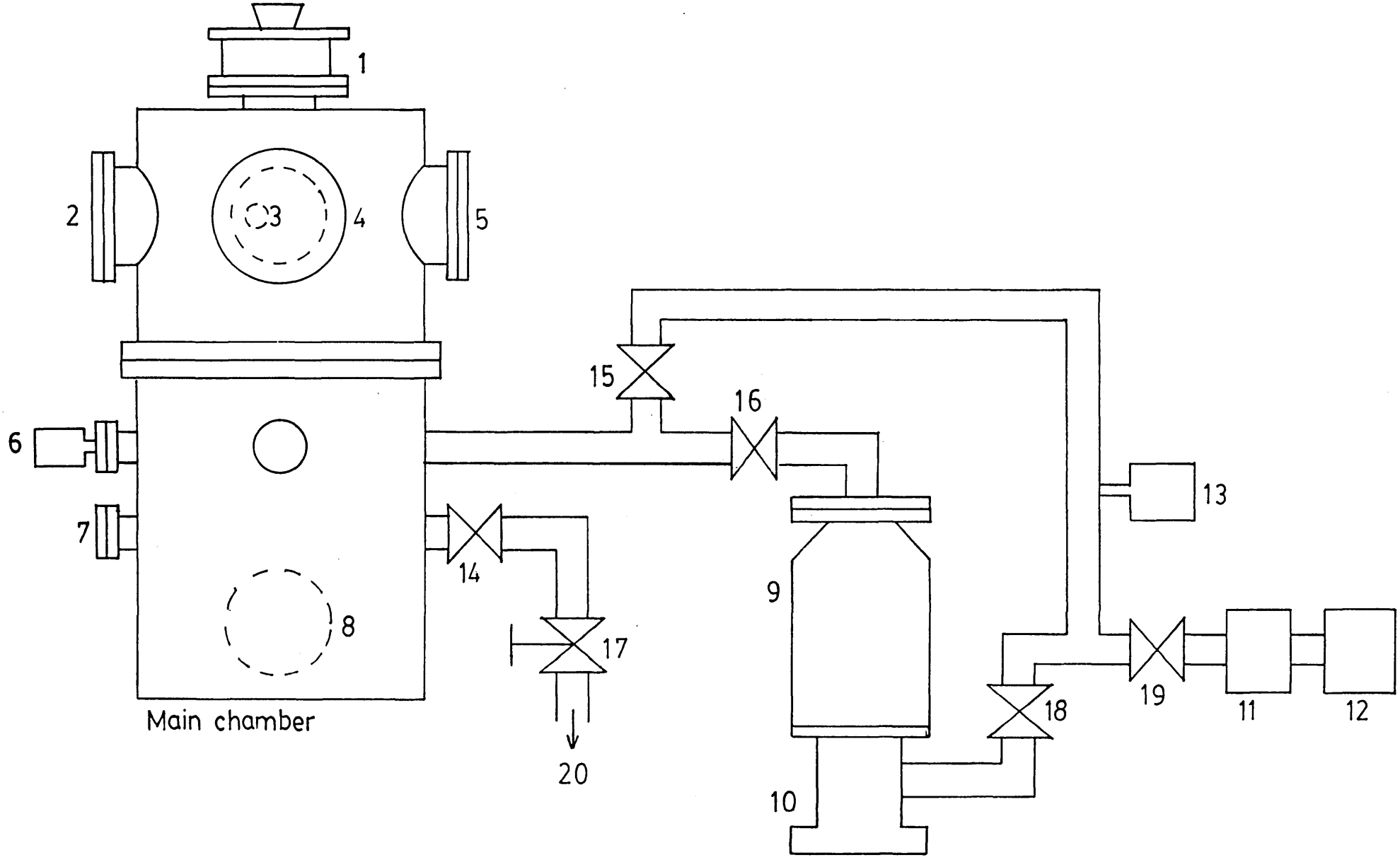

1
2
3
4
5
6
7
8
Main chamber
9
10
11
12
13
14
15
16
17
18
19
20

Figure 3.3.3:

Lay-out of various components(used for radiolysis) inside the vacuum chamber.

(a) Quadrupole Mass Spectrometer

(b) Sample holder

(c) Electron gun, showing the deflection plates assembly.

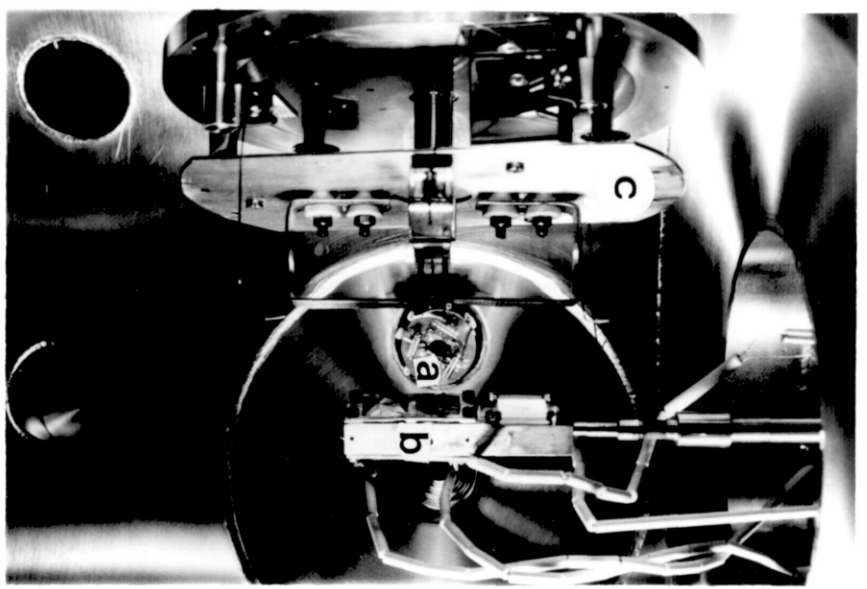

c
a
b

Figure 3.3.4:

(a) Sample manipulator.

(b) Sample holder.

(i) Decomposed specimen showing the 4mm x 4mm raster-scanned frames.

(ii) Phosphor screen, used for e-beam location.

(iii) Thermocouple lead, attached at the back of sample holder (see section 3.3.3 for discussion)

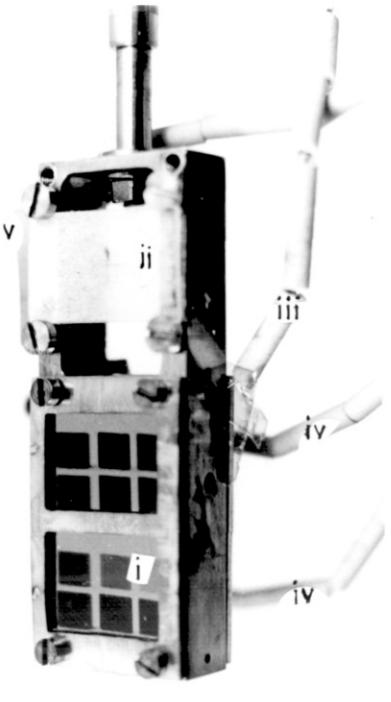
(iv) Heater connection wires.

(v) Faraday cage, an open rectangular box made with molybdenum, for beam current measurement

a



b



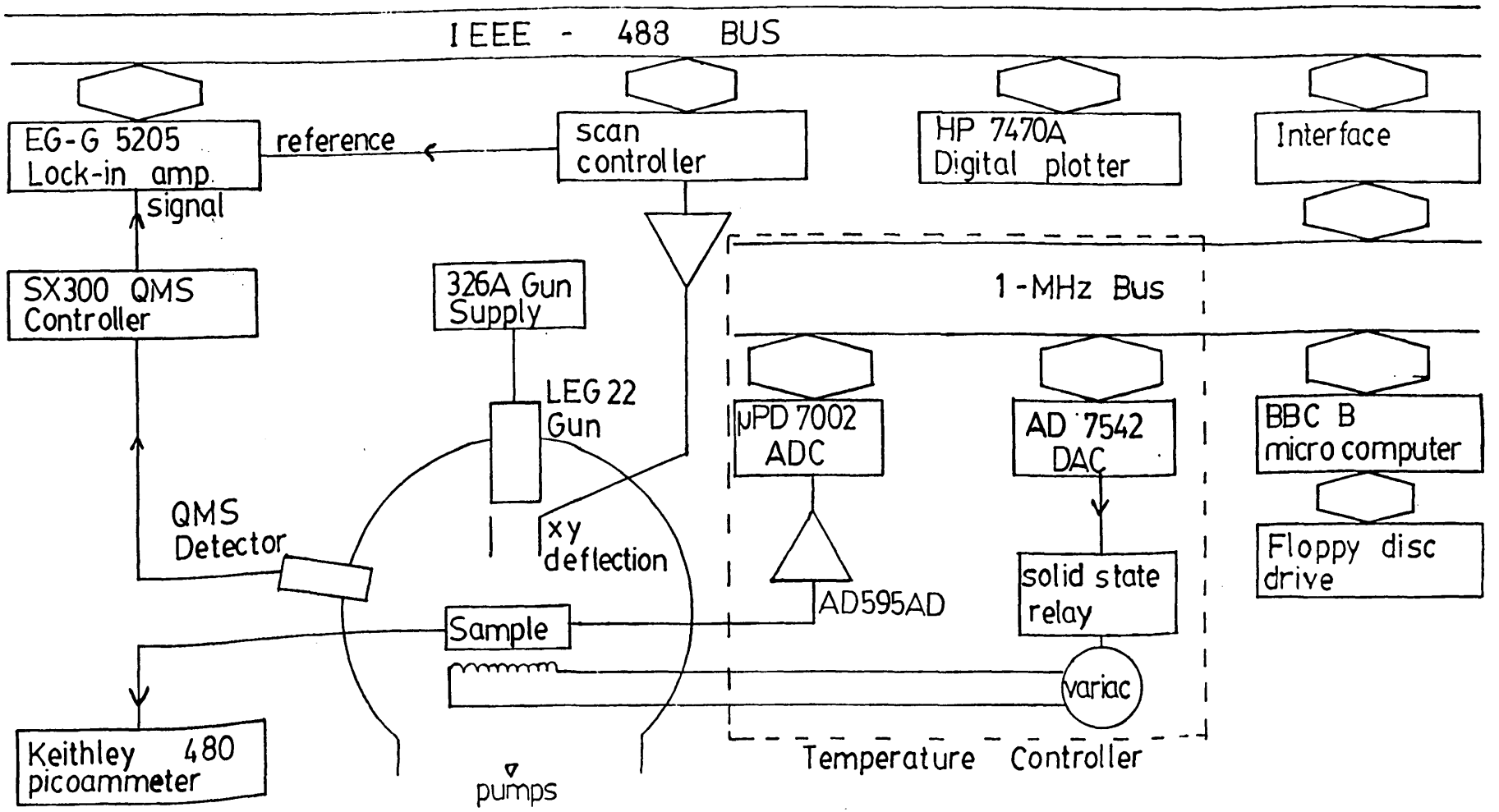


Figure 3.3.5:

Schematic diagram of the e-beam decomposition set-up

3.4 PLASMA-ASSISTED ETCHING AND END-POINT DETERMINATION: EXPERIMENTAL SET-UP.

3.4.1 Equipment.

A small commercial plasma etcher was extensively adapted such that both plasma etching and reactive-ion etching (RIE) work could be done, and an end-point detection unit using a QMS was added.

The modified equipment used is shown in Fig 3.4.1, and schematically represented in Fig. 3.4.2. It is essentially a parallel-plate radial flow reactor, that consist of two 18cm diameter water-cooled electrodes (made of aluminium), with an inter-electrode spacing of ~3cm. Power was generated by a r.f generator of fixed frequency of 13.56MHz with the impedance matching (tuning) done manually so as to have minimum reflected power and maximum forward power.

In the plasma mode, wafers were placed on the grounded electrode, known as the anode, and has electrical potential (0V) slightly less than the plasma potential. In the RIE mode, wafers were placed on the powered electrode (the cathode) and has electrical potential with respect to the plasma in the region of about -500 to -1000V peak-to-peak value.

Vacuum in the etching chamber was achieved by using a rotary pump (installed with a foreline trap) capable of a base pressure of $\sim 10^{-4}$ torr prior to introduction of etching gas. The chamber pressure was monitored using a tensioned diaphragm gauge (MKS baratron Type 222). The QMS used, is capable of detecting mass to charge ratio from 1 to 200 a.m.u. The QMS head column was maintained at pressure of $\sim 10^{-7}$ torr during effluent gas sampling by using an ion pump.

3.4.2 Etching and End-Point Detection Procedure.

Carbon tetrafluoride (CF_4) was the main etching gas used. In the plasma mode, oxygen (O_2) was added to CF_4 in order to prevent surface polymerisation on the $CdCl_2$ resist during etching.

To measure etch rates, film thickness was measured prior to introducing the specimen to plasma conditions, and also after the completion of etching. The change in thickness is divided by the etch

time to give an average etch rate. Film thickness measurements were by ellipsometry (Appendix III).

End-point determination was carried out in the RIE mode. Plasma etching was abandoned because of the inadequacy of the etching. Thus it was found there was polymerisation of the resist surface, poor etch rates of SiO_2 were obtained, as well as poor selectivity in etching SiO_2 and $CdCl_2$ when CF_4/O_2 etch-gas was used.

Compositional analyses of samples were carried out by means of electron probe micro-analysis (EPMA), electron spectroscopy for chemical analysis (ESCA), and secondary ion mass spectroscopy (SIMS). Surfaces of samples were examined using the scanning electron microscope.

The characteristic behaviour of the plasma chamber in terms of pressure and radial etch rate is presented in Figs. 3.4.3 and 3.4.4 respectively. The dotted lines in Fig. 3.4.3 represent the moment before the glow discharge was switched on. A slight increase in chamber pressure was observed at the instant the discharge started glowing. Etching conditions were kept constant by adjusting the main valve. A linear relationship exists (for each of the sample SiO_2 and $CdCl_2$) between the etch rate ratios and radial distances measured from the electrode centre (Fig 3.4.4), due to the non-uniformity in the etch gas distribution over the wafer surface.

3.5 THIN FILM ANALYSIS AND SURFACE MORPHOLOGY STUDIES.

Preparation of samples for EPMA and surface morphology studies was carried out by mounting specimen of required size onto a 1cm diameter brass or aluminium stub, using an electrically conducting silver paint. The sample was then gold coated for surface morphology studies, and carbon coated for EPMA. A film coating of about 10nm was found to be adequate for both studies. Compositional analyses by ESCA and SIMS were done without coating the samples.

The samples were examined in JSM-T100 scanning electron microscope, operating at 25kV, and has a resolution of 8nm. The examination was done with electron beam at an angle of 45^{o} to the samples. Therefore, the vertical scales of all micrographs presented in this thesis, are $2^{\frac{1}{2}}$ of the horizontal scales given.

Figure 3 .4 .1:

Plasma and Reactive-Ion etching apparatus

(a) Processing chamber

(b) r.f. power matching unit

(c) Gas flow meter

(d) Y-t plotter

(e) Etch-gas supply cylinder

(f) Oscilloscope for signal monitoring

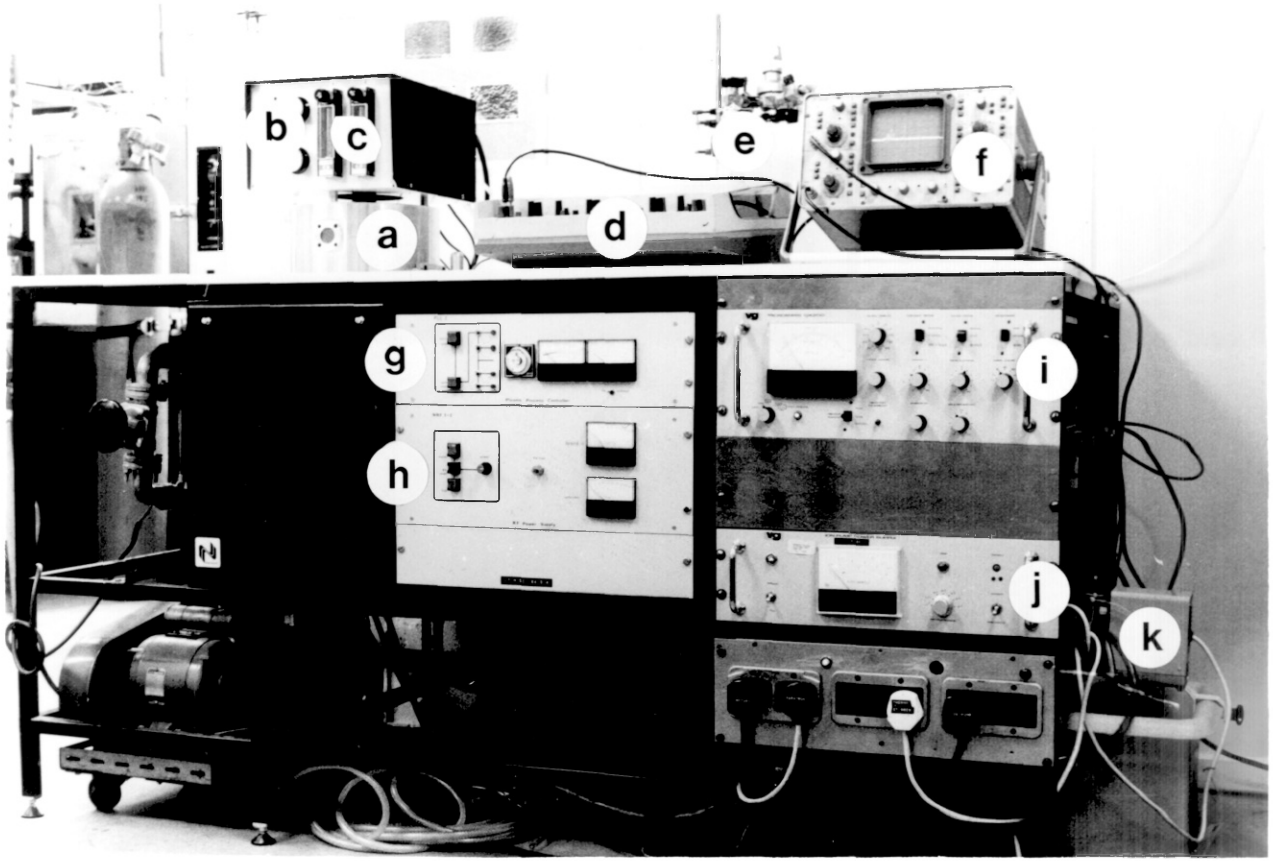
(g) Process controller

(h) r.f. power supply

(i) Micromass QX 200 QMS controller

(j) Ion pump power supply

(k) "Thermo-stirrer" for controlling the temperature of the circulating water passed through the electrodes.


a
b
c
d
e
f
g
h
i
j
k

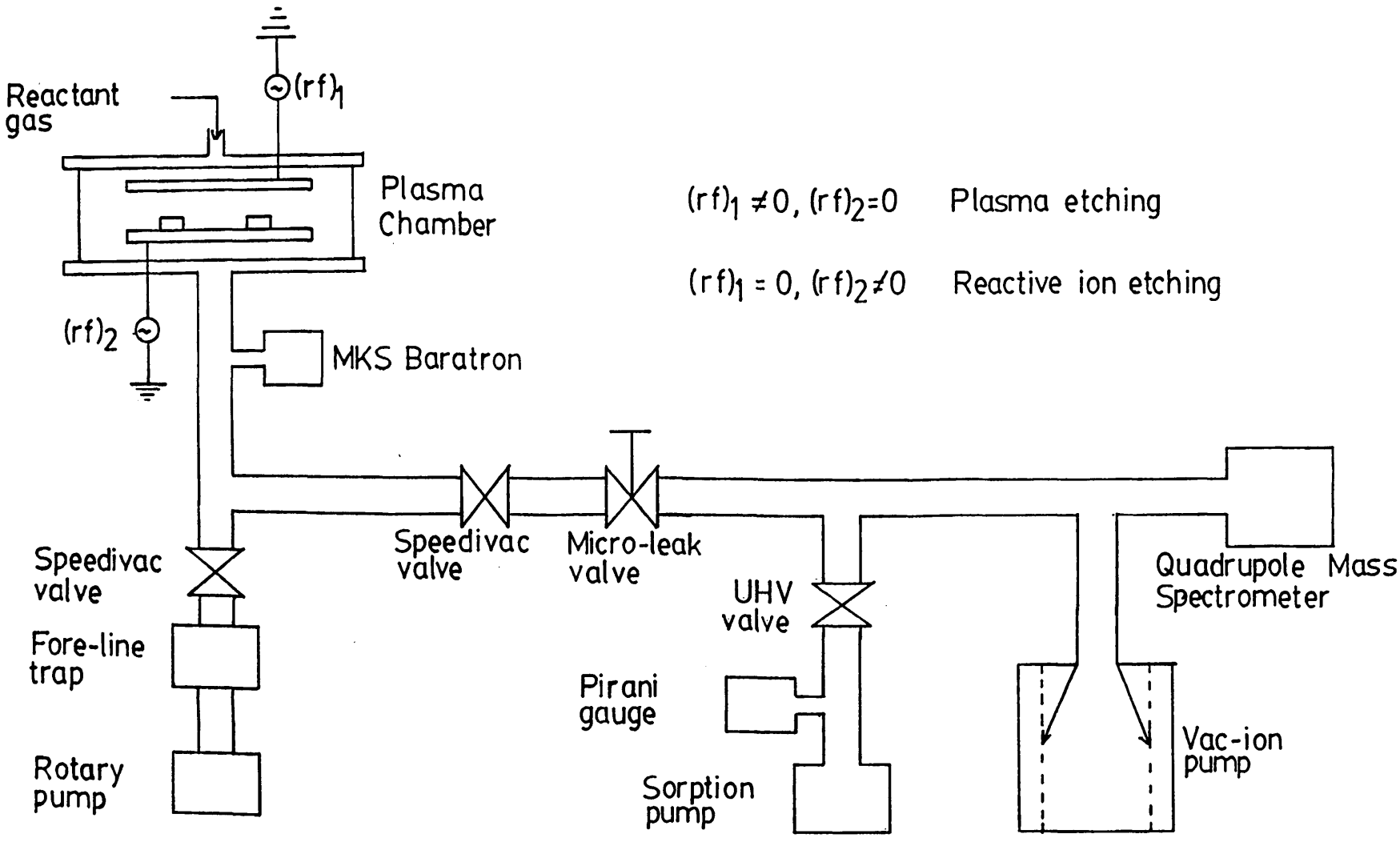


Figure 3.4.2:

Schematic diagram of the plasma-assisted etching apparatus, showing a quadrupole mass spectrometer attachment.

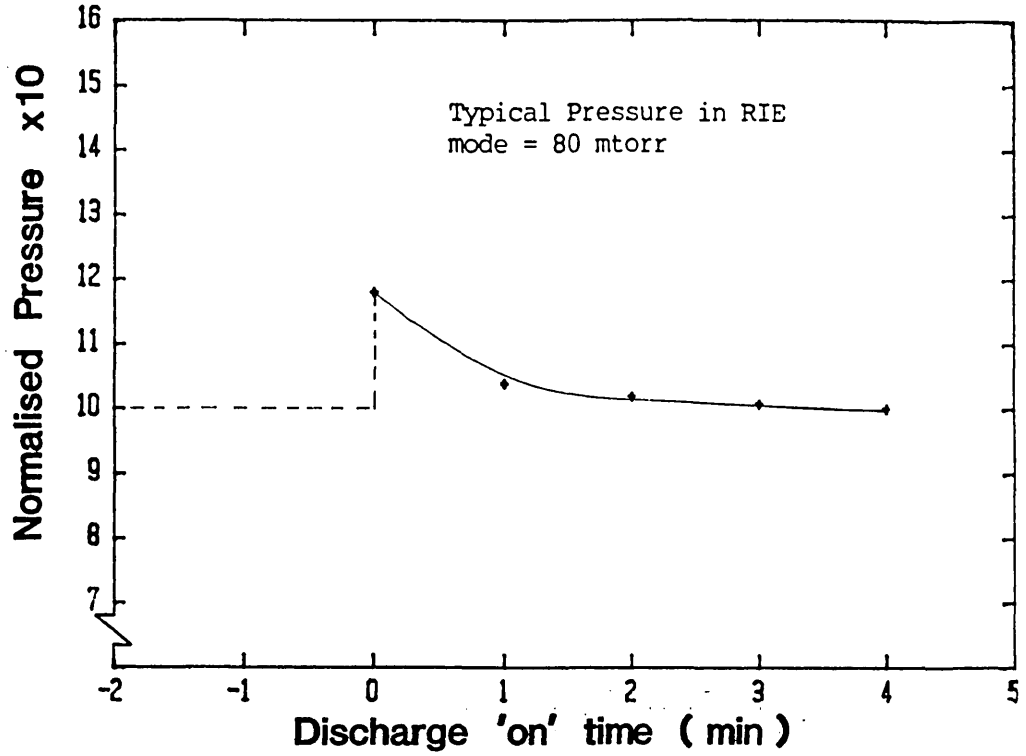


Figure 3.4.3: Time dependence of pressure before and after the discharge was "on".

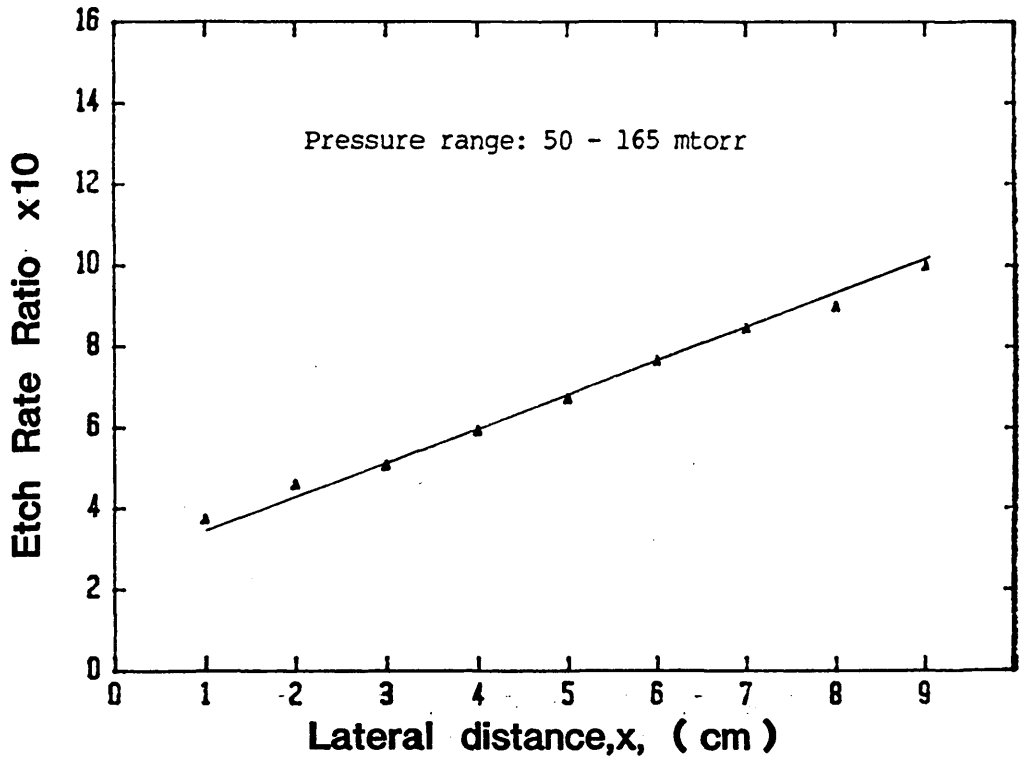


Figure 3.4.4: Radial etch rate effect on $CdCl_2$ and SiO_2 samples. x, is the lateral distance measured from the centre of substrate electrode. Taking the 9cm mark as 100%.

CHAPTER 4

$CdCl_2$ INORGANIC RESIST: RESULTS AND DISCUSSION.

4.1 $CdCl_2$ E-BEAM DECOMPOSITION RESULTS.

Electron beam decomposition of cadmium chloride ($CdCl_2$) thin film was carried out with 2keV electrons, using a Vacuum Generator (U.K. Ltd) Leg22 gun. Experiments were carried out at various temperature [1].

Fig. 4.1.1 is the "Taly-step" measurement of totally and partially decomposed areas of the $CdCl_2$ film, irradiated at an experimental temperature of 210°C.

The "efficiency" (α_T) in C cm^{-2} of the radiolysis process was measured for holes about 90nm in depth (in a 140nm thick film). The efficiency calculation was done by viewing the hole dug into the film as a Gaussian crater (Fig. 4.1.2).

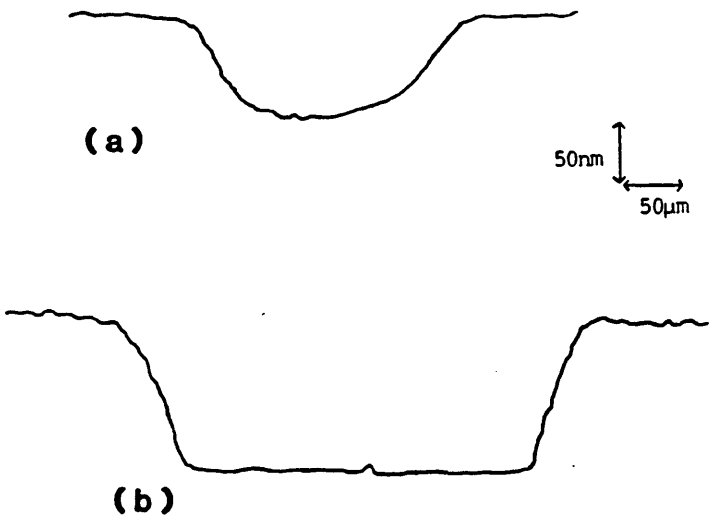


Figure 4.1.1: Depth profile of decomposed area (using a 300μm spot size beam, and beam energy of 2keV) in $CdCl_2$ film.

(a) Partially decomposed spot

(b) Totally decomposed spot

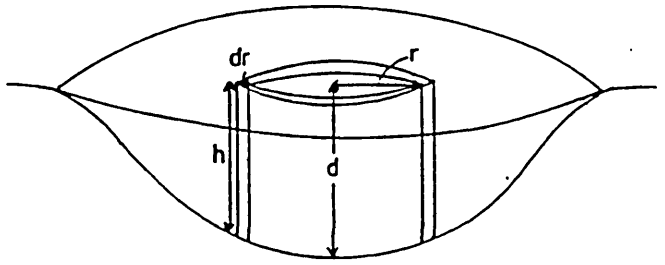


Figure 4.1.2: A crater representing the decomposed volume of $CdCl_2$ film, as measured by the "Talystep".

The height, h, measured at any particular point across the face of the hole is given by;

$$h = d.\exp(-r^2/r_o^2) \qquad \text{-------(4.1.1)}$$

where d is the depth at centre of the hole, r the distance from the centre of crater as shown in Fig.4.1.2, and r_o is the effective beam radius. The volume of a hollow cylinder of thickness (dr), radius r, and height h, is given by,

$$dV = h.2\pi r.(dr) \qquad \text{--------(4.1.2)}$$

Volume of crater V, $= \int_0^k \{h.2\pi r.dr\}$

k is the radius of the crater.

$$V = 2\pi d\int_0^k \{\exp(-r^2/r_o^2).r.dr\}$$

$$V = \pi dr_o^2[1-\exp(-k^2/r_o^2)] \qquad \text{-------(4.1.3)}$$

V = (molar volume of $CdCl_2$, V_m,) x (number of molecules removed, N,)

But Q, the amount of charge in coulomb is related to N by the equation,

$$N = \alpha Q$$

$$= \alpha i t$$

where i is the beam current, t is the decomposition time, and α is the efficiency in moles/coulomb. Therefore,

$$V = V_m \alpha i t \qquad \text{--------(4.1.4)}$$

Combining equations 4.1.3 and 4.1.4 gives,

$$V_m \alpha i t = \pi d r_o^2 [1-\exp(-k^2/r_o^2)]$$

$$\alpha = \{\pi d r_o^2 [1-\exp(-k^2/r_o^2)]\}/(V_m i t) \qquad \text{--(4.1.5)}$$

The molar volume of $CdCl_2$ is 45.32 cc mol^{-1}, which means that a 900Å decomposed thickness corresponds to $\sim 2 \times 10^{-7}$ moles cm^{-2} of film.

$$\alpha_T = (2 \times 10^{-7}/\alpha)\, C\ cm^{-2} \qquad \text{------(4.1.6)}$$

Film thickness was measured using the "Talystep" instrument. The multiplication factor of 0.8 (equation 2.5.3), was not used to convert the measured $CdCl_2.H_2O$ film thickness to $CdCl_2$ thickness. The conversion was not carried out, because the 0.8 scaling factor will cancel out for the efficiency, α_T, determination (cf. equations 4.1.5 and 4.1.6, and the value of 900Å used in obtaining 2×10^{-7} moles/cm^2).

Results for α_T were averaged for each temperature measurement, and presented in Table 4.1.1. A graphical representation is plotted in Fig. 4.1.3. ($\text{Log}(\frac{\alpha_T}{\alpha_{210}})$ vs. 1/T)

The activation energy in the temperature range $T<60^oC$ is 0.22eV, and a value of 0.16eV obtained for $90^oC<T<210^oC$. Comparing

these values of activation energy, decomposition could be said to be thermally enhanced and not thermally initiated (as discussed in section 4.3).

Table 4.1.1: Temperature dependence of efficiency for decomposing 900Å of a 1400Å thick film, using a 2keV electrons.

$(1/T) \times 10^3$ (K^{-1})	α_T $(C\ cm^{-2})$	$\text{Log}[(\alpha_T/\alpha_{210})\times 100\%]$
3.36	1.5	-0.66
3.00	0.61	-0.26
2.76	1.1×10^{-2}	1.45
2.55	1.0×10^{-2}	1.52
2.36	4.4×10^{-3}	1.88
2.21	4.2×10^{-3}	1.90
2.07	3.3×10^{-3}	2.00

Electron probe micro-analysis (EPMA) of irradiation done at temperatures of 90°C and 210°C are presented in Figs. 4.1.4(b) &(d). A brief note on EPMA data acquisition is given in Appendix V.

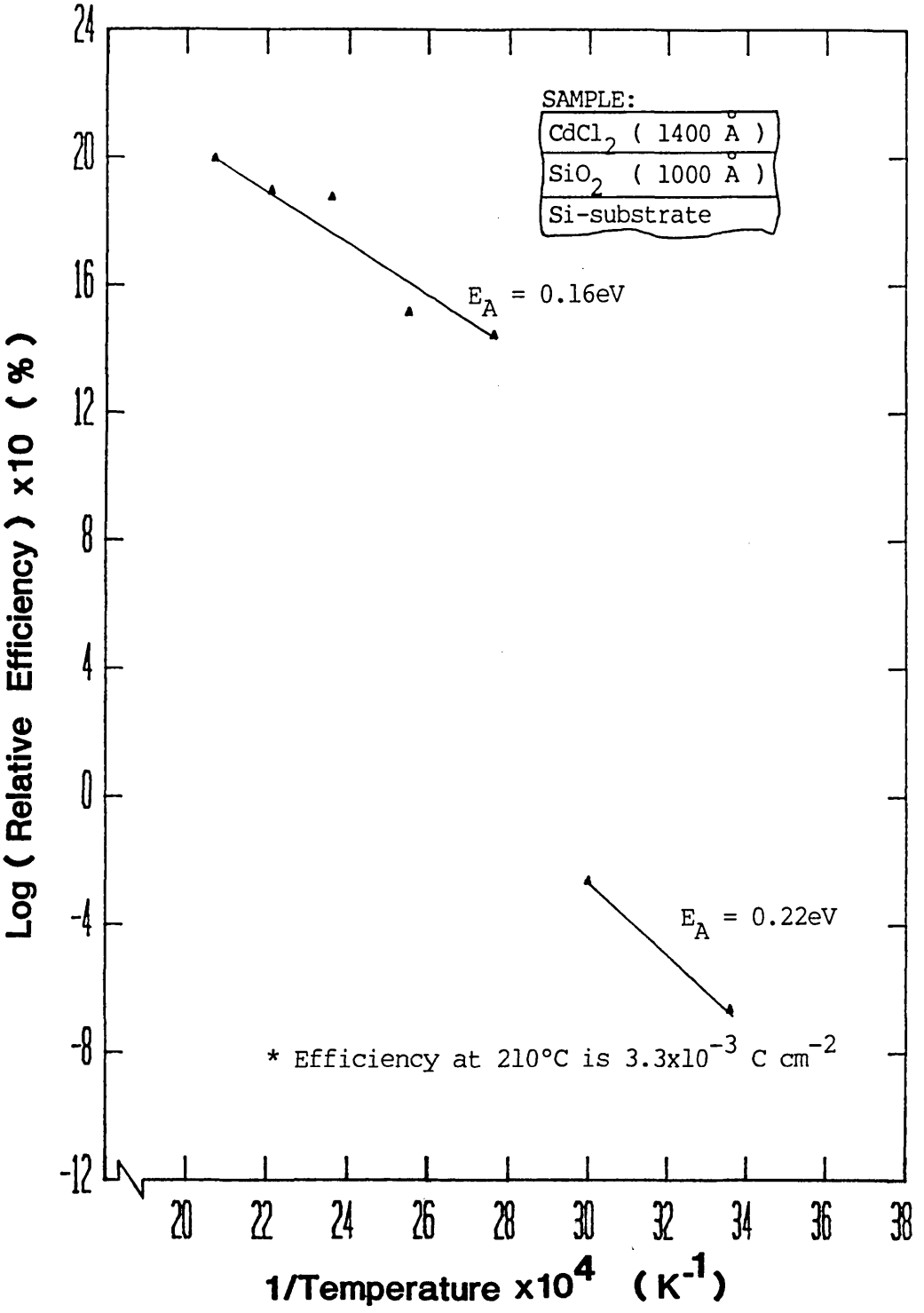


Figure 4.1.3: Temperature dependence of efficiency, for decomposing 90nm of $CdCl_2$
Beam energy = 2keV.

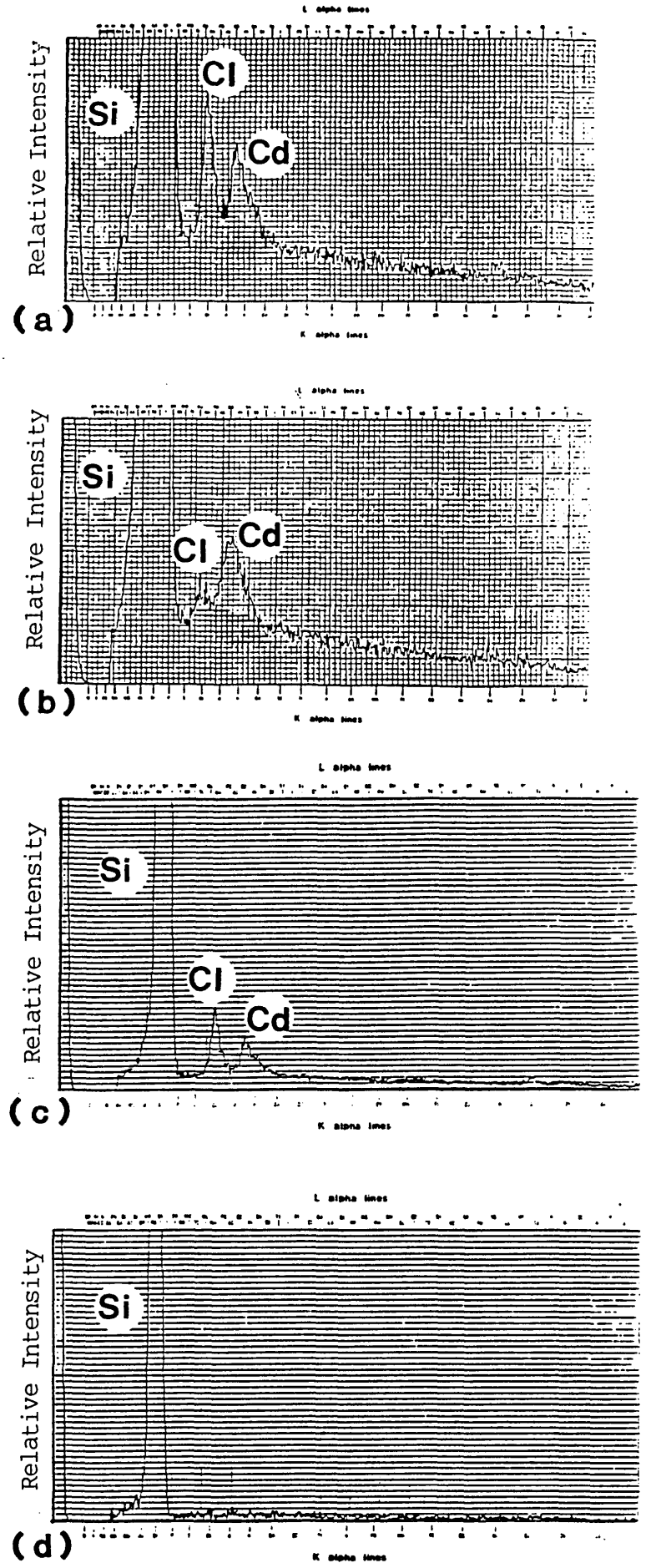


Figure 4.1.4: Electron-Probe Micro Analysis data.
(a) & (c) non-irradiated $CdCl_2$ samples.
(b) decomposed $CdCl_2$ film at 90°C
(d) decomposed $CdCl_2$ film at T = 210°C

4.2 PLASMA-ASSISTED ETCHING OF $CdCl_2$ AND SiO_2.

Plasma assisted etching was conducted on samples of silicon coated in thermally grown silicon oxide of average oxide thickness of 1000Å, on to which $CdCl_2$ films typically 1000Å thick were deposited at a rate of 40Å s^{-1}.

The $CdCl_2$ film was deposited from source material which was 95% pure cadmium chloride (BDH chemicals Ltd).

Each sample was a quadrant of a 75mm-diameter silicon wafer in area, and placed symmetrically, within two fixed radii distances (3cm<r<8cm) from the electrode centre. Ellipsometric measurements were at a point of ~4cm from electrode centre (lateral measurement). Electrodes temperature were kept constant at 22°C (as described in section 3.4.1).

In the presentation of data the terminology, sccm, is a unit of gas flow, representing the "standard" cubic centimetre per minute. The term "standard" is with reference to standard temperature (300K) and pressure, 760mmHg, (STP).

4.2.1 Plasma Etching Results.

Plasma etching was investigated by varying the following parameters, one at a time; the r.f. power, the oxygen concentration in the etch gas, and the etch time. The thickness loss as a function of etch time is presented in Fig. 4.2.1. The thickness loss of SiO_2 is linear with etch time, giving a steady etch rate (for the amount etched) when all etching parameters are kept constant. This linear etch rate relationship is shown in Fig. 4.2.2.

Thickness loss of $CdCl_2$ film shows a parabolic characteristic (Fig. 4.2.1). The continuous part of the curve is when the film was either being "etched" or a direct exchange of fluorine to chlorine atoms were taking place. The substitutional process was confirmed by the refractive index (obtained using the ellipsometer) of the etched film presented in Fig. 4.2.3. As etching progresses, contamination of sample was observed (dotted line). This fact was confirmed by the micrograghs of Fig.4.2.4. There was not any noticeable difference in SiO_2 surfaces before and after plasma etching. The contamination observed on the $CdCl_2$ sample surface then prompted compositional analysis.

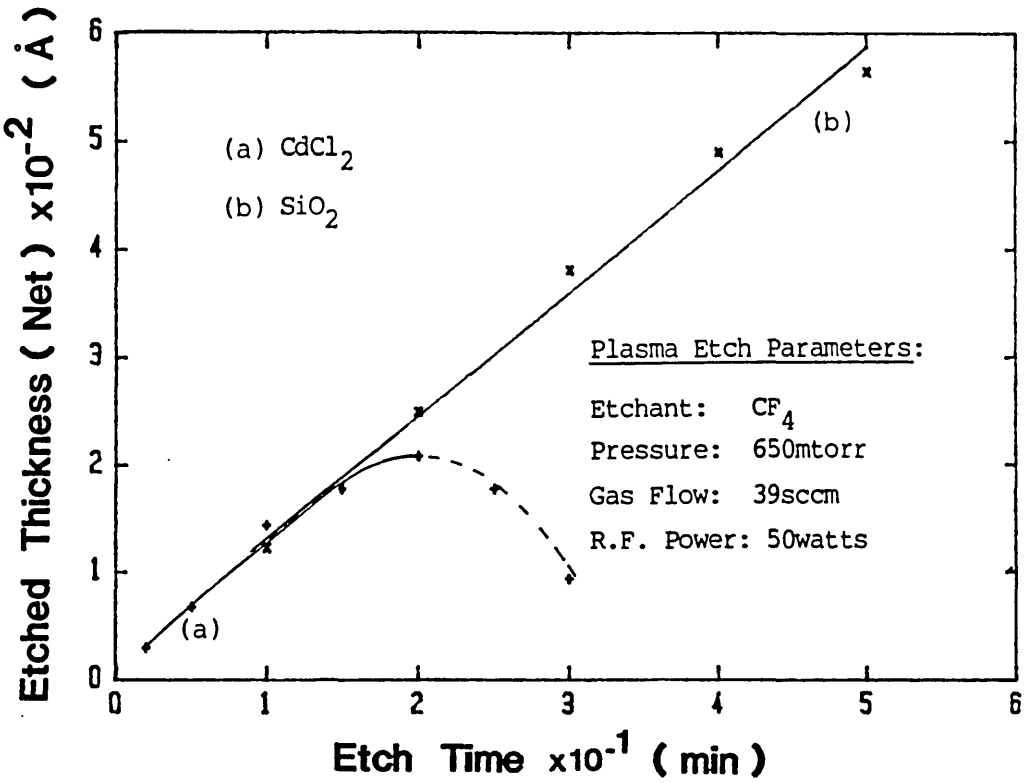


Figure 4.2.1: Time dependence of etched material.
Dotted line indicates polymer build-up

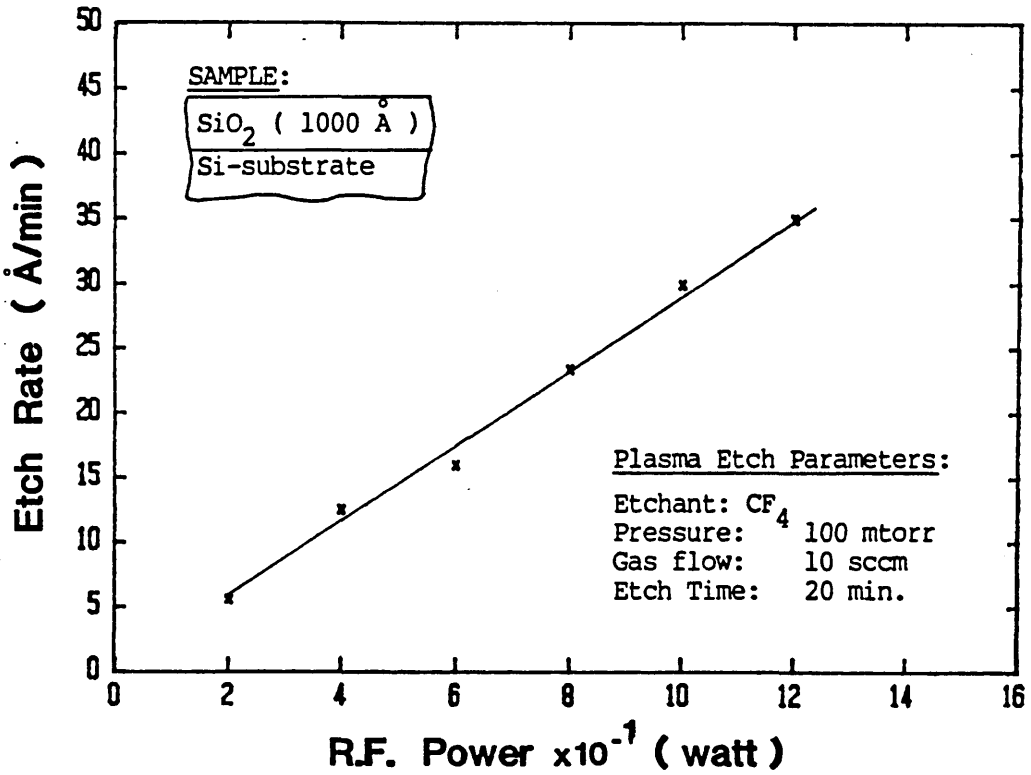


Figure 4.2.2: r.f. power dependence of SiO_2 etch rates.

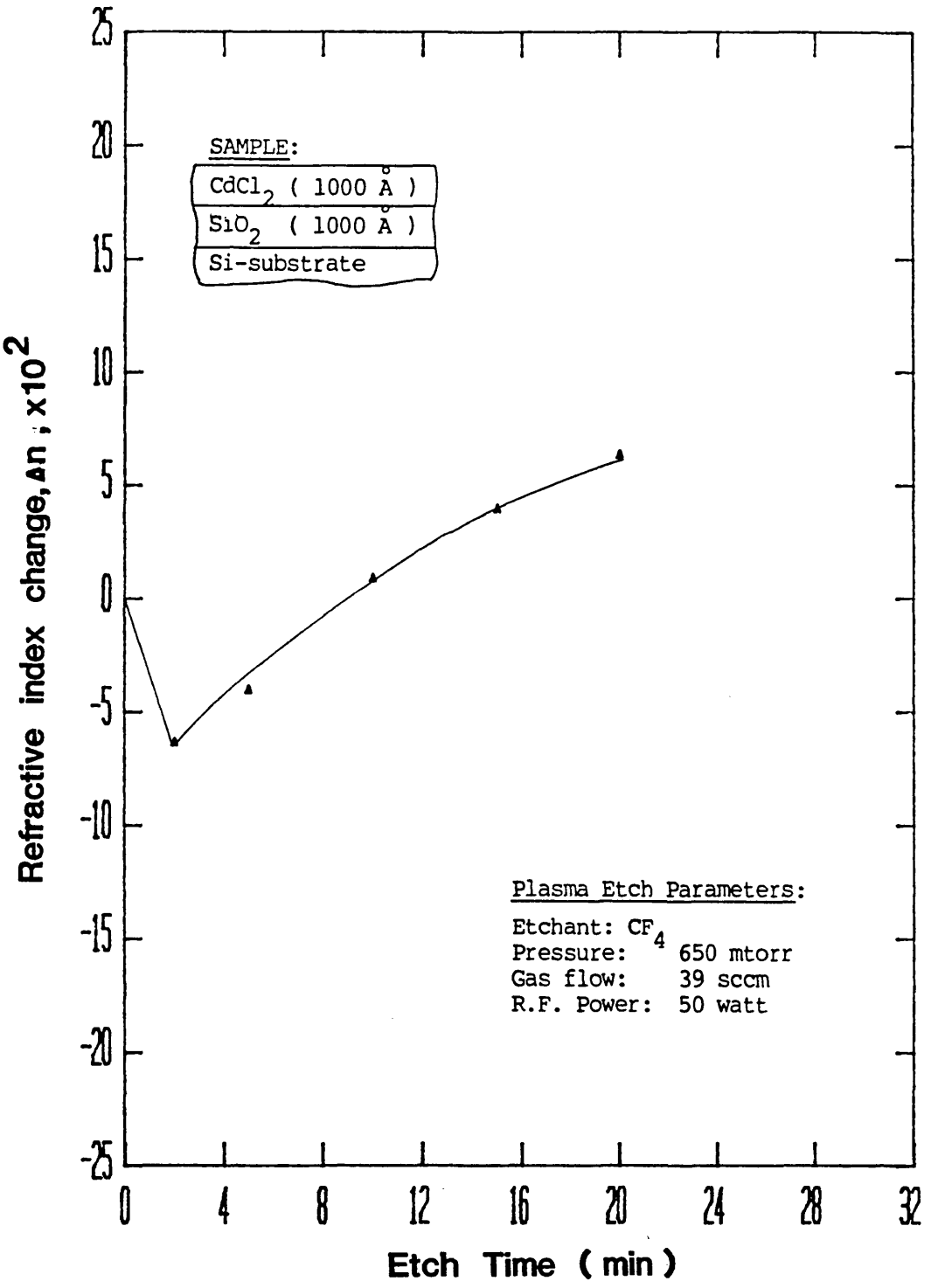


Figure 4.2.3: $CdCl_2$ refractive index change as a function of etch time. Unetched film has a refractive index change of zero.

Figure 4.2.4:

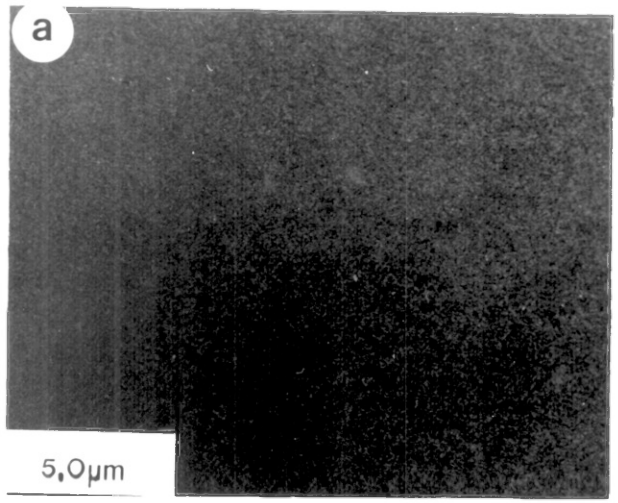
Effect of plasma etching on $CdCl_2$ and SiO_2 surfaces.
Plasma Condition: Etchant = CF_4
Pressure = 650 mtorr
Gas flow = 39 sccm
R.F. Power = 50 watt
Etch time = 30 min.

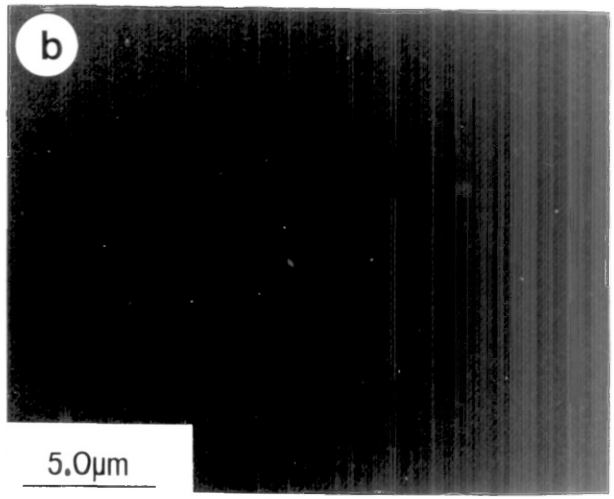
(a) SiO_2 surface before plasma etching.

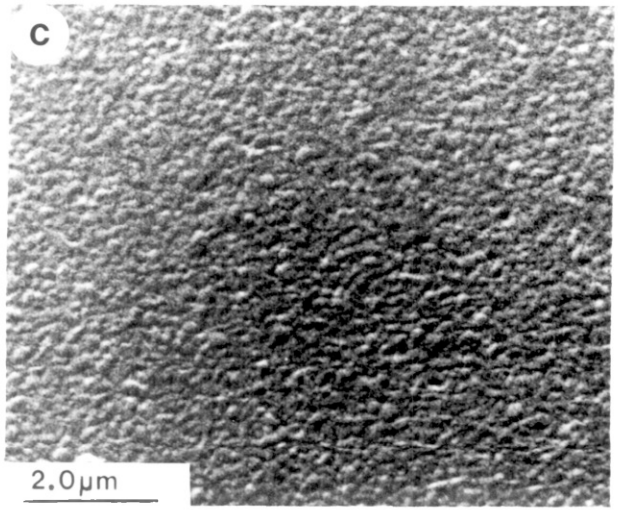
(b) SiO_2 surface after plasma etching.

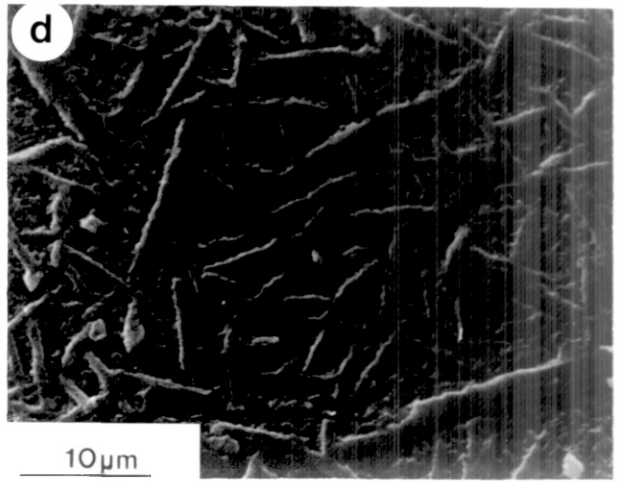
(c) $CdCl_2$ film surface before plasma etching.

(d) $CdCl_2$ film surface after plasma etching, with features showing the polymer deposit.


a
5.0μm


b
5.0μm


c
2.0μm


d
10μm

ESCA Results

ESCA of etched and freshly deposited $CdCl_2$ films were done using a Kratos ES200 analyser (magnesium kα used as the x-ray line). The spectra are of two types: Fixed Analyser Transmission (FAT) data, a measure of kinetic energy of the photoejected electrons, that has low binding energy resolution, but high signal to noise ratio (hence used for survey and quantification of surfaces); and Fixed Retard Ratio (FRR) data, a measure of the binding energy (i.e. the ionisation potential of ejected electrons), and have good energy resolution (0.1eV), but low signal to noise ratio, this gives chemical information of surfaces by the shifts in binding energy.

From the survey scan (FAT mode) over the kinetic energy (K.E.) range of the instrument, all lines are assigned on the basis of C, Cl, Cd, O on the surface of evaporated $CdCl_2$ film (Fig. 4.2.5). The absence of silicon (Si) line suggests, as indeed should be the case, that there were no substantial breaks in the $CdCl_2$ film.

Spectra were then analysed for each characteristic line for positive identification. The area measurements (by comparing Cd and Cl peaks) gave elemental composition of the film as 26.9% Cd and 73.1% Cl.

Fig. 4.2.6 is the FRR mode data, giving a noisy carbon, chlorine and cadmium spectra due to narrow slits on source and detector.

Uncoated samples were used, which were susceptible to charging due to slow conduction of electron build up at the surface of the sample during interaction of a molecule with a monoenergetic beam of soft x-ray. As a result of this, a single carbon peak was scanned to calibrate the energy scale. The magnitude of the sample charging is the difference between the photon energy and the sum of the kinetic energy and the binding energy. A charge correction value of 11.3eV is obtained.

The energy referencing was carried out as illustrated in Fig. 4.2.6 for Cl. A shift in energy, of about 1.25eV was observed for Cl (cf. Fig. 4.2.6), this being a result of decreasing oxygen level (associated with H_2O), while the sample was in the spectrometer. This is consistent with the dehydration of the film ($CdCl_2.H_2O \longrightarrow CdCl_2$), discussed in section 2.5.

The FAT data of etched $CdCl_2$ film, have lines assigned on basis of surface content of Cd, Cl, C, F and O. The elemental composition of the surface is 17.2%Cd, 3.7%Cl, 20.4%F, 41.1%C and 17.6%O (Fig. 4.2.7). This indicates extensive surface F/Cl exchange.

In the FRR mode (Fig. 4.2.8), the carbon 1s signal is of a complex shape, the peak at lowest binding energy (B.E.), can be assumed to be hydrocarbon, giving a charge correction value of 9.5eV. The carbon could be composed of a range of fluorinated carbon groups (CF_3 CF_2, CF, C) so that the shift of 2.5eV (cf. Fig. 4.2.8) observed in the carbon peak may be as a result of CF_2, suggesting a highly fluorinated polymeric species.

In order to have a contamination free $CdCl_2$ sample surface, varying percentage of oxygen was added to the etch gas. Fig. 4.2.9 shows the oxygen concentration (in the etch gas) dependence of $CdCl_2$ and SiO_2 etch rates. The effect of moist etch-gas on the etch rate of SiO_2 sample is also presented in Fig. 4.2.9. For up to 8% oxygen in CF_4/O_2 gas concentration, there was not a significant change in the etch rate of SiO_2. An increase of about a factor of 2 was achieved for the etch rates of SiO_2 and $CdCl_2$ samples, when the oxygen percentage in CF_4/O_2 gas was 8-16%. In terms of selectivity this approach does not prove to be useful, as a result of a decrease in selectivity from 7:1 to 9:2 in etching SiO_2 compared to $CdCl_2$. A reduction by half in the etch rate of SiO_2 was obtained when etching was done using a moist gas, although the degree of moisture was not known.

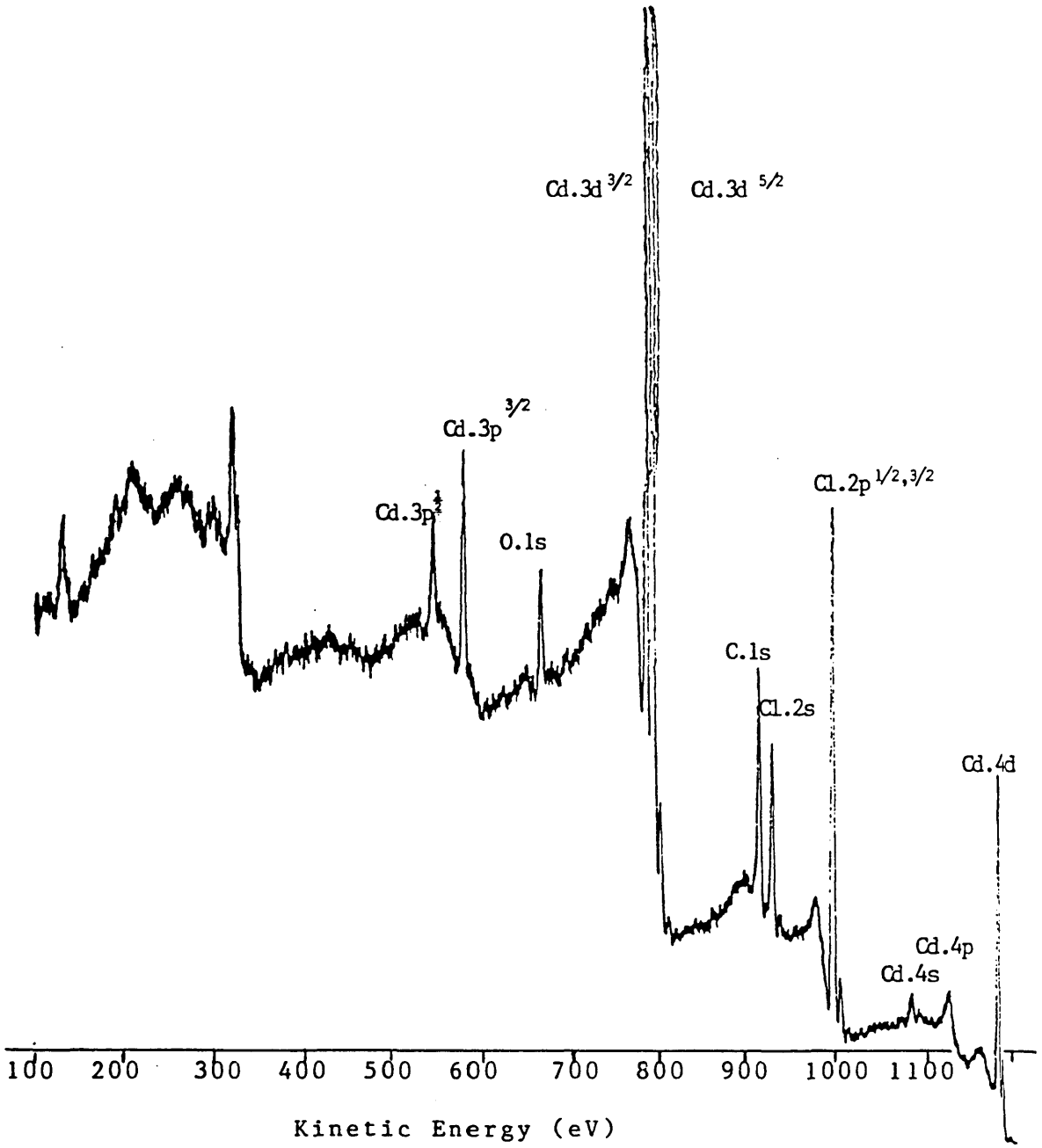


Figure 4.2.5: ESCA spectra of $CdCl_2$ before plasma etching (with changing base-line), measured in the FAT mode.

Analyser Parameters:

Energy = 12kV

Current = 14mA

Target: Mg kα(1253.6eV)

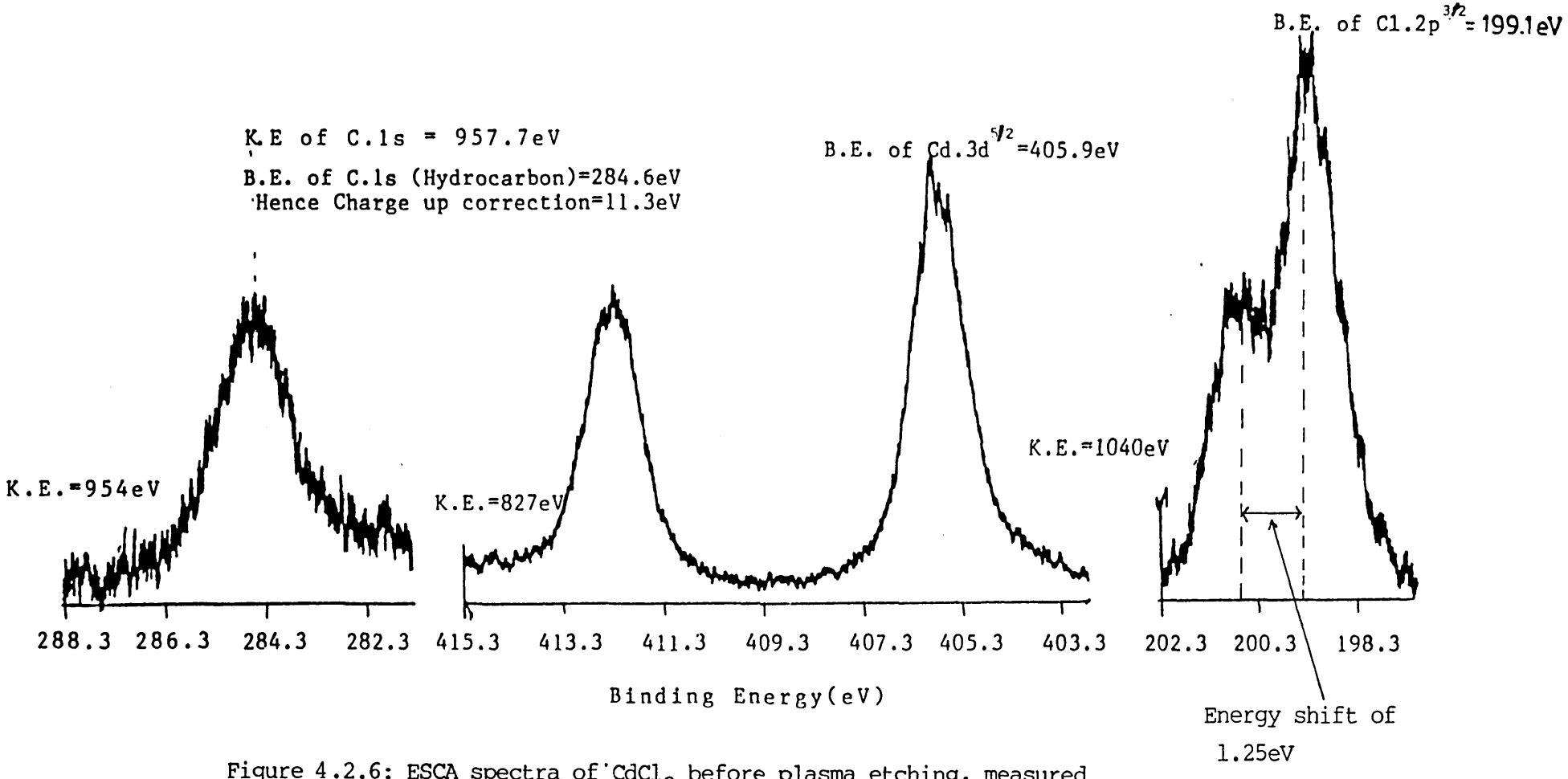


Figure 4.2.6: ESCA spectra of $CdCl_2$ before plasma etching, measured in FRR mode.

Analyser Parameters:

Energy = 8kV

Current = 10mA

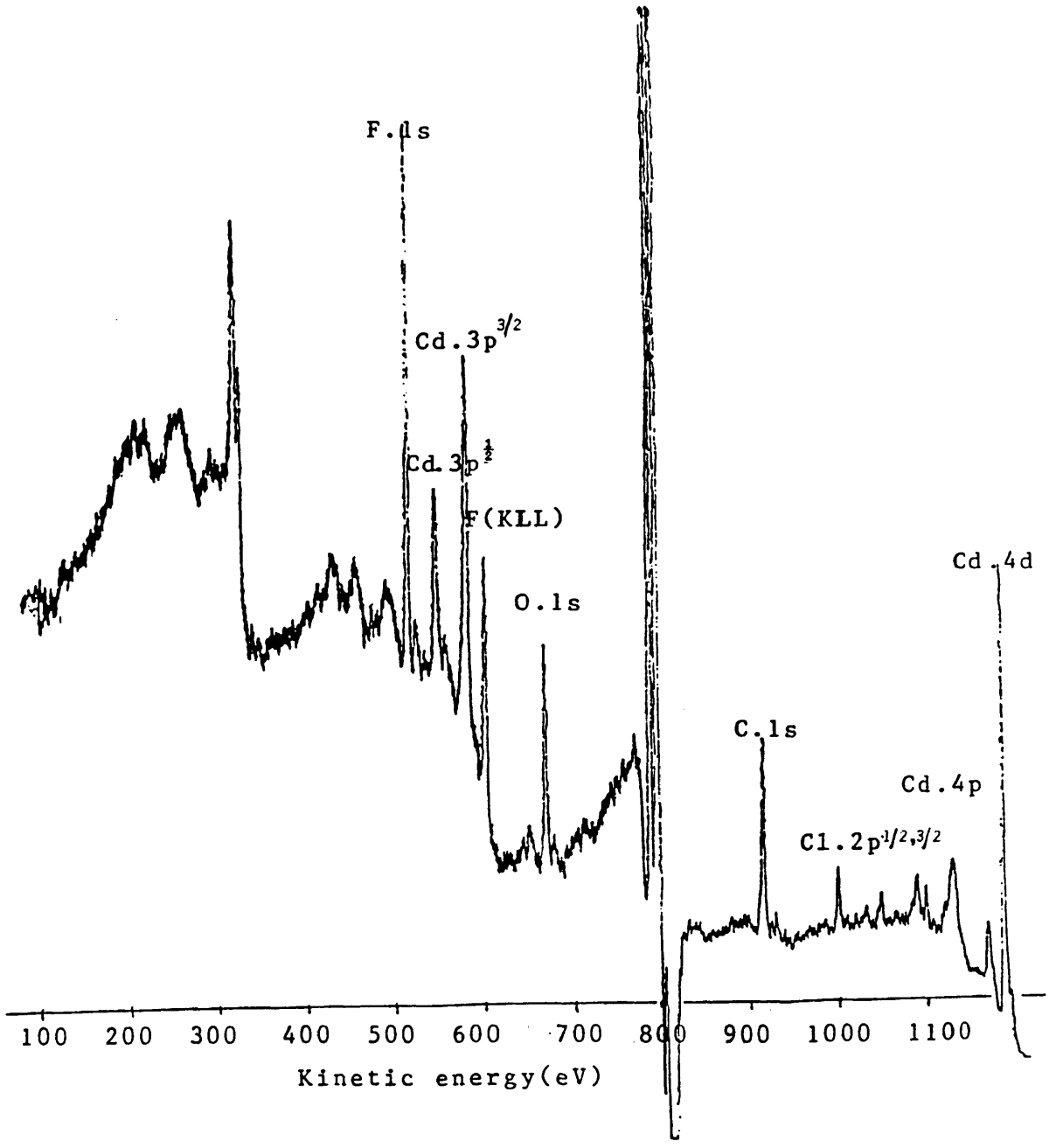


Figure 4.2.7: ESCA spectra of $CdCl_2$ after plasma etching (with changing base-line), measured in the FAT mode.

Analyser Parameters:

Energy = 12kV

Current = 14mA

Target : Mg kα(1253.6eV)

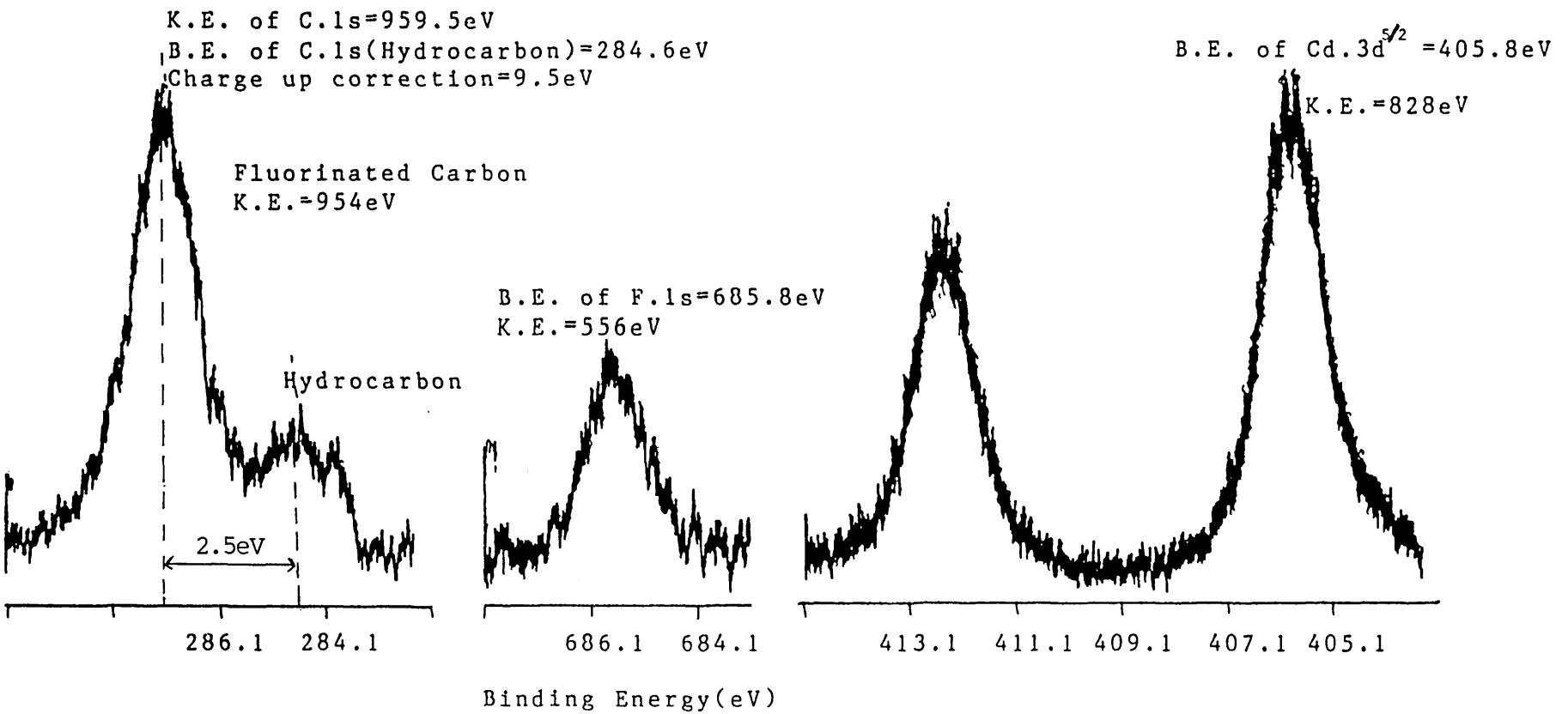


Figure 4.2.8: ESCA spectra of $CdCl_2$ after plasma etching, measured in the FRR mode.

Analyser Parameters:

Energy = 8kV

Current = 10mA

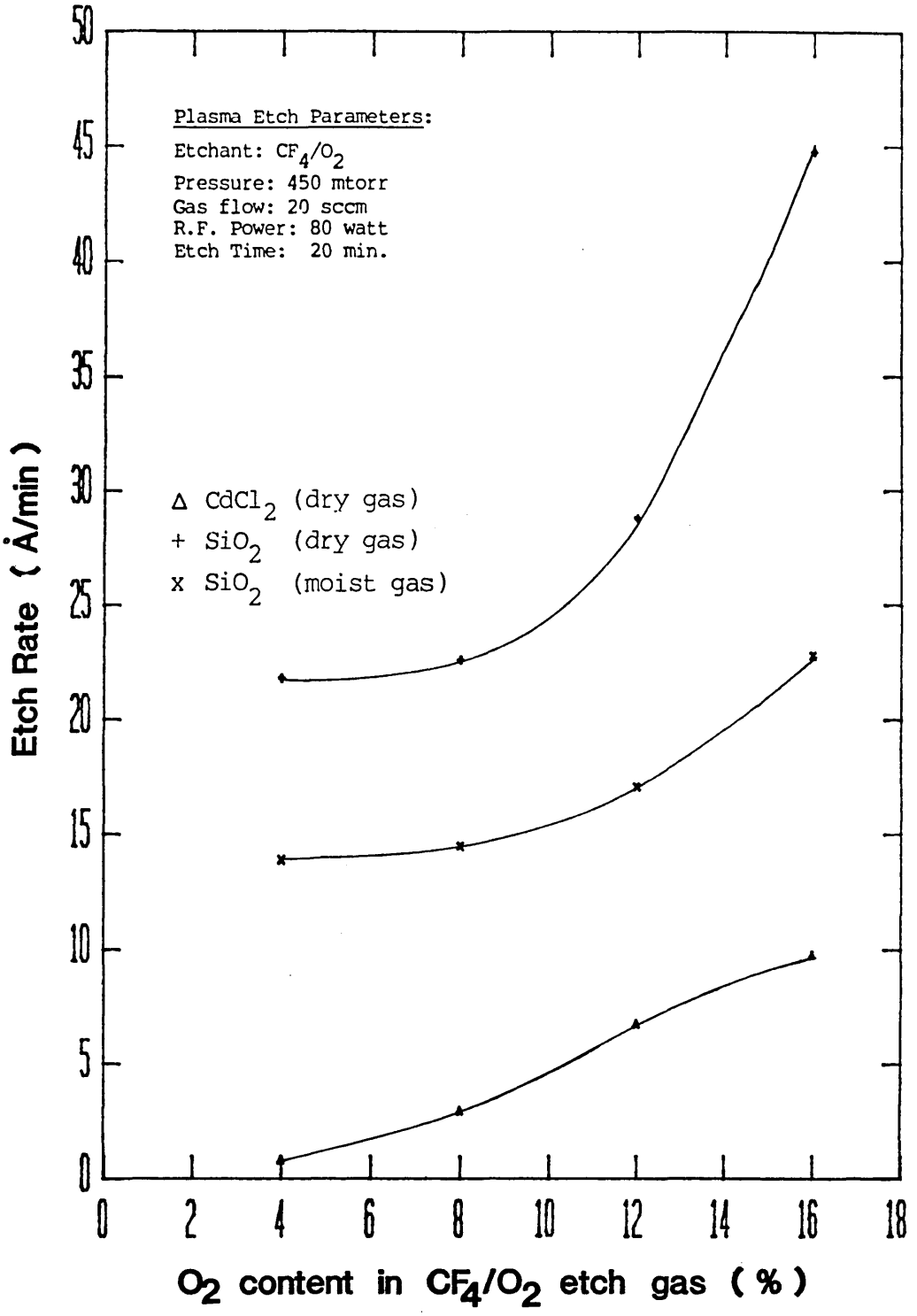


Figure 4.2.9: Effect of oxygen concentration in the etch-gas (CF_4/O_2), on etch rates of SiO_2 and $CdCl_2$. Effect of moist gas on SiO_2 etch rate also presented.

4.2.2 Reactive-Ion Etching (RIE) Results

In the plasma etching mode, the following observations were made, as has already been pointed out; polymerisation products on the $CdCl_2$ film surface when oxygen is absent from the etching gas. On the other hand, a low etch rate of SiO_2 and poor selectivity results when a mixture of CF_4 and O_2 gases are used.

All these factors rule out the possibility of plasma etching $CdCl_2$ sample, with SiO_2 as the underlayer, for integrated circuits applications.

This then led to the exploration of etching in the reactive-ion mode, namely RIE. Etch rates for both SiO_2 and $CdCl_2$ materials, for the etching conditions specified (Fig 4.2.10), is a linear relationship with input power. This gives a selectivity of 6.5:1.

Fig 4.2.11 shows the gas flow dependence of etch rates. In the gas flow range (5-20 sccm) investigated, there is only a small influence of gas flow on the etch rate of SiO_2.

Chamber pressure dependence of etch rate data is shown in Fig. 4.2.12, and the selectivity of this data is better than 16:1 for pressure below 60mtorr. With increase in pressure, the selectivity became worse, giving about 3:1 at a pressure of 120mtorr.

The EPMA result of etched $CdCl_2$ sample is shown in Fig. 4.2.13, which reveals a considerable reduction in the Cl signal. Suspicion of surface substitutional process (F atoms replacing Cl atoms), led to measurement of the refractive index of etched $CdCl_2$ films, and the results obtained was quite similar to the decreasing refractive index of Fig. 4.2.3. Further compositional analysis was carried out, using SIMS, which compares the spectra of $CdCl_2$ samples, before and after reactive-ion-etching.

SIMS Results

In-depth profile analyses of $CdCl_2$ samples (before and after RIE), were carried out by the SIMS method. This was accomplished using an ATOMIKA a-DIDA R-2010 quadrupole SIMS instrument.

A normal incidence primary ion beam of xenon (Xe^+), having an energy of 10keV, at constant current of 10nA with a spot size of 50μm, was used to raster scan a frame area of $1.2 \times 1.2 mm^2$. The scan

rate was 16sec/frame, a frame consisting of 256lines. Charge compensation was achieved by co-bombarding with 500eV electrons, at oblique incidence. The in-depth profiles (Figs. 4.2.14 & 4.2.15), were obtained by recording the logarithmic intensity of the signal level, due to the selected species of $^{16}O^-$, $^{19}F^-$, $^{28}Si^-$, and $^{35}Cl^-$, as a function of the frame number, that is, as a function of time.

The following facts are valid for the measurements obtained:

(i) The intensity profiles of the selected species are directly proportional to their respective number of ions that has been sputtered from the sample.

(ii) Sputtered frame (time), within a given layer is associated with depth into the sample, since the beam current is constant with time. This cannot be generalised for a multilayer specimen, because for example, sputter rates vary, and that of $CdCl_2$ is greater than SiO_2, therefore, there will be scale changes at the interface.

$CdCl_2$ film thickness was measured by ellipsometry. The thickness of 640Å (corrected for, using equation 2.5.3) was obtained for unetched film of $CdCl_2$, and this corresponds to the 'knee' point in both Figs. 4.2.14 & 4.2.15.

The intensity profile of the $CdCl_2$ film (as prepared), Fig. 4.2.14, has the ^{35}Cl signal exhibiting an exponential decay at the $CdCl_2$ - SiO_2 interface, instead of a sharp fall to zero. The decay was found to be exponential by correlating the decay depth at the 1/e point with the decay depth of a 10keV Xe^+ ion beam, both being in mutual agreement within experimental error. The decay is mainly due to the fact that, the primary ion beam has a depth resolution of ~70Å, which causes continuous atomic mixing of the profiles and thus broadening the total penetration profile. Also the decay can to some extent, be due to the differences in the sputter rate mentioned above, and the non-uniformity of the sputter rate across the crater caused by the synergistic effect of the electron and ion beams.

The in-depth profile of reactively ion etched film of $CdCl_2$ is presented in Fig. 4.2.15, and the decay of the ^{35}Cl intensity at the 'knee' point was found to be the same as in Fig. 4.2.14. The ^{19}F intensity profile can be divided into three regions namely I,

II, and III . Region I is the top layer of about 20Å or less of the etched sample, which has been highly fluorinated (cf. Figs. 4.2.5 - 4.2.8, ESCA results). Region II is presummed to exhibit an incomplete mixing of the profiles, followed by the steady-state decay of region III. A qualitative surface analysis of reactively etched $CdCl_2$ samples have been carried out by SIMS method. In conclusion, there was surface exchange of chlorine with fluorine, which occurred in the first three molecular layers of $CdCl_2$.

Electron Micrographs

Electron micrographs of reactively etched, and unetched samples of SiO_2 and $CdCl_2$ are shown in Fig. 4.2.16. The results show that there was no significant effect on the SiO_2 surface, and just a slight change in the $CdCl_2$ microstructure, without the introduction of contamination. The etch time for obtaining these micrographs was just sufficient to have removed about 70% of the oxide and less than 4% of the $CdCl_2$ film.

A 5μm Ni-mesh pattern (Fig. 4.2.17(a)) was transferred onto an oxidised silicon wafer by using $CdCl_2$ as the resist mask. A sample of $CdCl_2/SiO_2/Si$ was masked by the mesh pattern and electron beam decomposed at 210°C to achieve total decomposition of exposed areas. The electron beam exposed sample was then reactive-ion etched (without the mesh) so as to etch off exposed SiO_2 areas, resulting in Fig. 4.2.17(b). End-point detection was accomplished by using a quadrupole mass spetrometer (QMS). The QMS signal in the mass range 41-105amu is shown in Fig. 4.2.18, and mass 44 (CO_2^+) monitored for end-point detection. It is expected that at the completion of oxide etching, contribution of oxygen from the oxide would have ceased, and the CO_2^+ peak should start decreasing. However, considering the fact that etching was done at a pressure of 50mtorr, end-point detection monitoring by tuning to the CO_2^+ peak was a bit obscured, as a result of background pressure of oxygen in the chamber. Fig. 4.2.17(c) is a typical edge profile of Si-SiO_2 interface. The smooth area being the SiO_2, and the grainy area the Si surface, due to slight over etching (~10%).

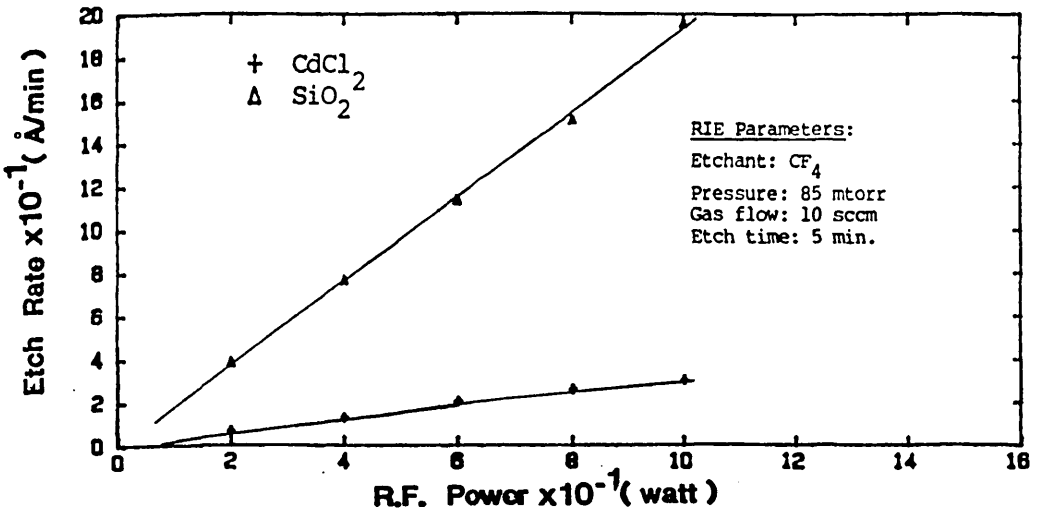


Figure 4.2.10: r.f. power dependence of etch rates (In RIE mode)

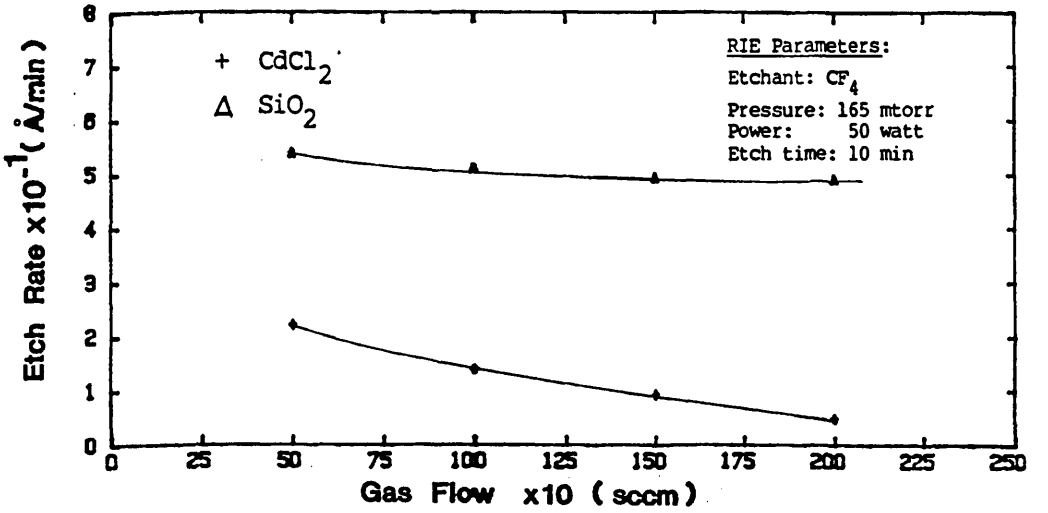


Figure 4.2.11: Gas flow dependence of etch rates (RIE mode)

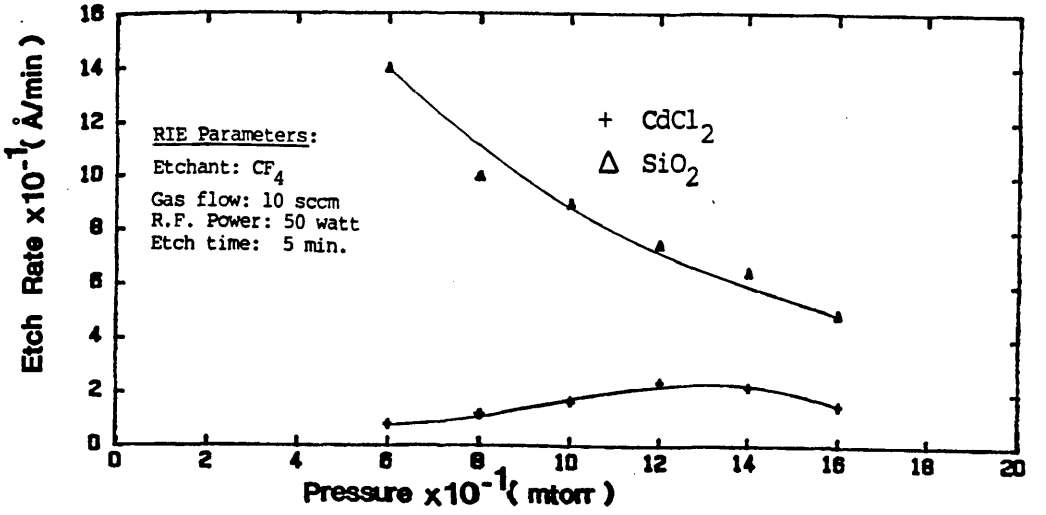


Figure 4.2.12: Pressure dependence of etch rates (RIE mode)

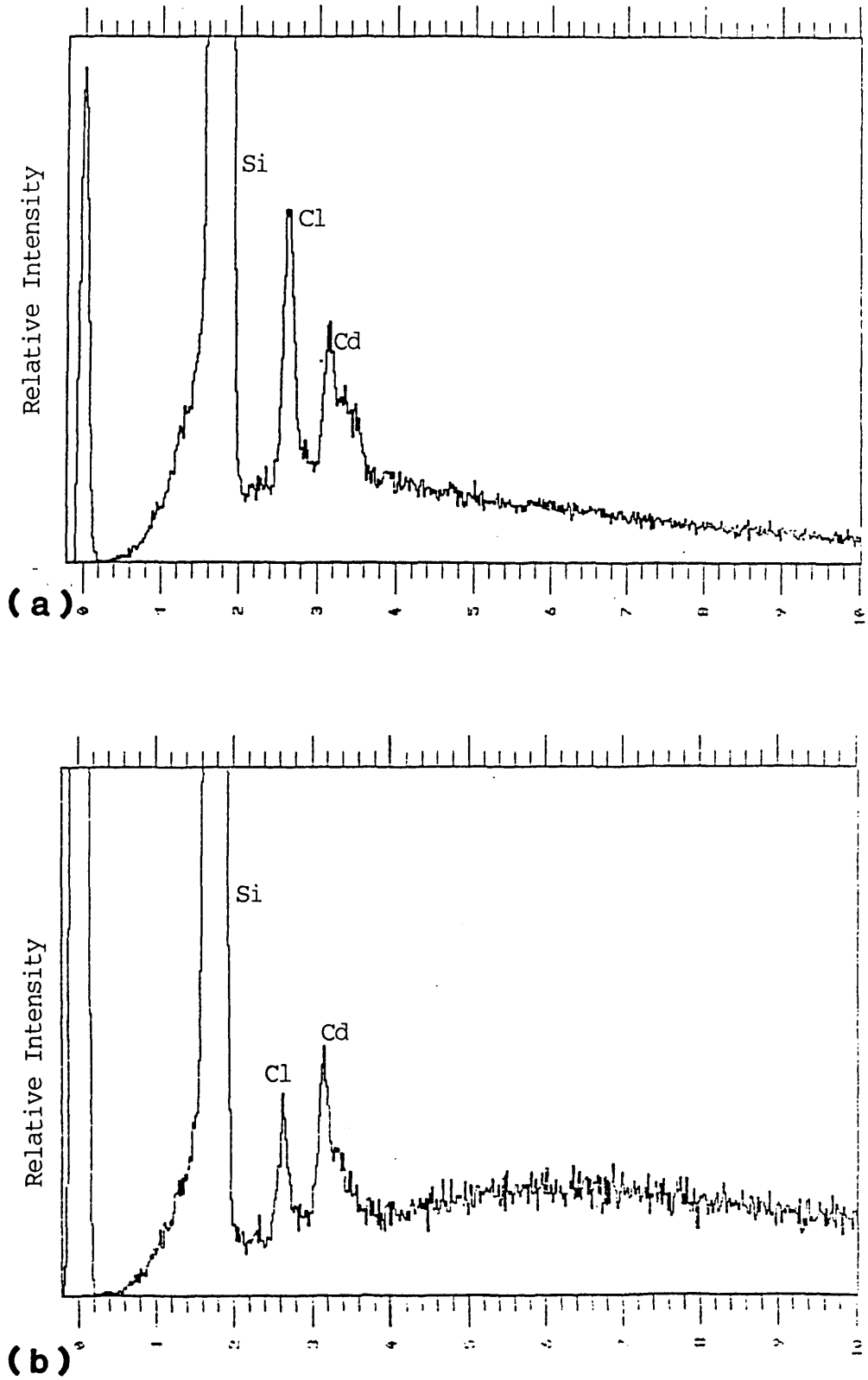


Figure 4.2.13: EPMA spectra of $CdCl_2$

(a) before RIE

(b) after RIE

RIE Parameters:

Pressure = 50mtorr r.f. power = 50watt

Gas flow = 10sccm etch time = 5min

Etchant = CF_4

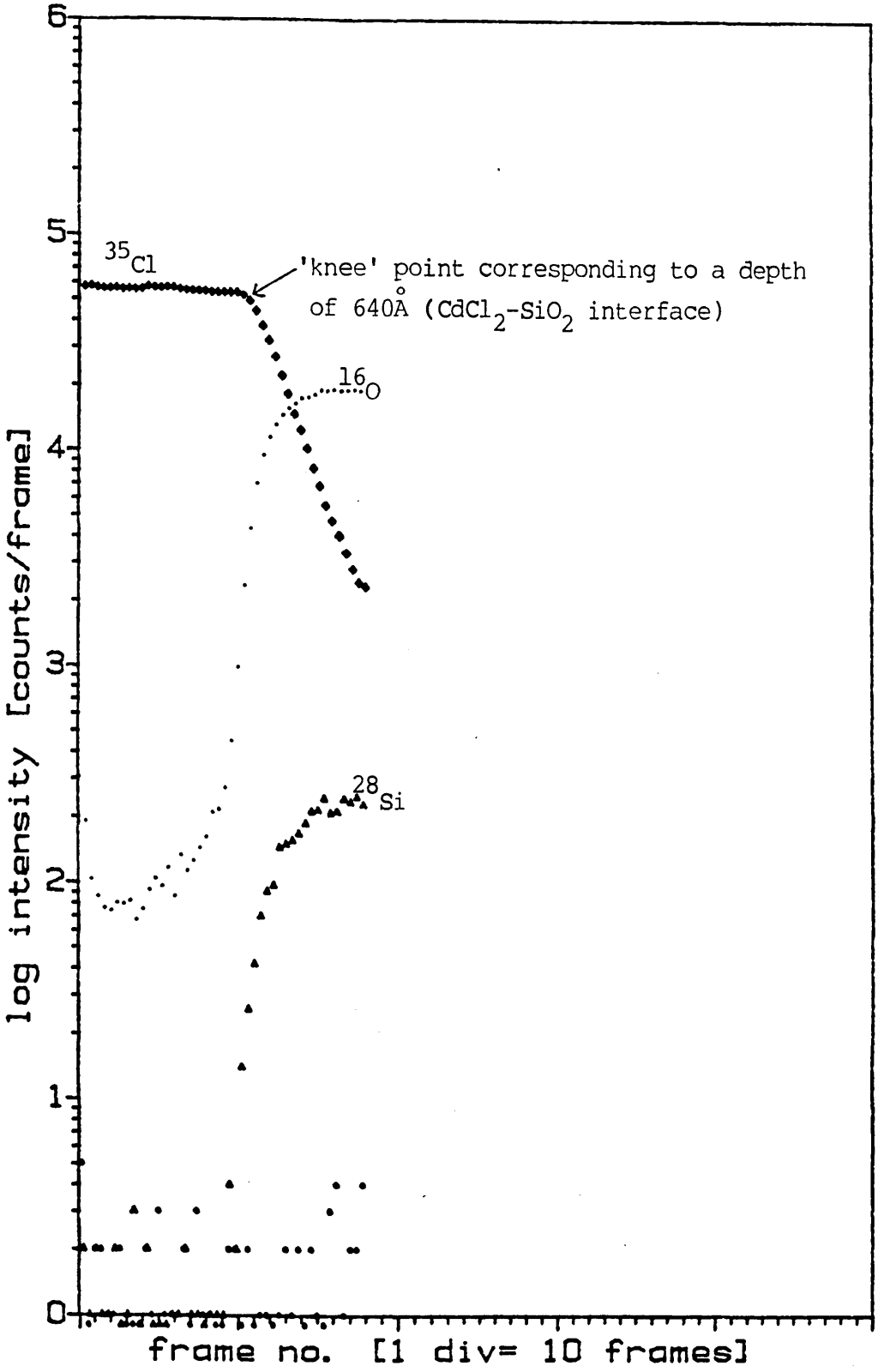


Figure 4.2.14: In-depth profile of SIMS analysis of $CdCl_2/SiO_2/Si$ sample, as prepared

$CdCl_2$ film thickness = 640Å

Deposition rate ≃ 45Å/s

Primary Ion Beam: Xe^+ Ion

Ion energy = 10keV

Ion current = 10nA

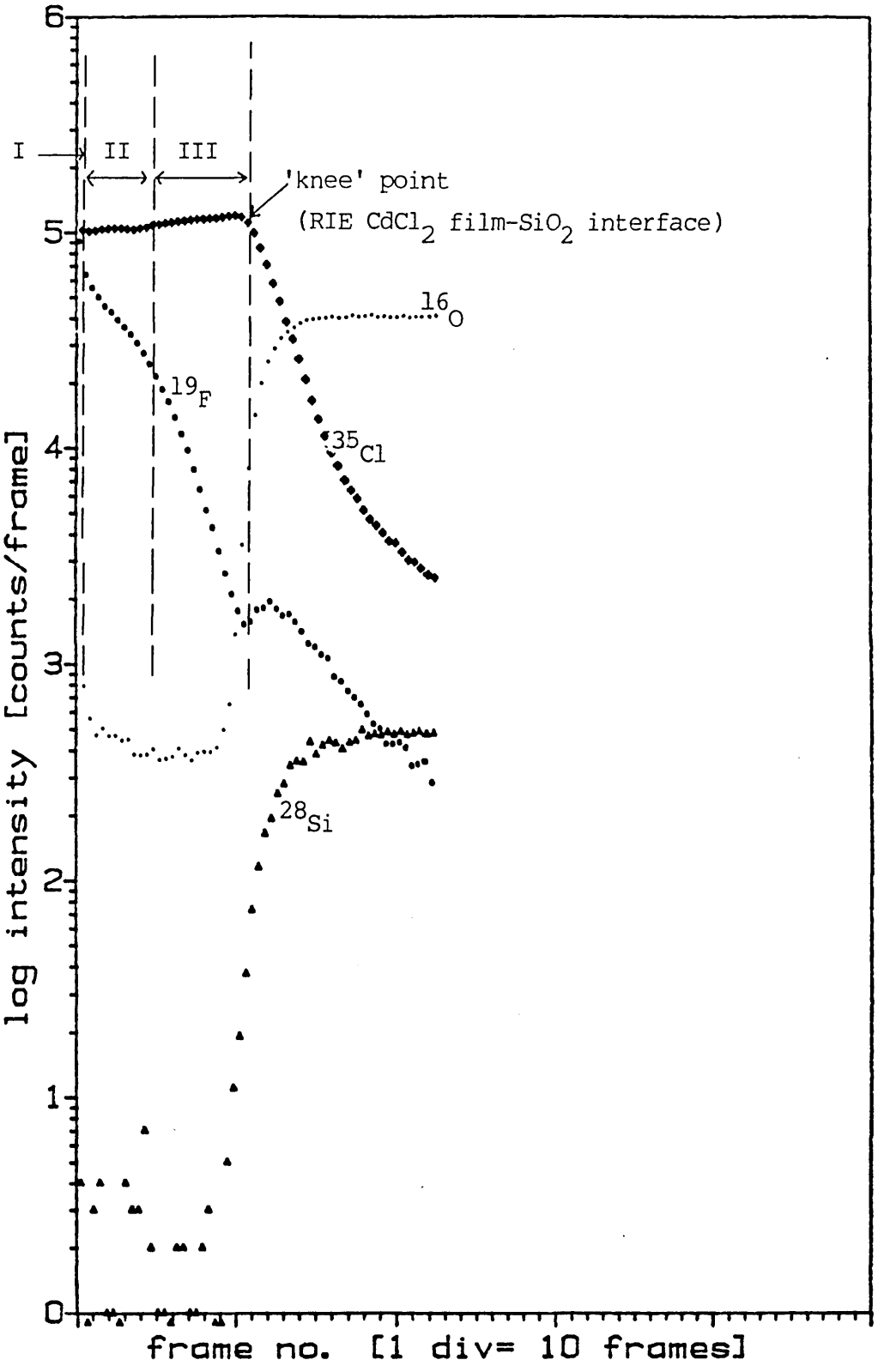


Figure 4.2.15: In-depth profile of SIMS analysis of RIE sample of $CdCl_2/SiO_2/Si$

RIE Parameters;

Pressure = 50mtorr r.f. power = 50watts

Gas flow = 10sccm etch time = 5min

Etchant = CF_4

Figure 4.2.16:

Effect of reactive ion etching (RIE) on $CdCl_2$ and SiO_2 surfaces.

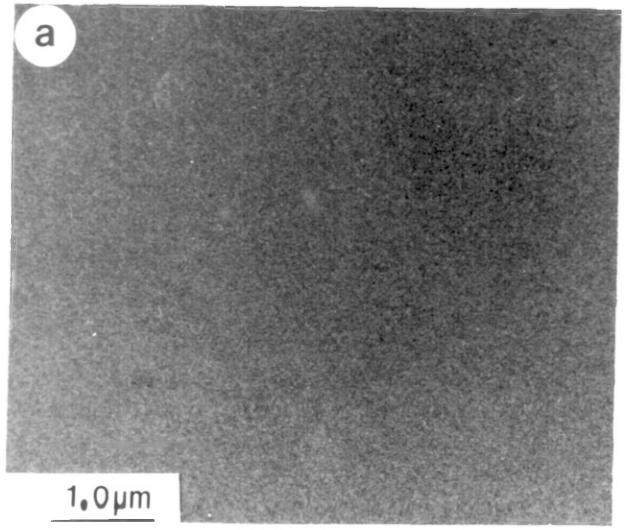
RIE condition: Etchant = CF_4
Pressure = 50 mtorr
Gas flow = 10 sccm
R.F. Power = 50 watt
Etch time = 5 min.

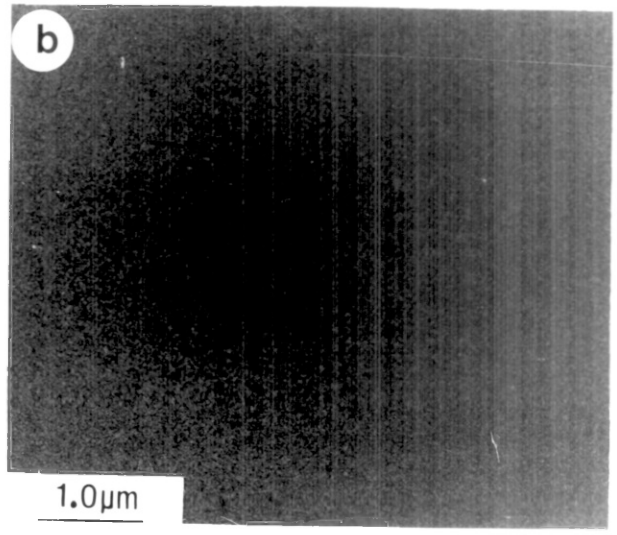
(a) SiO_2 surface before RIE

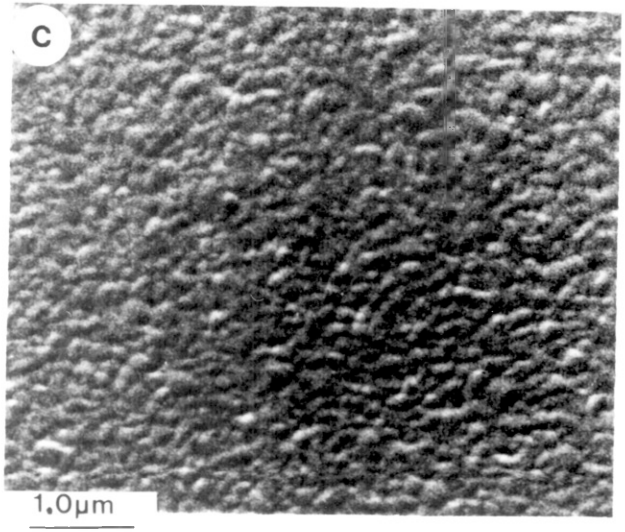
(b) SiO_2 surface after RIE

(c) $CdCl_2$ surface before RIE

(d) $CdCl_2$ surface after RIE


a
1.0μm


b
1.0μm


c
1.0μm

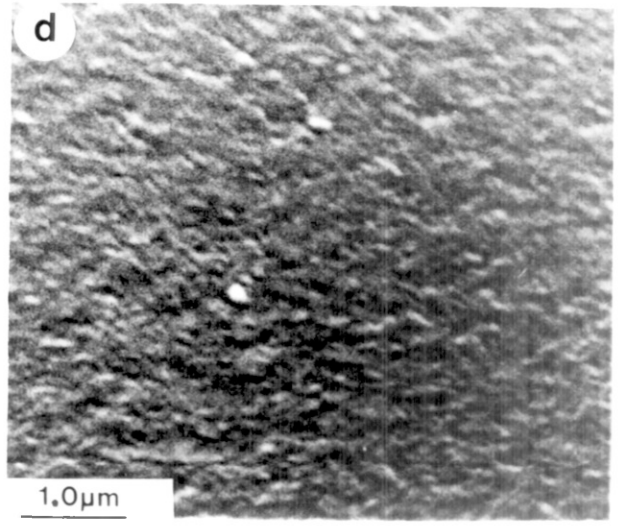

d
1.0μm

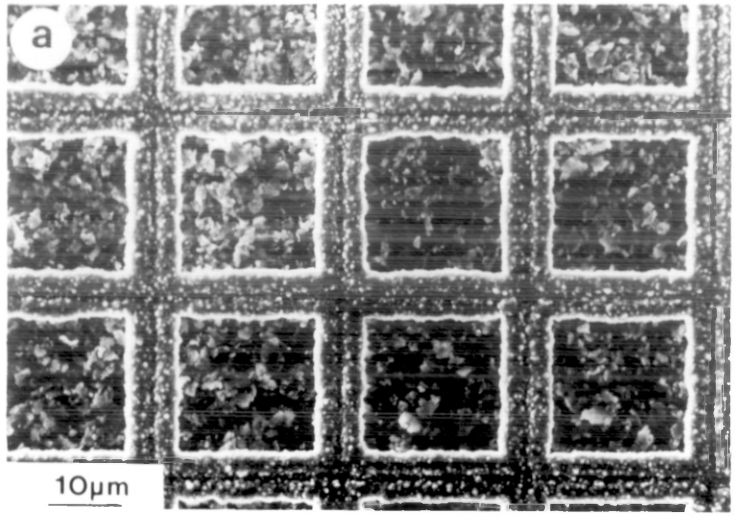
Figure 4.2.17:

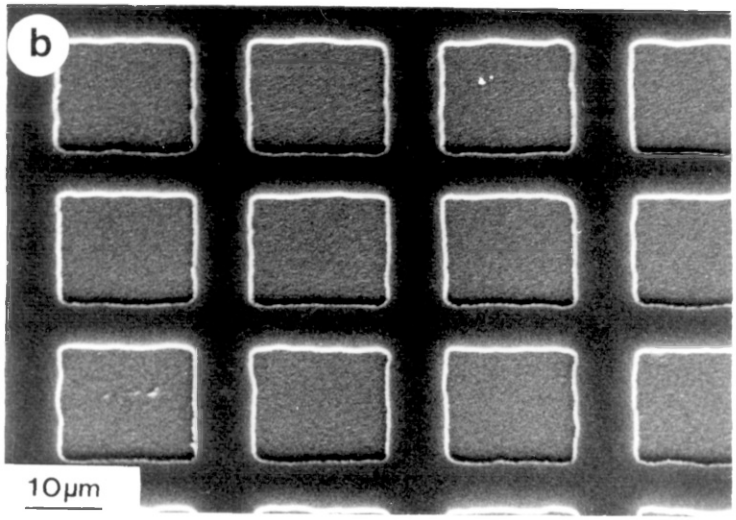
Written pattern of a 5μm Ni-mesh on SiO_2/Si substrate using $CdCl_2$ resist for pattern transfer.

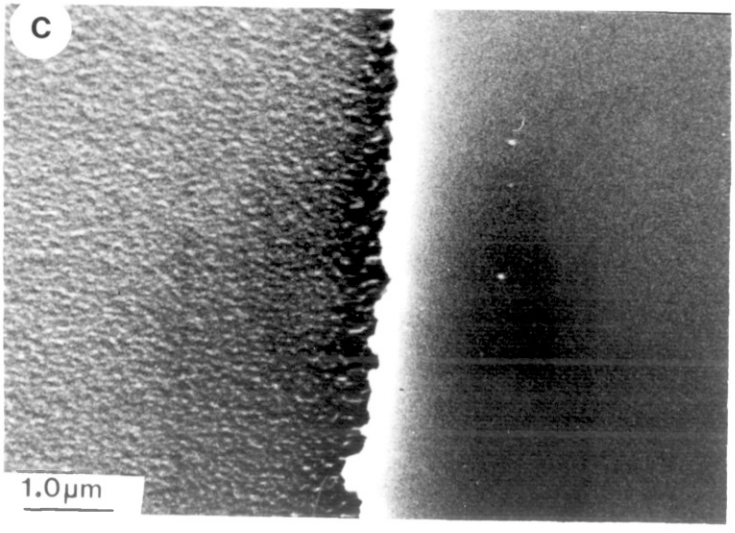
(a) 5μm Ni-mesh used in masking $CdCl_2$ resist during e-beam decomposition.
Features in the windows is due to the silver paint used in sticking the mesh on to a stub.

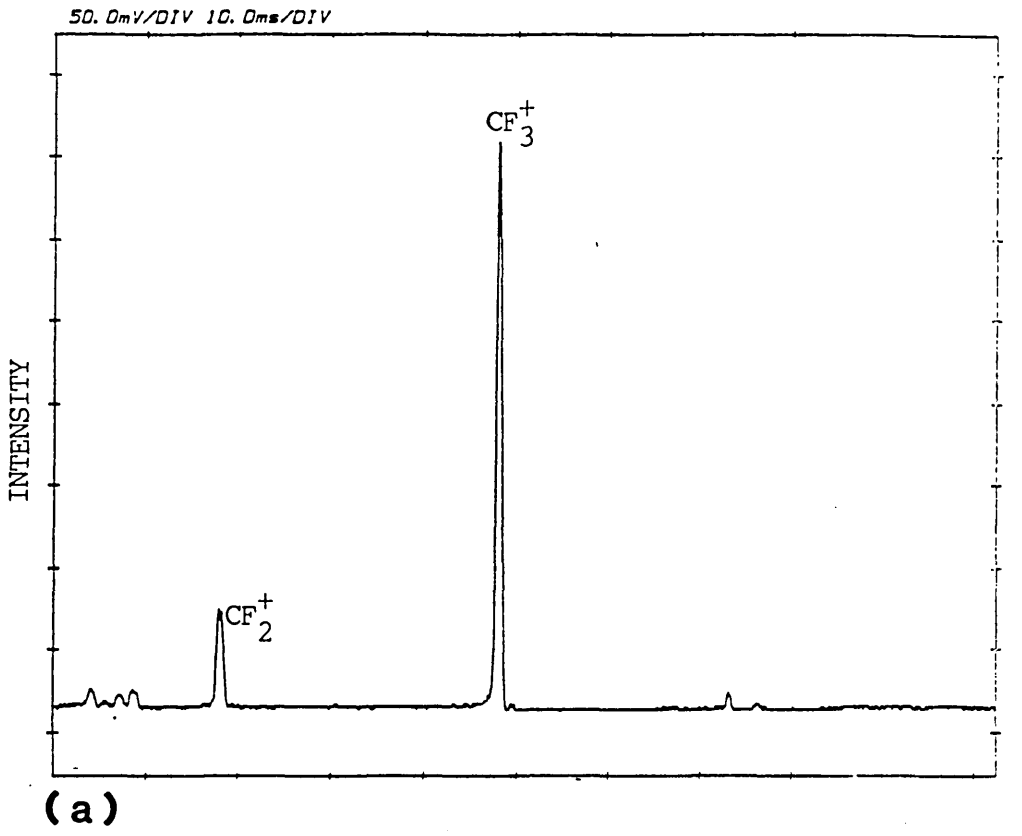
(b) Written pattern after e-beam exposure and RIE.

(c) Si-SiO_2 interface.
The smooth area is the SiO_2 surface, and the graining area, the Si surface, showing the effect of over etching the SiO_2 by about 10%.


a
10μm


b
10μm


c
1.0μm



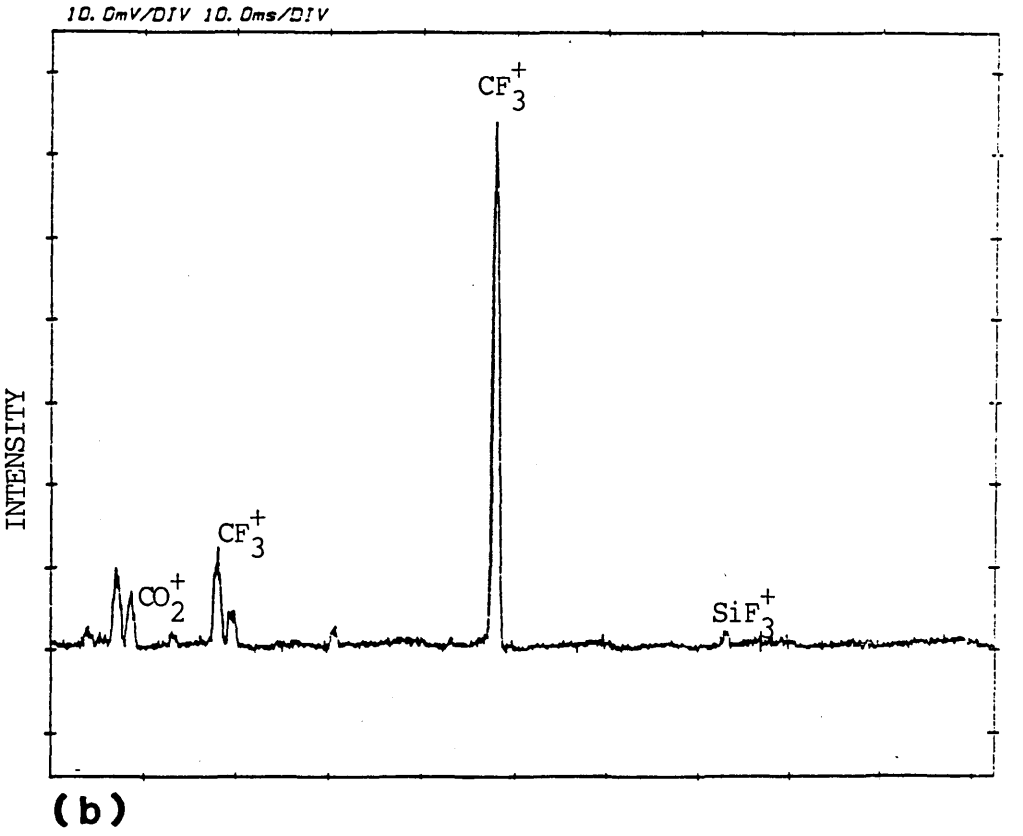


Figure 4.2.18: QMS signal (mass range 41 - 105 a.m.u.)
(a) CF_4 gas without a discharge.
(b) with the discharge on, and commencement of etching.

4.3 DISCUSSION

The results of e-beam decomposition of $CdCl_2$ indicate that the holes produced (Fig. 4.1.1) in the resist were a result of radiolysis and were not thermally induced. These results are in accordance with the temperature profile study of Iranmanesh and Pease [2]. The overall chemical reaction produced by the electron beam is

$$CdCl_2(s) \longrightarrow Cd(g) + 2Cl(g)$$

In particular, it was shown that for 2keV electrons, the dose required to totally decompose a 140nm thick film of $CdCl_2$ at 210^oC is $5x10^{-3}C\ cm^{-2}$, which corresponds to $3.2x10^7 J\ mol^{-1}$. Comparing this with the energy required for the standard heat of reaction ($6.3x10^5 J\ mol^{-1}$ [3])), gives a 2% "thermodynamic" efficiency.

On the other hand, the energy required to form two hole/electron (h/e) pairs to decompose a $CdCl_2$ molecule, viz:-

$$[Cd^{++}\ Cl_2^-] + 2e^- + 2h^+ \longrightarrow Cd + 2Cl$$

is estimated to be about $8.7x10^5 J\ mol^{-1}$. This then gives an "electronic" efficiency for 2keV electrons at 210^oC of about 2.7%.

The process of decomposition can be divided into two parts. Primary electrons creating a shower of electron/hole pairs, which rapidly decay to being electron/hole pairs at the conduction and valence-band edges of the resist material. The electron/hole pairs can then either recombine (at the surface or in the bulk) or take part in the chemical decomposition of the resist.

The EPMA results on low temperature irradiation (Cd not volatile) show broadening of the cadmium peaks, and an increase in the amount of cadmium. These are attributed to changes in the bonding of cadmium and the loss of chlorine.

For optimum behaviour of an etching process, the utilisation factor has to be substantially less than unity [4,5]. The utilisation factor is the ratio of the flow of etch products to the etch gas. All the etching processes carried out resulted in ultilisation factor of less than 0.05. Also, the gas flow rate had to be much higher than the dissociation rate. The dissociation rate of CF_4 molecules, for a cathode diameter of ~20cm is 10^{18}molecules/s [6]. A flow rate of at least 10sccm (1sccm = 4.48×10^{17} molecules/s) is desirable [6].

In CF_4 discharges, the most abundant positive ion is CF_3^+, most often formed by,

$$CF_4 + e^- \longrightarrow CF_3^+ + F + 2e^-$$

Other ions produced (such as F^+, CF_2^+, CF^+, C^+), have concentrations much less than CF_3^+, because of the lower probability of their being formed, and also because the majority of them react with CF_4 (e.g $CF_2^+ + CF_4 \longrightarrow CF_3^+ + CF_3$), whereas CF_3^+ does not. In addition to the presence of neutral CF_4 molecules and ions in the discharge, there exist radicals (e.g CF_3 radicals and also F atoms, generated through the process $CF_4 + e^- \longrightarrow CF_3 + F + e^-$). The high pressure employed in the plasma etching mode leads to little or no available energy for incident positive ions, due to collisional processes in the sheath [7]. As a result, etching is essentially by chemical reaction: chemisorption followed by product formation, and finally desorption of etch products. The main species available for etching are CF_3 radicals and F atoms, in mutual competition.

What at first sight appears to be a process of $CdCl_2$ being etched, corresponding to decreased refractive index, is in fact a substitutional process, represented by the reaction;

$$CdCl_2(s) + 2F(atom) \longrightarrow CdF_2(s) + Cl_2(g)$$

This then resulted in a layer of CdF_2 on top of the processed $CdCl_2$ film. Further processing of $CdCl_2$ resulted in the carbon/fluorine polymerisation reaction since CdF_2 is an oxygen free surface, and the adsorption of CF_3 on its surface will only result in polymer formation.

Under steady state etching conditions, the CF_x (x=0,1,2,3) polymeric film is relatively absent on SiO_2, because of the presence of oxygen atom which react with the carbon-containing species to form gaseous CO, CO_2, and COF_2 [8,9]. Addition of oxygen gas (O_2) to CF_4, so as to have up to 20% O_2 in the etch gas, increases the density of F atoms [9,10] by an order of magnitude through interactions with the radicals formed by the dissociation of CF_4. It is generally considered that CO or CO_2 is formed giving rise to an increased concentration of fluorine atoms which are then available for etching [6]. The overall effect is increased etch rates of SiO_2, and the absence of the polymer on $CdCl_2$.

The reduction in the etch rate of SiO_2 when processing was carried out with moist etch-gas, is attributed to reaction with hydrogen atom in the water molecule, thereby depleting the plasma of F atoms, and increasing the C:F ratio. In RIE mode the slight decrease in etch rate with increased gas flow rates could be due to the fact that the chamber pressure was quite high (~165mtorr), and many collisional processes were occurring, resulting in depletion of active species required for etching. The process then becomes more of a chemical than a physical process, and the only way to overcome this problem is to increase the r.f. power. Etch rates are higher at low pressure (<100mtorr) because the field has sufficient time to accelerate an electron to maximum potential between collisions [11].

For the etching conditions specified in Fig. 4.2.12, the substitutional process in $CdCl_2$ was found to progress at a linear rate with increase in pressure up to 120mtorr. The sudden decreasing "etch" rate of $CdCl_2$ at pressures above 120mtorr could be explained in terms of saturation of the substitional process. The high pressure of the etching process giving rise to a higher concentration of CF_x radicals and possible polymerisation on the resist surface.

The substitutional process theory proposed for $CdCl_2$ "etching" is substantiated by the following observations:

(i) Processed (dry etched) samples of polymer-free $CdCl_2$ were found not to be readily soluble in ethanol, whereas

deposited $CdCl_2$ films were readily soluble. This test accords with the established fact [12] that CdF_2 does not readily dissolve in ethanol, whereas other halides of cadmium are highly soluble.

(ii) EPMA spectra of processed sample of $CdCl_2$ (Fig. 4.2.13), revealed a decrease in the chlorine signal, with no observed change in the cadmium signal.

(iii) SIMS result of the in-depth profile of ^{19}F species (Figures 4.2.14 & 4.2.15), revealed the presence of fluorine up to a depth of about or less than 20Å.

(iv) The ESCA results of etching carried out in the plasma mode, revealed extensive surface F/Cl exchange.

(v) A processed sample of $CdCl_2$ did not evaporate appreciably (in minutes) in the temperature range of greater than or equal to 230^oC in contrast to pure $CdCl_2$.

4.4 SUMMARY

(i) At this stage in the study of $CdCl_2$ as an inorganic electron-beam resist, the kinetics and mechanism of decomposition follow broadly what occurs in photolysis [13,14].

(ii) It is proposed that $CdCl_2$ was not actually being etched, but fluorine was replacing chlorine: the etch selectivity should then be much greater than the 16:1 value obtained in section 4.2.2. Etching is best carried out in the RIE mode below a pressure of 60mtorr. Plasma etching was found to be undesirable because of the introduction of polymer contamination on the resist surface.

(iii) $CdCl_2$ as an inorganic e-beam resist has been successfully used in the fabrication of Si/SiO_2 feature (Figure 4.2.17b). The lithography process is shown in Figure 4.4.1.

(iv) A resolution of about 100nm is expected, since the grain size for room temperature deposited $CdCl_2$ is about equal to the film thickness, namely 100nm. This is because hole/electron pairs are not expected to spread beyond the thickness of a grain, due to recombination at the grain boundaries.

(v) The sensitivity (5×10^{-3} C cm^{-2}) of the resist can be improved by considering the following points:

(a) Increasing the beam energy to 4keV, which corresponds to a Grun electron range [15] of 100nm, giving a two-fold improvement.

(b) Increasing the beam intensity, by using brighter sources.

(c) Having a two-layer resist, the top layer acting as a cap.

Further e-beam studies of $CdCl_2$, taking into consideration the points specified for sensitivity improvement, has been carried out in the Department.

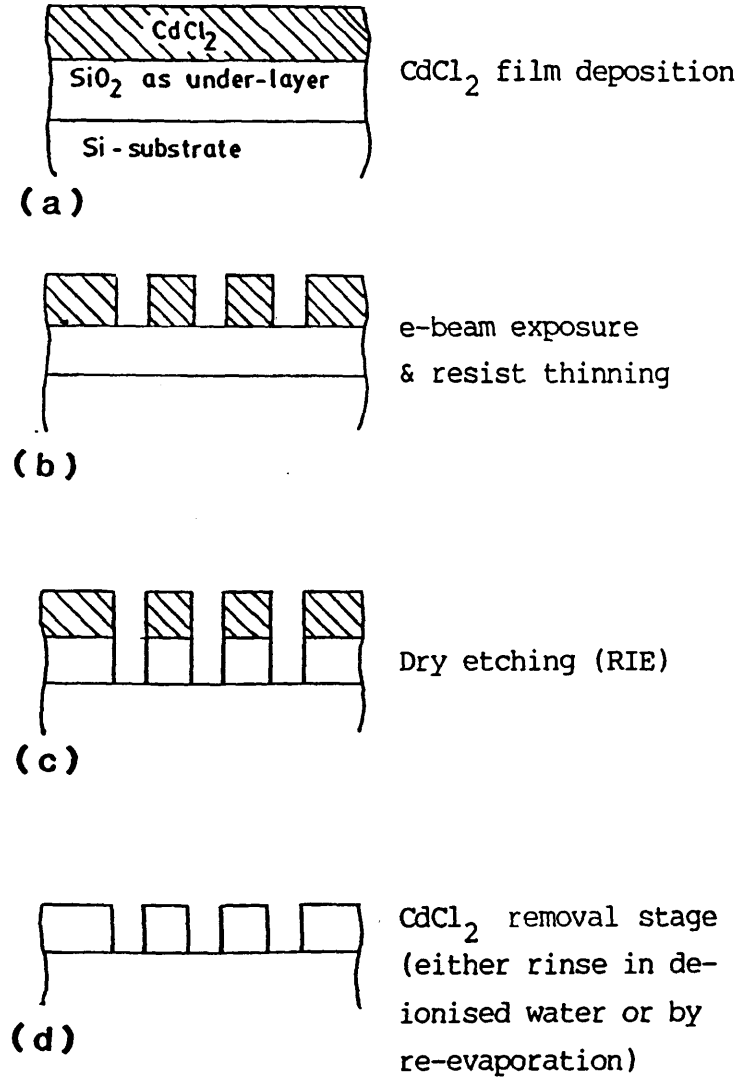


Figure 4.4.1: Si/SiO_2 feature fabrication process.

CHAPTER 5

MATERIALS FOR THE ABSORBER LAYER OF X-RAY MASK: RESULTS AND DISCUSSIONS

5.1 ELECTRON BEAM DECOMPOSITION KINETICS

Essentially all the work reported in this section was done by irradiating samples with 2keV electrons (generated by a V.G. Leg22 gun, at scan rates indicated in section 3.2.3.) under a vacuum pressure of 10^{-8} torr. Film preparations were carried out as described in section 3.1.2.

The decomposition kinetics were studied using a quadrupole mass spectrometer (QMS) to monitor the reaction products, namely cadmium and chlorine. In the temperature range of experimentation (120^{o}C to 220^{o}C), lead (Pb) is totally involatile (see Figures 3.1.1 & 3.1.2). The following relationship exists between the total amount of reaction products, R, and the current, I, measured at the QMS due to the reaction products.

$$dR/dt = KI$$

where K is the QMS calibration factor. The QMS calibration procedure, presented in Appendix I, was used to obtain values of K and R_T. Here, R_T is the total amount of available reaction product (i.e all that is present in the film). The extent of decomposition reaction, in percentage, is given by the expression $[(R/R_T) \times 100\%]$. For data collection, when silicon (Si) was used as the substrate, the QMS was aligned at an angle, Θ, of about 70 degrees to the sample surface normal, and at a distance, r, of about 20cm from the sample surface. When glass was used as the substrate, with aluminium (Al) as the inter-layer (Al/glass substrate), the settings were $\Theta = 45^{o}$ and r = 20cm. This enhanced the collection efficiency at the mass spectrometer. The K and R_T values for $PbCl_2$ film on Al/glass substrate are 1.51×10^{22}Cl atoms/cm^2/C and 1.27×10^{17}Cl atoms/cm^2 respectively. While $PbCl_2/CdCl_2$(20%) film on silicon substrate has K and R_T values of 3.13×10^{22}Cl atoms/cm^2/C and 2.05×10^{17} Cl atoms/cm^2

respectively. Measurements of the rate of reaction product evolution as a function of time were corrected, for instrumental delay, by using computer program A listed in Appendix II. All data presented are, after correction, line of sight values at the mass spectrometer.

5.1.1 TEMPERATURE AND SUBSTRATE DEPENDENCE RESULTS.

The experimental data for the rate of reaction product evolution as a function of temperature are presented in Figures 5.1.1 and 5.1.2. These graphs, normalised to their respective curve maxima, are presented in Figures 5.1.3 and 5.1.4.

Figs. 5.1.3a &b, representing the decomposition characteristics of $PbCl_2$ films on the Al/glass substrate and that of $PbCl_2$ films on silicon substrate, show that the time taken to achieve a maximum decomposition rate is independent of temperature; furthermore the decomposition kinetics are independent of substrate material.

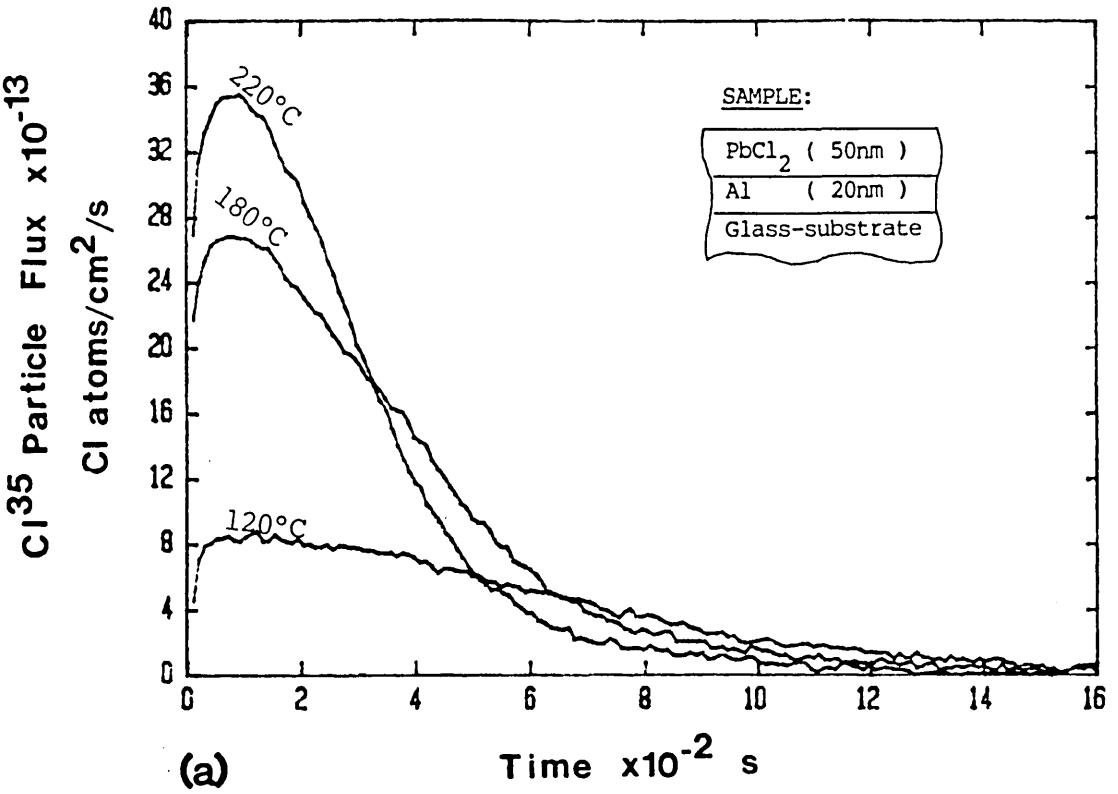
When $CdCl_2$ is incorporated into $PbCl_2$ resulting in a film of $PbCl_2/CdCl_2$(20%) (Pb:Cd elemental ratio is 4:1, EPMA data presented in section 5.2.1), the time taken to reach the maximum rate becomes a function of temperature. The results are presented in Figure 5.1.4a. At temperatures greater than 90^oC, Cd is volatile (vapour pressure curve of Figure 3.1.1). The result of Cd evolution rate when $PbCl_2/CdCl_2$(20%) film was decomposed at 180^oC is presented in Figure 5.1.2b. The replot in normalised form is presented in Figure 5.1.4b. The cadmium rate curves are similar to that of chlorine.

The extent of decomposition was investigated by integrating areas under the curves in Figures 5.1.1a and 5.1.2a with respect to the absicca (the computer program B listed in Appendix II was used to carry out the integration). The results obtained are presented in Figures 5.1.5a &b. These curves (Figures 5.1.5a &b) can be seen to saturate. For $PbCl_2$ films on Al/glass substrate, 100% decomposition was achieved for irradiation carried out at a temperature of 220^oC. This is equivalent to 1.27×10^{17} Cl atoms/cm^2 (determined in Appendix I). At lower temperatures, total decomposition was not achieved for the duration of experiments. For $PbCl_2/CdCl_2$(20%) films on Si-substrate, 100% decomposition was not achieved for all

irradiation temperatures; 100% decomposition corresponds to 2.05×10^{17} Cl atoms/cm^2 (determined in Appendix I). In situations when 100% decomposition was not achieved, longer exposure time may be required to achieve total decomposition of material, and the possibility exists of total decomposition not being accomplished even after very long exposure time (see section 5.1.3 for discussion). The effect of temperature on the proportion of material that was decomposed, given in percentage, are shown in Figures 5.1.6a & b. In both sets of curves in Figures 5.1.6a &b, the percentage decomposition increases with temperature. The change in extent of decomposition of $PbCl_2/CdCl_2$(20%), by increasing the decomposition temperature from 120°C to 150°C, is considerable.

The electron dose/temperature characteristics shown in Figures 5.1.7a &b are similar for both samples ($PbCl_2$ films on Al/glass substrate and $PbCl_2/CdCl_2$(20%) films on Si). The electron dose required to achieve a certain extent of decomposition decreases with increasing temperature, with an upward shift for higher extents of decomposition.

The logarithmic rate of reaction versus reciprocal irradiation temperature (absolute values) is shown in Figure 5.1.8.



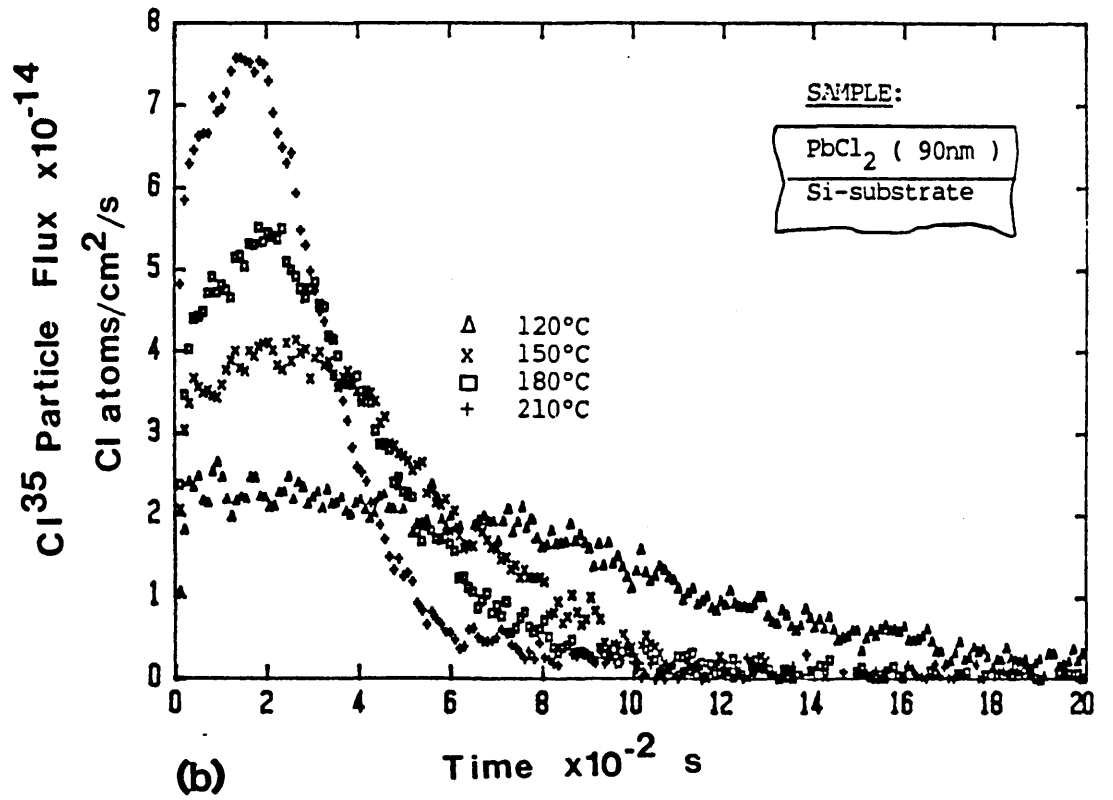
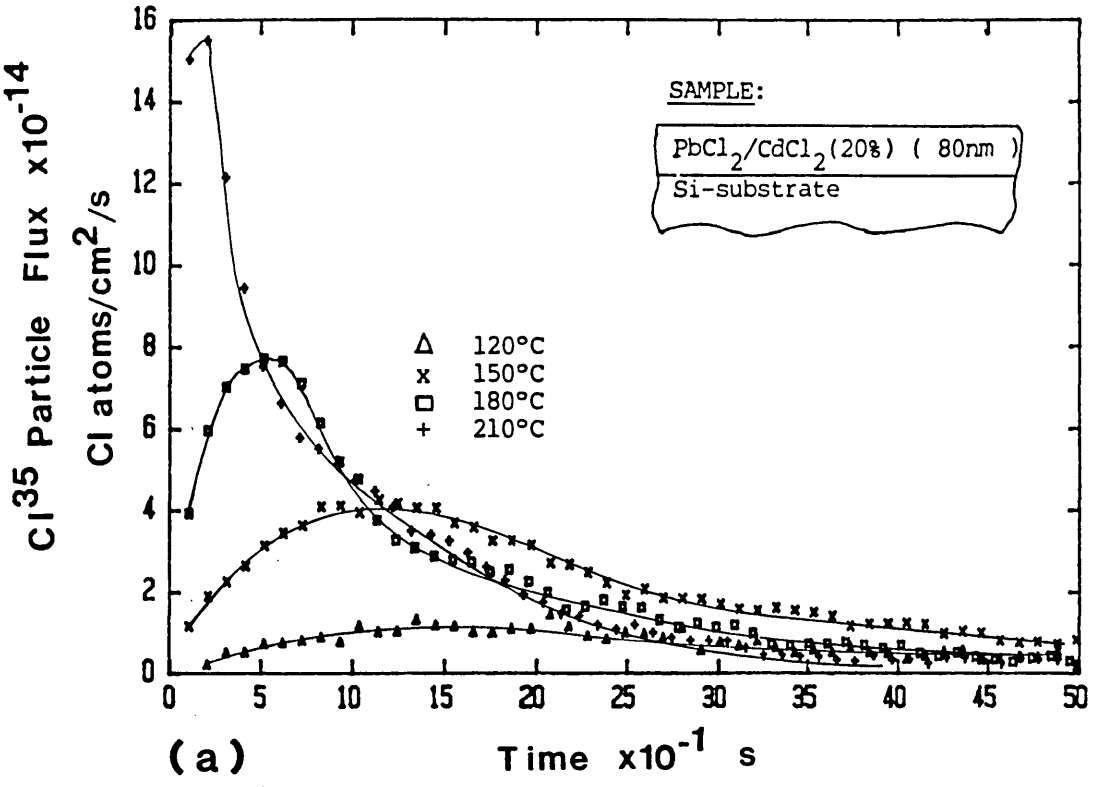


Figure 5.1.1: Cl^{35} particle flux vs. Time; showing the effects of temperature and substrate

(a) e-beam current density = 32μA cm^{-2}

(b) e-beam current density = 140μA cm^{-2}



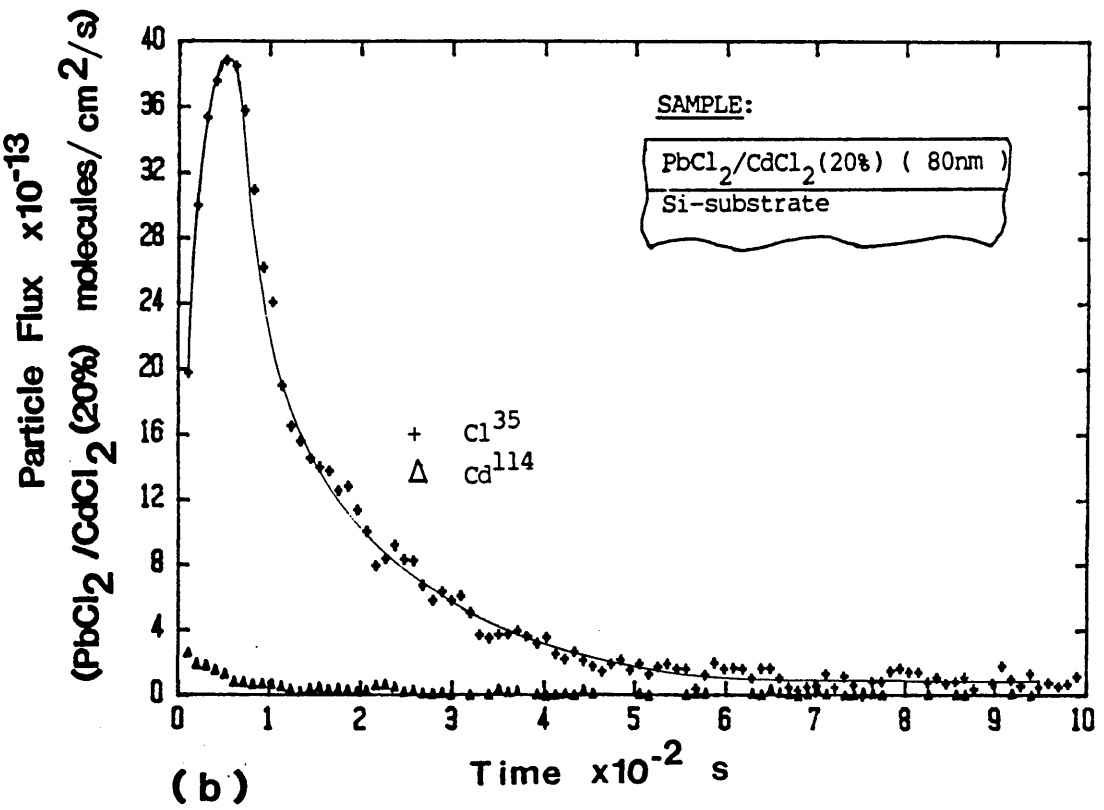


Figure 5.1.2: Particle flux vs. Time
e-beam current density = 70μA cm^{-2}

(a) Effect of temperature on Cl^{35} particle flux

(b) Cd^{114} and Cl^{35} particle flux at operating temperature of 180°C

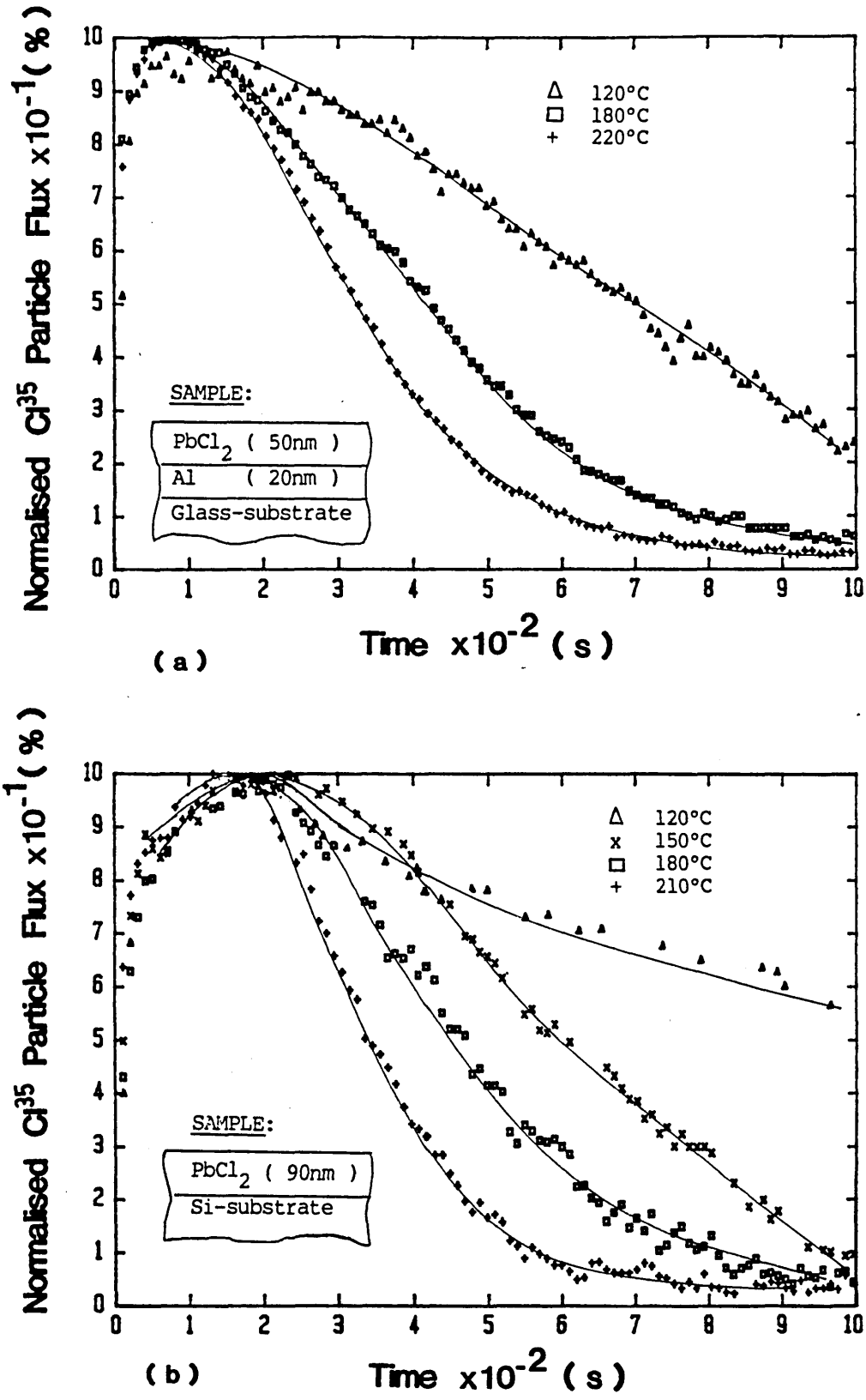
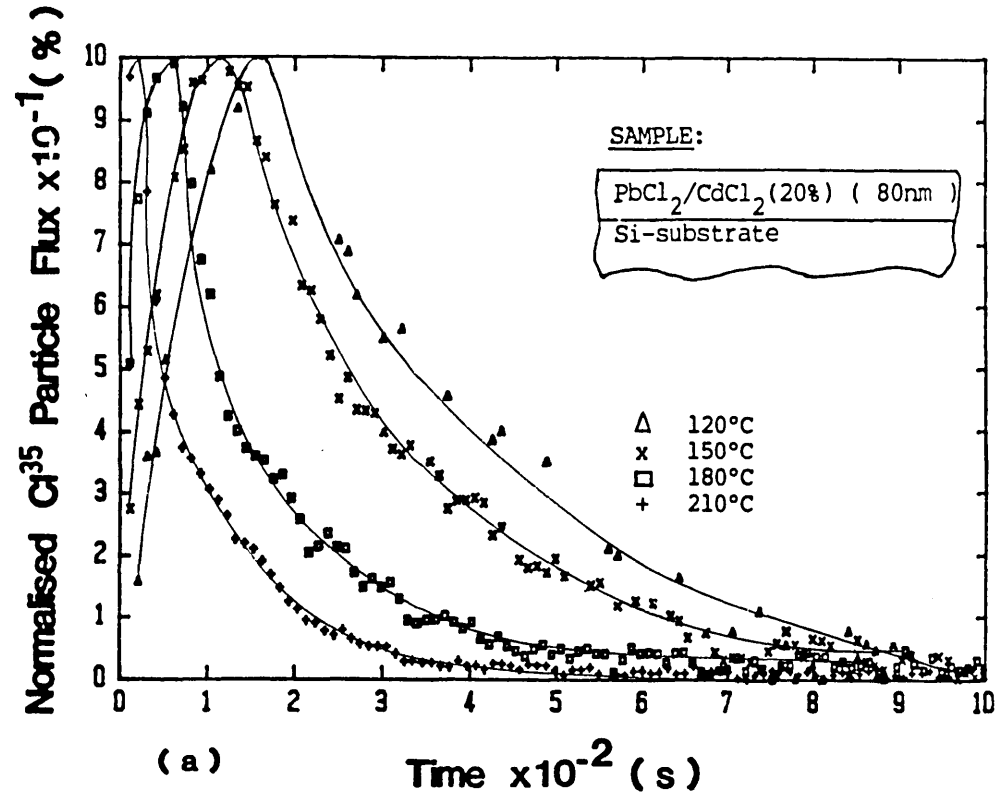


Figure 5.1.3: Normalised Cl^{35} particle flux vs. Time; showing temperature and substrate effects.

(a) e-beam current density = 32 μA cm^{-2}

(b) e-beam current density = 140 μA cm^{-2}



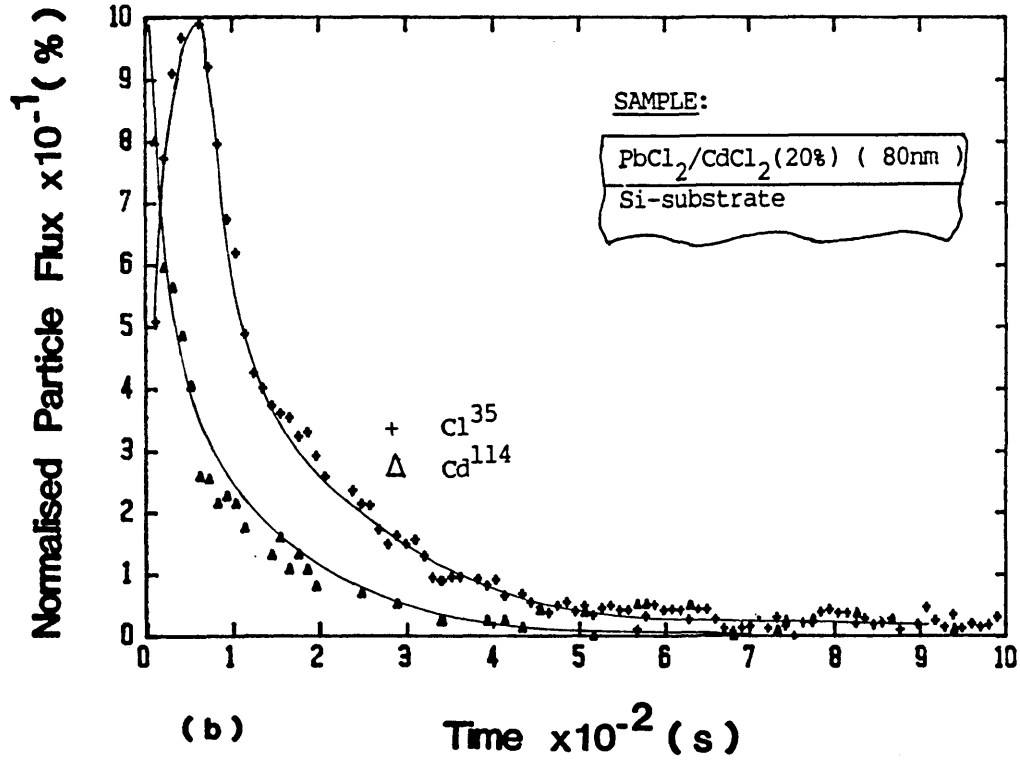
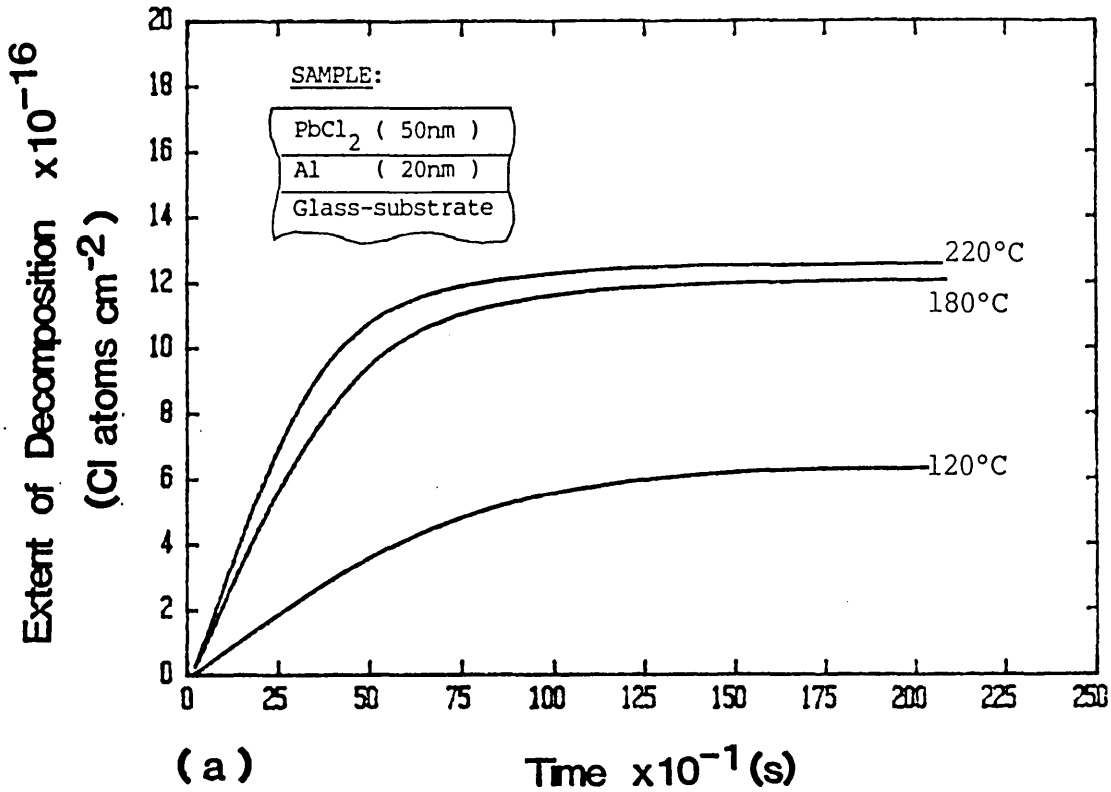


Figure 5.1.4: Normalised particle flux vs. Time
e-beam current density = 70 μA cm^{-2}
(a) Effect of temperature on Cl^{35} signal rate.
(b) Cd^{114} and Cl^{35} signal rate at temperature of 180°C



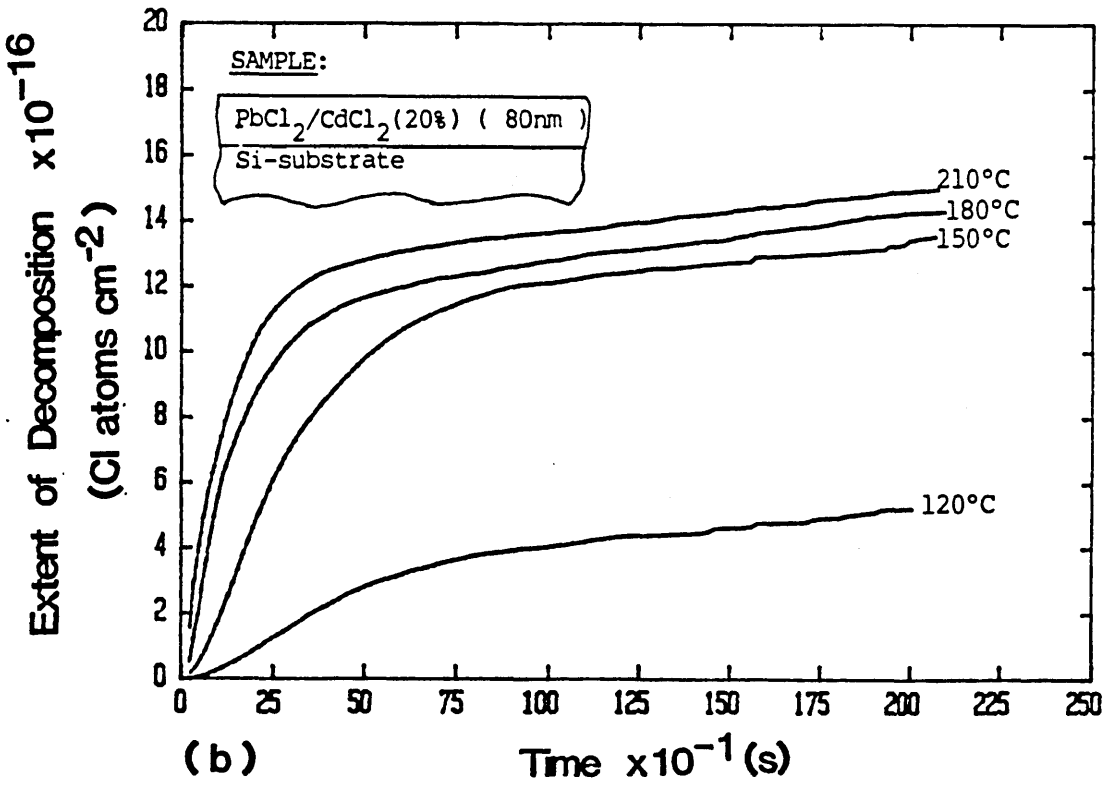
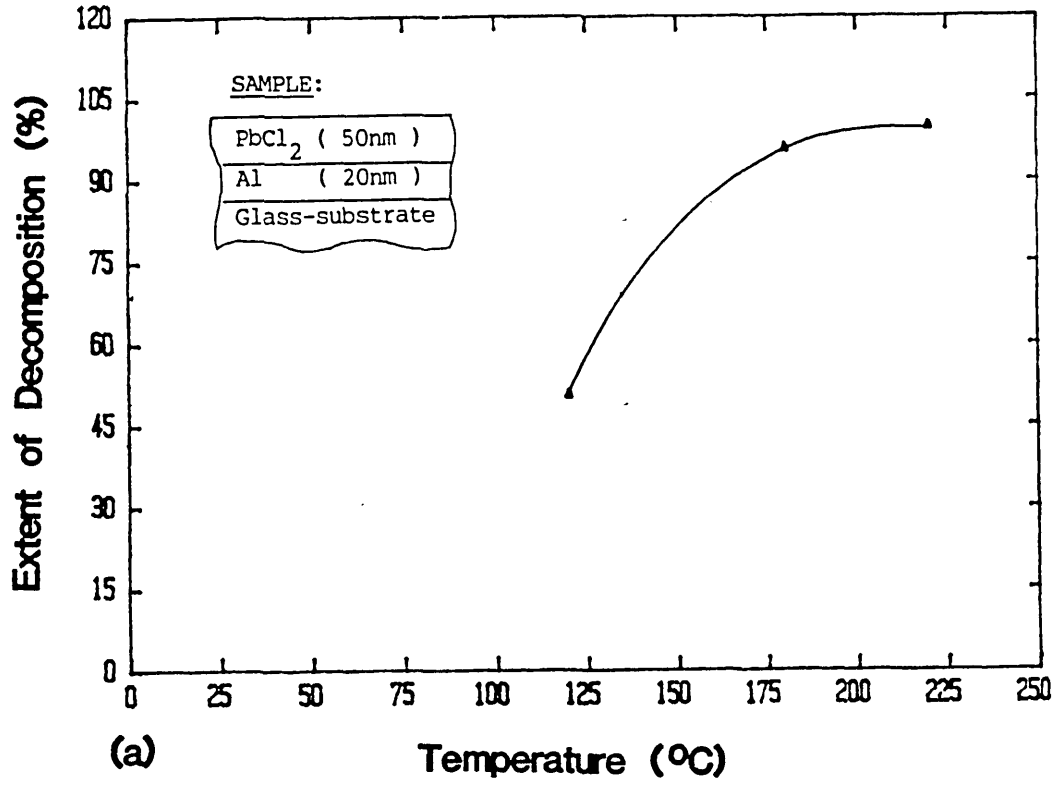


Figure 5.1.5: Extent of decomposition vs. Time; showing the effect of temperature

(a) e-beam current density = 32μA cm^{-2}

(b) e-beam current density = 70μA cm^{-2}



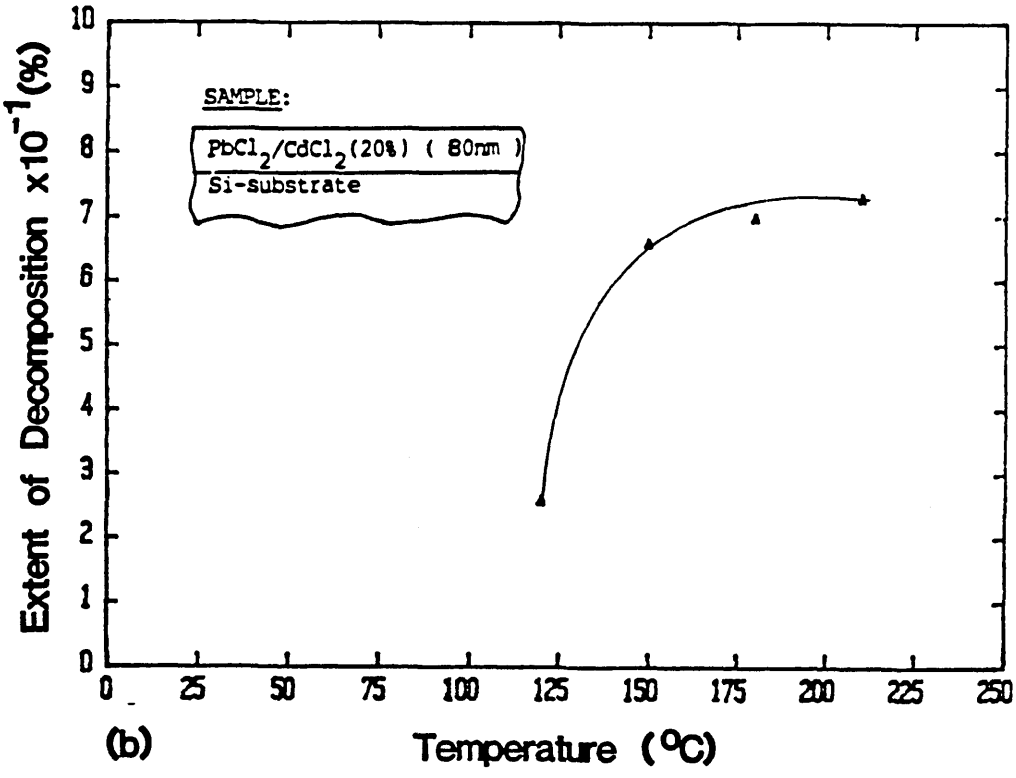
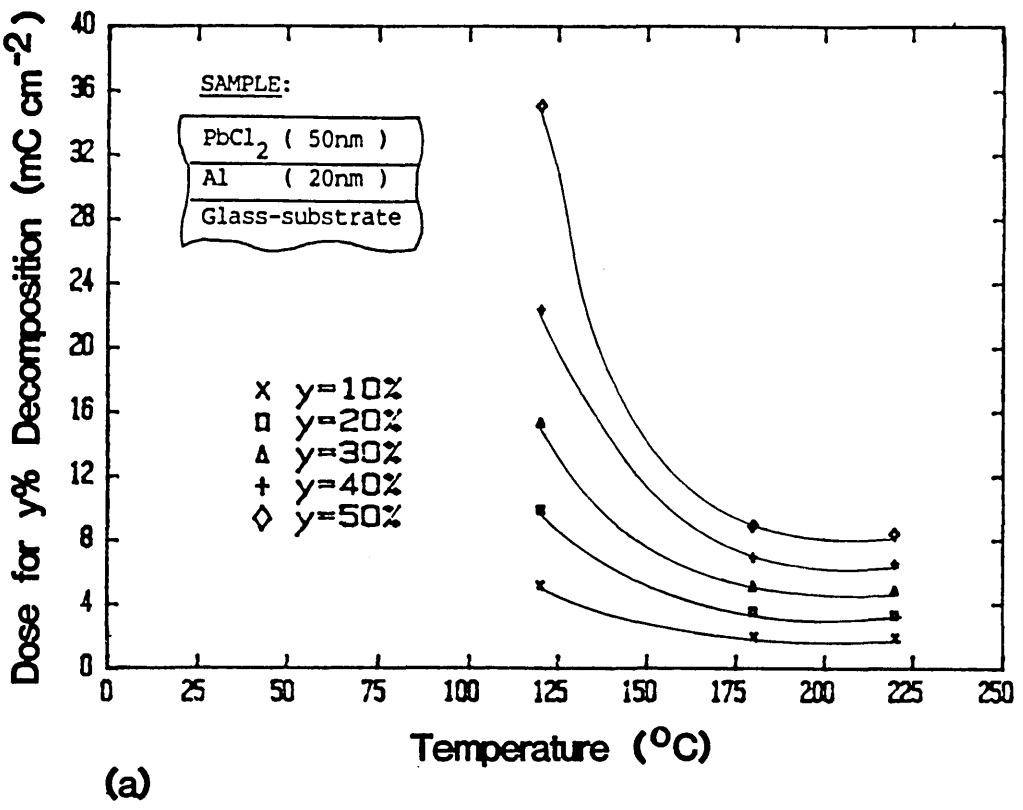


Figure 5.1.6: Effect of temperature on the extent of decomposition; Exposure time = 2100s.

(a) e-beam current density = 32μA cm^{-2}

(b) e-beam current density = 70μA cm^{-2}



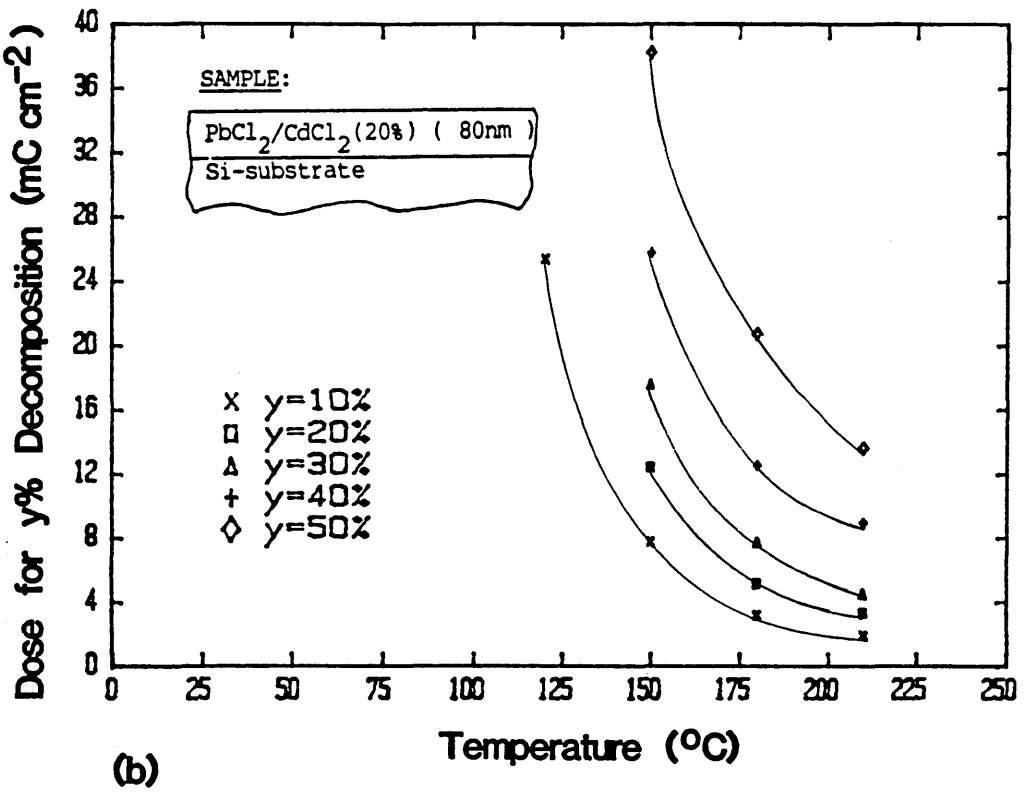


Figure 5.1.7: Effect of temperature on the dose required to achieve y% decomposition

(a) e-beam current density = 32μA cm^{-2}

(b) e-beam current density = 70μA cm^{-2}

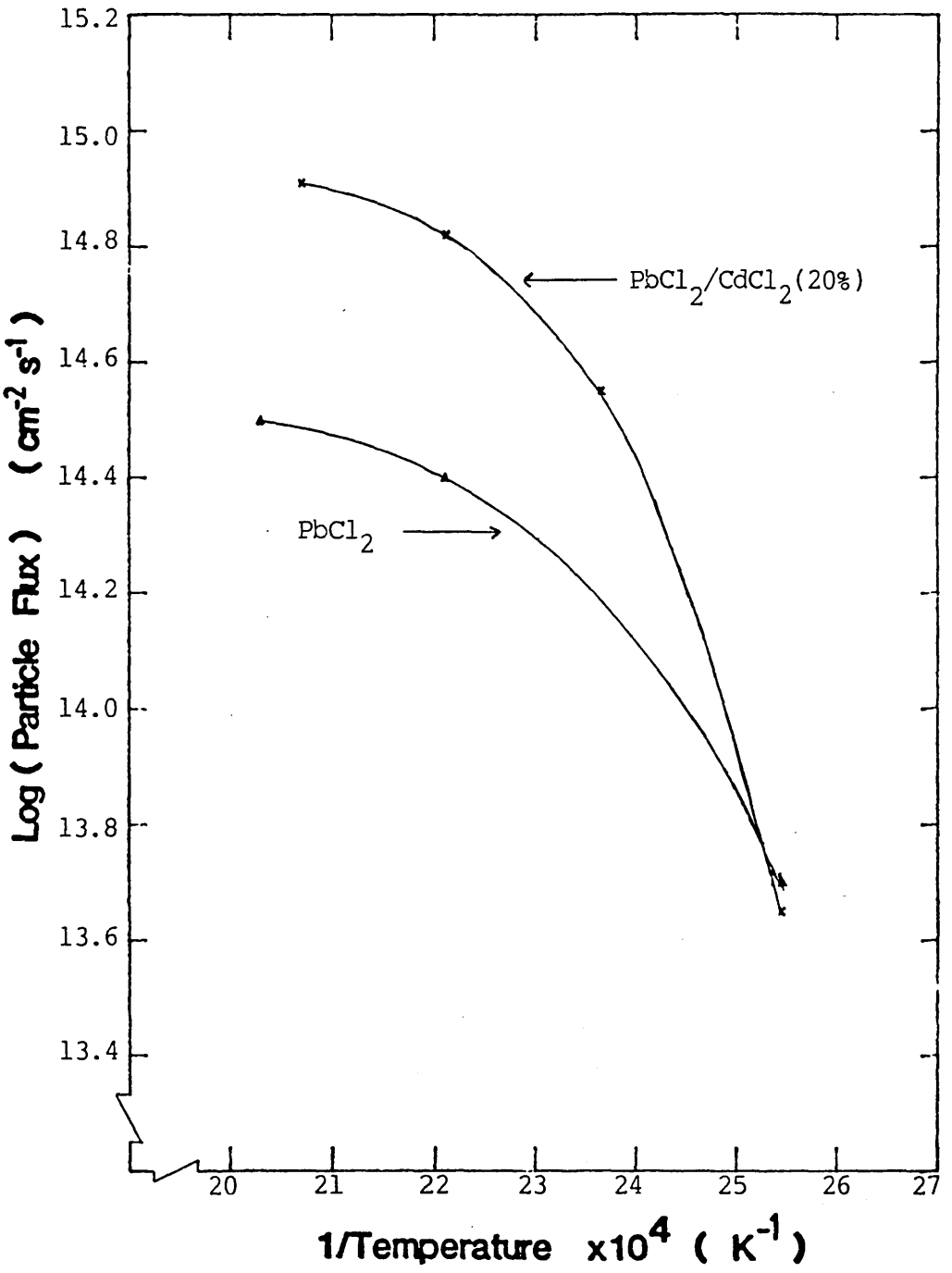


Figure 5.1.8: Log (Particle Flux) vs. 1/Temperature. Rate was taken at the time required to decompose 2×10^{16} molecules of material cm^{-2}

5.1.2 CURRENT DENSITY DEPENDENCE RESULTS.

The data presented below is given in a form similar to that of section 5.1.1, but here the dependency on current density is investigated.

The effect of using different substrates (Al/glass or Si) was found to be negligible just as in section 5.1.1, hence the results will be restricted to one type of substrate per material. Decomposition rate measurements are shown in Figures 5.1.9a &b. These are replotted in a normalised form, and the results presented in Figures 5.1.10a &b. The effect of current density on time taken to achieve a maximum rate of reaction product evolution is much clearer in the normalised plots. The time taken to reach the curve maxima for the $PbCl_2$ samples is independent of current density; in contrast, $PbCl_2/CdCl_2$(20%) samples show a current density dependency.

The results of the extent of decomposition are presented in Figures 5.1.11a &b. 100% decomposition of the sample was not achieved for the experimental condition specified. The extent of decomposition, representing the percentage of material that was decomposed, are presented in Figures 5.1.12a &b. The percentage decomposition increases with current density. For lower current density, more exposure time is required to attain the same percentage decomposition achieved for higher current density.

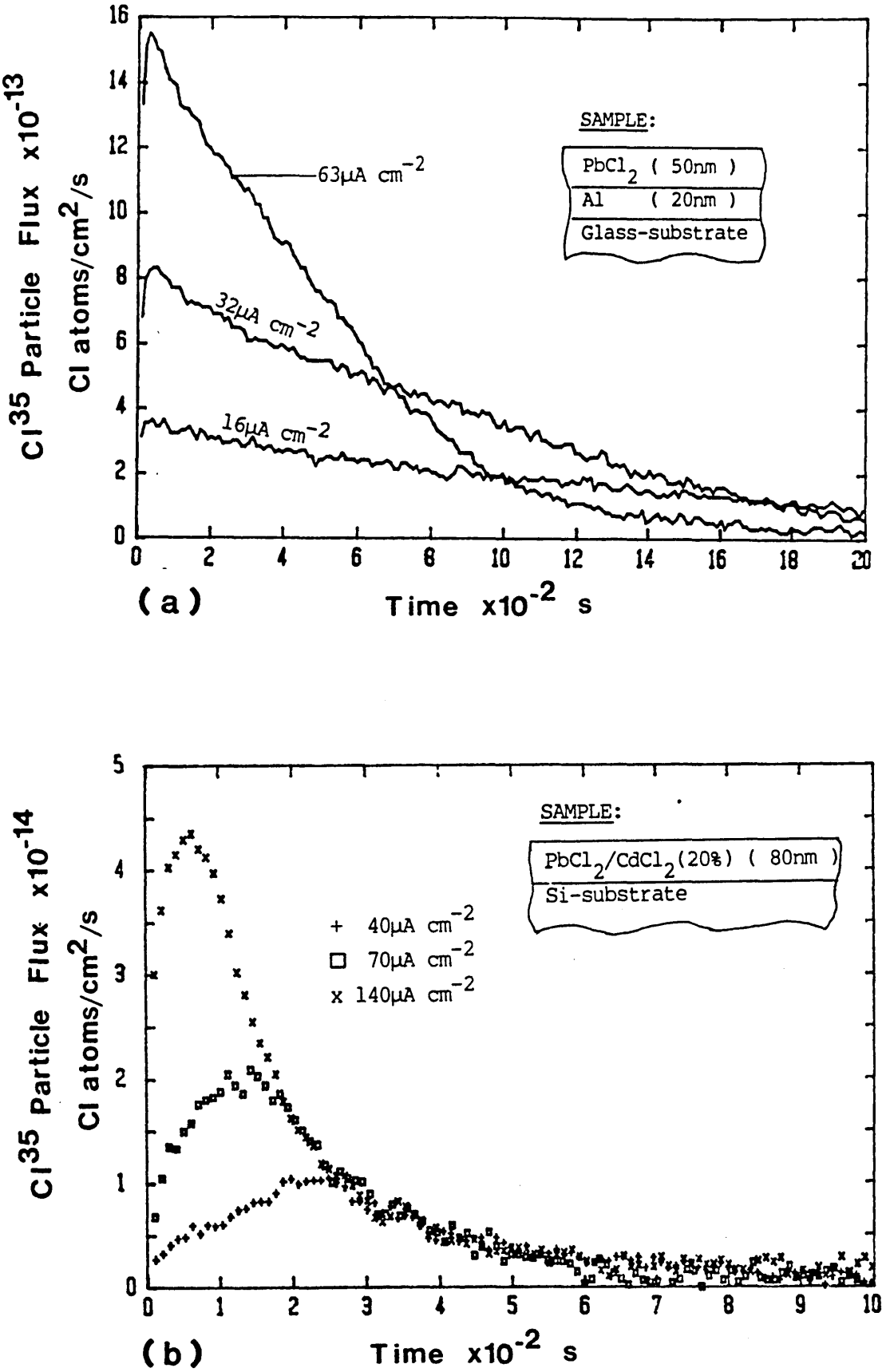


Figure 5.1.9 : Cl^{35} particle flux vs. Time; showing the effect of current density
Operating temperature = 120°C

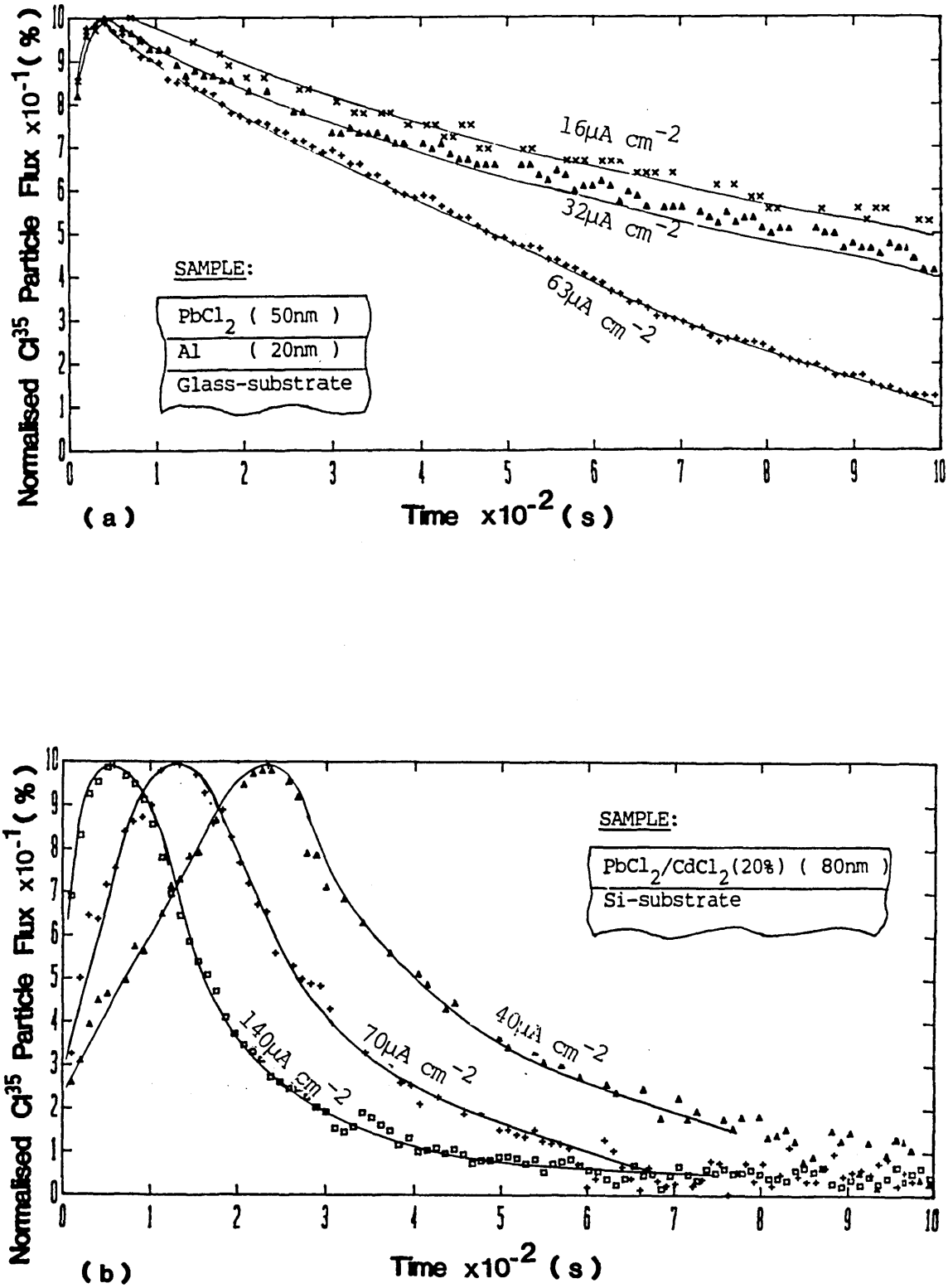
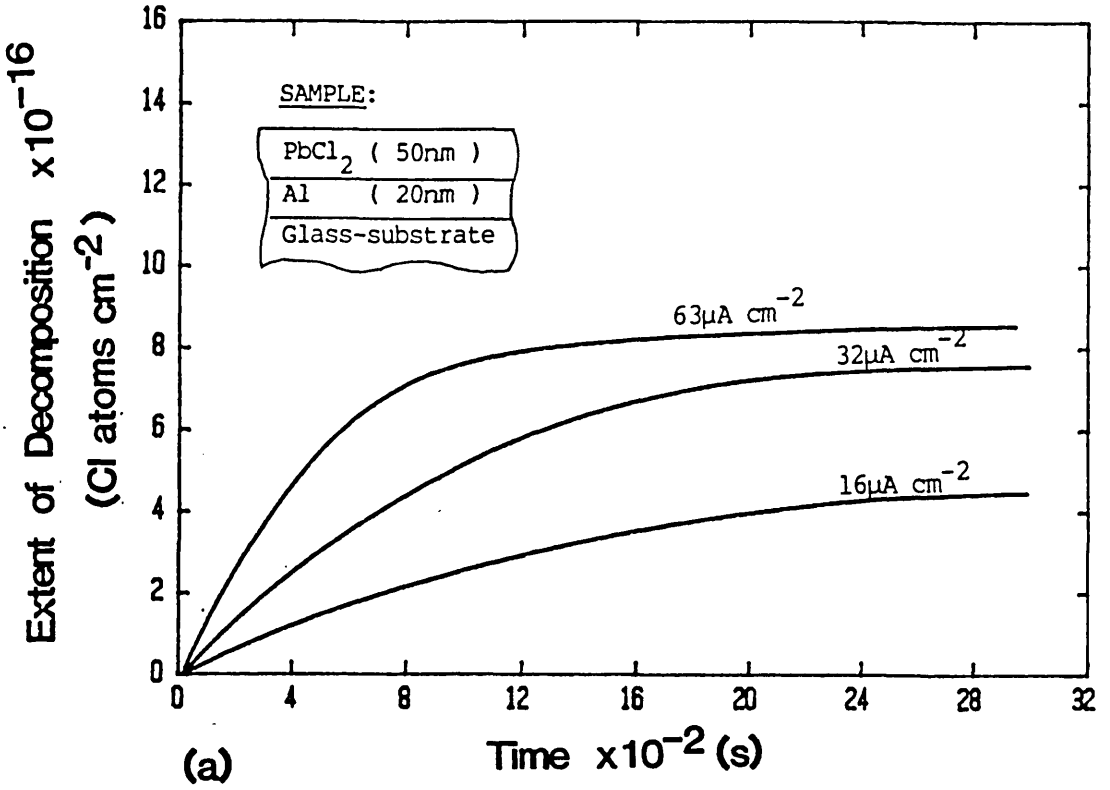


Figure 5.1.10 Normalised Cl^{35} particle flux vs. Time; showing the effect of e-beam current density.
Operating temperature = 120°C



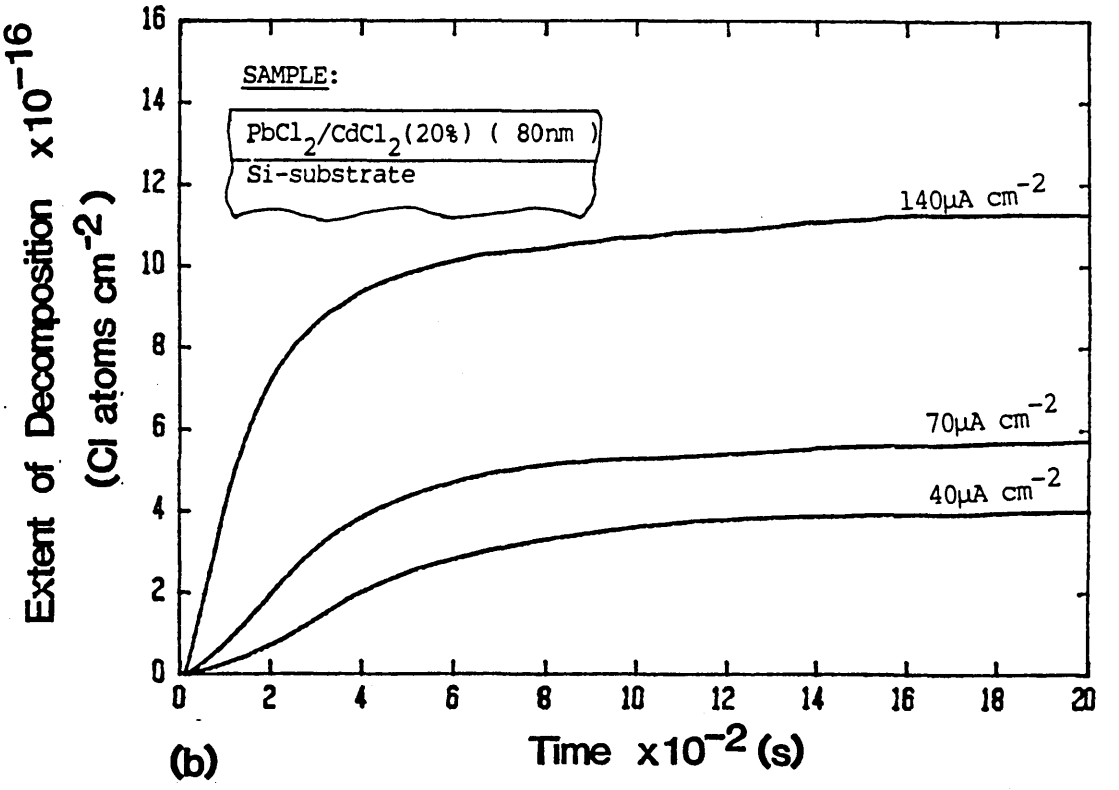
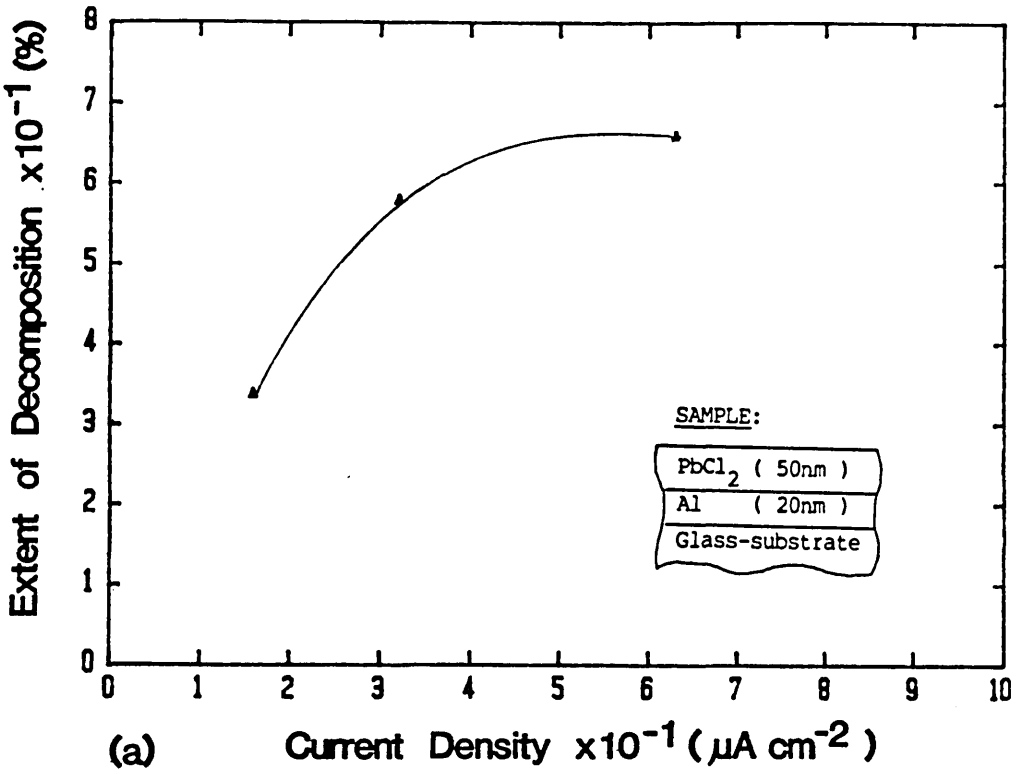


Figure 5.1.11 Extent of decomposition vs. Time; showing the effect of current density
Operating temperature = 120°C



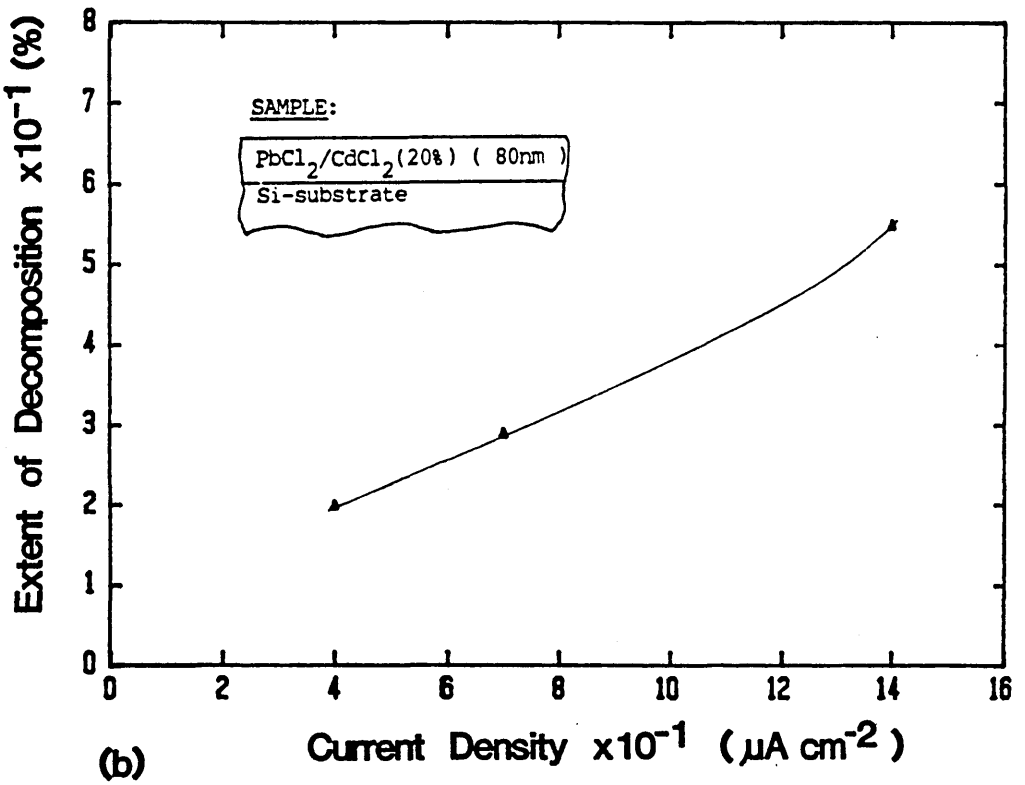


Figure 5.1.12 Effect of current density on the extent of decomposition. Operating temperature = 120°C

(a) Exposure time = 3000s

(b) Exposure time = 2400s

5.1.3 DISCUSSION

The decomposition mechanisms of lead chloride ($PbCl_2$) are temperature dependent. At temperatures higher than 120°C, there is an initial rise in the rate of decomposition (see Figures 5.1.1 and 5.1.3). This is followed by a peak and then an exponential decay. This is similar to the decomposition processes in $CdCl_2$ [1], in which the rate determining process occurs at the surface: call this "surface controlled." The rise in the rate of decomposition to a maximum value at temperatures of 120°C and less, is significantly faster than at temperatures higher than 120°C (compare Figure 5.1.9a with Figure 5.1.1). The decomposition mechanism in this case is bulk controlled; the in-diffusion of anion vacancies, such as in PbI_2 [2,3] and SnI_2 [4]. The two outlined decomposition processes can be summarised as "high" and "low" reaction rates respectively.

Also, it should be noted that structural changes such as voids, precipitates etc, were observed (see Figures 5.2.3 and 5.2.4) for all decomposed materials.

Electron beam decomposition involves electron-hole (e-h) pairs being generated at the band edges of the material being irradiated by the incoming primary electrons. The average energy, ε, required to create an e-h pair is about three times the bandgap energy ($\sim 3E_g$) of the material [5]. The bandgap energy, E_g, for $PbCl_2$ is ~4.7eV [6]. The concentration of the electron-hole pairs is proportional to the current density and the practical electron range (expression 1.1.2) of the primary electrons.

5.1.3.1 Reaction Sites.

The e-h pairs created in the material, either recombine via bulk or surface centres, or participate in the decomposition reaction. Bulk recombination processes occur within a grain or at grain boundaries and dislocations. This can be characterised by a lifetime τ_b. Surface recombination is characterised by either a surface recombination velocity S_r, or by a surface lifetime τ_s. At the onset

of decomposition (especially at "high" reaction rates), the probability of bulk recombination is small. This is due to the surface containing many more imperfections than the bulk. The results of Figures 5.2.3 and 5.2.4 reveals the presence of Pb balls at the surface. Therefore, radiolysis is dominated by free surface recombination process, and holes must be trapped at sites adjacent to a surface chlorine ion for chlorine evolution. The desorption of a chlorine atom or molecule, results in creation of anion vacancies. The anion vacancies diffuse either along the surface to special sites or into the bulk, to defect centres. Electrons are trapped at these defect centres (surface or bulk), where reaction with Pb^{2+} ions result in Pb precipitation accompanied by annihilation of the anion vacancies. The overall reaction is written as,

$$PbCl_2(s) \xrightarrow{\text{e-beam}} Pb(s) + Cl_2(g)\uparrow$$

5.1.3.2 Steady State Relation

At steady state, the concentration of the carriers is given by,

$$\frac{\partial n}{\partial t} = 0 = D\frac{\partial^2 n}{\partial x^2} - \frac{n}{\tau} + G \qquad \text{-----(5.1.1)}$$

where n is the carrier concentration in cm^{-3}, τ is composed of the bulk recombination time τ_b, and the surface recombination time, τ_s, which is given by the equation,

$$1/\tau = 1/\tau_b + 1/\tau_s$$

D ($=\mu kT/q$) is the diffusion constant in $cm^2 s^{-1}$, where μ is carrier mobility, k is Boltzmann's constant, T is absolute temperature, and q is electronic charge. G is the net carrier generating function, in $cm^{-3}s^{-1}$, and x is the distance into the film. The practical ranges of primary electrons, having 2keV energy, are 46nm and 23.8nm in $PbCl_2$ and Pb respectively. The film thicknesses do not differ much from the practical electron range, and the beam current which plays a more dominant role in the e-h pairs creation, is constant. Thus G can be assumed to be constant. The internal drift of carriers is neglected, by assuming that the carrier distribution for both electrons and holes are the same, with the same mobility and loss

rates. The boundary conditions for equation 5.1.1 under steady state irradiation are,

$$D\frac{\partial n}{\partial x}\Big|_{x=0} = S_r n_o$$

and $$\frac{\partial n}{\partial x}\Big|_{x=d} = 0$$

where n_o is the carrier concentration at the surface, and d is the film thickness. S_r is the surface recombination velocity, and is given by

$$S_r = \sigma\, v_{th}\, N_{st}$$

where,

σ is carrier capture cross-section

v_{th} is carrier thermal velocity

N_{st} is number of surface trapping centres per unit area.

The solution to equation 5.1.1 (see Appendix VI) is

$$n_o = \frac{G\tau}{1 + \frac{S_r L.\mathrm{Coth}(d/L)}{D}}$$

where $L = (D\tau)^{\frac{1}{2}}$, is the characteristic diffusion length. For small film thickness, $d \ll L$, therefore,

$$\frac{S_r L}{D}\mathrm{Coth}(d/L) \gg 1$$

and $$n_o = \frac{GL}{S_r}\tanh(d/L)$$

The net flux of carriers to the surface, Γ, expressed in $cm^{-2}s^{-1}$, is given by

$$\Gamma = S_r n_o = GL.\tanh(d/L) \qquad \text{------(5.1.2)}$$

For constant excitation, number of carriers generated per unit time per unit area within the film is Gd. Therefore, fraction of carriers lost at the surface is,

$$\Gamma/(Gd) = (L/d)\tanh(d/L)$$

Even in the case when d = L, $\Gamma/(Gd) = 0.76$ and recombination is

surface dominated. For d<<L (tanh(d/L)≈ d/L) $\Gamma \approx Gd$, and recombination is clearly surface dominated.

5.1.3.3 Decomposition Mechanisms

The following reaction sequence is proposed,

$$V_{Pb,s} + h^+ \rightleftharpoons V^+_{Pb,s} \qquad \text{----(A)}$$

$$V^+_{Pb,s} + e^- \rightleftharpoons V_{Pb,s} \qquad \text{----(AA)}$$

$$V^+_{Pb,s} + Cl^-_s \rightleftharpoons V_{Pb,s} + (Cl^\circ_s)_{adj} \qquad \text{----(B)}$$

$$(Cl^\circ_s)_{adj} \longrightarrow Cl^\circ_a\uparrow + V_{Cl,s} \qquad \text{----(C)}$$

$$Cl^\circ_a + Cl^\circ_a \longrightarrow Cl_2(g)\uparrow \qquad \text{----(D)}$$

$$V_{Cl,s} + Cl^-_{ss} \longrightarrow V_{Cl} + (Cl^-_{ss})_{adj} \qquad \text{----(E)}$$

$$V_{Cl,s} + Cl^-_{bulk} \longrightarrow V_{Cl} + (Cl^-_{bulk})_{adj} \qquad \text{----(F)}$$

$$V_{Cl} + e^- \longrightarrow V^-_{Cl} \qquad \text{----(G)}$$

$$V^-_{Cl} + e^- + Pb^{2+} \longrightarrow Pb \qquad \text{----(H)}$$

The lattice of $PbCl_2$ consists of Pb^{2+} ions and Cl^- ions.

$V_{Pb,s}$: surface Pb^{2+} vacancy
$V^+_{Pb,s}$: surface Pb^{2+} vacancy with trapped hole
Cl^-_s : chlorine surface ion, next to lead ion vacancy
$V_{Cl,s}$: surface Cl^- vacancy
Cl°_a : neutral chlorine ad-atom
Cl^-_{ss} : special site chlorine ion
$(Cl^-_{bulk})_{adj}$: bulk chlorine ion adjacent to anion vacancy
$(Cl^\circ_s)_{adj}$: surface chlorine ad-atom adjacent to Pb^{2+} vacancy
$(Cl^-_{ss})_{adj}$: special site chlorine ion adjacent to anion vacancy

Reaction A is the trapping of holes by cation vacancies which could lead to further reaction involving desorption of chlorine, or alternatively electron trapping for recombination of e-h pairs. Recombination of e-h pairs at a surface Pb^{2+} vacancy trapped hole, is a physical process represented by reaction AA, but is unlikely.

Chlorine ad-atoms adjacent to the cation vacancies are created via reactions A and B. Reaction C is the creation of free chlorine ad-atoms, which either desorbs or reacts with other chlorine ad-atoms to form chlorine molecules which desorb (reaction D). The desorption of chlorine atoms or molecules is accompanied by the formation of anion vacancies, this being reaction C. The diffusion of the anion vacancies and the subsequent reactions are described by one of the following:

(i) For "low" reaction rates, these anion vacancies in-diffuse into the bulk, resetting the chlorine ion sites at the surface for subsequent trapping of holes. The in-diffusion of the anion vacancies is represented by reaction F. In the bulk, electrons are trapped at defect centres (reaction G), and reactions with Pb ions produce lead atoms which aggregate together (reaction H). The aggregation of Pb atoms is accompanied by the annihilation of the anion vacancies.

(ii) For "high" reaction rates, the anion vacancies diffuse over the surface to special sites (defect centres) where electrons are trapped. The diffusion process and the trapping of electrons are represented by reactions E and G respectively. Eventually, electrons trapped at anion vacancies react with Pb ions, to produce Pb aggregates, accompanied by annihilation of the anion vacancies.

There is the possibilty of electrons being trapped at other types of defect centres created by bulk imperfections. But the essential thing is that, the anion vacancies generated at the surface must diffuse to defect centres, where reactions take place to produce Pb atoms, accompanied by annihilated $PbCl_2$ sites. As decomposition progresses, the net flux of carriers, Γ, to the surface decreases with the effective film thickness (as given in equation 5.1.2). This then results in a decrease in the rate of decomposition. Secondly, the change in composition of the material from pure $PbCl_2$ to Pb-$PbCl_2$ matrix, with the lead content increasing all the time, is to cause a decrease in the rate of decomposition with increasing exposure time.

This is probably due to the diffusion length of the carriers decreasing with the growth of lead particles. So that carriers generated at distances greater than a diffusion length from the surface will be lost, and the efficiency of electrochemical reaction will be low. Put in another way, the appearance of Pb particles at the surface will result in a film dominated by bulk defect centres, and the carrier lifetime τ, is essentially τ_b.

The reaction sequence described above for "low" and "high" reaction rates are similar to those of PbI_2 [2,3] and $CdCl_2$ [1] respectively. This is because the reaction rate curves for "low" and "high" reaction rates are of similar form to those of PbI_2 [2,3] and $CdCl_2$ [1] respectively. In the case of PbI_2 decomposition, charge carriers (holes and electrons) were created by photo absorption in the sample. The holes diffuse to the surface where they react with the iodine ions adjacent to cation vacancies, thereby leading to the eventual desorption of iodine atoms or molecules. The desorption process then resulted in the in-diffusion of the surface generated excesses of anion vacancies. Electrons trapped by bulk anion vacancies react with Pb ions producing Pb atoms. The rate determining step is the in-diffusion of the anion vacancies. An activation energy of 0.45eV was obtained, and associated with the in-diffusion mechanism. The mechanism of $CdCl_2$ [1] was based on having the reaction products, Cd and Cl, being volatile. Electron-hole pairs are generated within the $CdCl_2$ film, and these carriers diffuse to the surface. Holes are trapped at special chlorine ion sites, which results in either electron-hole pair recombination or the desorption of chlorine atoms or molecules. The activation energy of 0.2eV was associated with the rate determining step, being the chlorine atoms leaving the surface crystal sites. The cadmium ions associated with the chlorine at the special sites react with electrons, resulting in the desorption of cadmium atoms.

With respect to PbI_2 and $CdCl_2$ decomposition mechanisms, the rate determining steps for the "low" and "high" reaction rates are the in-diffusion of surface generated anion vacancies and the discharge of chlorine atoms respectively.

5.1.3.4 Effect of Extent of Reaction on Radiolysis Rate

As chlorine is evolved from the sample, the composition of the material is continually changing. This makes it difficult to provide a detailed model of the on-going processes. But to a first approximation, the anion vacancy concentration for "high" reaction rate can be related to the extent of decomposition by the equation [8],

$$[V_{Cl,s}]_q = KI\{1-bexp((q-Q_o)/Q^*)\} \qquad \text{-------(5.1.3)}$$

where Q_o is Cl particles/cm^2 present in the film before irradiation, Q* is a constant, which is inversely proportional to the initial rate of increase in the density of anion vacancy. q is the Cl particles/cm^2 at any instant of time. I is beam intensity, which is related to the carrier generating function, G. K is proportional to the reaction rate constant and the initial concentration of anion vacancy. b is related to the factor by which initial density of vacancies increases over the full course of the decomposition. The change in material composition is to initially result in an increase to a limiting value KI, of the anion vacancies concentration (equation 5.1.3), with a resultant increase in the rate of decomposition. The chemical rate of reaction (derived from reactions B and C) is given by,

$$R_C = K_F[Cl_S^-].[V_{Cl,s}] \qquad \text{------(5.1.4)}$$

K_F is the reaction constant. But

$$[Cl_S^-] \equiv q \qquad \text{-------(5.1.5)}$$

Combining equations 5.1.3, 5.1.4 and 5.1.5,

$$R_c = K_c q\{1 - b.\exp((q-Q_o)/Q^*)\} \qquad ----(5.1.6)$$

$K_c=K_F K K_q I$, where K_q is the constant of proportionality of equation 5.1.5. But

$$R_c \equiv dCl/dt \equiv dq/dt,$$

Therefore,

$$dq/dt = K'K_c q\{1 - b.\exp((q-Q_o)/Q^*)\} \qquad ----(5.1.7)$$

K' is a constant introduced from equation 5.1.7. Representing $K'K_c$ by K" , equation 5.1.7 becomes,

$$dq/dt = K"q\{1 - b.\exp((q-Q_o)/Q^*)\} \qquad ----(5.1.8)$$

Equation 5.1.8 describes the rate of decrease of the chlorine present in the film, this being equivalent to the rate of loss of film thickness. Figure 5.1.13 shows the rates of loss of material (in the form of chlorine signal) versus chlorine signal present in the film, as a function of sample temperature. The model described by equation 5.1.8 closely fits the curves of 180°C and 220°C, both being "high" reaction rates. The deviation between the theoretical model and experimental data is due to error in K" , b, and Q* measurements. The influence of temperature on both the anion vacancies population $[V_{Cl,s}]$ and the activated rates of the reactions is reflected in all the three parameters K", b, and Q* of the model of equation 5.1.8. For decomposition at 220°C, an average value of b of 0.6 indicates roughly a two-fold increase in the anion vacancies over its initial value for a non-irradiated sample.

For "low" reaction rates, the chemical rate of reactions follows an exponential decay (Figure 5.1.9a). It is proposed that equation 5.1.8, without the build-up term (K"q(1-b) to maximum value K"q), can possibly be used to describe the chemical rate of reactions.

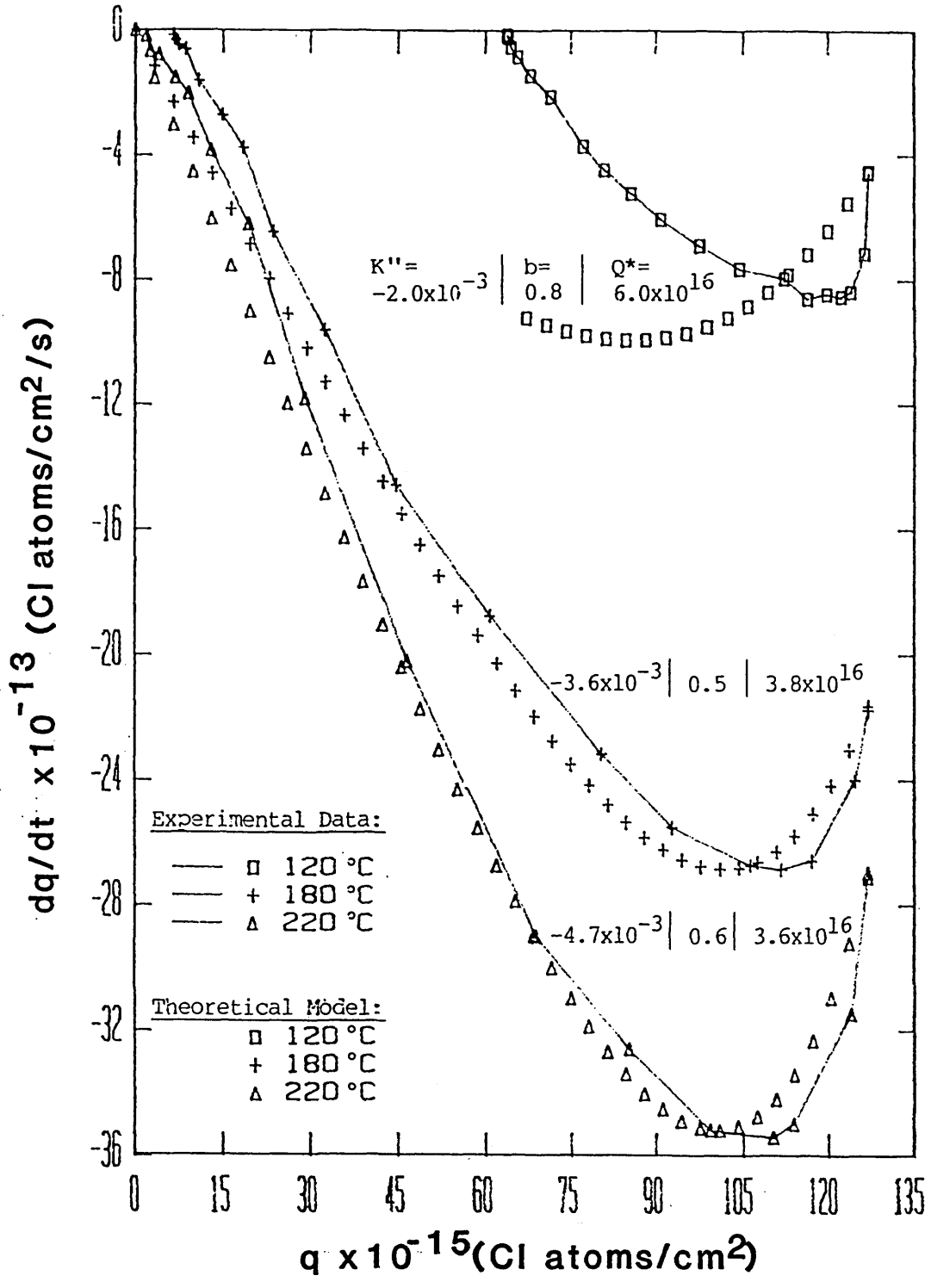


Figure 5.1.13: Correlation of experimental data with the theoretical model, described by equation 5.1.8. K'' is in s^{-1}, Q* is in Cl atoms cm^{-2}, and b is dimensionless.

Experimental Conditions:

$PbCl_2$ film (50nm thick) on Al/glass substrate

Beam energy = 2keV

Current density = 32μA cm^{-2}

5.1.3.5 Effect of doping $PbCl_2$ with $CdCl_2$

The decomposition kinetics of $PbCl_2/CdCl_2$(20%) (results presented in Figures 5.1.2 and 5.1.9(b)) are similar to that of $PbCl_2$ at temperatures above 120°C; which is of "high" decomposition reaction rate. The only difference is that, unlike in the latter where the peaks of the rate curves are independent of exposure time, the former exhibit a time dependence characteristic (see Figures 5.1.4(a) and 5.1.10(b)). The partial loss of Cd atoms from decomposed $PbCl_2/CdCl_2$(20%) film (see Figure 5.2.7), is due to the absence of an adjacent Pb atom (to which it might bond). This occurs during the first stage of decomposition, that is the period of increase in decomposition rate, see Figure 5.1.4(b).

The effect of extent of reaction on radiolysis rate can be described by the model of equation 5.1.8. Curves similar to those in Figure 5.1.13 (decomposition of $PbCl_2$ at "high" reaction rates) can be drawn to compare experimental data with the theoretical model. The experimental data and the theoretical models are expected to be closely fitted if K" (hence b and Q* values) values can be estimated accurately. Such accuracy can only be expected when K" values are calculated from the reaction curves after extensive decomposition, probably of more than 70%. The extent of reactions for $PbCl_2/CdCl_2$(20%) decomposition are not adequate enough to give reasonably accurate estimations of K" , b, and Q*. Therefore, poor graphical fit will not necessarily suggest that the model does not apply.

5.2 LITHOGRAPHY

5.2.1 RESULTS

Electron micrographs of deposited $PbCl_2$ and $PbCl_2/CdCl_2$(20%) films are presented in Figures 5.2.1a &b, with their respective electron probe micro analysis (EPMA) data given in Figures 5.2.2a &b. A brief account of EPMA data acquisition is given in Appendix V. The atomic doping of $CdCl_2$ in $PbCl_2/CdCl_2$(20%) solid solution film was found to be 20% within a few percent error.

Films of $PbCl_2$ and $PbCl_2/CdCl_2$(20%) separately deposited on oxidised silicon wafer (ca. 100nm oxide thickness) were e-beam irradiated. The irradiation was carried out at sample temperature in the range of 120-180^{o}C. The e-beam diameter was 300μm, and the beam energy was 2keV. The current density was approximately 30μA cm^{-2}. Effects of temperature and electron dose on the morphology of e-beam decomposed $PbCl_2$ and $PbCl_2/CdCl_2$(20%) films are presented in Figures 5.2.3 and 5.2.4 respectively. By increasing the electron dose from 42mC/cm^2 to 290mC/cm^2, the composition of irradiated area of $PbCl_2$ films changed considerably from one having a low concentration of Pb in Pb-$PbCl_2$ matrix to one of predominantly Pb clusters. Similarly, for the $PbCl_2/CdCl_2$(20%) sample, increasing the substrate temperature from 120^{o}C to 180^{o}C, and using an electron dose of 150mC/cm^2, produced a change from low concentration of Pb-Cd alloy in Pb-Cd - $PbCl_2/CdCl_2$(20%) matrix to one of predominantly Pb-Cd alloy. The mean grain size (m.g.s) of the resulting metallic films (reported in Figures 5.2.3 and 5.2.4) show that the grain size increases with temperature of irradiation. Smaller grains are produced in Pb-Cd films compared to that in Pb. Also the Pb films were not continuous, whereas Pb-Cd films were continuous. The extent of decomposition was found to increase with temperature, as reported in section 5.1.1. With increase in irradition temperature, the resolution of any pattern to be written will decrease because of the increasing metallic grain size. Therefore to have good resolution and acceptable level of decomposition (sensitivity), a temperature of 135^{o}C was found to be close to the optimum for further experimentation.

$PbCl_2$ and $PbCl_2/CdCl_2$(20%) typically of about 120nm film thicknesses were uniformly e-beam irradiated over an area of $4x4mm^2$. The electron dose applied was $150mC/cm^2$. These experimental conditions are similar to those whose kinetics are reported in section 5.1. Irradiation was followed by developing the samples in a solution of ammonium chloride (16g of NH_4Cl salt per $100cm^3$ of deionised water at 25^oC), for a period of a minute. The developer was flooded out, using deionised water, to stop the developing process. [The NH_4Cl salt was obtained from Hopkins and Williams (U.K) Ltd, and has a purity of not less than 99.5%]. Figs. 5.2.5a &b are the eventual results obtained from $PbCl_2$ and $PbCl_2/CdCl_2$(20%) samples respectively. Decomposition of $PbCl_2$ resulted in Pb-$PbCl_2$ matrix (as explained previously) and the oxidised silicon substrate was found to be visible after development in NH_4Cl solution. On the other hand, $PbCl_2/CdCl_2$(20%) sample produced continuous film of essentially Pb-Cd. These observations are in accord with earlier results reported in this section. EPMA data for the three stages of the lithography (namely, the film deposition, the e-beam exposure, and the development stages) are presented in Figures 5.2.6 and 5.2.7 for $PbCl_2$ and $PbCl_2/CdCl_2$(20%) samples respectively.

Further lithography work was carried out, using two types of contact masking. The first masking was done by using a copper wire mesh shown in Figures 5.2.8a &b. The copper mesh masking was used in determining how accurately patterns can be transferred onto both sets of samples. The defined patterns were found to be precise within the grain size, and the results shown in Figures 5.2.9 and 5.2.10 for $PbCl_2$ and $PbCl_2/CdCl_2$(20%) samples respectively. The second masking was by the use of a rectangular metal (Ni) sheet for edge resolution determination. The edge resolution results are presented in Figures 5.2.11a &b. The edge resolutions obtained, by using about 200nm thick films of $PbCl_2$ and $PbCl_2/CdCl_2$(20%), are 0.29μm and 0.18μm respectively.

From the lithography results presented so far, non-continuous Pb film patterns are produced from $PbCl_2$ films. This is highly unsuitable for use as the absorber layer of an x-ray masks. Therefore,

further lithography work was limited to $PbCl_2/CdCl_2$(20%) samples, which has produced good results.

A fine e-beam of about 0.5-1.0μm diameter in a scanning micro Auger system was used to expose a set of lines over a rectangular region (600μm long by 250μm wide) in $PbCl_2/CdCl_2$(20%) film. The rectangle contained 18 lines. The electron beam energy was 10keV, and the beam current was 5nA. Scan time of 3000s (~167s/line, for a typical 2x600μm^2 line dimension) was employed for all experimentation, resulting in line dose of ~14μA/cm. The sample temperature during e-beam irradiation was ~135^oC. Irradiated samples were further treated in three different ways, vis-a-vis:-

(i) The irradiated sample was developed in NH_4Cl solution to produce continuous Pb-Cd lines, which are broken in some places and overlap each other (see Figure 5.2.12a). Detailed examination of the Pb-Cd lines revealed ribbon-like structures, which have rolled-up in various places (Figures 5.2.12b &c). The width of the Pb-Cd ribbon-like lines produced was found to be about 2.4μm, which rolled-up to a minimum width of approximately 0.8μm.

(ii) The irradiated sample was oxidised in an oxygen plasma in a reactive-ion-etcher (see chapter 3 for detailed description of the system). Oxidation was carried out with oxygen gas at a flow rate of 10sccm and, power density of 0.4W cm^{-2}. The substrate temperature during oxidation was maintained at 80^oC and, the chamber pressure was approximately 100mtorr. Oxidation time was 10minutes. The oxidation process was then followed by development in NH_4Cl solution. The results obtained are shown in Figures 5.2.13a-c. The oxidised Pb-Cd lines produced were found to be continuous and unbroken. The lines adhered properly onto the substrate. The linewidth is about 1.3μm.

(iii) The irradiated sample was oxidised as described in (ii) above. This was followed by re-evaporation at a temperature of about 250^{o}C for 40minutes. The result obtained is presented in Figures 5.2.14a &b. The linewidth of the oxidised Pb-Cd is about 3μm. Residues of $PbCl_2/CdCl_2$(20%) were observed in areas where re-evaporation has taken place. This resulted in poorly resolved lines.

The variation in the linewidths of the three different types of treat-ment reported above, stem mainly from inconsistent electron beam diameter used.

Figure 5.2.1:

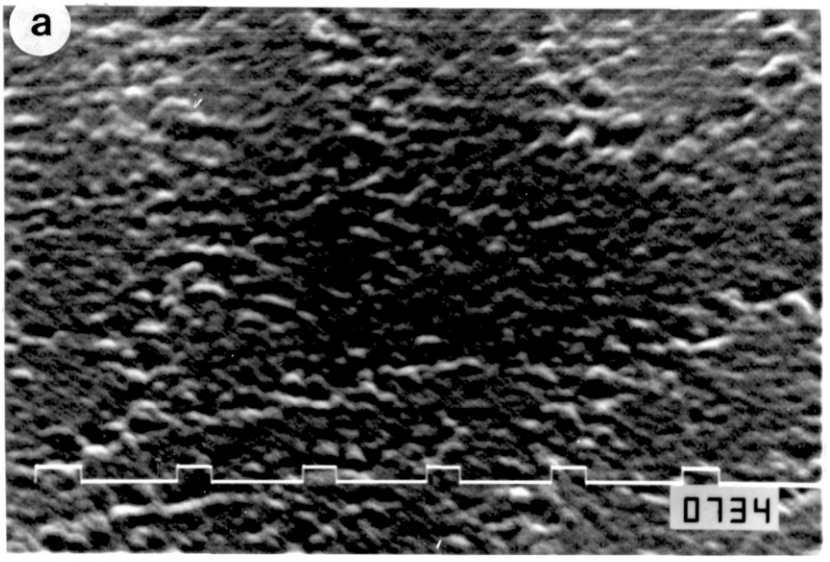
Electron micrographs of vacuum evaporated films

(a) $PbCl_2$ film

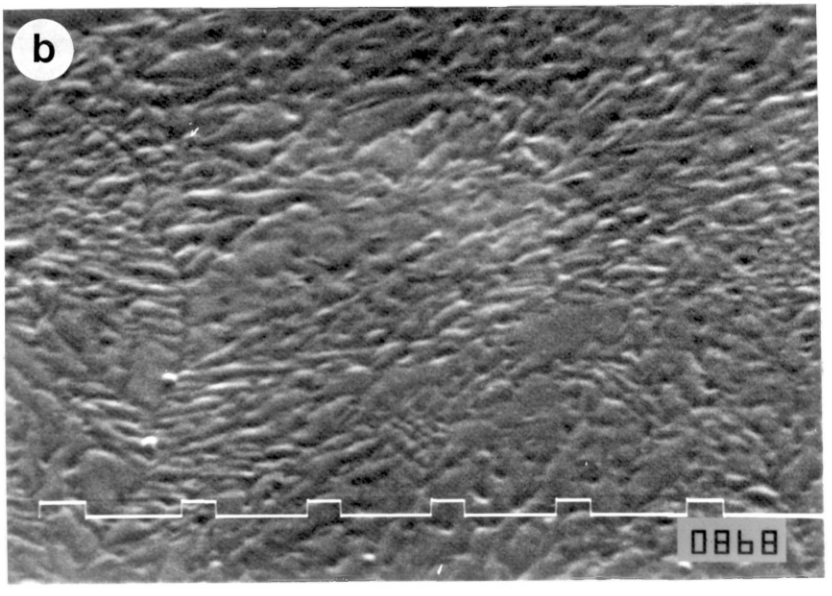
(b) $PbCl_2/CdCl_2$(20%) film

Evaporation Conditions

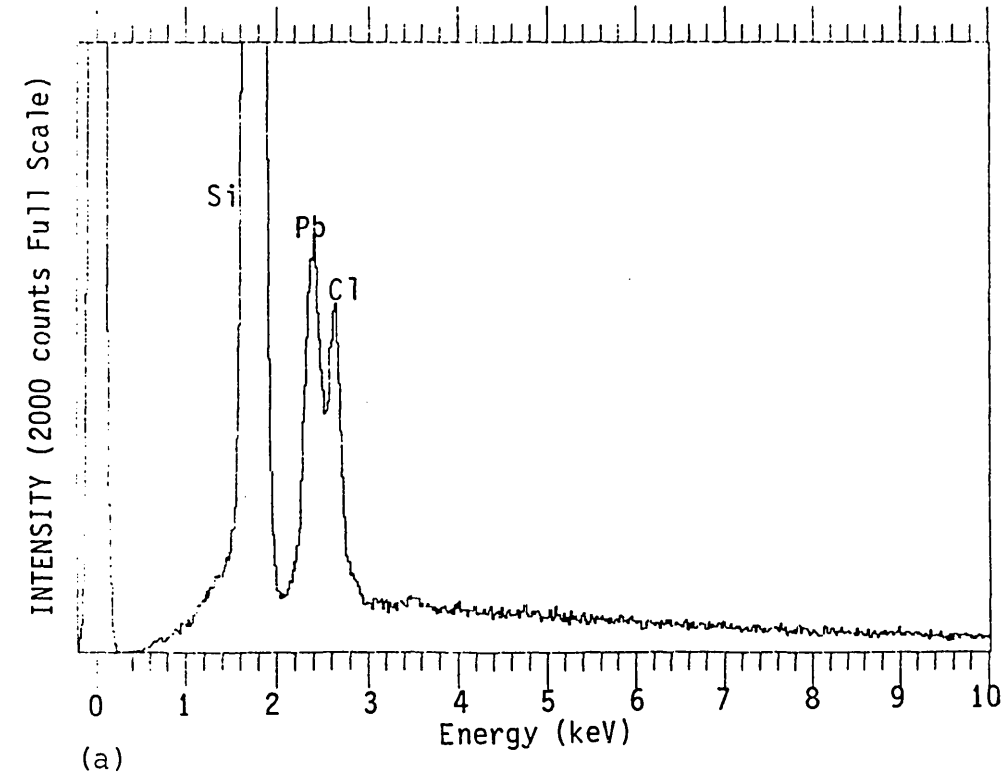
Film thickness = 120nm
Deposition rate = 3nm/s
Source Temperature = 350°C
Substrate Temperature = 25°C



1.0μm



1.0μm



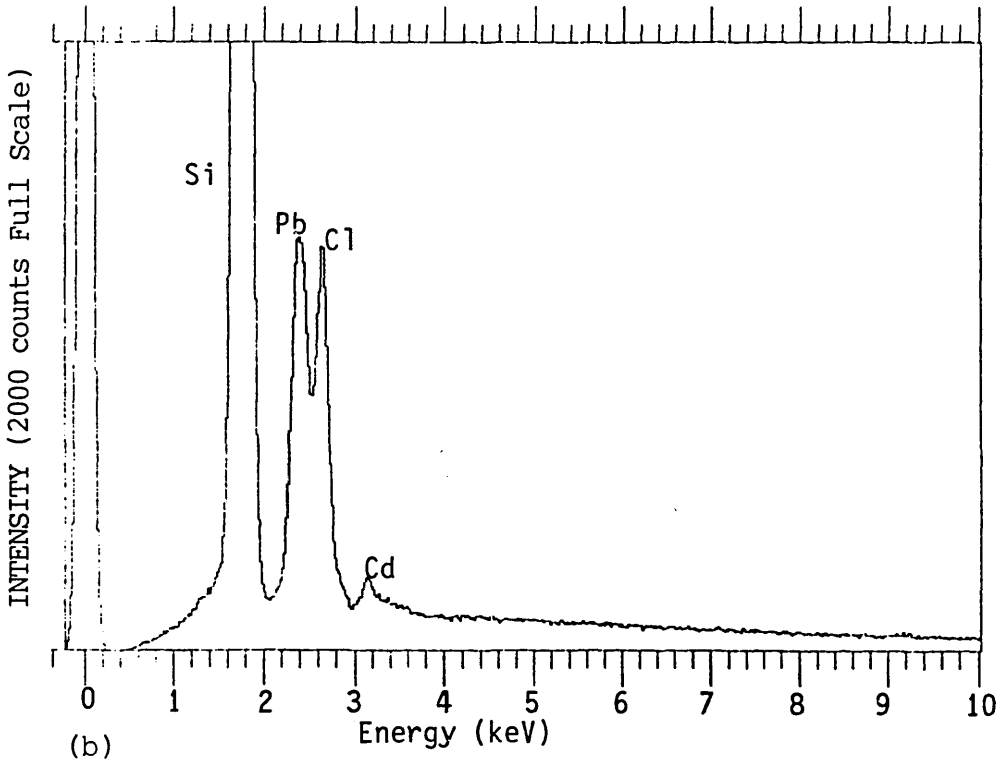


Figure 5.2.2: EPMA spectra of deposited films

(a) $PbCl_2$ film

(b) $PbCl_2/CdCl_2$(20%) film

Figure 5.2.3:

Micrographs of different extents of decomposition of $PbCl_2$ at various temperatures. Starting film thickness = 90nm

Beam Parameters:
Energy = 2keV
Current density = 140μA cm^{-2}

(a) 30% decomposition
Temperature = 120°C
Electron dose = 42mC cm^{-2}

(b) 70% decomposition
Temperature = 120°C
Electron dose = 290mC cm^{-2}
Mean grain size = 120nm

(c) 40% decomposition
Temperature = 150°C
Electron dose =42mC cm^{-2}

(d) 95% decomposition
Temperature = 150°C
Electron dose = 290mC cm^{-2}
Mean grain size = 140nm

(e) 52% decomposition
Temperature = 180°C
Electron dose = 42mC cm^{-2}

(f) 100% decomposition
Temperature = 180°C
Electron dose = 290mC cm^{-2}
Mean grain size = 180nm

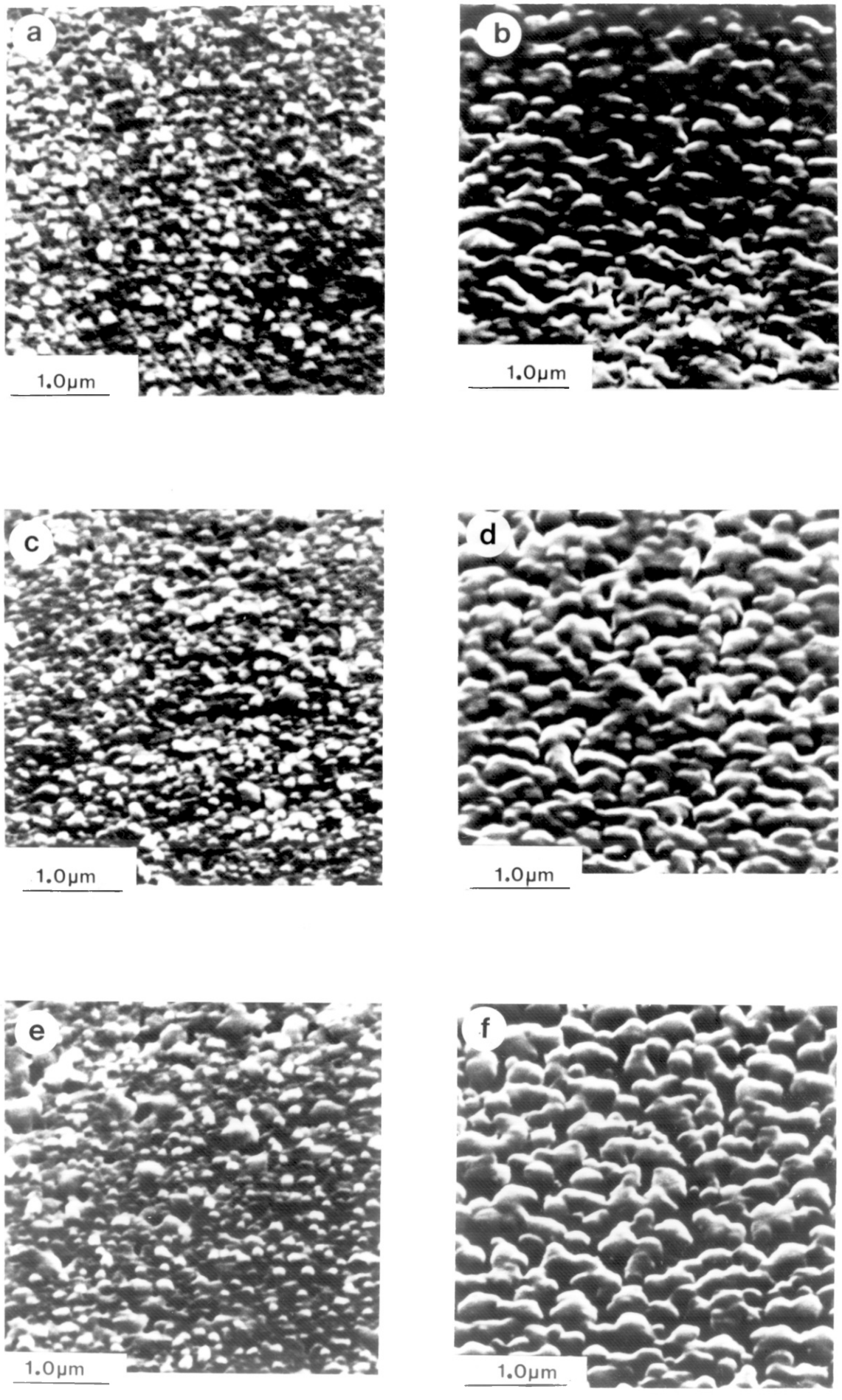

a
1.0μm
b
1.0μm
c
1.0μm
d
1.0μm
e
1.0μm
f
1.0μm

Figure 5.2.4:

Electron micrographs of different extents of decomposition of $PbCl_2/CdCl_2$(20%) film. Starting film thickness = 80nm.

Beam Parameters:

Energy = 2keV

Current density = 70μA cm^{-2}

(a) 7% decomposition

Temperature = 120°C

Electron dose = 20mC cm^{-2}

(b) 30% decomposition

Temperature = 120°C

Electron dose = 150mC cm^{-2}

Mean grain size = 40nm

(c) 40% decomposition

Temperature = 180°C

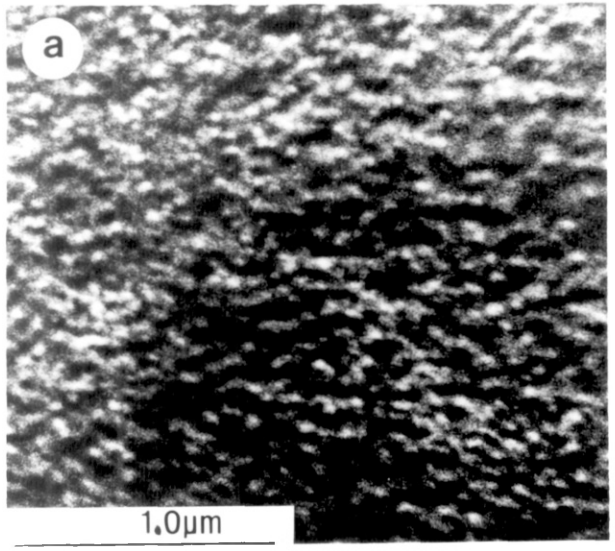
Electron dose = 20mC cm^{-2}

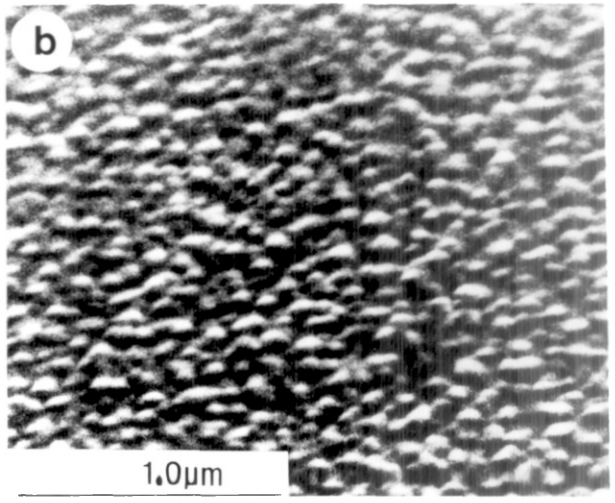
(d) 70% decomposition

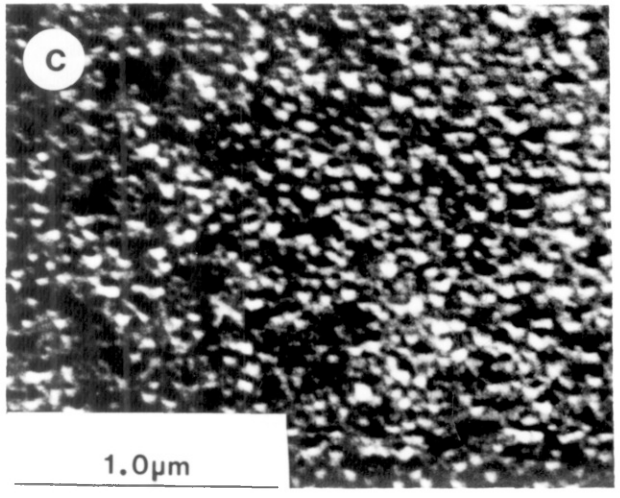
Temperature = 180°C

Electron dose = 150mC cm^{-2}

Mean grain size = 50nm


a
1.0μm


b
1.0μm


c
1.0μm

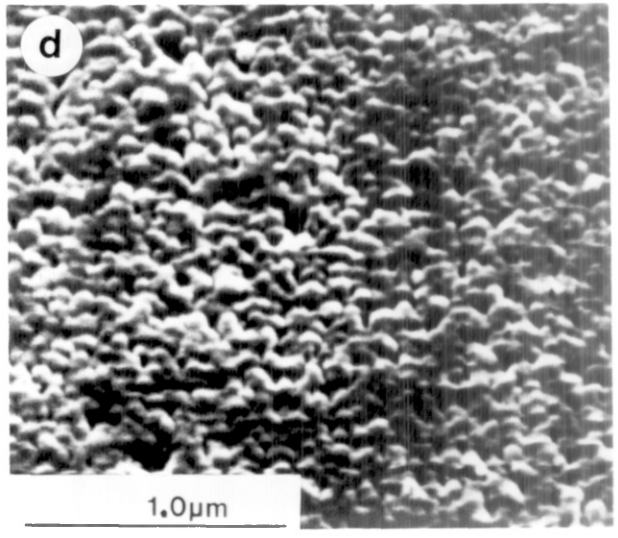

d
1.0μm

Figure 5.2.5:

Micrographs of $PbCl_2$ and $PbCl_2/CdCl_2$(20%) samples, after completing the three stages of lithography. Starting film thickness = 120nm

Irradiation Conditions:

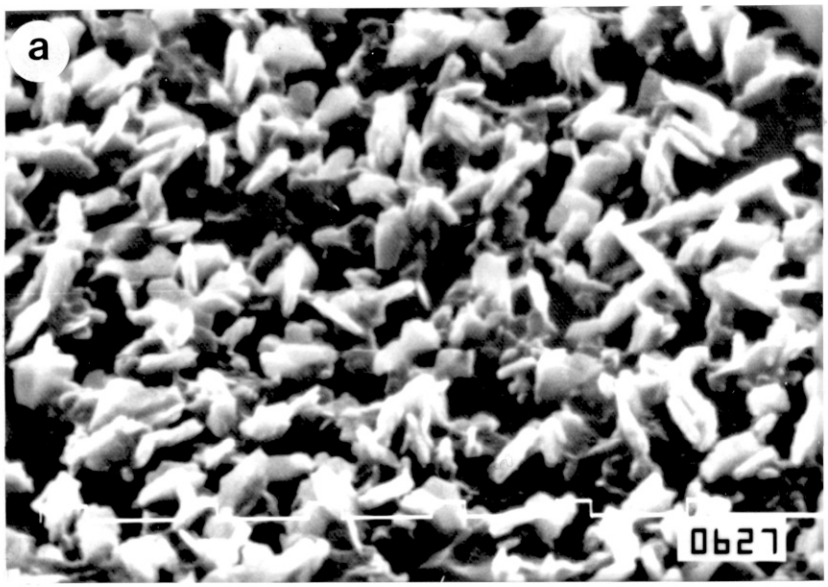
Beam energy = 2keV

Electron dose = $0.15C/cm^2$

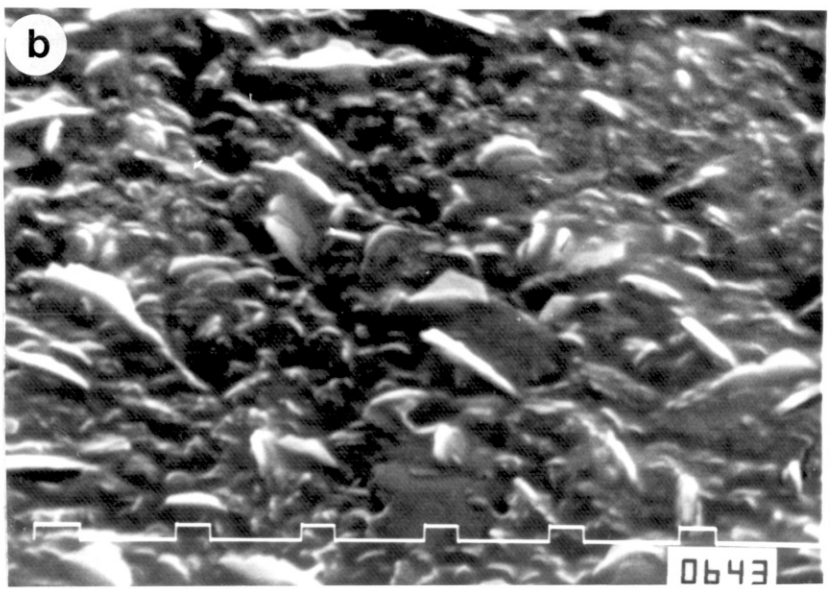
Temperature = 135°C

(a) $PbCl_2$ sample, showing non-continuous Pb film.

(b) $PbCl_2/CdCl_2$(20%) sample, showing continuous Pb-Cd film.



1.0μm



1.0μm

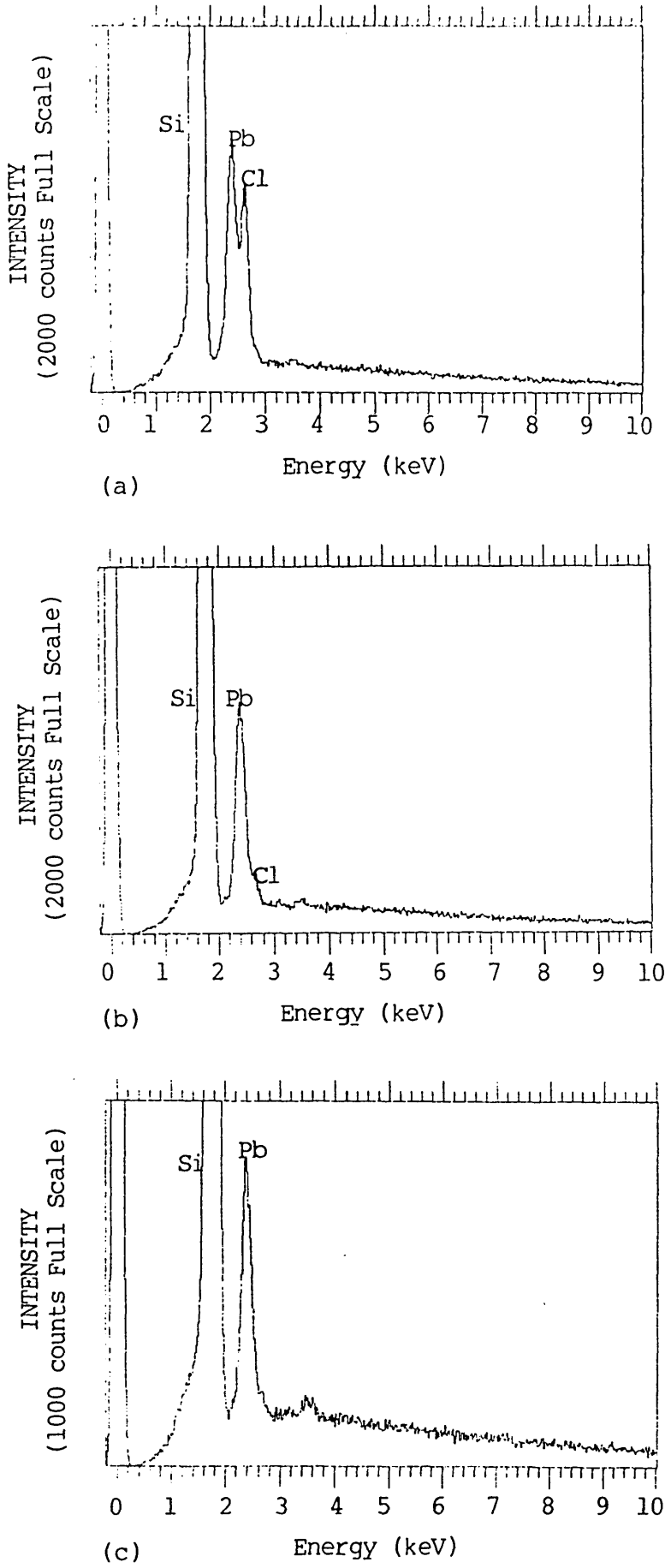
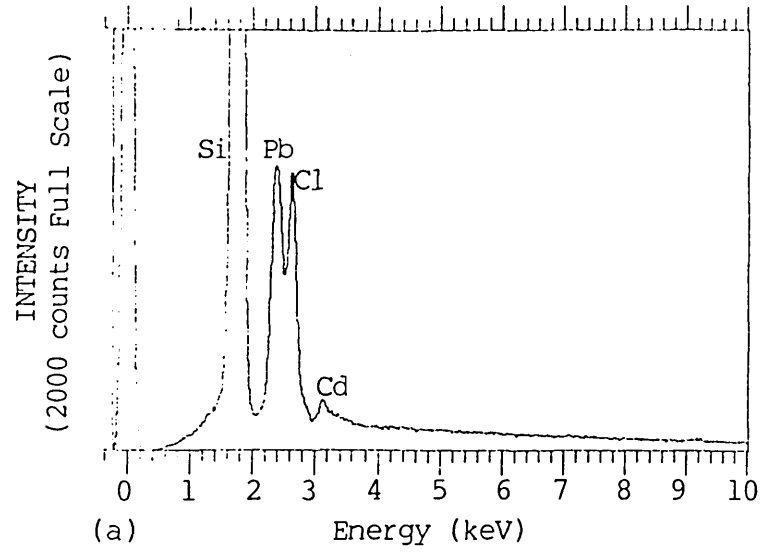
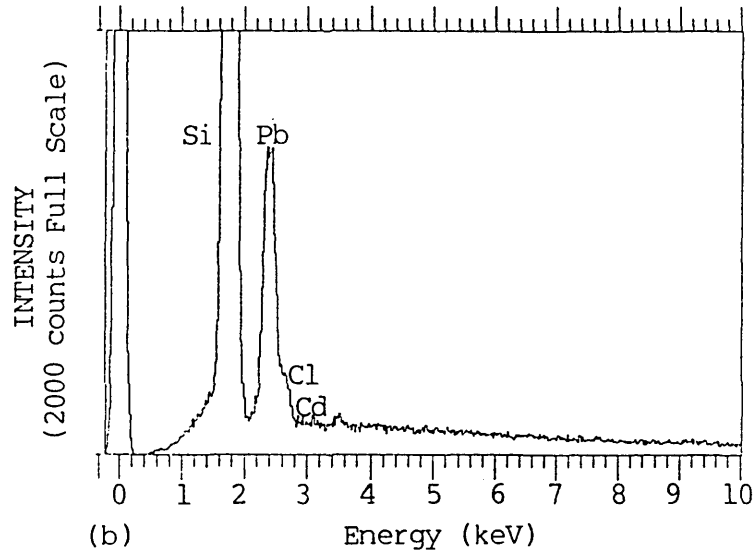


Figure 5.2.6: EPMA spectra of the lithography steps for $PbCl_2$

(a) Deposited film
(b) After e-beam exposure
(c) After development in NH_4Cl solution





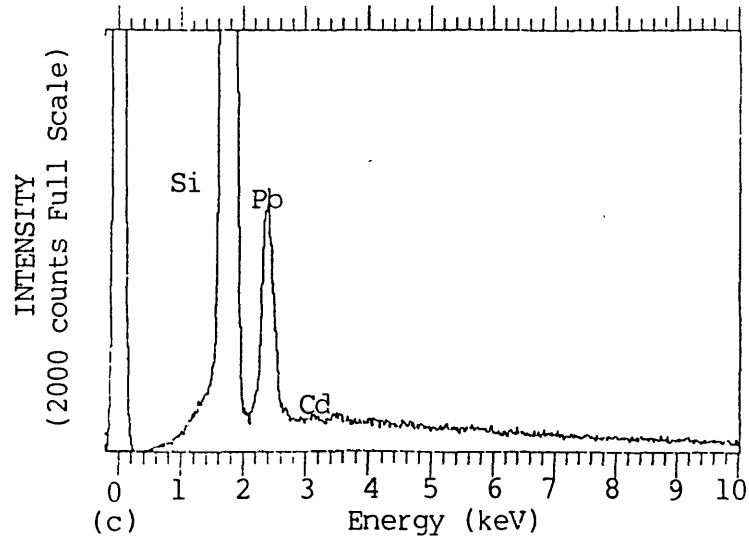
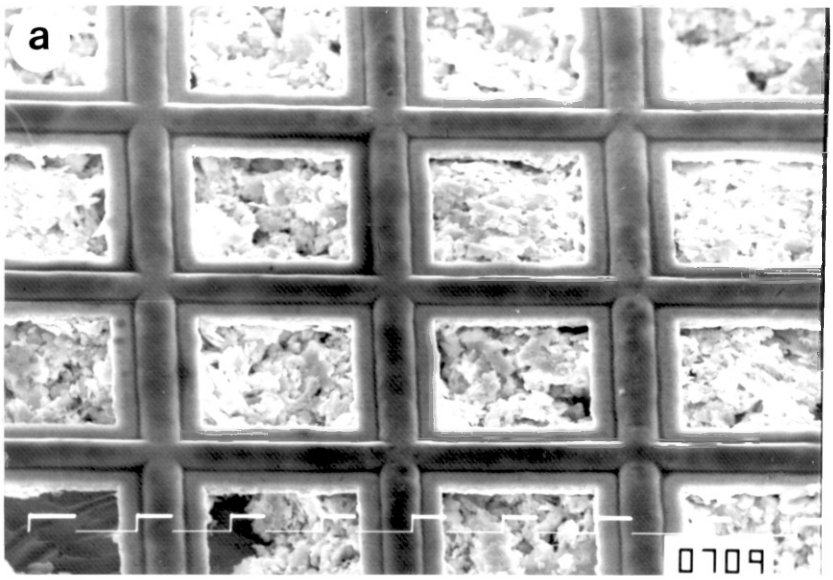


Figure 5.2.7 : EPMA spectra of the lithography steps for $PbCl_2/CdCl_2$(20%)

(a) Deposited film
(b) After e-beam exposure
(c) After development in NH_4Cl solution



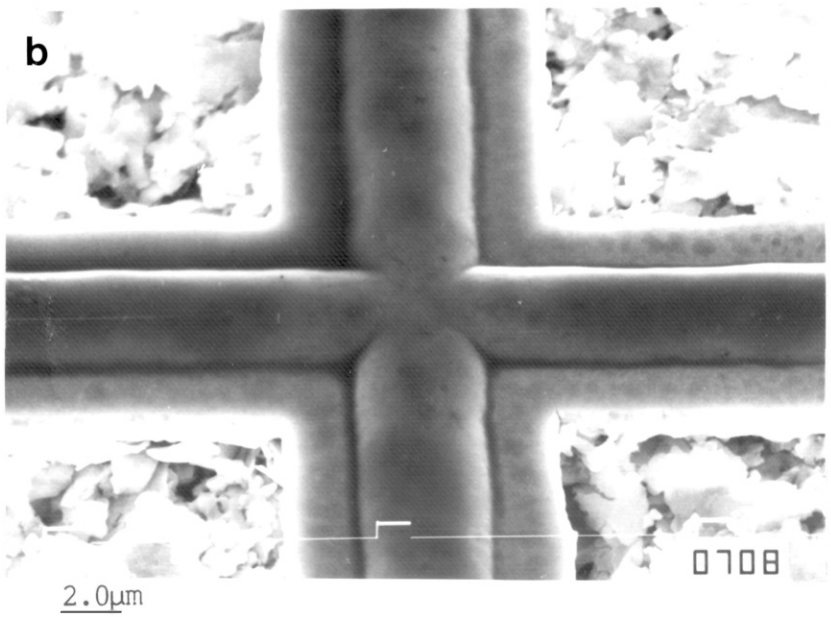


Figure 5.2.8a &b: Micrographs of copper wire mesh, showing white specks of silver paint.

Figure 5.2.9 a & b:

Reproduced Cu-mesh pattern in Pb film. Areas of big grains consist of Pb balls, and the darker area, with smaller grains, is due to incomplete development of $PbCl_2$ in NH_4Cl solution.

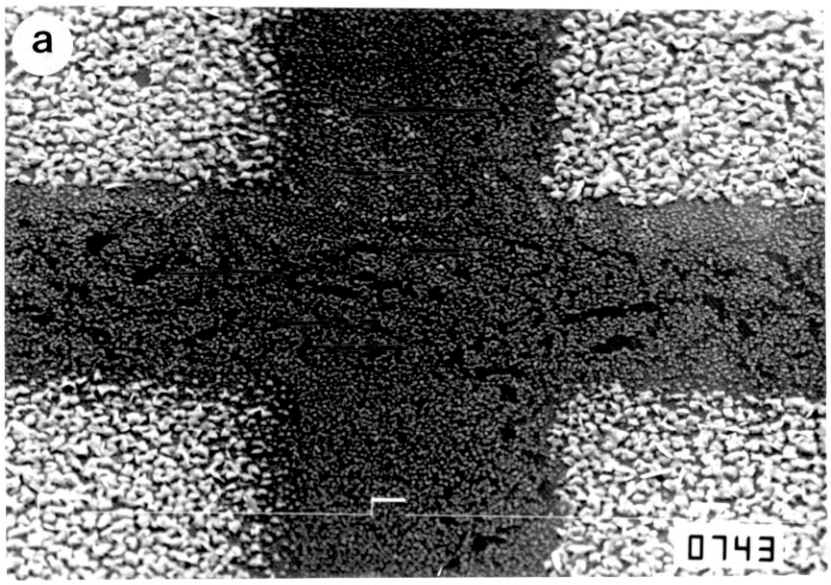
Irradiation Conditions:

Beam energy = 2keV

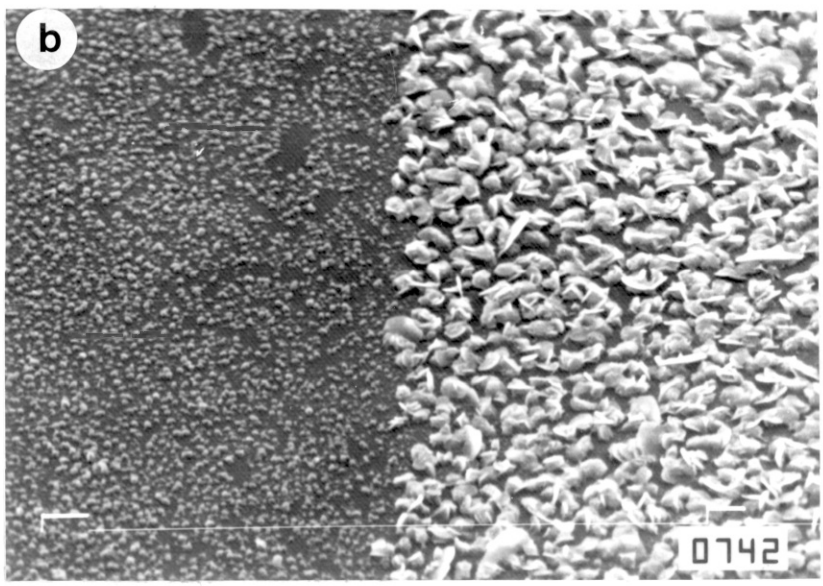
Electron dose = $0.2C/cm^2$

Temperature = 135°C

Starting film thickness = 200nm



2.0μm



1.0μm

Figure 5.2.10 a & b:

Reproduced Cu-mesh pattern in Pb-Cd film. The white and grainy areas are composed of Pb-Cd, and the smooth surface, the oxidised silicon wafer.

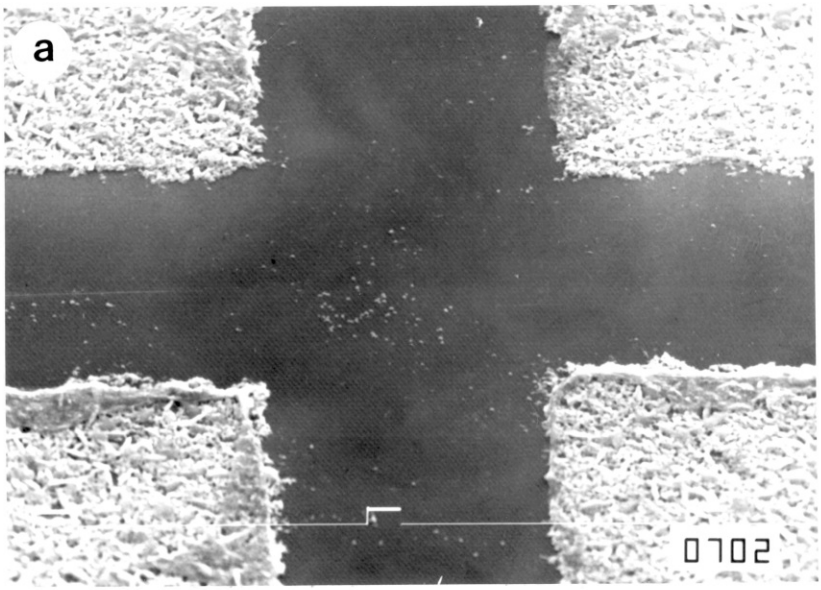
Irradiation Conditions:

Beam energy = 2keV

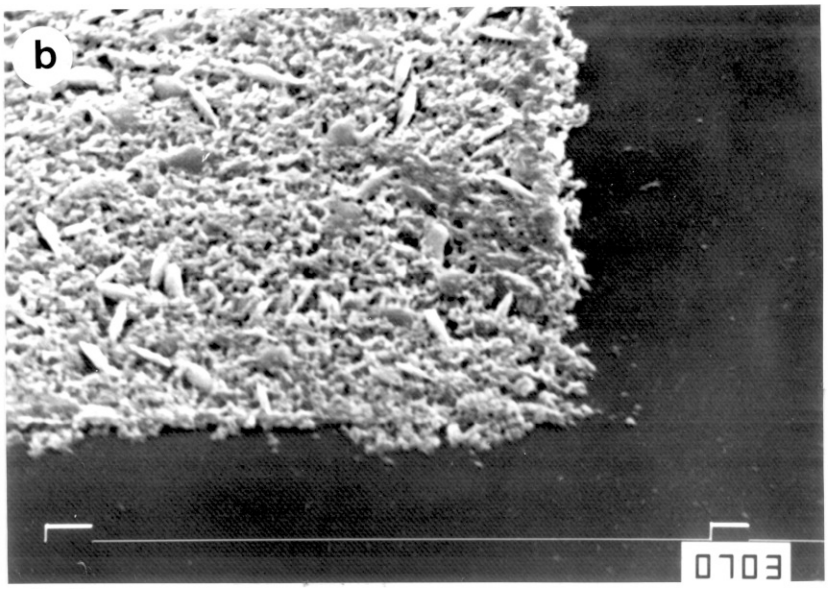
Electron dose = $0.2C/cm^2$

Temperature = 135°C

Starting film thickness = 200nm



2.0μm



1.0μm

Figure 5.2.11:

Edge resolution patterns

(a) Pb-SiO_2 interface
Edge resolution = 0.29μm

(b) Pb-Cd - SiO_2 interface
Edge resolution = 0.18μm

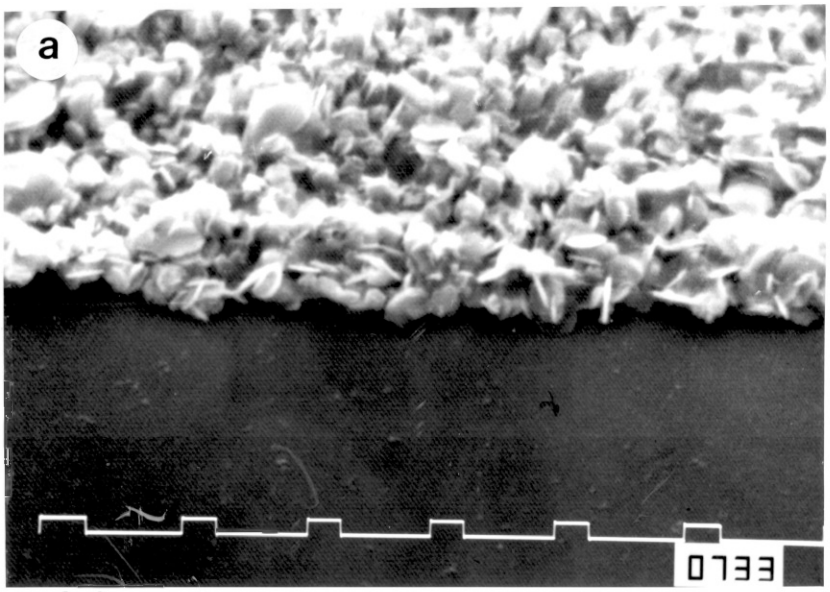
Irradiation Conditions:

Beam energy = 2keV

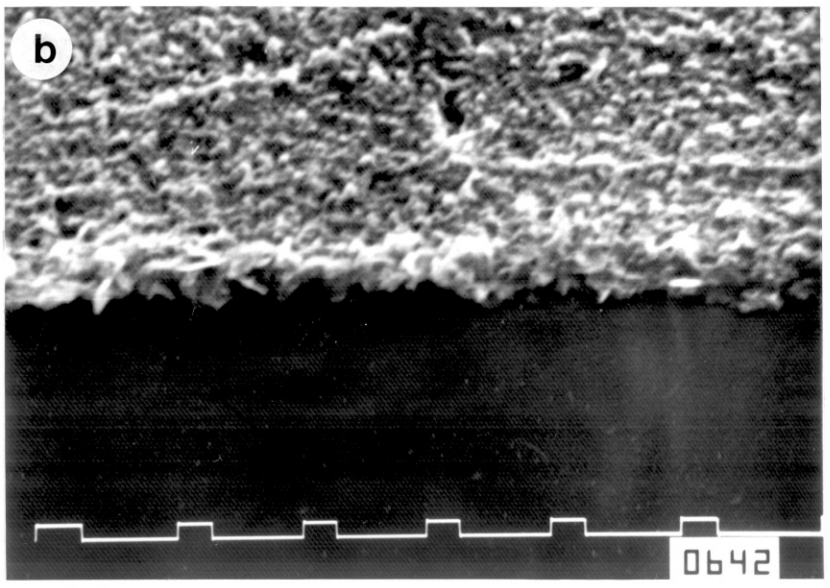
Electron dose = $0.2C/cm^2$

Temperature = 135°C

Starting film thickness = 200nm



1.0μm



1.0μm

Figure 5.2.12 a-c:

Patterned Pb-Cd on oxidised silicon substrate

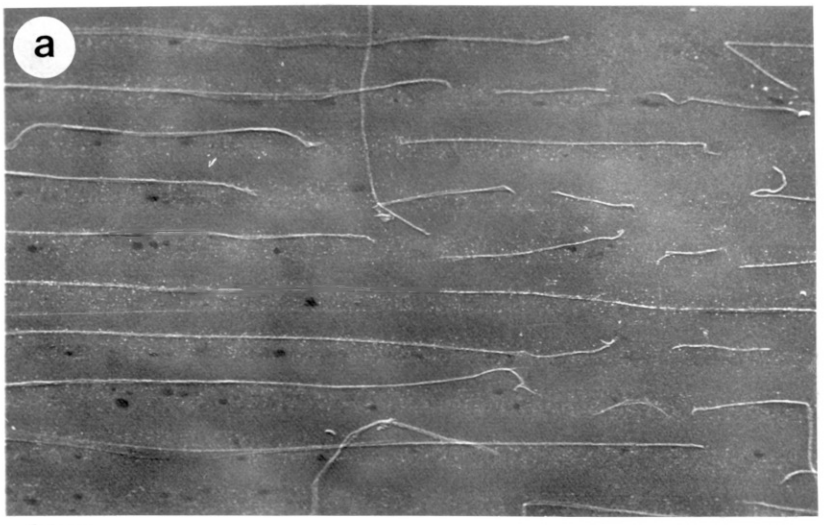
Irradiation Conditions:

Beam energy = 10keV

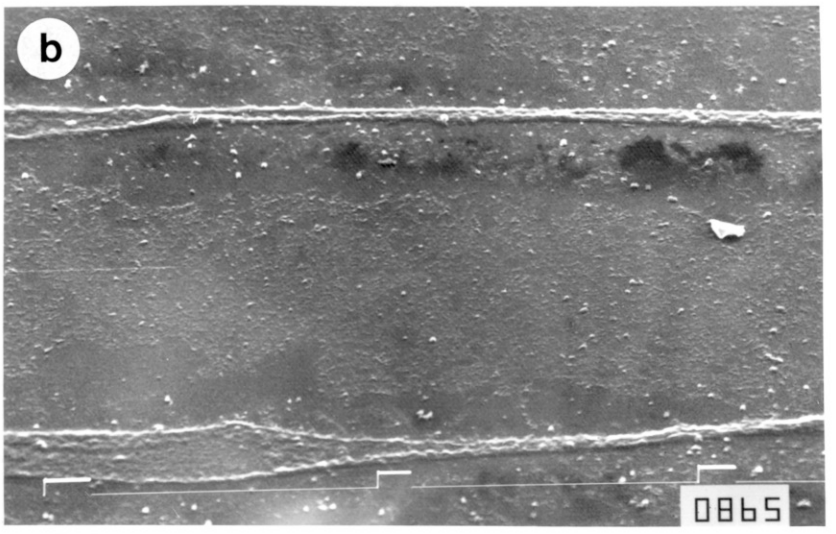
Input line dose = 14μC/cm

Temperature = 135°C

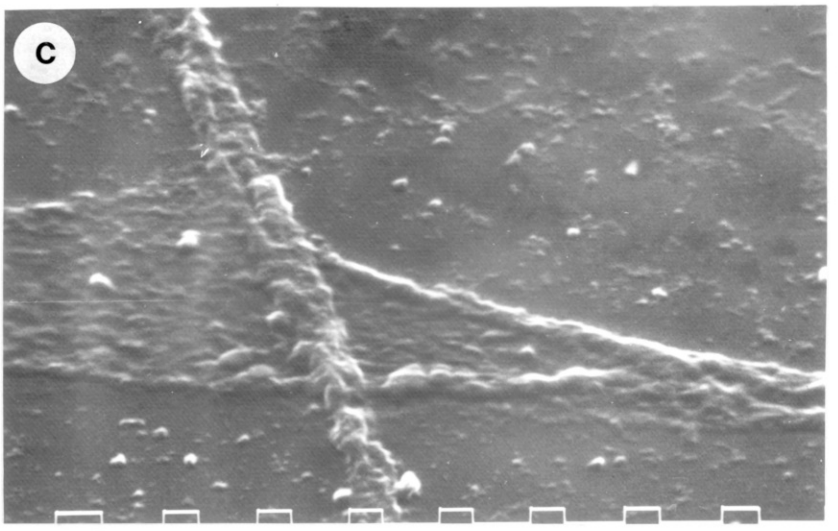
Starting film thickness = 130nm



10μm



2.0μm



1.0μm

Figure 5.2.13 a-c:

Patterned oxidised Pb-Cd on silicon substrate.

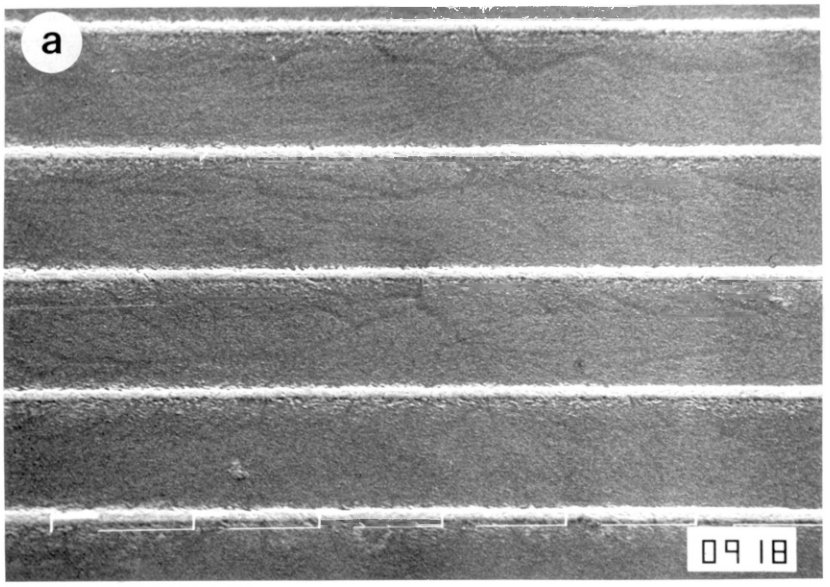
Irradiation Conditions:

Beam energy = 10keV

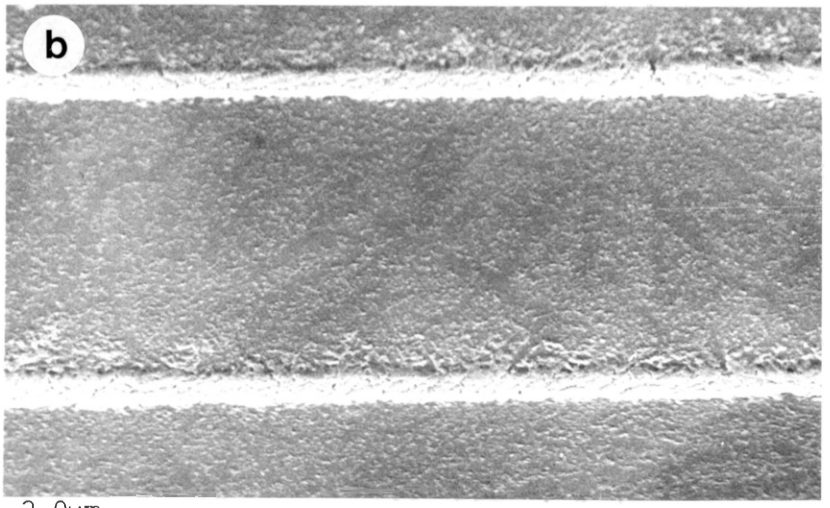
Input line dose = 14μC/cm

Temperature = 135°C

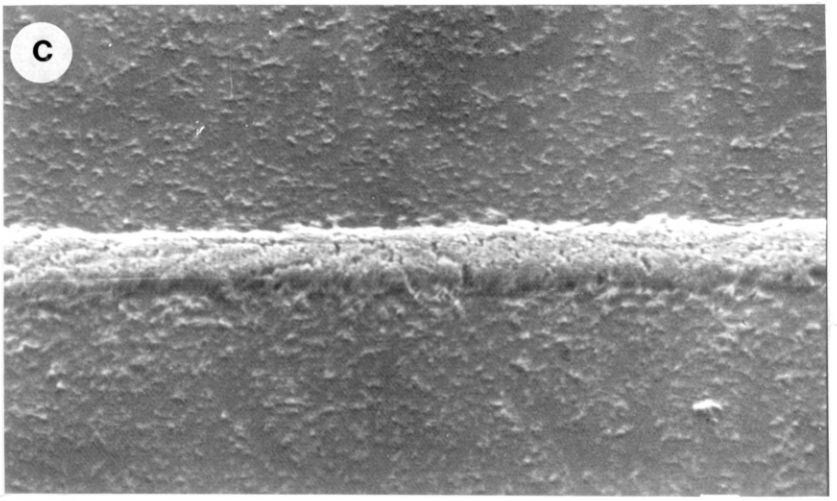
Starting film thickness = 130nm



10μm



2.0μm



1.0μm

Figure 5.2.14 a & b:

Patterned oxidised Pb-Cd on silicon oxide substrate, showing $PbCl_2/CdCl_2$(20%) residues after re-evaporation.

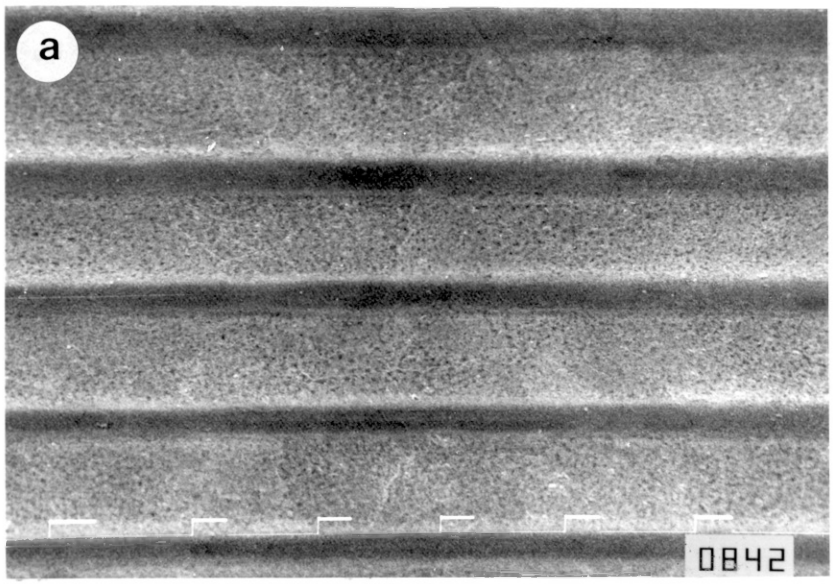
Irradiation Conditions:

Beam energy = 10keV

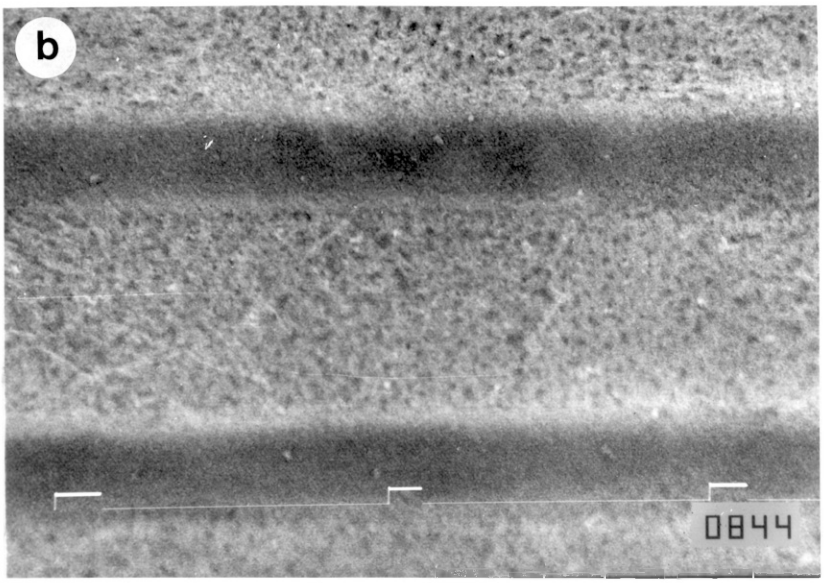
Input line dose = 14μC/cm

Temperature = 135°C

Starting film thickness = 130nm



10μm



5.0μm

5.2.2 DISCUSSION

The results obtained in the lithography experiments will be discussed in the light of the properties of the chosen materials (Pb, Pb-Cd, and oxide of Pb-Cd). Since the principal aim of the lithography experiment is to write either metallic, or metallic oxide patterns for use as the absorber layer of an x-ray mask, the discussion will be on the material properties as they affect requirements of such x-ray masks. The effect of the forward and backscattered electrons as they affect the width of written lines will be mentioned. A comparison between the chosen materials and the existing absorber materials, gold (Au) and tungsten (W), will be made. Figure 5.2.20 illustrates the stages of the lithography process.

The mean grain size of metallic films of Pb and Pb-Cd, produced as a result of e-beam irradiating $PbCl_2$ and $PbCl_2/CdCl_2$(20%) films, increases with the irradiation temperature. The Pb metal was found to aggregate into grains, larger than those of Pb-Cd, due, probably to the higher mobility of pure lead, as compared to a Pb-Cd solid solution. As a result, Pb films were not continuous, whereas Pb-Cd films were continuous, for average film thickness of about 80nm. The copper grid pattern transfer, in both Pb and Pb-Cd were of good fidelity. Edge resolutions of 0.29μm and 0.18μm were obtained in Pb and Pb-Cd metallic patterns, which are twice the $PbCl_2$ and $PbCl_2/CdCl_2$(20%) grain sizes respectively, for 200nm thick films. These values of resolutions are expected to be better, for direct writing without a mask, and should be in direct proportion to film grain size. The variation in the linewidths of Pb-Cd and its oxide (1.3-2.4μm), was as a result of varying effective e-beam diameter from experiment to experiment (reckoned to vary between 0.5μm and 1μm), see discussion below. The e-beam profile is described by a Gaussian distribution function (Figure 5.2.15). The spread of electrons in the material being decomposed is also shown. The profile of the exposed material depends on the exposure time. This profile is expressed as the sum of two Gaussian distributions: that due to incident electrons, and that due to the backscattered electrons. The backscattered contribution from the substrate is as a result of the practical electron range of 460nm in $PbCl_2$ for 10keV primary electrons. This is 260nm beyond the film thickness of 200nm.

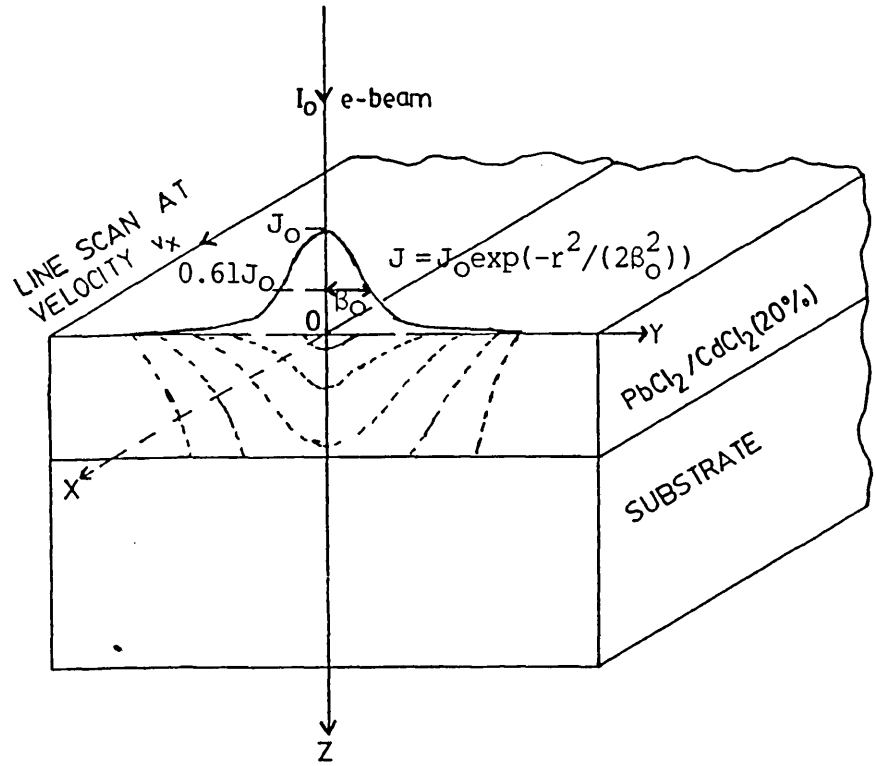


Figure 5.2.15: Gaussian distribution profile of e-beam current density; showing the distribution of electrons as a function of vertical penetration and exposure time.
J_o is the peak current density at r=0
r is the radial distance from the beam axis.
β_o is the standard deviation
The dotted lines are the profiles of the decomposed material, the linewidth increasing with exposure time (that is decrease in scan speed). I_o is the measured beam current.

The mathematical representation of the two Gaussian distributions is as follows. For a line scan exposure, obtained by scanning the beam at a velocity v_x ($v_x \simeq 3.7\mu m/s$), the energy deposited per unit volume, E, is given by [9],

$$E = E(y,z).D_x^\circ \qquad \text{----(5.2.1)}$$

where D_x° ($D_x^\circ = I_o/v_x \simeq 14\mu C/cm$) is the line input dose. E(y,z) is the energy deposited per unit volume per coulomb per centimeter,

and is represented by,

$$E(y,z) = \int_{-\infty}^{\infty}\{q.I(r,z)dx\} \qquad \text{-----(5.2.2)}$$

q is the number of electrons per coulomb, and I(r,z) is the energy deposited per unit volume per electron.

$$I(r,z) \equiv f(r)$$

where f(r) is the energy deposition function (proximity function) expressed in electron volt per unit volume per electron. f(r) is the sum of the two Gaussian distributions discussed above, and is represented as shown in Figure 5.2.16.

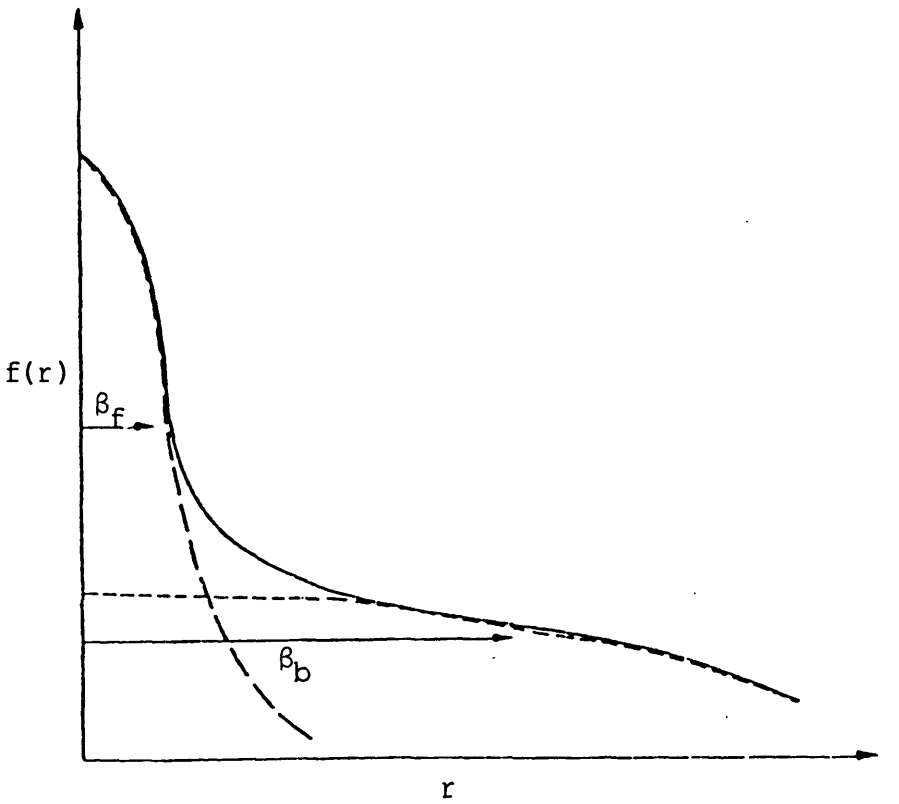


Figure 5.2.16: Radial distribution of total energy deposition function.
(– – – –) forward-scattered distribution
(------) backscattered distribution
β_f and β_b are the standard deviations of the forward-scattered and backscattered distributions respectively. [After Parikh, ref.12]

f(r) is given by the equation [10,11,12],

$$f(r) = k\{\exp(-r^2/\beta_f^2) + (\eta_E\beta_f^2/\beta_b^2).\exp(-r^2/\beta_b^2)\} \quad ----(5.2.3)$$

β_f and β_b are the forward and backscattered standard deviations respectively (see Figure 5.2.16). k is a normalisation constant, and is equal to c_f, where c_f is the forward-scattered weighting constant.

$$\eta_E = I_b/I_f \quad ----(5.2.4)$$

where I_i is the energy deposited in the z-direction, and is given by,

$$I_i = c_i\int_0^\infty\int_0^{2\pi}\{r.\exp(-r^2/\beta_i^2)\,d\Theta dr\} \quad ----(5.2.5)$$

and c_i is a weighting constant. Alternately, η_E can be represented by,

$$\eta_E = \eta_o K_\varepsilon$$

where $$\eta_o = \frac{\text{number of backscattered electrons}}{\text{number of forward-scattered electrons}}$$

at a particular depth in the material, and

$$K_\varepsilon = \frac{\text{Average energy deposited by backscattered electrons}}{\text{Average energy deposited by forward-scattered electrons}}$$

The forward scattered distribution (the first term in equation 5.2.3), depends on the thickness of the material and its composition, while the backscattered distribution depends solely on the composition of the substrate. The parameters η_E, β_f and β_b for a particular resist-substrate and incident energy situation, can be obtained, either by computer simulations [11,12,13], or by experimental techniques [14,15]. For a given electron energy, β_f increases with depth in the resist, while β_b is relatively constant. β_f decreases with increasing electron energy, while β_b increases with electron energy. For a fixed beam voltage and a fixed depth in the resist, β_f is

constant for different film thicknesses. η_E is independent of film thickness and electron energy, because of the decrease in K_ε and a simultaneous increase in η_o with increasing film thickness and electron energy.

The energy deposition function (Figure 5.2.16), is an intra proximity function of the electron beam. For a very fine e-beam, the spread of electrons within a thin film, caused by the forward scattering is quite small. Also the backscattered distribution function which depends on the substrate is greatly reduced for low atomic weight substrate material. Therefore, it could be said that the linewidth of the metallic patterns is in direct relation to the gaussian beam size, for a given substrate and film thickness. Subsequently, the linewidth of the metallic patterns, therefore, increases with the exposure time, that is with total dose. During NH_4Cl development, edges of lines are either completely eroded or undecomposed material is selectively removed. The selective removal of undecomposed material at edges of lines will results in discontinuous metallic films at the edges of written lines, that is, little islands are left along the edges. In the region across the linewidth where continuous metallic films are produced, it is likely however, that decomposition was not complete through the entire film thickness. Therefore, during NH_4Cl develop-ment, the sets of Pb-Cd lines (Figure 5.2.12) were eroded underneath. This resulted in displaced lines, of which some are broken and some overlapping one another. The success in producing lines of such linewidths, has been limited by the e-beam diameter, and not by the lithography process employed. It should perhaps be recalled at this point that the Pb-Cd lines formed under the electron beam are continuous ribbons, hundreds of microns long, about 2μm wide, and about 500Å thick.

The lithographic results discussed so far, have a final stage of NH_4Cl development, so as to remove unexposed $PbCl_2$ and $PbCl_2/CdCl_2$(20%) films, leaving behind the metal (and its oxide) patterns. A preliminary study of final stage re-evaporation of $PbCl_2/CdCl_2$(20%) films, so as to have a completely dry process, resulted in poorly resolved oxidised Pb-Cd lines (3μm linewidth). This was due to residues of $PbCl_2/CdCl_2$(20%) left behind after re-evaporation. It is then difficult to make a conclusive remark about this latter process.

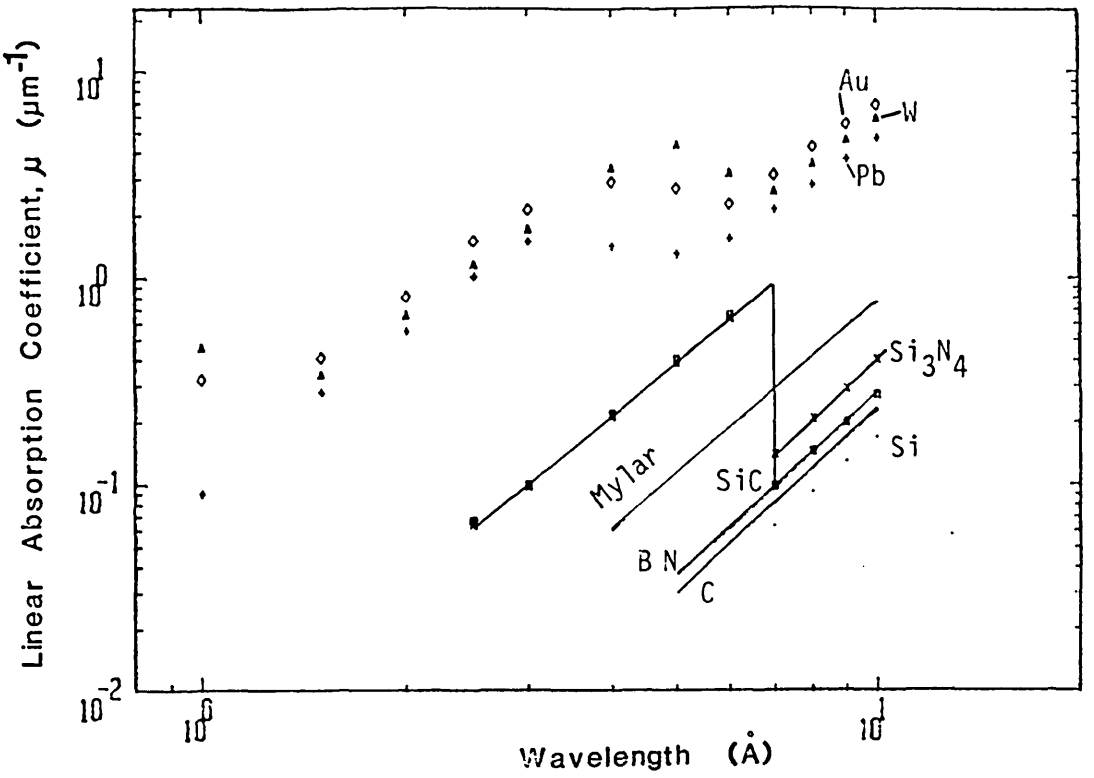


Figure 5.2.17: X-ray absorption coefficients, in the wavelength range 1-10Å of materials commonly used in x-ray masks.

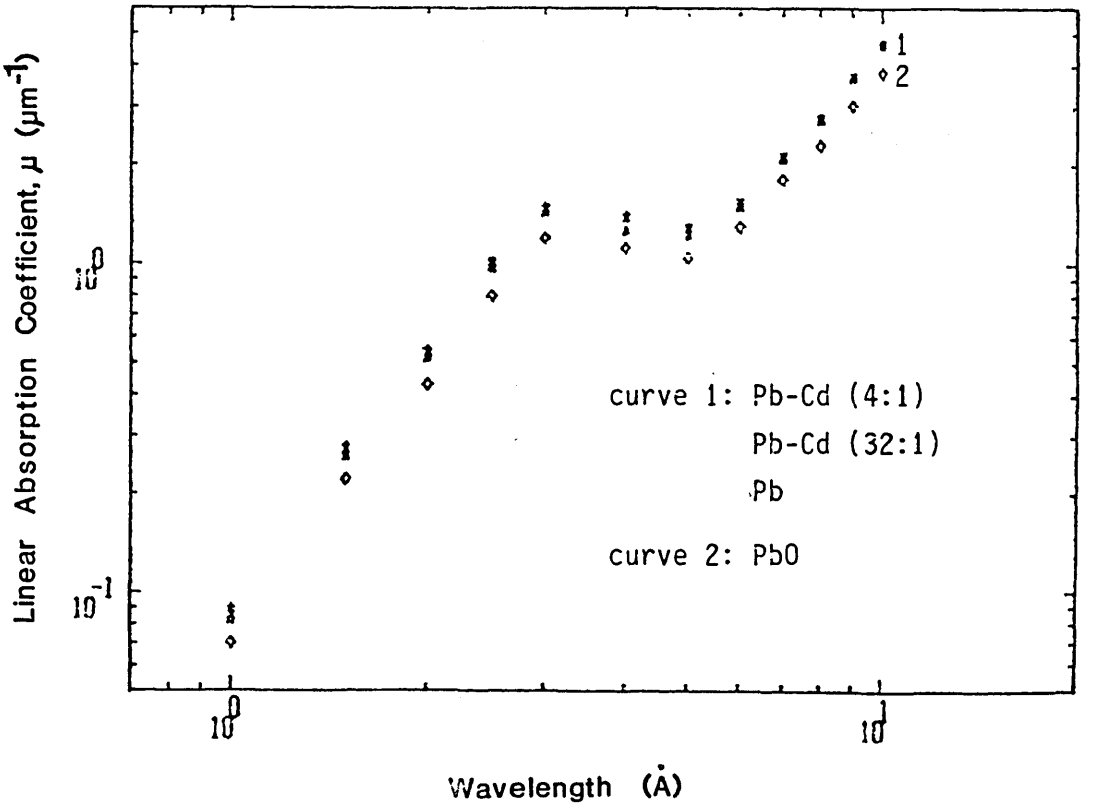


Figure 5.2.18: X-ray absorption coefficients of Pb, PbO, and Pb_xCd_y (x:y = 4:1 & 32:1).

Description of an x-ray mask and its requirement for x-ray lithography, has been given in section 1.1.4. The choice of materials for use in x-ray mask fabrication, depends on the x-ray absorption properties of the materials in the wavelength range of 1-50Å. The mass absorption coefficient, α, in cm^2/g, is related to the atomic number (Z), and the x-ray wavelength, λ (expressed in Å), by the equation [16,17,18],

$$\alpha = CZ^4\lambda^3 \qquad \text{-----(5.2.6)}$$

where C for each element is a constant only in the region between the discrete absorption edges, and expressed in $cm^2/g/Å^3$. The value of which changes abruptly at wavelengths characteristic of the element. α is independent of the physical state of the absorber, state of aggregation, and also temperature. The linear absorption coefficients μ, of materials commonly used in x-ray lithography is given in Figure 5.2.17 [16]. Where $\mu = \rho\alpha$ in reciprocal unit length, and ρ is the density of material, in g/c.c. The choice of high Z value for the absorber, and the use of longer wavelength greatly increases the mass absorption coefficient of the absorber layer. Absorber support materials are those that have low Z values resulting in low mass absorption coefficient, thereby being "transparent" to x-rays. The absorption coefficient of Pb is comparable to that of either Au or W in the wavelength range of 1 to 10 Å. By extrapolation, this should be true in the wavelength range of 1 to 50Å which is of interest to x-ray lithography. The atomic proportion of Pb to Cd, after complete processing, was found to be about 32:1 (EPMA data of Figure 5.2.7). The reduction in the Cd concentration is associated with the notion that Cd discharged at the surface with no adjacent Pb atoms, will volatilise at once. The effective mass absorption coefficient (α_E) of a compound or an alloy, is given by the equation,

$$\alpha_E = \sum_i g_i\alpha_i \qquad \text{-----(5.2.7)}$$

where α_i is the mass absorption coefficient of element i, and g_i its

mass fraction. The mass fraction is the ratio of atomic weight of element i, to the molecular weight of the compound. The absorbing power of Pb-Cd (both of atomic ratio 4:1 and 32:1), and the oxide of Pb, behaves like that of pure lead (Figure 5.2.18).

Table 5.2.1 : Some properties of materials used in x-ray masks [19,20].

	Au	W	Pb	Polyimide	Boron Nitride
Density (g/c.c)	18.88	19.35	11.34	1.2	2.25
Thermal Expansion ($\times 10^{-6}$ /°C)	14.2	4.5	29	23	2.2
Thermal Conductivity (W/cm.°C)	3.15	1.78	0.346	0.0017	0.7
Specific heat (J/g.°C)	0.13	0.134	0.13	1.5	1.0

Table 5.2.1 [19,20], is a comparison of selected properties of materials used in x-ray masks. The thermal expansion coefficients of Pb and polyimide are comparable, therefore, distortions induced by thermal gradients should be small. This is of great advantage over either tungsten (W) or gold (Au). Karnezos et al [12] pattered W directly on boron nitride (BN) membrane so as to match the thermal expansion coefficients of W and BN. The absence of a polyimide underlying film, means forfeiting the advantage of increased strength and improved surface flatness of the substrate offered by the polyimide.

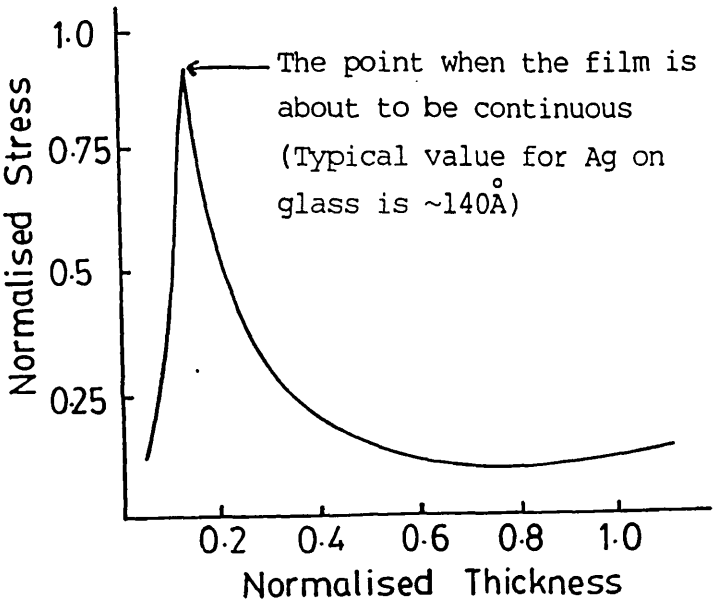


Figure 5.2.19: Stress-Film thickness relationship [After Maissel and Glang, ref.21]

The metallic film stress is also of prime importance when choosing the absorber material: absorber films having low stress values are required. The requirement of low stress values is to prevent pattern distortion which may arise as a result of high stress value. Although stress values cannot be given, the Pb-Cd (and its oxide) film stresses, are likely to be related to the stress of the deposited $PbCl_2/CdCl_2$(20%) film. The process of vacuum deposition is expected to produce a low stress value [21]. The film thickness-stress relationship, is hypothetically represented in Figure 5.2.19 [21]. This places a minimum requirement on the film thickness, in having low stress film.

Since x-ray masks are used for 1:1 proximity printing, defects $\geq$0.15μm size [22] in the x-ray masks can cause severe damage in the printed circuit. This then requires that the absorber layer have low defect density; as is the case in vacuum evaporated films [21].

Table 5.2.2: Characteristic wavelengths of target materials.

Material	Atomic No.	Type of Line	Wavelength (Å)	Energy (keV)
Pd	46	L	4.4	2.83
Rh	45	L	4.6	2.69
Mo	42	L	5.4	2.29
Si	14	K	7.1	1.75
Al	13	K	8.3	1.49
Cu	29	L	13.3	0.93
C	6	K	44.7	0.28

The target materials commonly used in x-ray sources for lithography are shown in Table 5.2.2 [23]. Low Z target materials, having low accelerating voltages (high λ) are chosen. This is to reduce any unwanted background high energy of x-rays which could reduce the contrast of the x-ray mask. X-ray mask contrast (MC) is theoretically defined as [24],

$$MC = I_T/I_A \qquad \text{----------(5.2.8)}$$

where I_T and I_A are the x-ray intensities under the "transparent" and absorbing areas of the mask, repectively. I_T and I_A are expressed as,

$$I_T = I_o \exp(-\mu_T t_T) \qquad \text{---------(5.2.9)}$$

$$I_A = I_T \exp(-\mu_A t_A) \qquad \text{---------(5.2.10)}$$

where I_o is the incident x-ray intensity, μ_T and t_T are the

linear absorption coefficient and thickness of the "transparent" layers respectively. μ_A and t_A are the linear absorption coefficient and thickness of the absorber layer respectively. Combining equations 5.2.8 to 5.2.10,

$$MC = \exp(\mu_A t_A) \qquad \text{--------(5.2.11)}$$

In practice, the effective mask contrast is generally much lower than the value obtained from equation 5.2.11. This is due to photoelectrons or Auger electrons produced by the absorber. These electrons thereby contributing to the dose (that is I_A) received by the resist under the absorber layer.

The resolution of the metal (Pb-Cd) and the metal oxide patterns is approximately equal to the film ($PbCl_2/CdCl_2$(20%)) mean grain size, which is related to the film thickness. Multiplication factors of 0.4 and 0.6 can be used to convert the film thickness to the metal and the metal oxide thicknesses respectively. These factors were obtained by "Talystep" measurements (Appendix III). For a mask contrast of about 5, the thickness and resolution of a Pb-Cd or oxidised Pb-Cd absorber layer for various target materials are presented in Table 5.2.3.

Table 5.2.3: Resolutions of Pb-Cd and oxidised Pb-Cd of various thicknesses and target materials. Typical substrate thickness is about 5μm.

Wavelengths (Å)	Absorber Thickness (nm)	Pb-Cd Resolution (nm)	Oxidised Pb-Cd Resolution (nm)
4.4(Pd_L)	300	430	290
13.3(Cu_L)	120	170	110
44.7(C_K)	50	70	50

The results presented in Table 5.2.3 show that the absorber thickness required for a given contrast ratio is dependent on the wavelength. Also the absorber resolution decreases with increase in thickness. The resolution of the x-ray mask is determined by that of the absorber, and is limited by the x-ray wavelength and the contrast ratio required for the resist (that is the resist sensitivity) being used. Some characteristics of x-ray resists are presented in Table 5.2.4 below. Longer x-ray wavelengths and higher contrast resists will both lead to improved mask resolution as a result of reduction in the required absorber thickness. Even for low sensitive resists, longer wavelengths will cause an improvement in the resist sensitivity, because higher mass absorption coefficients of the x-ray resist. This improved sensitivity can partly compensate for the higher absorption losses in the substrate; however, thinner mask substrates would be required.

Table 5.2.4: Some typical charateristics of x-ray resists [23]

Resist*	Type	Sensitivity (J/cm^2)	Minimum Linewidth(μm)	Contrast
PMMA	positive	1-2(at 8.3Å)	0.1	High
PBS	positive	0.1(at 8.3Å)	1.0	Low
FBM(F)	positive	0.05(at 5.4Å)	0.3	High
PGMA	negative	0.05(at 8.3Å)	2.0	Low
Bell(Cl)	negative	0.01(at 4.4Å)	1.0	Low

* PMMA = poly-methyl-meth-acrylate, PBS = poly butene-1- sulfone, FBM(F) is a fluorine doped resist, developed in Japan, PGMA = poly glycidyl meth acrylate, Bell(Cl) = Bell laboratory developed resist (chlorine based).

The need to have good dimensionally stable masks, places a restriction on how thin the mask substrate can be, probably not less than 4μm in thickness, (see Fig. 1.1.3 for typical dimensions of an x-ray mask). Therefore, either the resist sensitivity is good so that longer wavelengths can be used in fabrication without resorting to thin substrates, or mask resolution will have to be traded-off for thicker absorber layer. Hence, the need for fine structures, and also the need for high resolution and sufficient mask contrast may require x-ray lithography to be operated at longer wavelengths.

The lithography process employed in this work is summarised as shown in Figure 5.2.20. In terms of processing simplicity, the illustrated lithography process does not require additional etch resist(s), in contrast to the conventional fabrication of Au and W absorber layers. This lithography process can be applied, without any modification, to the fabrication of Pb-Cd or Pb-Cd oxide absorber layer of an x-ray mask.

Since the first application of x-ray lithography [25], subtractive methods have been commonly used for the patterning of gold. This method results in a sloped-wall (~70^{o}) absorber layer, and features down to 0.75μm have been defined. Significant linewidth loss has been experienced [26] in writing submicron features. The problem associated with the subtractive techniques was overcomed by using additive techniques [27]. Features down to about 0.3μm have been reproduced. Karnezos et al [20] used W as the absorber layer of an x-ray mask, and were able to write lines of about 0.25μm wide. Resolution of about 0.25μm was achieved in the process. Therefore W offered better resolution compared to Au. Also it was claimed that W and BN thermal expansion coefficient are better matched, resulting in low distortion. The advantages offered by a polyimide interlayer (as discussed earlier on) is forfeited.

In comparison to these two materials, Pb-Cd and oxidised Pb-Cd offer better resolutions (Table 5.2.3). The ultimate mask resolution is proposed to be 0.05μm. Secondly, the likelihood of distortion being introduced, as a result of incompatible thermal expansion coefficient of the absorber and the polyimide, is quite small. Finally, the simplicity of the fabrication process (Figure 5.2.20) should make it

comparatively cheaper than either the substractive or the additive techniques, thereby crowning the attractiveness of this lithography process.

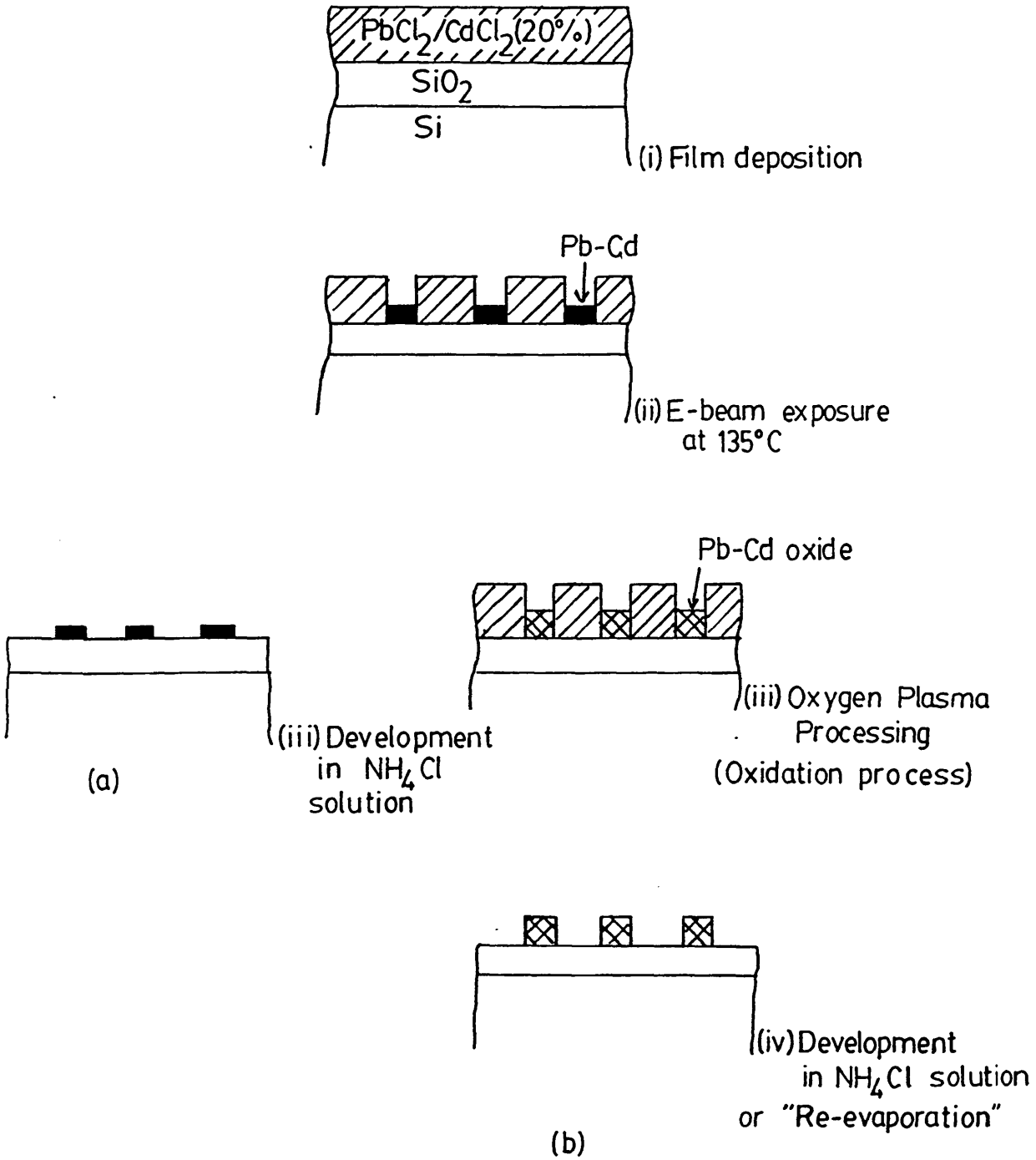


Figure 5.2.20: Schematic diagram of the lithography process, for the absorber pattern definition.

(a) Pb-Cd pattern

(b) Oxidised Pb-Cd pattern

5.3 SUMMARY

5.3.1 Decomposition Kinetics

The decomposition kinetics of $PbCl_2$ and $PbCl_2/CdCl_2$(20%) films have been categorized into two types of reactions. These are "low" reaction rates (decomposition of $PbCl_2$ at temperatures of 120^oC and less) and "high" reaction rates (decomposition of $PbCl_2$ at temperatures higher than 120^oC and of $PbCl_2/CdCl_2$(20%) at temperatures from 120^oC to 210^oC). The decomposition mechanisms of "low" and "high" reaction rates have been explained by two types of reaction mechanisms namely, PbI_2 [2,3] and $CdCl_2$[1] mechanisms respectively.

In the $CdCl_2$ type reaction mechanism, carriers (electrons and holes) are generated by in-coming primary electrons. The concentration of these e-h pairs in the sample is proportional to the current density and the practical electron range (expression 1.1.2) of the primary electrons. The energy required to create an e-h pair is about three times the band-gap energy of the material being irradiated. These carriers diffuse to the surface, where holes are trapped at special chlorine ion sites. A trapped hole at the special site could either capture an electron for recombination purposes, or result in the decomposition of chlorine atom or molecule. The discharge of chlorine atom results in the creation of anion vacancy, which diffuses to a defect centre. At this centre, Pb ion react with electrons to form Pb atom. The aggregation of Pb atoms is accompanied by annihilation of $PbCl_2$ sites, and the surface is reset for subsequent repitition of the reaction processes. The rate determining step in this case is the chlorine atom or molecule leaving the surface crystal sites. An activation energy E_A is associated with this step.

In the PbI_2 type reaction mechanism, carriers are generated as described above. It is proposed that holes are trapped at the surface by cation vacancies, at sites adjacent to surface chlorine ions. A hole trapped by the cation vacancy could either capture an electron for recombination purposes, or reacts with an adjacent chlorine ion, leading to the discharge and subsequent desorption of

either chlorine atom or chlorine molecule. The desorption process then resulted in surface generated anion vacancy, which diffuse into the bulk to defect centres, where electrons are trapped. Electrons trapped in the bulk by anion vacancy reacts with Pb ions, and this results in Pb atom precipitation. The formation of Pb atom is accompanied by annihilation of the $PbCl_2$ sites. The rate determining step is the in-diffusion of the anion vacancy, and is associated with an activation energy, E_A.

For "high" reaction rates, the initial rising portion of the reaction rate curves is a result of an increase (from KI(1-b) up to a limiting value KI, equation 5.1.3) in the anion vacancy concentration as the decomposition of the film progresses. The decaying portion of the rate curves, in both "low" and "high" reaction rates, is due to the increasing production of Pb atoms which act as recombination centre for the generated e-h pairs.

5.3.2 Lithography

Decomposition of $PbCl_2$ films at various temperatures (from 120°C to 220°C inclusive) produced non-continuous Pb films, which are unsuitable for the absorber layers of x-ray masks. Whereas decomposed $PbCl_2/CdCl_2$(20%) films resulted in continuous Pb-Cd films, adaptable for the fabrication of absorber layers of x-ray masks. The following points are outlined in respect of $PbCl_2/CdCl_2$(20%) samples:-

(i) $PbCl_2/CdCl_2$(20%) films can be vacuum deposited, resulting in low stress and low defect films.

(ii) Selected areas of $PbCl_2/CdCl_2$(20%) films can be decomposed to yield metallic Pb-Cd alloy upon e-beam irradiation, at a temperature of ~135°C.

(iii) Areas of $PbCl_2/CdCl_2$(20%) films not exposed to e-beam irradiation, readily dissolve in NH_4Cl solution at ambient temperature.

(iv) Alternately non-irradiated areas of $PbCl_2/CdCl_2$(20%) films volatilise at elevated temperature, under vacuum conditions.

The results presented in Figures 5.2.12(a-c) show that the metallic ribbons of Pb-Cd are not well attached to the SiO_2 surface. Since on NH_4Cl solution development, some of the ribbons moved. It was however established that after exposure to an oxygen plasma that:

(a) Pb-Cd oxidises in an oxygen plasma.

(b) Oxidised Pb-Cd lines did not move on development in NH_4Cl solution.

(c) An ultimate resolution of 50nm is achievable for an x-ray mask with oxidised Pb-Cd film (~50nm thick) as the absorber layer. This value of resolution is equivalent to the grain size of the deposited film of $PbCl_2/CdCl_2$(20%).

5.3.3 Proposal for Further Work

The following measurements could be carried out to supplement the results presented in this chapter:-

(i) $PbCl_2/CdCl_2$(20%) film stress measurements as a function of film thickness.

(ii) Stress measurements of Pb-Cd and oxidised Pb-Cd films versus film thickness.

(iii) Contrast measurements of x-ray masks, that have Pb-Cd or oxidised Pb-Cd as the absorber layer.

Finally, this work could be extended to other heavy metal halides such as the halides of uranium (U) and bismuth (Bi), with the intention of writing either metallic or metallic oxide patterns for use as the absorber layer of x-ray masks.

APPENDIX I

CALIBRATION OF THE QUADRUPOLE MASS SPECTROMETER (QMS)

To investigate the extent of decomposition, the QMS was calibrated to obtain the factor K (K_1 for $PbCl_2$ film on Al/glass substrate and K_2 for $PbCl_2/CdCl_2$(20%) film on silicon substrate). This was then used to determine the number of chlorine (Cl) atoms decomposed from a given volume of material.

The following relationship exist between the actual value of reaction product, R, and the current, I, due to the reaction product at the QMS.

$$dR/dt = KI \qquad \text{-------(I-1)}$$

where K depends on the parameters Θ, r, Ω, G, and γ. Θ is the angle between the QMS and normal to the sample surface, r is the sample-to-detector distance, Ω is the collection solid angle of the detector, G is the gain of the electron multiplier, and γ is the ionisation efficiency of the detector. Value of R_T, representing the total decomposition reaction product, is also evaluated.

The molecular volume of $PbCl_2$ is 47.54 cm^{-3}/mol. The number of $PbCl_2$ molecules in a 50nm thick film of $PbCl_2$, 0.16cm^2 in area, is 1.014×10^{16}. There are 2moles of Cl atoms per mole of $PbCl_2$. Hence the number of Cl atoms in a 50nm thick film of $PbCl_2$ is 2.03×10^{16}. At 220°C, 100% decomposition of $PbCl_2$ film on Al/glass substrate was achieved (as mentioned in section 5.1). Therefore $R_T = 1.27 \times 10^{17}$ Cl atoms cm^{-2}.

Integrating equation I-1, gives the extent of $PbCl_2$ decomposition reaction

$$R = K \int_0^{\tau} I dt \qquad \text{-----(I-2)}$$

where τ is the exposure time.

For 100% decomposition reaction of $PbCl_2$,

$$R = R_T = 1.27 \times 10^{17} \text{Cl atoms cm}^{-2},$$

But $\int_0^\tau Idt = 8.4 \times 10^{-6}$ coulomb, obtained from experimental data.

Substituting these values into equation I-2,

$$K_1 = 1.51 \times 10^{22} \text{ Cl atoms/cm}^2\text{/coulomb}$$

For $PbCl_2/CdCl_2$(20%) film on Si-substrate, a different value of Θ was used. The cosine distribution law is employed, and it is trusted that this within experimental error will be adequate. So that a direct proportionality exist between $\cos\Theta$ and I. The following relationship is obtained to evaluate K_2.

$$K_2 = (K_1 . \cos 45)/\cos 70$$

$\Theta = 45^o$ and 70^o are values given in chapter 5, for the position of the QMS with respect to the sample. The value of K_2 was found to be 3.13×10^{22}Cl atoms/cm^2/coulomb.

For 100% decomposition of $PbCl_2/CdCl_2$(20%) film, the value of R_T is evaluated as follows: molar additivity of $PbCl_2$(80%) and $CdCl_2$(20%) is permitted, within the experimental error of measurements. Molar volume of $PbCl_2/CdCl_2$(20%) was found to be 47.1cm^{-3}/mol. Therefore, 80nm thick film of $PbCl_2/CdCl_2$(20%) would give an R_T value of 2.05×10^{17} Cl atoms cm^{-2}.

APPENDIX II

Listing of computer programs used for data correction and integration, in presenting results of section 5.1

(A) Data Correction Program

```
10REM "CORRE"
20REM DIFFERENTIATION
30MODE 3:PRINT"DATA CORRECTION"
40VDU 28,0,24,79,5
50DIM X(306):DIM Y(306):DIM C(50):IF C%=1 GOTO 131
60C%=0
70INPUT '"SUBFILE NAME : "name$
80INPUT'"y-multiplier";ym
90OSCLI "ACCESS G.GRADUMP"
100d%=OPENUP "G.GRADUMP"
110PRINT#d%,"G.CORRE",":2.STDAT",-10,10000,-10,10000,1,ym,0,0,name$
120CLOSE#d%
130C%=1:CHAIN "G.GRAFDAT"
131a%=0:yo=0:PRINT"AUTO OFFSET?  (Y/N):"
132KEY$=GET$:PRINTKEY$:IFKEY$="Y"OR KEY$="y":a%=1 :GOTO140
133INPUT '"y - offset:   "yo
140INPUT '"CORRECTED FILE NAME: "anam$
150 INPUT '"TIME CONSTANT :" t
155INPUT '"X - multiplier  :"XM
160sc%=0:PRINT'"% SCALE ? (Y/N)"
170KEY$=GET$:IF KEY$="Y"OR KEY$= "y" PRINT;KEY$: sc%=1
180d%=OPENIN "G.GRADUMP"
190INPUT #d%,n%
200IF n%=0 INPUT #d%,mes$:PRINT mes$:STOP
210FOR I%=1 TO n%
220INPUT#d%,X,Y
230X(I%)=X:Y(I%)=Y
240NEXT
250CLOSE#d%
251IF a%=0 GOTO 253
252yo=(-1)*Y(n%)
```

```
253FOR I%=1 TO n%
254Y(I%)=Y(I%)+yo
255NEXT
260Q%=0:T%=0
270FOR I%=1 TO (n%-1)
280Y(I%)=Y(I%)+t*(Y(I%+1)-Y(I%))/(X(I%+1)-X(I%))
290NEXT
300 Y(0)=Y(1)-X(1)*(Y(2)-Y(1))/(X(2)-X(1))
310Y(n%)=Y(n%-1)
320PROCscale
330OSCLI "ACCESS G.GRADUMP"
340d%=OPENUP "G.GRADUMP"
350PRINT#d%,"G.MENU",":0.ODATA",.1,.1,.1,.1,.1,.1,0,0,anam$,
                                * (-1)*(n%+1),0,XM*X(n%)

360FOR I%=0 TO n%
370PRINT#d%,Y(I%)
380NEXT
390CLOSE #d%
400C%=2: CHAIN "G.GRAFDAT"
410END
420DEFPROCscale
430IF sc%=0 ENDPROC
440MAX=0
450FOR I%=0 TO n%
460IF Y(I%)>MAX THEN MAX=Y(I%)
470NEXT
480FOR I%=0 TO n%
490Y(I%)=Y(I%)*100/MAX
500NEXT
510ENDPROC
```

(B) Integration Program

```
 10 REM "FILE INTEGRATION"
 20MODE 3:PRINT"FILE INTEGRATION"
 30VDU 28,0,24,79,5
 40DIM Y(303):DIM X(303)
 50IF C%=1 THEN PROCinte ELSE PROCnext
 60DEFPROCload
 70CLS:INPUT'"Database:  "dbase$
 80INPUT'"Filename:  "name$
 90 INPUT'"x-limits xl, x2  " xl,x2
100 INPUT'"y-limits yl, y2  " yl,y2
110INPUT'"y-multiplier"yx
120OSCLI"ACCESS G.GRADUMP"
130d%=OPENUP("G.GRADUMP")
140PRINT#d%,"G.INTE",dbase$,xl,x2,yl,y2,1,yx,0,0,name$
150CLOSE#d%:OSCLI "ACCESS G.GRADUMP L"
160C%=1:CHAIN "G.GRAFDAT"
170ENDPROC
180DEFPROCinte
190CLS:INPUT'"Return database:  "rbase$
200INPUT'"Return filename:  "rname$
210INPUT'"Y-multiplier:  "Yx
220INPUT'"X-multiplier:  "Xx
230a%=0:yo=0:PRINT'"AUTO OFFSET? (Y?N) :"
240KEY$=GET$:PRINT;KEY$:IF KEY$="Y" OR KEY$="y":a%=1:GOTO 260
250INPUT'"y-offset:   "yo
260INPUT'"Y-offset:   "Yo
270t=0:de%=0:PRINT'"TIME DELAY ? (Y/N): "
280KEY$=GET$:PRINT;KEY$:IF KEY$="Y" OR KEY$="y"THEN GOTO 290 ELSE
290 de%=1:INPUT'"TIME CONSTANT :" t                    GOTO 320
300INPUT '"How much percent ?   " p
310IF p>100 OR p<0 THEN PRINT'"I said PERCENT !!":GOTO 300
320d%=OPENIN("G.GRADUMP")
330INPUT#d%,np%
340IF np%=0  INPUT#d%,error$:PRINTerror$:C%=0:STOP
350FOR I%=1 TO np%
360INPUT#d%,X(I%),Y(I%)
```

```
370NEXT
380CLOSE#d%:OSCLI "ACCESS G.GRADUMP L"
390IF a%=1 yo=Y(np%)*(-1)
400A=0:B=0
410B=Y(1):Y(1)=(Y(1)+yo)*t
420FOR I%=2 TO np%
430A=Y(I%)
440Y(I%)=(Y(I%)+yo)*t+(Y(I%)+B+2*yo)*(X(I%)-X(I%-1))/2+Y(I%-1)
450B=A
460NEXT
470PROCscale
480PROCdectime
490PROCreturn
500ENDPROC
510DEFPROCreturn
520OSCLI "ACCESS G.GRADUMP"
530d%=OPENUP  ("G.GRADUMP")
540PRINT#d%,"G.INTE",rbase$,.1,.1,.1,.1,.1,0,0,rname$,-1*(np%+de%),
                                                    X(1-de%)*Xx,X(np%)*Xx
550FOR I%=(1-de%)TO np%
560PRINT#d%,Y(I%)*Yx+Yo
570NEXT
580CLOSE#d%:OSCLI "ACCESS G.GRADUMP L"
590C%=2:CHAIN "G.GRAFDAT"
600ENDPROC
610DEFPROCnext
620CLS:PRINT'"HIT 'I' TO INTEGRATE"
630KEY$=GET$:IF KEY$="I" OR KEY$="i" THEN PROCload ELSE STOP
640DEFPROCscale
650IF de%=0 ENDPROC
660MAX=0
670FOR I%=0 TO np%
680IF Y(I%)> MAX THEN MAX=Y(I%)
690NEXT
700FOR I%=0 TO np%
710Y(I%)=Y(I%)*100/MAX
720NEXT
730ENDPROC
```

```
740DEFPROCdectime
750IF de%=0 ENDPROC
760dec%=0:Id%=0:I%=0
770REPEAT
780IF Y(I%)>=p THEN Id%=I%:dec%=1
790I%=I%+1
800UNTIL dec%=1
810PRINT p;"% OF MATERIAL GONE AT t=";INT(X(Id%));"sec"
820PRINT'"INTEGRAL ="; INT(MAX)
830PRINT'"Hit 'c' to continue"
840KEY$=GET$:IF KEY$="C" OR KEY$="c" THEN GOTO 860
850GOTO840
860ENDPROC
```

APPENDIX III

ELLIPSOMETRIC AND "TALYSTEP" FILM THICKNESS MEASUREMENTS (DESCRIPTION OF BASIC OPERATING PRINCIPLE).

III-1 INTRODUCTION

For a specific film application or process the film thickness measurement technique to be used depends upon the film, its thickness, and the accuracy desired. These requirements include such properties as the film thickness, film transparency, film hardness, thickness uniformity, substrate smoothness, substrate optical properties, and substrate size. In many cases there is no single best technique, and the one chosen for measurement is a matter of choice by the investigator. In general, film thickness is of the order of a wavelength of light and can be measured by various types of optical techniques. One of such techniques is the ellipsometry which will be described, as Auto EL-III ellipsometer was used. Results of film thickness measured by the ellipsometer was verified using a "Talystep" (stylus) instrument, a brief description of measurement procedure is also reported.

III-2 ELLIPSOMETRY FOR FILM THICKNESS MEASUREMENT.

Ellipsometry provides a non-destructive method for measuring film thickness and refractive index of transparent films. Measurements could be carried out in optically transparent environments such as air or liquids, and no special conditions are required (for example, vacuum, heat, or electron bombardment) which may change the optical properties of surfaces being studied [1,2].

The method is based upon the classic theory of Drude [3], concerning the change in the state of polarisation of light upon reflection from a bare surface or a surface covered with film. The state of polarisation is determined by the relative amplitude of the

parallel ($|E_p|$) and perpendicular ($|E_s|$) components of the electric vector of the radiation (see Fig. III-1), and the phase difference between the two components, $\varepsilon_p - \varepsilon_s$ [1,2,4].

In principle, with complete knowledge of the state of polarisation of the incident and reflected light, both thickness and refractive index of a transparent film can be determined.

The high resolution of the technique is due [1] firstly to the fact that relative, rather than absolute measurements are made. Secondly, the technique employs a built-in reference that largely eliminates effects due to external fluctuations, such as those due to light source. Finally, azimuth angles (that is, angles resulting from rotation around an optic axis) are measured and angular measurements can easily be made with high precision.

(a) Basic Theory.

The instantaneous amplitude of electric field, E_t of a monochromatic light can be represented by;

$$E_t = |E| \exp i(wt + \varepsilon) = |E| \exp(i\varepsilon).\exp(iwt) \qquad \text{----(III-1)}$$

where $|E|$ is the real amplitude (that is modulus) of electric field, ε the phase of the light wave relative to a reference, and w the angular frequency.

The time-dependent part of equation III-1, exp(iwt), is not particularly important and often is disregarded [1] in the case of monochromatic light. The basic theory of an ellipsometer and its technique is founded on the time independent part ($|E|\exp(i\varepsilon)$) of equation III-1.

In carrying out the analysis of reflected light from sample surfaces, the electric fields of the incident and reflected waves can each be resolved into two orthogonal linearly-polarised components. One with its electric field vector parallel to the plane of incidence ('p' component), and the other component has it's electric vector normal to the plane of incidence ('s' component) as shown in Fig. III-1.

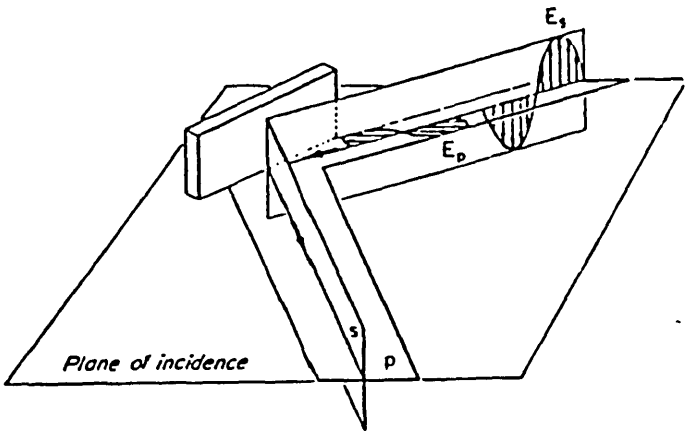


Figure III-1: Reflection of polarised light. Plane of incidence defined by incident and reflected beam. The s and p components indicated in incident light, with electric vector normal and parallel, respectively, to the plane of incidence. [After Muller ref.1]

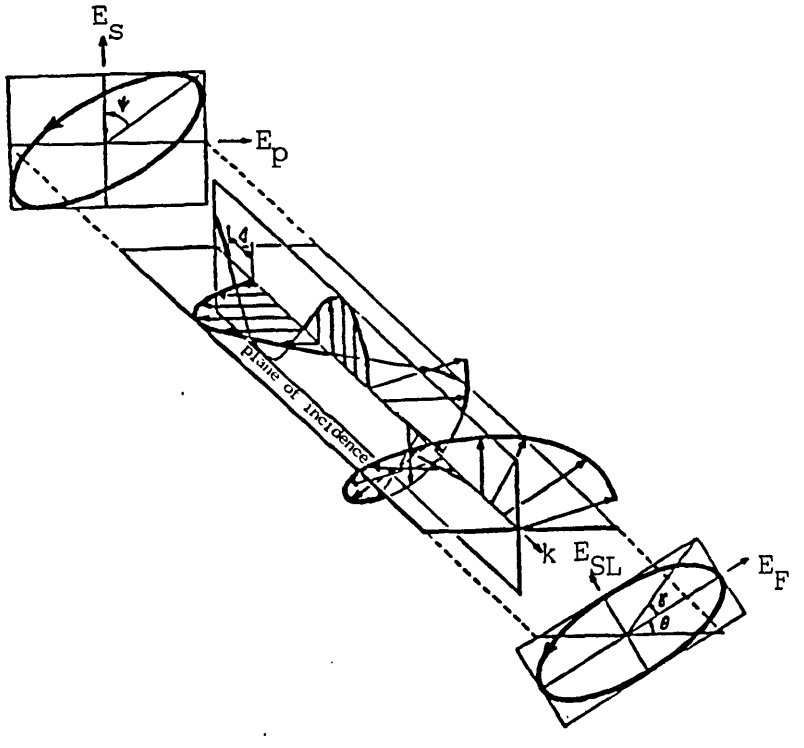


Figure III-2: Elliptic polarisation resulting from the superposition of two linear components of different phase and amplitude. Representation as a helix in space or an ellipse in a plane normal to the propagation direction k. Physical parameters Δ, ψ, and geometric parameters θ, γ define the state of polarisation. E_F, E_{SL} orthogonal fast and slow components ahead or lagging each other in phase repectively, by a quarter wave (90°). [After Muller ref.1]

A linearly polarised beam is such that the phase difference (Δ) between the p and s components is either 0^{o} or 180^{o}, all other phase differences resulting in elliptical polarisation, which is the most general state of polarisation [1]. It is the superposition of linearly polarised s and p components of the same frequency, but different phase and amplitude that result in Fig. III-2. The state of polarisation is characterised by the ratio of the electric field amplitudes $|E|$ of p and s components, expressed as;

$$\frac{|E_p|}{|E_s|} = \tan\psi \qquad \text{---------- (III-2)}$$

and the phase difference Δ of the time-independent phase ε of the two components is;

$$\Delta = \varepsilon_p - \varepsilon_s \qquad \text{----------(III-3)}$$

Δ and ψ are indicated in Fig. III-2. The range of values for the two physical parameters are;

$$0° \leqq \psi \leqq 90° \qquad \text{---------- (III-4)}$$

$$0° \leqq \Delta \leqq 360° \qquad \text{---------- (III-5)}$$

Fresnel reflection coefficients (r), describe the reflection of light on a dielectric interface [1], and these coefficients represent the ratio of the reflected to incident electric field amplitude, and are different for s and p components; (Fig. III-3)

$$r_p = \frac{E_p''}{E_p} \qquad \text{---------- (III-6)}$$

$$r_s = \frac{E_s''}{E_s} \qquad \text{----------(III-7)}$$

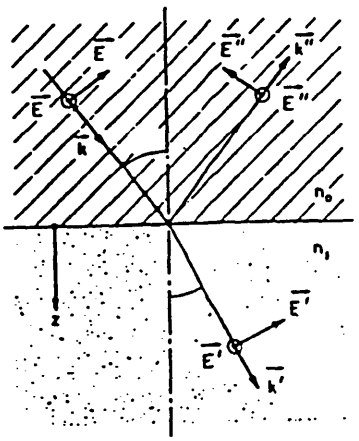


Figure III-3: Reflection and refraction at a dielectric interface. Definition of symbols and of positive coordinate directions for p and s components of electric field vector E in incident, reflected, and refracted waves. (Circles represent arrows pointing out of the plane of the drawing.) k, propagation direction of the three waves; $\emptyset$, angle of incident; $\emptyset'$, angle of refraction; n_0, refractive index of incident medium; n_1, refractive index of reflecting medium; z, coordinate direction for amplitude attenuation if the reflecting medium is absorbing [After Muller ref.1]

The double-primed quantities refer to the reflected wave, and unprimed to the incident wave. In exponential form,

$$r_p = \frac{|E_p''|}{|E_p|} \exp i(\epsilon_p'' - \epsilon_p) \qquad \text{------ (III-8)}$$

$$r_s = \frac{|E_s''|}{|E_s|} \exp i(\epsilon_s'' - \epsilon_s) \qquad \text{------ (III-9)}$$

from equations III-8 and III-9, the magnitude of the Fresnel reflection coefficients are;

$$|r_p| = \frac{|E_p''|}{|E_p|} \qquad \text{------ (III-10)}$$

$$|r_s| = \frac{|E_s''|}{|E_s|} \qquad \text{------ (III-11)}$$

and these represent the amplitude attenuation due to reflection. The absolute change in phase δ due to reflection is represented by,

$$\delta_p = \epsilon_p'' - \epsilon_p \qquad \text{------ (III-12)}$$

$$\delta_s = \epsilon_s'' - \epsilon_s \qquad \text{-------(III-13)}$$

The complex reflection coefficients r_p and r_s are not separately measurable, but their ratio ρ can be measured by ellipsometric methods. ρ is defined as,

$$\rho = \frac{r_p}{r_s} \qquad \text{------ (III-14)}$$

Combining equations III-8, III-9,and III-14,

$$\rho = \frac{(|E_p''|/|E_s''|)}{(|E_p|/|E_s|)} \exp\{i[(\epsilon_p'' - \epsilon_s'') - (\epsilon_p - \epsilon_s)]\} \qquad \text{----(III-15)}$$

but

$$\tan\psi = |E_p|/|E_s| \qquad \text{(from equation III-2)}$$

$$\tan\psi_i = |E_p|/|E_s| \qquad \text{------ (III-16)}$$

$$\tan\psi_r = |E_p''|/|E_s''| \qquad \text{------ (III-17)}$$

subscripts r and i refer to reflected and incident waves respectively. So also,

$$\Delta_r = \epsilon_p'' - \epsilon_s'' \qquad \text{------ (III-18)}$$

$$\Delta_i = \epsilon_p - \epsilon_s \qquad \text{------ (III-19)}$$

Combining equations III-15 to III-19,

$$\rho = \frac{\tan\psi_r}{\tan\psi_i} \exp\{i(\Delta_r - \Delta_i)\} \qquad \text{------ (III-20)}$$

which could be further simplified to

$$\rho = \tan\psi \exp(i\Delta) \qquad \text{------ (III-21)}$$

where $\tan\psi = \frac{\tan\psi_r}{\tan\psi_i}$, and $\Delta = \Delta_r - \Delta_i$

(b) Experimental Applications.

There are two basic types of ellipsometers; rotating analyser type , and the nulling type (for example, the Auto EL, used in the course of this research).

The basic arrangement of a nulling ellipsometer is as shown in Fig. III-4. It employs a polariser, a compensator, and an analyser, each aligned along the axis in which it is located. This sequence (common in the Auto EL), called the PCSA configuration for Polariser, Compensator, Sample, Analyser, describe the sequence of optical elements in the instrument. The PSCA configuration [5] is also possible.

Collimated monochromatic light (λ = 632.8nm) is first linearly polarised by the polariser, and then elliptically polarised by a quarter-wave compensator. After reflection from the sample surface, the light is transmitted through an analyser and a 632.8nm filter, and finally detected by a photo-detector.

During measurement, the compensator is fixed with its fast axis at an azimuthal angle ($\pm 45^{o}$) with respect to the plane of incidence. The polariser and analyser are alternately rotated automatically until the intensity of the reflected beam (as sensed by the photo-detector) is reduced to a minimum (known as the null or "extinction" condition). The use of a quarter-wave compensator before reflection is shown in Fig. III-5. The 45^{o} azimuth q of the quarter-wave plate results in equal amplitudes of p and s components incident on the specimen. At extinction, the angular azimuths P, of the polariser, and A, of the analyser, determine respectively, Δ and ψ due to the reflection.

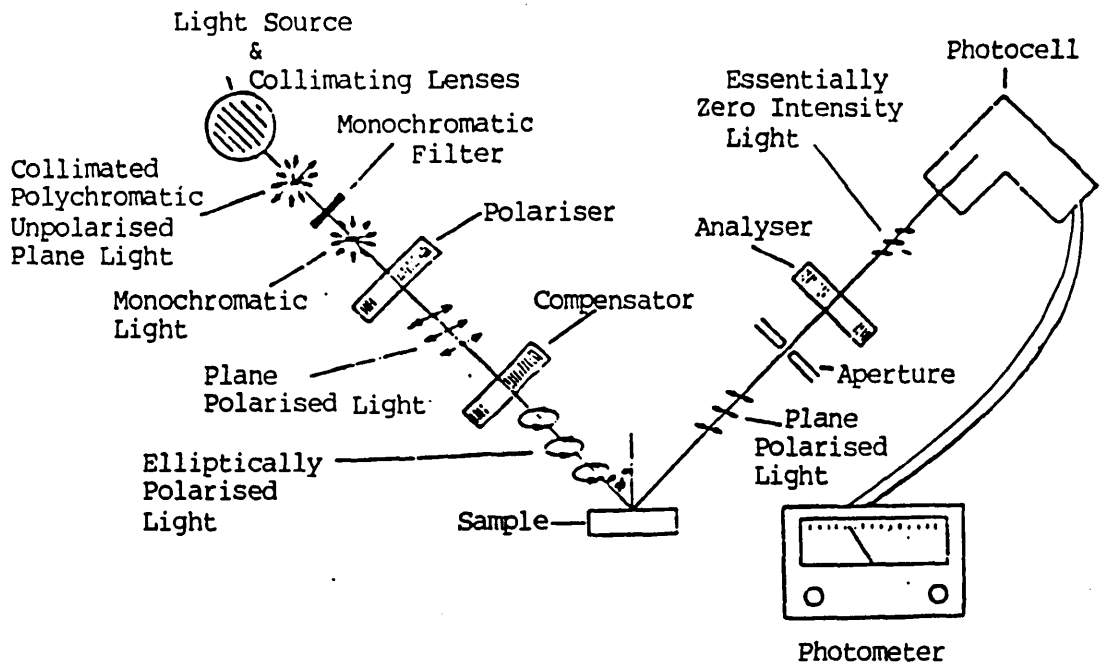


Figure III-4: Schematic diagram of an ellipsometer [After Muller ref.1]

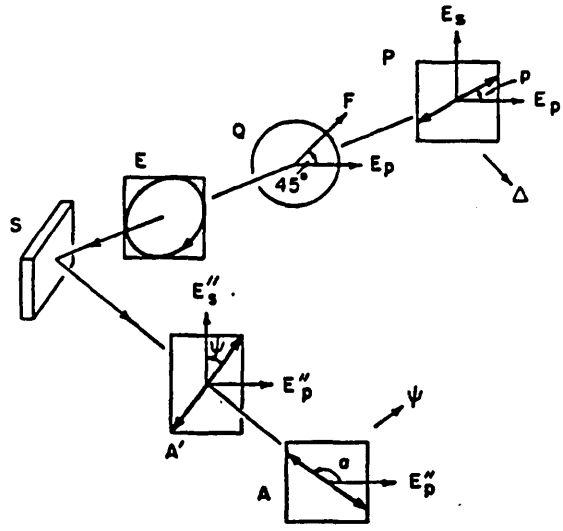


Figure III-5: Ellipsometer with elliptic polarisation incident and compensator of fixed retardation. P -Polariser with transmitted electric field direction. Azimuth p at extinction is a measure of Δ. Q -Fixed compensator (quarter wave plate) of fixed azimuth (fast axis F at 45° to plane of incidence). E -Elliptic state of polarisation before reflection. S- Reflecting specimen surface. A' -Restored linear state of polarisation. A -Analyser with transmitted electric field direction. azimuth α at extinction is a measure of ψ [After Muller ref.1]

Although a nulling ellipsometer (Auto EL-III) was used, P and A (hence Δ and ψ) measurements could be carried out by the process known as the method of swings. After obtaining a preliminary "extinction" point by proper adjustment of P and A, the analyser orientation is fixed, while readings are taken of the polariser azimuth at equal signal levels on both sides of extinction. These give the average value, $\overline{P}$. With the polariser set at $\overline{P}$, the same procedure is repeated with the analyser, giving the average value $\overline{A}$, of the two analyser settings on either side of extinction.

(i) Conversion of P and A to Δ and ψ

There are 32 different combinations of polariser, analyser and compensator settings which can result in a given pair of values of Δ and ψ. These can be reduced to 16 if all azimuths are restricted to ranges less than 180^{o}. The restriction is due to the fact that any two azimuths of a polariser, compensator, or analyser that are 180^{o} apart are optically identical [1]. The 16 pairs [8] are;

$$\psi = A,\ 180\text{-}A \qquad \text{---- (III-22)}$$

$$\Delta = 2P\text{-}90°,\ 2P\text{-}270°,\ (2m\text{-}1)90° \pm 2P \qquad \text{------(III-23)}$$

where m = 1,2,3, or 4

By setting the compensator azimuths at 45^{o}, and restricting the ranges of P and A to two zones (designated 2 and 4), the sixteen pairs of Δ and ψ values in equations III-22 and III-23 can be reduced to two pairs of equations.

Zones 2 and 4 as denoted by the subscript, are defined as follows;

Zone 2: $-45° \leqq P_2 \leqq 135°,\ 0° \leqq A_2 \leqq 90°,\ C=45°$

Zone 4: $-135° \leqq P_4 \leqq 45°,\ -90° \leqq A_4 \leqq 0°,\ C=45°$

Δ and ψ are related to P and A in each of the two zones by the following equations;

$$\Delta_2 = 270° - P_2 \qquad \psi_2 = A_2 \qquad \text{------(III-24)}$$

$$\Delta_4 = 90° - 2P_4 \qquad \psi_4 = -A_4 \qquad \text{------(III-25)}$$

In either zone 2 or 4, equally valid measurements can be made, but errors in measurements that are likely to arise due to slight malfunctioning of the compensator, can be eliminated by making

measurements in both zones. The results of which is averaged to obtain mean values $\overline{\Delta}$ and $\overline{\psi}$, given by,

$$\overline{\Delta} = (\Delta_2 + \Delta_4)/2 = 180° - (P_2+2P_4)/2 \quad \text{-----} \quad \text{(III-26)}$$

$$\overline{\psi} = (\psi_2 + \psi_4)/2 = (A_2 - A_4)/2 \quad \text{------(III-27)}$$

(ii) Conversion of Δ and ψ to Physical Parameters.

The Auto EL applications deal with samples for which Δ and ψ could be measured, and not necessarily those samples for which the optical constants of the substrate, and film refractive index and thickness can be computed internally. Δ and ψ can be externally converted to physical parameters by such means as remote computers, pre-computed graphs (such as Fig. III-6), and empirical calibration [1].

For a film-free surface (Fig. III-3), Δ and ψ are functions of the angle of incidence, $\emptyset$, the wavelength λ of the light, the refractive index n_0 of the ambient medium, as well as the substrate optical constants, $n_s - ik_s$, as expressed in equations III-28 and III-29:

$$\Delta = \Delta(\emptyset,\lambda,n_0,n_s,k_s) \quad \text{-----} \quad \text{(III-28)}$$

$$\psi = \psi(\emptyset,\lambda,n_0,n_s,k_s) \quad \text{-----} \quad \text{(III-29)}$$

Since $\emptyset$, λ, and n_0 are known, equations III-28 and III-29 may be solved uniquely and in closed form for n_s and k_s [1].

(iii) Film-Substrate Models.

The film-substrate models for single and double transparent films on substrate are both represented in Fig. III-7. In the single film model, Δ and ψ depend on the film refractive index (both the real and imaginary parts; n_1 and k_1 respectively) and on the film thickness d_1, as well as on all the other parameters in equation III-28. That is;

$$\Delta = \Delta(\emptyset,\ \lambda,\ n_0,\ n_s,\ k_s,\ n_1,\ k_1,\ d_1) \quad \text{-----} \quad \text{(III-30)}$$

$$\psi = \psi(\emptyset,\ \lambda,\ n_0,\ n_s,\ k_s,\ n_1,\ k_1,\ d_1) \quad \text{------} \quad \text{(III-31)}$$

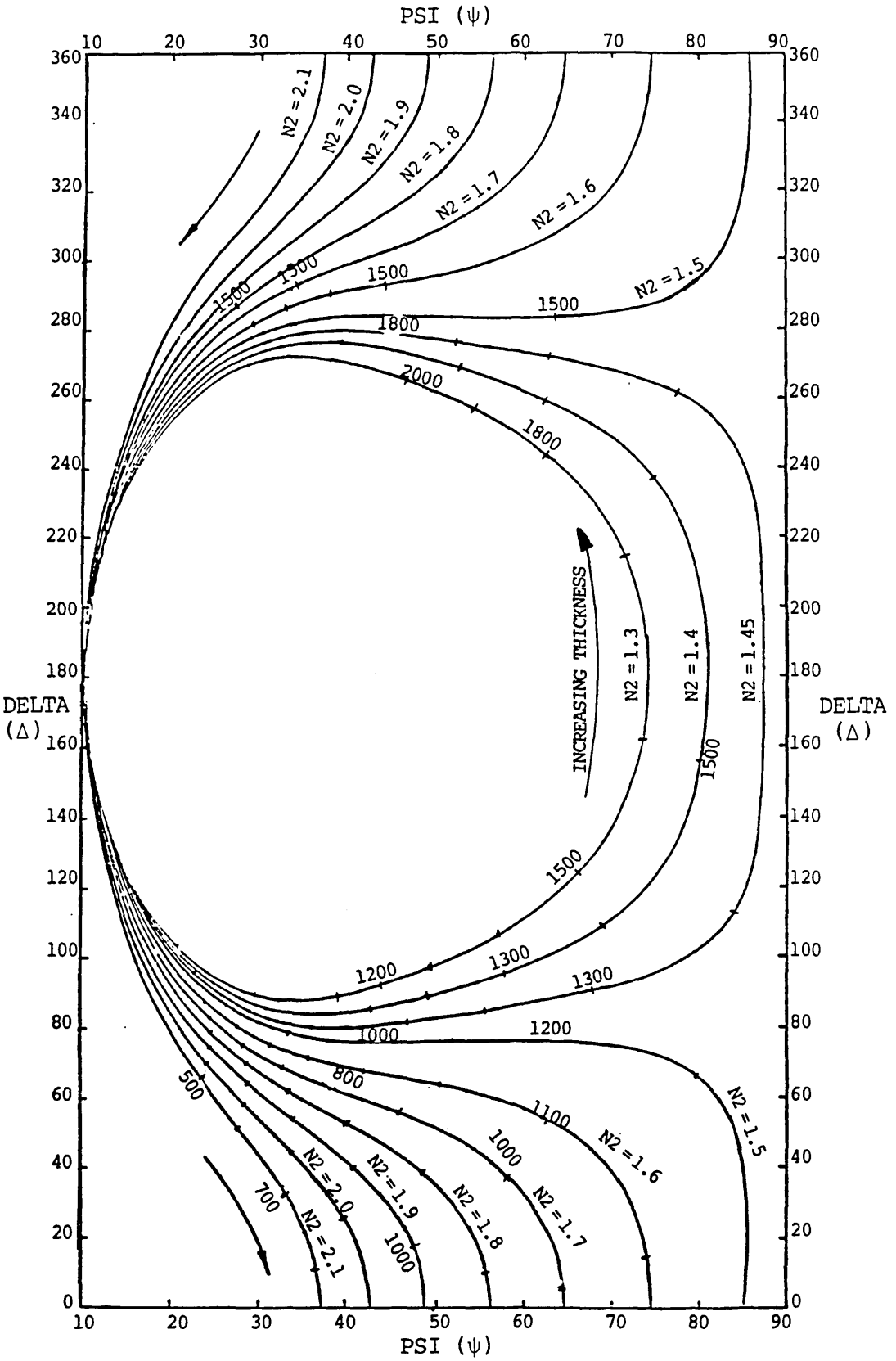


Figure III-6: Δ and ψ vs. refractive index and thickness of transparent film on silicon substrate
λ=632.8nm and Ø = 70° [ref.8]
Film thickness is in Å

For a transparent film ($k_1 = 0$), the film thickness d_1, and refractive index n_1 are the only unknowns in equations III-30 and III-31. For external computation, d_1 and n_1 are determined by numerical techniques which requires a computer program [6].

In another form, the film thickness (for non-absorbing film), d_1 could be expressed as [1,7],

$$d_1 = \frac{(\beta + 180N)\lambda}{360(n_1^2 - \sin^2\phi)^{\frac{1}{2}}} \qquad \text{---------- (III-32)}$$

where N is an integral value that depends on the film thickness. β (same as Archer's δ [7]) is the change in phase of the beam of wavelength λ caused by transversing the film of thickness d_1 and index of refraction n_1. The Δ/ψ plot [8] is graphically represented by Fig. III-6 for single transparent films of various refractive indices on silicon, for $\lambda = 632.8$nm and $\phi = 70°$. Each line in the family of closed curved curves is the locus of the Δ and ψ produced by films of increasing thickness but constant refractive index. All curves of constant refractive index have a common origin at 0^o; the Δ,ψ point characteristic of bare silicon substrate. Δ and ψ are cyclic (N = 1,2,...) functions of thickness and the curves repeat periodically with every 180^o change in β. Significantly, for all practical cases (with the exception of very low and very high indices), no two curves overlap or intersect, consequently, each point in the plane corresponds to a unique value for the index of refraction of the film.

This method provides a means of estimating d_1 and n_1 from a single Δ and ψ measurement. The method requires a high resolution and accuracy in the measurement of Δ and ψ in determining the thickness, d_1, and index of refraction, n_1. It has a major draw-back in that, if (Δ,ψ) point is near the origin, there is a relatively large uncertainty in the value to be assigned for the refractive index, and also for the thickness, because of the near coincidence of the curves in this region. As pointed out in the Auto EL-III manual, most accurate determination of film refractive index and thickness occurs when the film thickness is between $\frac{1}{3}$ and $\frac{2}{3}$ the full-cycle thickness ($\beta = 0$ in equation III-32).

For an absorbing ($k_1 \neq 0$) film, n_1, k_1, and d_1 cannot be uniquely determined from a single measurement of Δ and ψ. This is because each point in the Δ,ψ plane corresponds to an unlimited number of different sets of film properties. It is then necessary to obtain enough data from films of different thicknesses to construct an experimental Δ,ψ curve that can be fitted by a calculated curve with an unambiguous choice of values for the optical constants. In the double-film model (Fig. III-7b), the parameters Δ and ψ are defined by the following equations:

$$\Delta = \Delta(\phi, \lambda, n_0, n_s, k_s, n_1, k_1, d_1, n_2, k_2, d_2) \quad ---(III-33)$$

$$\psi = \psi(\phi, \lambda, n_0, n_s, k_s, n_1, k_1, d_1, n_2, k_2, d_2) \quad ---(III-34)$$

Subscripts 1 and 2 refer to lower and upper films parameter, respectively.

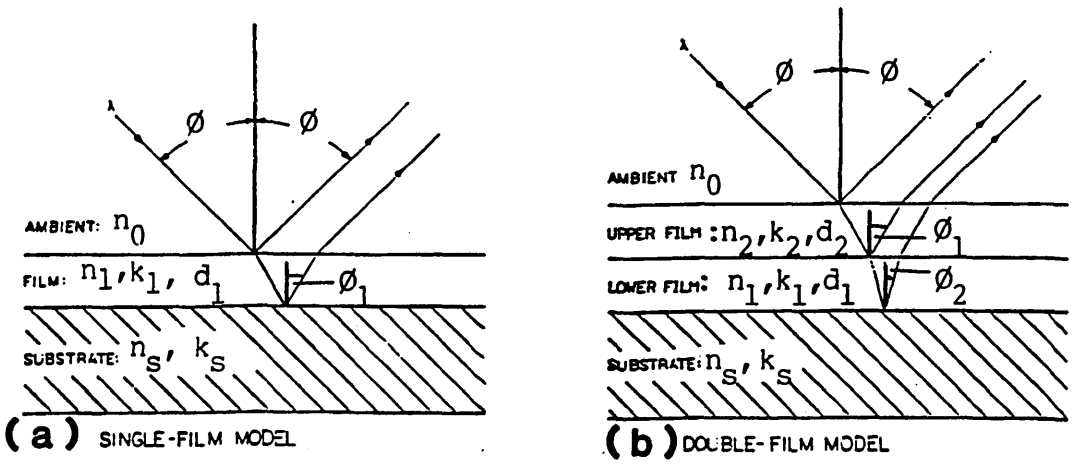


Figure III-7: Film-Substrate model. $n_i \pm k_i$ the refractive index, d_i the film thickness, where i = 0,1,2, and s. Ø the angle of incident, $Ø_1$ and $Ø_2$ the angle of refractions.

(iv) Summary

The basic theory of ellipsometry and its experimental application has been briefly described.

As observed from readings obtained in using the Auto EL ellipsometer, the accuracy and precision in measuring Δ and ψ (hence optical parameters of sample) could be attributed to two factors [7]: a lack of uniformity in the thickness of the films and small variations in index of refraction from film to film. The last effect is due to the fact that cadmium chloride ($CdCl_2$) or rather hydrated cadmium chloride ($CdCl_2.H_2O$) is birefringent.

III-3 STYLUS INSTRUMENT ("TALYSTEP")

Stylus instruments are widely used for the measurement of surface roughness, and surface finishing. The instrument is also used to measure film thickness. "Talystep" measures the film thickness by traversing the stylus across a "step" (formed by masking a portion of the substrate during the film deposition). The vertical displacement is converted to electrical signals by means of a transducer, the signal amplified and recorded (see Fig. 4.1.1)

A Rank Taylor Hobson (U.K.) Ltd Talystep instrument was used, and as various vertical amplification can be achieved with this instrument: film thickness in the range of 2nm up to 10μm is possible. The accuracy of film thickness measured was within ±5% when compared to ellipsometer measurement.

In situation where the trace on both sides leading to the step has gradients other than zero, the slopes have to be considered, and film thickness corresponds to the vertical distance between linear extrapolations of the lower and upper portions of the trace.

The main advantage of this film thickness measurement technique is that any type of surface can be examined, provided it is not so soft as to be deformed by the stylus.

APPENDIX IV

PRELIMINARY INVESTIGATION OF ELECTRON BEAM IRRADIATION OF URANIUM TETRA-CHLORIDE (UCl_4) FILMS

As discussed in section 5.2.2, the x-ray absorption coefficient, α, (in cm^2/g) of a material is given by;

$$\alpha = CZ^4\lambda^3$$

where Z is the atomic number of the material, λ is the x-ray wavelength in Å, and C for each material is a constant only in the region between the discrete absorption edges. The value of C changes abruptly at the wavelengths characteristic of the material. Thus, uranium which has a high atomic number, should be highly suitable for the absorbing layer of an x-ray mask. It was proposed (see section 5.3) that the absorber pattern might be written by the e-beam decomposition of UCl_4.

Synthesis of UCl_4 was carried out as follows. Uranium was heated in a stream of chlorine gas, in which it ignited. Solubility tests [1,2] on the synthesised product were carried out, which produced hissing sound. The synthesised product was exposed to laboratory air for a period long enough to form a yellowish-green liquid. These two tests could only imply that the synthesised material was uranium penta-chloride (UCl_5) [1,2]. The process of formation was via the following reaction.

$$2U(s) + 6Cl_2(g) \xrightarrow{\text{heat}} 2UCl_5(s) + Cl_2(g)$$

The dissociation reaction of UCl_5, which is a reversible process is given according to the following equation [2],

$$2UCl_5 \rightleftharpoons 2UCl_4 + Cl_2$$

The dissociation process could proceed at ambient temperature, at a very slow rate, or during the degassing stage that preceeded the vacuum deposition of UCl_4 film.

Thin films of UCl_4 (ca. 100nm in thickness) deposited on oxidised silicon wafers, were e-beam irradiated at a temperature of $230^{o}C$. The e-beam had a diameter of 300μm, the beam energy was 2keV, and the current density was $140\mu A/cm^2$. The total number of coulombs per unit area, delivered to the material was $1C/cm^2$. The material was found not to decompose. UCl_4 films prepared as described above did not decompose under the specified experimental conditions, due probably to the formation of a pro-tective coating (most likely an oxide) on the surface. This could act as a barrier to electron beam-UCl_4 interaction. This conclusion stems from the general model for the decomposition of inorganic solids [3]. The model proposes that e-h pairs are produced (at the band edges) by in-coming primary electrons. The process is chemically activated, the activation energy for the process is related to the binding energy of the solid, which in turn is related to the melting point. The temperature at which significant e-beam induced decomposition mostly commences is $0.6T_m$, where T_m is the melting point of the material in degree Kelvin. The value of T_m for uranium di-oxide (UO_2) is 3151 ±20K [1]. Hence, a preceeding stage of surface atomic cleaning of the sample, might be necessary before decomposition can proceed.

APPENDIX V

A BRIEF NOTE ON EPMA MEASUREMENTS.

A JEOL JSM 35-CF scanning electron microscope (SEM) equipped with Link Analytical Systems was used for EPMA.

X-ray photons are generated as a result of electron beam - sample interaction, the energy of which is characteristic of the element which generated the x-ray photons. In addition to element identification, x-ray intensity of element relative to the intensity of characteristic x-rays of a known reference element, cobalt (Co), gives a measurement of the element concentration. The generated x-rays are converted to voltage pulses by a lithium doped silicon (Si) detector, usually with a thin beryllium window to reduce the background radiation. The voltage pulses are refined by a pulse processor, amplified and stored in a computer, in different memory locations (channels), according to their energy levels. Errors in analysis could be due to the atomic number (Z), absorption within the interaction volume (A), and fluorescence (F), collectively known as the ZAF effect [1]. Other sources of error are related to the statistics of x-ray counting signal measurement, physical condition and position of the samples, and the equipment calibration [2]. The computer was used to carried out the tedious task of error corrections.

The excitation depth of interaction was ~2μm (analysed film thickness was in the range of 50-150nm), which explains the huge Si signal in all the EPMA results. Element concentration analyses were normalised for the respective film composition (by subtraction of the Si concentration).

APPENDIX VI

SOLUTION OF THE ORDINARY DIFFERENTIAL EQUATION:-

$$\frac{\partial^2 n}{\partial x^2} - \frac{n}{\tau D} = -\frac{G}{D} \qquad \text{--------(1)}$$

The corresponding homogeneous equation is,

$$\frac{\partial^2 n}{\partial x^2} - \frac{n}{\tau D} = 0 \qquad \text{--------(2)}$$

Substituting $n = e^{mx}$ in the homogeneous equation, gives the characteristic equation, $m^2 - 1/L^2 = 0$, where $L = (\tau D)^{\frac{1}{2}}$.
Thus the complementary solution is

$$n = Ae^{-x/L} + Be^{x/L} \qquad \text{--------(3)}$$

A and B are constants.
Since G/D is a constant, the particular solution is of the form $n = K$, where K is a constant.
Thus the particular solution is,

$$n = G\tau \qquad \text{--------(4)}$$

Therefore the general solution is

$$n = Ae^{-x/L} + Be^{x/L} + G\tau \qquad \text{--------(5)}$$

Solution of equation (1) is subject to the following boundary conditions,

$$D\frac{\partial n}{\partial x}\Big|_{x=0} = S_r n_o \text{ , and } \frac{\partial n}{\partial x}\Big|_{x=d} = 0$$

Using these boundary conditions, the constants A and B are,

$$A = \frac{S_r n_o L e^{d/L}}{D(e^{-d/L} - e^{d/L})}, \text{ and } B = \frac{S_r n_o L e^{-d/L}}{D(e^{-d/L} - e^{d/L})}$$

REFERENCES

References for Chapter 1

[1] M. Hatzakis, "Lithographic Processes in VLSI Circuit Fabrication" in Scanning Electron Microscopy Meeting, Washington D.C, part 1, page 275-284 (1979)

[2] D.A. McGillis, "Lithography" in S.M. Sze (Ed.), VLSI Technology, chapter 7, McGraw-Hill Book Co., New York (1983).

[3] D.A. McGillis, and D.L. Fehrs, IEEE Trans. Electron Devices ED-22, 471 (1975).

[4] R.K. Watts, and J.H. Bruning, Solid State Technol. 24 (No.5), 99 (1981).

[5] J.S. Greeneich, "Electron-Beam Processes" in G.R. Brewer (Ed.), Electron-Beam Technology in Microelectronic Fabrication, Academic Press, New York (1980).

[6] P.R. Thornton, Advances in Electronics and Electron Physics 48, 271 (1979).

[7] I. Brodie and J.J. Muray, The Physics of Microfabrication, Plenum Press, New York (1982).

[8] B. Fay, "X-Ray Techniques and Registration Methods: Micro-Lithography" in H. Ahmed and W.C. Nixon (Eds.), Microcircuit Engineering, Cambridge University Press, London (1980).

[9] R.K. Watts, Solid State Technol. 22 (No.5), 68 (1979).

[10] D. Maydan, J. Vac. Sci. Technol. 17, 1164 (1980).

[11] B.T. Lin, "Optical Methods for Fine Line Lithography" in R. Newman (Ed.), Fine Line Lithography, North Holland, Amsterdam (1980).

[12] E.A. Chandross, E. Reichmanis, C.W. Wilkins Jr., and R.L. Hartless, Solid State Technol. 24 (No.8), 81 (1981).

[13] M. Hatzakis, Solid State Technol. 24 (No.8), 74 (1981).

[14] B.J. Lin, E. Bassous, V.W. Chao, and K.E. Petrillo, J. Vac. Sci. Technol. 19, 1313 (1981).

[15] W.L. Brown, T. Venkatesan, and A. Wagner, Solid State Technol. 24 (No.8), 60 (1981).

[16] T.W. O'Keeffe, and R.M. Handy, Solid State Electron. 11, 261 (1968)

[17] A. Yoshikawa, O. Ochi, H. Nagai, and Y. Mizushima, Appl. Phy. Lett. 31, 161 (1977).

[18] K.L. Tai, R.G. Vadimsky, C.T. Kemmerer, J.S. Wagner, V.E. Lamberti, and A.G. Timko, J. Vac. Sci. Technol. 17, 1169 (1980).

[19] B. Singh, S.P. Beaumont, P.G. Bower, and C.D.W. Wilkinson, Appl. Phy. Lett. 41, 1002 (1982).

[20] A. Murray, M. Scheinfein, M. Isaacson, and I. Adesida, J. Vac. Sci. Technol. B3(1), 367 (1985).

[21] M. Isaacson, and A. Murray, J. Vac. Sci. Technol. 19, 1117 (1981)

[22] K.D. Kolwicz, and M.S. Chang, J. Electrochem. Soc., 127, 135 (1980).

[23] G.W. Kammlott, and W. Robert Sinclair, J. Electrochem. Soc. 121, 929 (1974).

[24] T.R. Harrison, P.M. Mankiewich, and A.H. Dayem, Appl. Phys. Lett. 41, 1102 (1982).

[25] P.M. Mankiewich, H.G. Craighead, T.R. Harrison, and A.H. Dayem, Appl. Phys. Lett. 44, 468 (1984).

[26] I.G. Salisbury, R.S. Timsit, S.D. Berger, and C.J. Humphreys, Appl. Phys. Lett. 45, 1289 (1984).

[27] D.L. Flamm, V.M. Donnelly, and D.E. Ibbotson, "Basic Principles of Plasma Etching for Silicon Devices" in N.G. Einspruch and D.M. Brown (Eds.), VLSI Electronics: Microstructure Science 8, chapter 8, Academic Press Inc., London (1984).

[28] S.J. Fonash, Solid State Technol. 28 (No.1), 150 (1985).

[29] A.N. Broers, W.W. Molzen, J.J. Cuomo, and N.D. Wittels, Appl. Phys. Lett. 29, 596 (1976).

[30] Alan R. Reinberg, "Dry Processing for Fabrication of VLSI Devices" in N.G. Einspruch (Ed.), VLSI Electronics: Microstructure Science 2, chapter 1, Academic Press Inc., London (1981).

[31] H.F. Winters, and J.W. Coburn, Appl. Phys. Lett. 34, 70 (1979).

[32] D.E. Ibbotson, D.L. Flamm, and V.M. Donnelly, J. Appl. Phys. 54, 5974 (1983).

[33] S. Dzioba, Electrochemical Society Meeting, New Orleans, Oct. 1984.

[34] D.J. Ehrlich, and J.Y. Tsao, J. Vac. Sci. Technol. B1(4), 969 (1983).

[35] C.J. Mogab, "Dry Etching", in S.M. Sze (Ed.), VLSI Technology, chapter 8, McGraw-Hill Book Co., New York, (1983).

[36] (a) D. Bollinger, S. Lida, and O. Matsumoto, Solid State Technol. 27 (No.5), 111 (1984).
(b) D. Bollinger, S. Lida, and O. Matsumoto, Solid State Technol. 27 (No.6), 167 (1984).

[37] J.W. Coburn, and H.F. Winters, J. Vac. Sci. Technol. 16, 391 (1979).

[38] A. Jacob, Solid State Technol. 26 (No.4), 151 (1983).

[39] D.L. Flamm, and V.M. Donnelly, Plasma Chem. and Plasma Process. 1, 317 (1981).

[40] C.J. Mogab, A.C. Adams, and D.L. Flamm, J. Appl. Phys. 49, 3796 (1978).

[41] L.M. Ephrath, J. Electrochem. Soc. 126, 1419 (1979).

[42] K. Hirata, Y. Ozaki, M. Oda, and M. Kimizuka, IEEE Trans. Electron. Devices ED-28, 1323 (1981).

[43] G.C. Schwartz, and P.M. Schaible, J. Vac. Sci. Technol. 16, 410 (1979).

[44] C.J. Mogab, J. Electrochem. Soc. 124, 1262 (1977).

[45] B. Gorowitz, and R.J. Saia, "Reactive Ion Etching" in N.G. Einspruch and D.M. Brown (Eds.), VLSI Electronics: Microstructure Science 8, chapter 10, Academic Press Inc., London (1984).

[46] C.J. Mogab, and H.J. Levinstein, J. Vac. Sci. Technol. 17, 721 (1980).

[47] L.M. Ephrath, D.J. DiMaria, and F.L. Pesavento, J. Electrochem. Soc. 128, 2415 (1981).

[48] R.A.H. Heinecke, Solid State Electron. 19, 1039 (1976).

[49] R.A.H. Heinecke, Solid State Electron. 18, 1146 (1975).

[50] S. Matsuo, and Y. Takehara, Jpn. J. Appl. Phys. 16, 175 (1977).

[51] S. Matsuo, Jpn. J. Appl. Phys. 17, 235 (1978).

[52] H.W. Lehmann, and R. Widmer, J. Vac. Sci. Technol. 15, 319 (1978).

[53] H.W. Lehmann, and R. Widmer, Appl. Phys. Lett 32, 163 (1978).

[54] J.W. Coburn, and H.F. Winters, Ann. Rev. Mater. Sci. 13, 91 (1983).

[55] J.W. Coburn, H.F. Winters, and T.J. Chuang, J. Appl. Phys. 48, 3532 (1977).

[56] (a) J.W. Coburn, J. Appl. Phys. 50, 5210 (1979).
(b) J.W. Coburn, and H.F. Winters, J. Appl. Phys. 50, 3189 (1979).

[57] F.D. Egitto, D.N.K. Wang, D. Maydan, and D. Benzing, Solid State Technol. 24 (No.12), 71 (1981).

[58] G. Smolinsky, D.N.K. Wang, and D. Maydan, in J.Dieleman and R.G. Frieser (Eds.), Plasma Processing vol 82-6, Electrochem. Soc., Pennington, New Jersey (1982).

[59] L.M. Ephrath and R.S. Bennett, J. Electrochem. Soc. 129, 1822 (1982).

[60] J.P. Roland, P.J. Marcoux, G.W. Ray, and G.H. Rankin, J. Vac. Sci. Technol. A3(3), 631 (1985).

[61] P.J. Marcoux, and P.W. Foo, Solid State Technol. 24 (No.4), 115 (1981).

References for Chapter 2

[1] J.C. Bailar, H.J. Emeleus, Sir Ronald Nyholm, and A.F. Trotman-Dickenson, Comprehensive Inorganic Chemistry vol.3, Pergamon Press, Oxford (1973).

[2] Ralph W.G. Wyckoff, Crystal Structures vol.1 2nd edition, John Wiley and Sons, New York (1963).

[3] A.F. Wells, Structural Inorganic Chemistry 5th edition, Clarendon Press, Oxford (1984).

[4] D.M. Adams, Inorganic Solids: An Introduction to Concepts in Solid State Structural Chemistry, John Wiley and Sons, London (1974).

[5] J.C. Slater, J. Chem. Phys. 41, 3199 (1964).

[6] Mino Green and M.J. Lee "Simple Complexes on Semiconductor Surfaces" in Mino Green (Ed.), Solid State Surface Science vol.1, Marcel Dekker Inc., New York (1969).

[7] C. Kittel, Introduction to Solid State Physics 5th edition, John Wiley and Sons, New York (1976).

[8] J.D.H. Donnay, and Helen M. Ondik (Eds.), Crystal Data Determinative Tables: Inorganic Compounds, vol.2 3rd edition, (1973).

[9] C.R.M. Grovenor, H.T.G. Hentzell, and D.A. Smith, Acta Metall. 32, 773 (1984).

[10] B.A. Movchan, and A.V. Demchishin, Fizika Metall. 28, 83 (1969).

[11] J.A. Thornton, Ann. Rev. Mater. Sci. 7, 239 (1977).

[12] E. Eser, and R.B. Hall, Thin Solid Films 86, 31 (1981).

[13] B.D.Cullity, Elements of X-Ray Diffraction 2nd edition, Addison-Wesley Inc., (1978).

[14] Harold P. Klug, and Leroy E. Alexander, X-Ray Diffraction Procedures 2nd edition, John Wiley and Sons, New York (1974).

[15] Powder Diffraction File, Compiled by the Joint Committee on Powder Diffraction Standards (JCPDS): 27-1402, 27-73, 26-1150

[16] C.A. Wallace, and R.C.C. Ward, J. Appl. Crystal. 8, 255 (1975).

[17] A.W. Warner, "Ultra Micro Weight Determination in Controlled Environments" in S.P. Wolsky and E.J. Zdanu (Eds.), Interscience, New York (1969).

[18] A.W. Warner, and C.D. Stockbridge, Vac. Mic. Tech. 3, 55 (1963).

[19] G. Sauerbrey, Z.f. Phys. 155, 206 (1959).

[20] Mino Green, and O.A. Fakolujo, Thin Solid Films 150, L93 (1987).

References for Chapter 3

[1] O. Kubaschewski and C.B. Alcock, Metallurgical Thermochemistry 5th edition, Pergamon Press, Oxford (1979).

[2] John F. O'Hanlon, A User's Guide to Vacuum Technology, John Wiley and Sons, New York (1980).

[3] I. Brodie, and J.J. Muray, The Physics of Microfabrication, Plenum, New York (1982).

References for Chapter 4

[1] Mino Green, C.J. Aidinis, and O.A. Fakolujo, J. Appl. Phys. 57, 631 (1985).

[2] A.A. Iranmanesh, and R.F.W. Pease, J. Vac. Sci. Technol. B1(1), 91 (1983).

[3] O. Kubaschewski, and C.B. Alcock, Metallurgical Thermochemistry 5th edition, Pergamon Press, Oxford (1979).

[4] J.W. Coburn, "Plasma Etching and Reactive Ion Etching" in N. Rey Whetten (Ed.), American Vacuum Society Monograph Series, New York (1982).

[5] B.N. Chapman, T.A. Hansen, and V.J. Minkiewicz, J. Appl. Phys. 51, 3608 (1980).

[6] H.F. Winters, J.W. Coburn, and E. Kay, J. Appl. Phys. 48, 4973 (1977)

[7] W.D. Davis, and T.A. Vanderslice, Phys. Rev. 131, 219 (1963).

[8] J.W. Coburn, and H.F. Winters, J. Vac. Sci. Technol. 16, 391 (1979).

[9] C.J. Mogab, A.C. Adams, and D.L. Flamm, J. Appl. Phys. 49, 3796 (1978).

[10] W.R. Harshbarger, R.A. Porter, T.A. Miller, and P. Norton, Appl. Spectrosc. 31, 201 (1977).

[11] R.N. Castellano, Solid State Technol. 27 (No.5), 203 (1984).

[12] J.C. Bailar, H.J. Emeleus, Sir Ronald Nyholm, and A.F. Trotman-Dickenson, Comprehensive Inorganic Chemistry vol.3, Pergamon Press, Oxford (1973).

[13] M.G. Albrecht, and Mino Green, J. Phys. Chem. Solids, 38, 297 (1977).

[14] Mino Green, and T.A. Kuku, J. Phys. Chem. Solids 44, 999 (1983).

[15] I. Brodie, and J.J. Muray, The Physics of Microfabrication, Plenum, New York (1982).

References for Chapter 5

[1] Mino Green and C.J. Aidinis, "The Decomposition Kinetics of $CdCl_2$ Thin Films," Private communication.
C.J. Aidinis, Ph.D. Thesis, University of London (1987)

[2] M.G. Albrecht, and Mino Green, J. Phys. Chem. Solids 38, 297 (1977)

[3] M.G. Albrecht, Ph.D. Thesis, University of London (1975)

[4] Mino Green and T.A. Kuku, J. Phys. Chem. Solids 44, 999 (1983)

[5] A.C. Klein, J. Appl. Phys. 39, 2029 (1968)

[6] S.P. Tandom, and J.P. Gupta, Appl. Spectrosc. 25(2), 233 (1971).

[7] W. Shockley, Solid State Electronics 2 (No.1), 35 (1961)

[8] Mino Green, C. Aidinis, and O. Fakolujo, "E-beam Induced Decomposition of Inoraganic Solids," in V.T. Nguyen, and D.J. Ehrlich (eds.), NATO ASI Series on Workshop on Emerging Technologies for in-situ Processing, 1987.

[9] M.J. Bowden, "Electron Irradiation of Polymers and its Applications to Resists for Electron-Beam Lithography," in D.E. Schuele, and R.W. Hoffman (eds.), CRC Critical Reviews in Solid State and Materials Science, vol 8 (no.3) pg 223, (1979).

[10] M. Parikh, J. Vac. Sci. Technol. 15, 931 (1978).

[11] M. Parikh, and D.F. Kyser, J.Appl. Phys. 50, 1104 (1979).

[12] M. Parikh, J.Appl. Phys. 50, 4371, 4378, 4383 (1979).

[13] D.F. Kyser, D.E. Schreiber, C.H. Ting, and R. Pyle, "Proximity Function Approximations for Electron-Beam Lithography from Resist Profile Simulation," in R. Bakish (ed.), Proceedings of the 9th International Conference on Electron and Ion Beam Science and Technology, The Electrochemical Society, Princeton, N.J. (1980).

[14] N.D. Wittels, "Fundamentals of Electron and X-ray Lithography," in R. Newman (ed.), Fine-Line Lithography, North-Holland, New York, (1980).

[15] W.D. Grobman, and A.J. Speth, in R. Bakish (ed.), Proceedings of the 8th International Conference on Electron and Ion Beam Science and Technology, The Electrochemical Society, Princeton, N.J. (1978).

[16] E.F. Kaelble (Ed.), Handbook of X-rays, McGraw-Hill Inc. London (1967).

[17] Leonid V. Azaroff (Ed.), X-ray Spectroscopy, McGraw-Hill Inc. New York (1974).

[18] J.G. Brown, "X-rays and Their Applications," Plenum Press, London (1966).

[19] R.C. Weast (Ed.), Chemical Rubber Co. Handbook of Chemistry and Physics, 62nd edition, CRC Press Inc., Florida (1981-82).

[20] M. Karnezos, R. Ruby, B. Heflinger, H. Nakano, and R.Jones, J. Vac. Sci. Technol. B5(1), 283 (1987).

[21] Leon I. Maissel, and Reinhard Glang (Eds.), Handbook of Thin Film Technology, McGraw-Hill Inc. London (1970).

[22] A. Kluwe, and K.H. Muller, "Simple Method for the Defect Control in X-ray Mask Fabrication," in Microelectron. Eng. (Netherlands) vol. 5, No. 1-4, Dec. 1986.

[23] B. Fay, "X-ray Techniques and Registration Methods," in Microcircuit Eng., edited by H. Ahmed and W.C. Nixon, Cambridge University Press (New York) 1980.

[24] K. Suzuki, and J. Matsui, J. Vac. Sci. Technol. B4(1), 221 (1986).

[25] D.L. Spears, and H.I. Smith, Electronics Letters 8, 102 (1972).

[26] P.G. Gloersen, J. Vac. Sci. Technol. 12, 28 (1975).

[27] G.E. Georgiou, C.A. Jankoski, and T.A. Palumbo, Proc. SPIE 471, 96 (1984).

References for Appendix III

[1] Rolf H. Muller, "Principles of Ellipsometry" in Advances in Electrochemistry and Electrochemical Engineering 9, Optical Techniques in Electrochemistry, John Wiley and Sons, New York (1973).

[2] R.M.A. Azzam, and N.M. Bashara, "Ellipsometry and Polarised Light", North Holland, Amsterdam (1977).

[3] P. Drude, Ann. Phys. Chem. N.F. 36, 865 (1889).

[4] E. Passaglia, R.R. Stromberg, and J. Kruger, Eds., "Ellipsometry in the Measurement of Surfaces and Thin Films," Proc. Symposium Washington (1963), Nat. Bur. Stand. Misc. Publ. 256 (1964).

[5] U. Merkt, Appl. Optics 20, 307 (1981).

[6] Frank L. McCrackin, "Technical Note 479, A Fortran Program for Analysis of Ellipsometer Measurements," National Bureau of Standard, Washington D.C. (1969).

[7] R.J. Archer, J. Opt. Soc. Am. 52, 970 (1962).

[8] AutoEL^{R}-III Automatic Ellipsometer Instruction Manual.

[9] Talystep Operating Instructions Manual, "Rank Hobson (U.K) Ltd."

References for Appendix IV

[1] R.C. Weast (Ed.), Chemical Rubber Co. Handbook of Chemistry and Physics, 62nd edition, CRC Press Inc., Florida (1981-82).

[2] J.W. Mellor (Ed.), A comprehensive Treatise on Inorganic and Theoretical Chemistry, vol. XII, Pg. 84, Longmans, Green and Co. Ltd, London (1965).

[3] Mino Green, C. Aidinis, and O. Fakolujo, "E-beam Induced Decomposition of Inoraganic Solids," in V.T. Nguyen, and D.J. Ehrlich (eds.), NATO ASI Series on Workshop on Emerging Technologies for in-situ Processing, 1987.

References for Appendix V

[1] D.K. Bowen, and C.R. Hall (Eds.), "Microscopy of Materials," Macmillan Press Ltd, (1975).

[2] T.O. Ziebold, Anal. Chem. 39, 858 (1967).